Principles of Magnetic Resonance Imaging

Dwight G. Nishimura

Principles of

Magnetic Resonance Imaging

Principles of

Magnetic Resonance Imaging

Dwight G. Nishimura

Department of Electrical Engineering
Stanford University

© Copyright 2010 by Dwight G. Nishimura
All Rights Reserved
Edition 1.2 (August 2016)

Printed by www.lulu.com

To Ann, Mark, and Peter

Contents

Contents vii
Preface . . . xi
Acknowledgements . . . xii

1 Introduction 1
1.1 Magnetic Resonance Imaging . . . 1
1.2 Historical Notes . . . 2
1.3 Organization . . . 2

2 Preliminaries 5
2.1 Complex Numbers . . . 5
2.2 Fourier Transforms . . . 6
2.2.1 One Dimensional . . . 6
2.2.2 Two Dimensional . . . 7
2.3 Projections and the Central Section Theorem . . . 10
2.3.1 Projections . . . 10
2.3.2 The Central Section Theorem . . . 11
2.4 Sampling . . . 12
2.5 Rotation Matrices . . . 15
2.6 Basic Probability . . . 17
2.6.1 Random Variables . . . 17
2.6.2 Random Processes . . . 19
2.7 Problems . . . 21

3 Overview 23
3.1 Classical Description of MR . . . 23
3.1.1 Main Field $\mathbf{B}_0$ . . . 24
3.1.2 Radiofrequency Field $\mathbf{B}_1$ . . . 24
3.1.3 Linear Gradient Fields $\mathbf{G}$ . . . 26
3.1.4 Bloch Equation . . . 27
3.2 Conventional MR Imaging Methods . . . 29

3.2.1 Selective Excitation 29
3.2.2 2D Imaging Methods 31
3.3 Other Approaches to MR Imaging 40
3.4 Imaging Considerations 41
3.5 Instrumentation 41
3.6 Problems 43

4 Physics **45**
4.1 Nuclear Spins 45
4.2 Interaction with a Static Magnetic Field 46
4.2.1 Magnetization 46
4.2.2 Precession 47
4.3 Interaction with a Radiofrequency Field 48
4.4 Relaxation 50
4.4.1 Longitudinal Relaxation 50
4.4.2 Transverse Relaxation 50
4.4.3 Relaxation Times of Biological Tissue 51
4.5 Bloch Equation 51
4.6 Chemical Shift 53
4.7 Problems 56

5 Imaging Principles **57**
5.1 Bloch Equation 57
5.1.1 Homogeneous Object, Uniform Field 58
5.1.2 Inhomogeneous Object, Nonuniform Field 61
5.2 Signal Equation 63
5.2.1 Other Considerations of the Signal Equation 65
5.3 Alternate Derivation: Signal Equation 69
5.4 Fourier Interpretation of the Signal Equation 70
5.5 Illustration of the *k*-Space Perspective 72
5.6 Basic 2D Imaging Methods 74
5.6.1 2D Projection Reconstruction 74
5.6.2 2D Fourier Transform 78
5.7 Sampling Requirements: 2DFT Imaging 84
5.7.1 Field of View 84
5.7.2 Spatial Resolution 89
5.7.3 DFT Image Reconstruction 93
5.8 Problems 94

6 Excitation **99**
6.1 Basic Excitation Principles 100
6.1.1 General Formulation 100
6.1.2 Rotating Frame Transformation 102
6.1.3 Graphical and Analytical Solutions 104
6.2 Selective Excitation 107
6.2.1 General Formulation 109
6.2.2 Small Tip-Angle Approximation 111
6.2.3 Refocusing 112
6.2.4 General Selective Excitation Example 114
6.3 Excitation k-Space Interpretation 118
6.4 Selective Excitation Pulse Design 120
6.5 Problems 124

7 Imaging Considerations **127**
7.1 Off-Resonance Sources 127
7.1.1 Off-Resonance Effects on the FID 129
7.1.2 Off-Resonance Effects on Imaging 129
7.1.3 Echoes 134
7.1.4 Spin Echoes in Imaging 140
7.2 T_2 Relaxation 144
7.3 Other Nonidealities 145
7.3.1 Radiofrequency Field Considerations 145
7.3.2 Gradient Field Considerations 146
7.4 Image Contrast 147
7.4.1 Saturation Recovery 148
7.4.2 Inversion Recovery 152
7.5 Noise Considerations 154
7.5.1 Physical and Instrumental Parameters 155
7.5.2 Imaging Sequence Parameters 160
7.6 Problems 167

8 Volumetric Imaging and Fast Imaging **175**
8.1 Volumetric Imaging 175
8.1.1 3D Imaging by Multiple 2D Slice Acquisition 175
8.1.2 3D *k*-Space Acquisition 178
8.1.3 Projective Imaging 185
8.2 Fast Imaging 186
8.2.1 **k**-Space Trajectories 186
8.2.2 Signal-Generation Approaches 191

9 Spectroscopic Imaging **193**
9.1 Effect of Chemical Shift on the Signal Equation 193
9.2 Spectroscopic Imaging Methods 194
9.2.1 3D Fourier Transform Spectroscopic Imaging 195
9.2.2 Spectroscopic Imaging with Time-Varying Gradients . . 198
9.2.3 N-Component Chemical Shift Imaging 199

10 Flow Imaging **203**
10.1 Flow Effects 203
10.1.1 TOF Effects 203
10.1.2 Phase Effects 205
10.2 Flow Imaging Methods 208
10.2.1 TOF-Based Methods 208
10.2.2 Phase-Based Methods 210

11 Instrumentation **213**
11.1 Main Field 213
11.2 Radiofrequency Field 214
11.3 Gradient Fields 217

A Useful Constants and Conversions **219**

Bibliography **221**

Index **224**

Preface

This book gives an introduction to magnetic resonance (MR) imaging, a remarkably rich field that touches on many disciplines in medicine, science, and engineering. Because of this richness, this book makes no attempt to provide a comprehensive treatment. Instead, the goal is to present a manageable introduction to MR imaging by focusing on the basic principles of image formation, image content, and performance considerations. Greater emphasis is given to the signal processing elements than to the physics and life-science elements of MR imaging.

This book grew out of notes prepared for a graduate-level course in electrical engineering at Stanford. A background in Fourier transforms serves as the primary prerequisite. Elegant Fourier descriptions pervade the analysis of MR. Likewise, MR serves as a beautiful physical example of Fourier transforms.

Although structured for electrical engineering students, the material should be accessible to those from other technical fields. In a 10-week quarter (approximately 27 lecture hours), it is reasonable to cover Chapters 3–7, which represent the bulk of the material. The latter chapters (Chapters 8–11) provide brief overviews of imaging extensions and selected topics. A semester-long course could cover the entire book, with time for additional topics such as image reconstruction and imaging applications. Problems at the end of the chapters are provided not only to review the concepts but to challenge the student to apply these concepts in new situations.

Finally, it is worth mentioning that this book has long been a work-in-progress. Much more material could be included. However, I have received feedback that the book is usable in its current form so I have decided to make it available now.

Dwight G. Nishimura

Acknowledgements

For over 25 years, I have had the pleasure and privilege of working in MR with many talented people at Stanford in the Magnetic Resonance Systems Research Lab (MRSRL). These people, too numerous to list (see www-mrsrl.stanford.edu for a partial list), have substantially shaped the content of this book. I am particularly indebted to Albert Macovski who introduced me to medical imaging and whose profound insights are an important part of this book. Special thanks go to Steven Conolly, Bob Hu, Craig Meyer, John Pauly, Greig Scott, and Graham Wright for many helpful discussions. I also express my appreciation to Shuye Huan for her tireless handling of past printings of this book.

I wish to acknowledge Ronald Bracewell and Joseph Goodman for their early guidance and inspiration. I also wish to thank the students and teaching assistants of EE 369B (formerly EE 492B) who endured early versions of this book, toiled diligently through the problems, and provided invaluable feedback.

Finally, I am extremely grateful to my family and, most importantly, to Ann for their unwavering and unconditional support.

Dwight G. Nishimura

Chapter 1

Introduction

The discovery of x-rays by Roentgen in 1895 brought a new and powerful capability to the practice of medicine—visualizing the interior of the human body without surgical intervention. Today, an array of medical imaging modalities exist, including x-ray computed tomography (CT), ultrasound, nuclear medicine, and magnetic resonance (MR).

1.1 Magnetic Resonance Imaging

This book is about magnetic resonance, a powerful noninvasive imaging modality that has gained widespread usage. Standard applications of MR include diagnostic studies of the central nervous system and musculoskeletal system. MR imaging remains a very active area of research and entirely new medical applications may eventually emerge. Although referred to as *nuclear* magnetic resonance (NMR) in the chemistry and physics communities, the imaging community often omits the word "nuclear" to avoid the negative connotations associated with that word. Ironically, MR imaging involves no ionizing radiation and presents no known health risk under normal operating conditions. (Note: "MR imaging" is commonly referred to as "MRI" and occasionally though awkwardly as "MRI Imaging.")

An important characteristic of MR imaging is its flexibility. MR offers a wide range of physical parameters to image and a plethora of instrumental parameters to set for control of image content. In addition to anatomic imaging, valuable metabolic information is available with MR, thereby opening the possibilities of noninvasive *in vivo* physiological studies. MR is often compared to x-ray CT because both enable cross-sectional imaging. Although physical constraints restrict CT images to transverse

cross-sections, MR images can be made of planes at an arbitrary orientation. Moreover, MR images possess comparable spatial resolution and far superior soft-tissue contrast. Representative MR images in Fig. 1.1 demonstrate the exquisite anatomical detail possible with MR. Shortcomings of MR include the sophisticated and expensive hardware required, the centerpiece of which is a large powerful magnet that can present siting challenges in a hospital. Also, conventional MR imaging methods may involve scan times of several minutes, making nonstationary regions (e.g., abdomen) more difficult to image.

1.2 Historical Notes

NMR in condensed matter was discovered independently by Felix Bloch [Blo46] and Edward Purcell [PTP46] in 1946, a discovery for which they shared the Nobel Prize in Physics. NMR has long been used in chemistry and physics for studying molecular structure and diffusion. In 1973, Paul Lauterbur reported the first MR image [Lau73] using linear gradient fields. During the 1970s, most of the work in MR imaging took place in academia—primarily in the United Kingdom. In the 1980s however, industry joined forces with universities, investing substantial resources to develop imaging systems for clinical use in medical centers. As a result, image quality improved dramatically and clinical imagers proliferated across the world. Overall, this rapidly-growing field encompasses an array of disciplines and many new developments continue to emerge. In 2003, the Nobel Prize in Physiology or Medicine was awarded to Lauterbur and Sir Peter Mansfield for their discoveries in MR imaging.

1.3 Organization

The emphasis of this textbook is on developing a description of MR imaging from a systems perspective. Fourier-domain descriptions pervade MR analyses; hence, the material in this book is founded largely on Fourier transform and linear systems theory, the basic principles of which are reviewed in Chapter 2. Those readers unfamiliar with multi-dimensional Fourier transform theory may find Chapter 2 particularly useful. Chapter 2 also contains other mathematical preliminaries such as rotation matrices and basic probability.

Chapter 3 provides a general overview of the material on MR imaging that will be more fully developed in the subsequent chapters. The goal of this early chapter is to foster a physical intuition of the fundamental

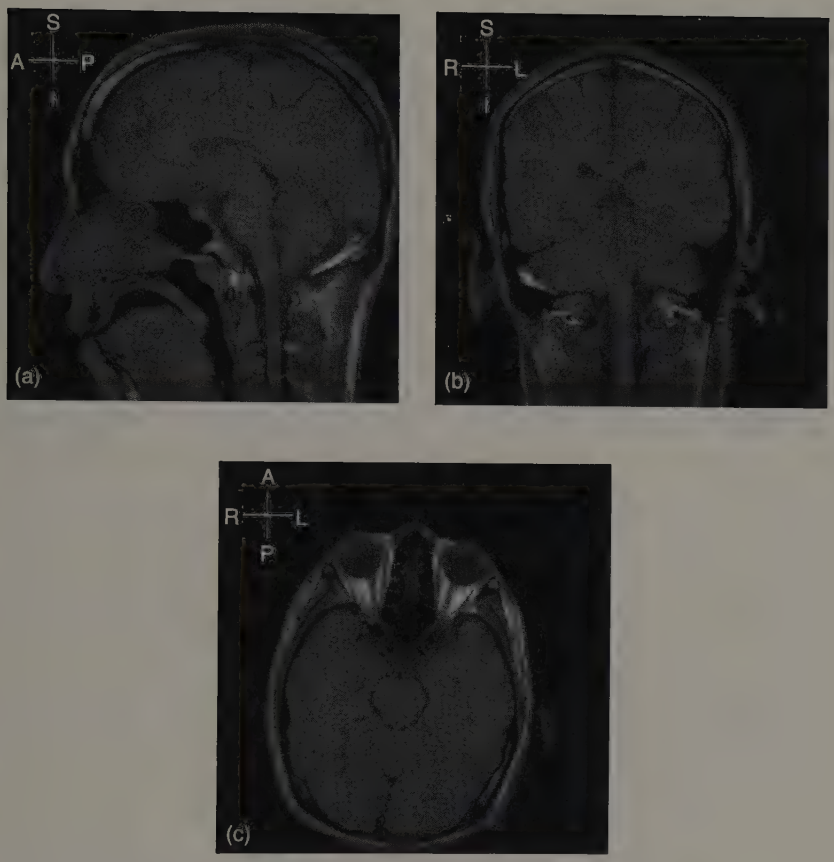

Figure 1.1: Representative Cross-Sectional Brain Images: (a) Sagittal cross section; (b) Coronal cross section; (c) Transaxial cross section. Sagittal, coronal, and transaxial (or simply axial) refer to the slice orientation as illustrated. The images are presented in a standard display format with anatomical location labels: anterior (A), posterior (P), superior (S), inferior (I), left (L), and right (R). Note that the "anatomic right" appears on the "image left" in the coronal and axial images.

concepts. Those who have studied MR imaging would probably agree that the underlying principles, while elegant, may lack intuitive appeal initially. Therefore, Chapter 3 should be viewed as a gentle survey of the material.

Although the emphasis of this book is on the systems analysis of MR imaging, Chapter 4 gives background information on the basic physics of nuclear magnetic resonance. For the purposes of this book, a classical description of the physics will suffice.

Conventional MR imaging sequences may be divided into two parts: excitation and reception. Nuclei are excited by a radiofrequency magnetic field and produce a time signal which is recorded and processed to form an image. Chapter 5 delves into the basic principles involved in the reception portion of imaging while Chapter 6 deals with the excitation portion. It will be easier and more convenient to discuss the reception portion first. In both chapters however, elegant Fourier-domain perspectives will emerge from the analyses.

While Chapter 5 describes imaging from an idealized perspective, Chapter 7 considers the effects of system imperfections and physical constraints on imaging. Also considered are image contrast and noise, both of which are important issues with respect to disease diagnosis. In Chapter 8, extensions to the basic imaging sequences are examined, specifically volumetric (3D) imaging and fast imaging.

Chapter 9 touches on another imaging extension, spectroscopic imaging, which concerns the imaging of specific chemical species with subtle frequency differences. Mapping of such species can provide useful physiological information. Flow imaging is the topic of Chapter 10. Several approaches exist to make MR sensitive to flowing material, enabling direct imaging or measurement of flowing material. The final chapter, Chapter 11, gives a brief overview of MR instrumentation issues.

Chapter 2

Preliminaries

This chapter contains a review of some mathematics and principles that will be useful for understanding the concepts that follow in the subsequent chapters.

2.1 Complex Numbers

A complex number c can be expressed as

$$c = a + ib \tag{2.1}$$

where $i = \sqrt{-1}$. Hence the real and imaginary parts of c are simply

$$\begin{aligned} \mathrm{Re}\{c\} &= a \\ \mathrm{Im}\{c\} &= b \end{aligned} \tag{2.2}$$

Alternatively, c can be expressed as

$$c = Ae^{i\phi} = A(\cos\phi + i\sin\phi) \tag{2.3}$$

where A, the magnitude, and ϕ, the phase, are given by

$$\begin{aligned} A &= \sqrt{a^2 + b^2} \\ \phi &= \tan^{-1}\frac{b}{a} \end{aligned} \tag{2.4}$$

In MR, phase plays an extremely important role. Phase is typically referenced with respect to the x-axis ($\phi = 0$), although the relative phase is often the important quantity.

It is convenient to use the complex number c to describe a vector residing in a plane with axes, say, in x and y. Hence a and b correspond to the x and y components respectively, while A and ϕ pertain to the vector's length and direction. Often considered is the case of a vector of magnitude A rotating in the xy plane at some angular frequency ω in the clockwise direction and some starting phase $\phi_\circ$. This time-varying vector can be expressed as

$$c(t) = Ae^{i(-\omega)t}e^{i\phi_\circ} = Ae^{-i\omega t}e^{i\phi_\circ} \tag{2.5}$$

where the $-\omega$ suggests clockwise rotation.

2.2 Fourier Transforms

This section surveys the basic principles and theorems of Fourier transforms. A more in-depth coverage can be found in [Bra00, Pap62].

2.2.1 One Dimensional

The one-dimensional (1D) Fourier transform of a function $f(x)$ is

$$F(k_x) = \int_{-\infty}^{\infty} f(x)e^{-i2\pi k_x x}\, dx \tag{2.6}$$

where $F(k_x)$ is commonly called the frequency spectrum of $f(x)$. The Fourier transform integral can be rewritten as

$$F(k_x) = \int_{-\infty}^{\infty} f(x)\cos 2\pi k_x x\, dx - i\int_{-\infty}^{\infty} f(x)\sin 2\pi k_x x\, dx \tag{2.7}$$

The Fourier transform decomposes the function $f(x)$ into its cosinusoidal and sinusoidal components at all frequencies k_x. If $f(x)$ is real-valued, then—from Eq. 2.7 and the fact that $f(x)$ is decomposable into the sum of an even function and an odd function—$F(k_x)$ possesses *Hermitian* symmetry; that is,

$$F(-k_x) = F^*(k_x) \tag{2.8}$$

Therefore the real part of $F(k_x)$ is an even function while the imaginary part of $F(k_x)$ is an odd function. Similarly, if $f(x)$ is strictly imaginary-valued, then

$$F(-k_x) = -F^*(k_x) \tag{2.9}$$

a symmetry referred to as *anti-Hermitian*. Table 2.1 lists some functions and their Fourier transforms. The units of x and k_x are the reciprocal of

each other; hence if x is in mm, then k_x is in cycles/mm. Also common is the use of reciprocal variables t and f, where t is in units of sec and f in units of cycles/sec or Hertz (Hz).

To recover $f(x)$ from $F(k_x)$, the inverse 1D Fourier transform is

$$f(x) = \int_{-\infty}^{\infty} F(k_x) e^{+i2\pi k_x x}\, dk_x \tag{2.10}$$

2.2.2 Two Dimensional

The Fourier integral expands into multiple dimensions by the inclusion of additional integrals and complex exponentials. For the case of a two-dimensional (2D) Fourier transform, the integral becomes

$$\begin{aligned} F(k_x, k_y) &= \int_{-\infty}^{\infty}\int_{-\infty}^{\infty} f(x,y) e^{-i2\pi(k_x x + k_y y)}\, dx\, dy && (2.11) \\ &= \int_{-\infty}^{\infty}\int_{-\infty}^{\infty} f(x,y) \cos 2\pi(k_x x + k_y y)\, dx\, dy \\ &\quad -i\int_{-\infty}^{\infty}\int_{-\infty}^{\infty} f(x,y) \sin 2\pi(k_x x + k_y y)\, dx\, dy && (2.12) \end{aligned}$$

Because the variables x and y often correspond to spatial coordinates when dealing with 2D functions, the typical unit for x and y is mm and thus the unit for k_x and k_y is cycles/mm. Therefore k_x and k_y are variables representing *spatial frequency* (as opposed to temporal frequency as in the 1D case when the dimension of x is time). A spatial frequency component is a sinusoidal variation over 2D space. For example, when dealing with images, the amplitude that varies over space is the gray level.

The 2D Fourier transform decomposes the 2D function into its spatial frequency components. Figure 2.1 shows an example of a cosinusoidal component at a particular spatial frequency. Figure 2.1a depicts this component as an grayscale image while Fig. 2.1b is a mesh plot representation. In two dimensions, a spatial frequency component is defined by two parameters, k_x and k_y, or, equivalently, its magnitude $|k|$ and direction θ. The period L of the sinusoid is given by $1/|k|$.

Two special cases of 2D functions are separable functions and circularly symmetric functions.

Separable Functions

A function $f(x,y)$ is separable in Cartesian coordinates if it can be written as $f_X(x) f_Y(y)$. For example, the box function $^2\sqcap(x,y)$ is separable, being equal to $\sqcap(x)\sqcap(y)$. With separable 2D functions, their 2D Fourier

$f(x)$	$F(k_x)$
$\sqcap(x) \triangleq \begin{cases} 1 & \text{if } \lvert x \rvert \leq 1/2 \\ 0 & \text{otherwise} \end{cases}$	$\frac{\sin \pi k_x}{\pi k_x} \triangleq \operatorname{sinc}(k_x)$
$e^{-\pi x^2}$	$e^{-\pi {k_x}^2}$
1	$\delta(k_x)$
$e^{i2\pi k_\circ x}$	$\delta(k_x - k_\circ)$
$\delta(x - x_\circ)$	$e^{-i2\pi k_x x_\circ}$
$\text{Ш}(x) \triangleq \sum_{i=-\infty}^{\infty} \delta(x - i)$	$\text{Ш}(k_x)$
$\cos 2\pi k_\circ x$	$\frac{1}{2}[\delta(k_x + k_\circ) + \delta(k_x - k_\circ)]$
$\sin 2\pi k_\circ x$	$i\frac{1}{2}[\delta(k_x + k_\circ) - \delta(k_x - k_\circ)]$

Table 2.1: 1D Fourier Transforms.

$f(x,y)$ or $f(r)$	$F(k_x,k_y)$ or $F(\varrho_k)$
${}^2\sqcap(x,y) \triangleq \sqcap(x)\sqcap(y)$	$\operatorname{sinc}(k_x)\operatorname{sinc}(k_y)$
$e^{-\pi(x^2+y^2)} = e^{-\pi r^2}$	$e^{-\pi({k_x}^2+{k_y}^2)} = e^{-\pi {\varrho_k}^2}$
1	${}^2\delta(k_x,k_y)$
${}^2\delta(x - x_\circ, y - y_\circ)$	$e^{-i2\pi(k_x x_\circ + k_y y_\circ)}$
$\cos 2\pi(k_1 x + k_2 y)$	$\frac{1}{2}[{}^2\delta(k_x + k_1, k_y + k_2) + {}^2\delta(k_x - k_1, k_y - k_2)]$
$\sin 2\pi(k_1 x + k_2 y)$	$i\frac{1}{2}[{}^2\delta(k_x + k_1, k_y + k_2) - {}^2\delta(k_x - k_1, k_y - k_2)]$
$\sqcap(r)$	$\frac{J_1(\pi\varrho_k)}{2\varrho_k} \triangleq \operatorname{jinc}(\varrho_k)$

Table 2.2: 2D Fourier Transforms.

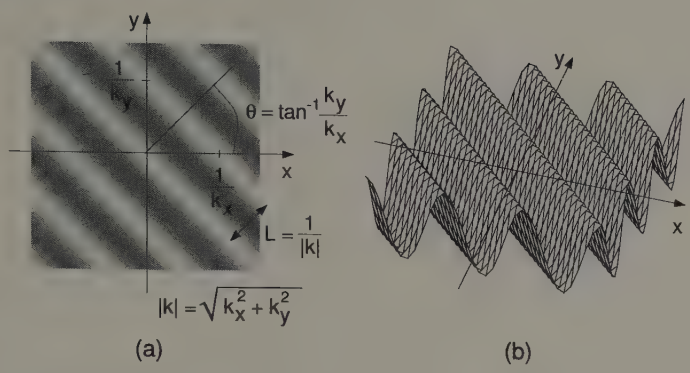

Figure 2.1: $\cos 2\pi(k_x x + k_y y)$: (a) grayscale representation; (b) mesh plot representation.

transforms are simply the product of the individual 1D Fourier transforms. Thus,

$$\mathcal{F}_{2D}\{f(x,y)\} = \mathcal{F}_{1D}\{f_X(x)\}\,\mathcal{F}_{1D}\{f_Y(y)\} \tag{2.13}$$

Circularly Symmetric Functions

A 2D function with circular symmetry may be expressed as $f(r)$ where r is the radial distance from the origin. An example is $\sqcap(r)$ which represents a circle function with unit diameter. If the object is circularly symmetric, then its 2D Fourier transform will also be circularly symmetric, expressible as $F(\varrho_k)$, where ϱ_k is the radial spatial frequency variable. In this special case, the 2D Fourier transform integral can be rewritten as an integral over just the variable r. The transform becomes

$$\mathcal{F}_{2D}\{f(r)\} = F(\varrho_k) = 2\pi \int_0^\infty r f(r) J_0(2\pi r \varrho_k)\, dr \tag{2.14}$$

This expression is called the *Hankel transform of zero order.* The inverse Hankel transform (and hence the inverse 2D Fourier transform) takes the same form as the forward Hankel transform. Thus

$$\mathcal{F}_{2D}^{-1}\{F(\varrho_k)\} = f(r) = 2\pi \int_0^\infty \varrho_k F(\varrho_k) J_0(2\pi r \varrho_k)\, d\varrho_k \tag{2.15}$$

Table 2.2 lists several 2D Fourier transforms of some useful functions.

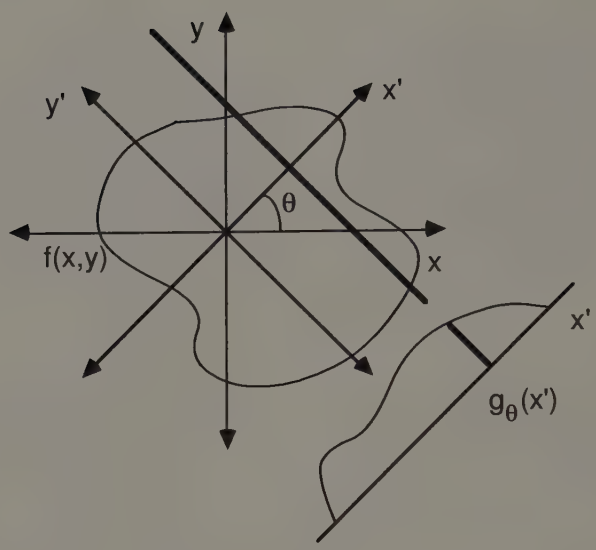

Figure 2.2: 1D Projection $g_\theta(x')$ of a 2D Function $f(x,y)$ obtained by integrating $f(x,y)$ along the y' direction.

2.3 Projections and the Central Section Theorem

2.3.1 Projections

A 1D parallel projection of a 2D function arises by integrating the 2D function along some direction. The projection represents a compressed or "shadow" version of the 2D function. For example, a projection taken along the y-axis is

$$g(x) = \int_y f(x,y)\, dy \tag{2.16}$$

More generally, a projection taken along an arbitrary direction parameterized by θ is depicted in Fig. 2.2. Using a rotated coordinate system, the projection along y' is

$$g_\theta(x') = \int_{y'} f(x' \cos\theta - y' \sin\theta, x' \sin\theta + y' \cos\theta)\, dy' \tag{2.17}$$

where x' is the distance from the origin to the particular projection line of interest. For any given x' and θ, the value of $g_\theta(x')$ equals the integral of $f(x,y)$ along the line $x\cos\theta + y\sin\theta = x'$. The projection values are said to correspond to the *line integrals* of $f(x,y)$.

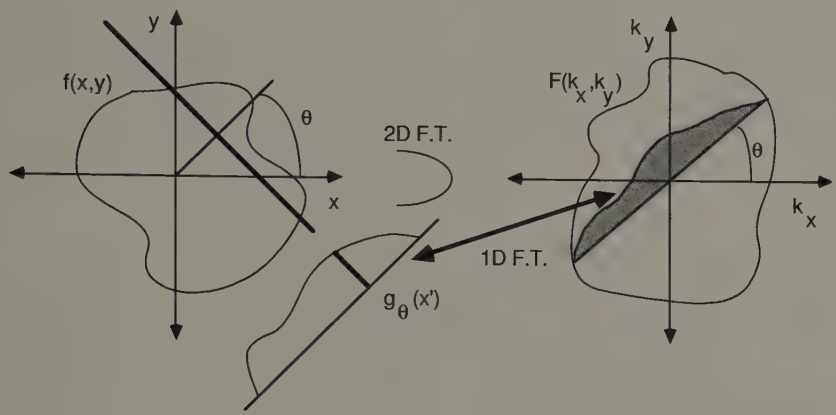

Figure 2.3: Central Section Theorem: The 1D Fourier transform of $g_\theta(x')$ equals the radial slice of $F(k_x, k_y)$ at that same angle θ.

2.3.2 The Central Section Theorem

Often, $f(x,y)$ is the function of interest but only projections of $f(x,y)$ are obtainable. For example, in a simple x-ray imaging setup, a source emits x-rays photons collimated into a pencil beam passing through the object. An x-ray detector measures the x-ray photons transmitted through object, providing the line-integral of the object's x-ray attenuation coefficient along the beam path. A 1D parallel projection is collected by sweeping this pencil beam in a linear fashion across the object. In x-ray computed tomography (CT), a set of such projections is accumulated at all angles about the object. The problem is how to reconstruct $f(x,y)$ given all of its projections.

The theorem that lends powerful insight into the information content of $g_\theta(x')$ is the Central Section Theorem (or Projection Slice Theorem), derived by Bracewell [Bra56].

> **Central Section Theorem:** Let $g_\theta(x')$ be the projection of $f(x,y)$ at some angle θ and let $F(k_x, k_y)$ be the 2D Fourier transform of $f(x,y)$. Then the 1D Fourier transform of the projection $g_\theta(x')$ equals the 2D Fourier transform $F(k_x, k_y)$ along the radial line at that same angle θ.

Figure 2.3 illustrates this theorem. The proof of this theorem can be shown

easily for the $\theta = 0$ case as

$$\begin{aligned}
\mathcal{F}_{1D}\{g(x)\} &= \int_x \left[\int_y f(x,y)\, dy\right] e^{-i2\pi k_x x}\, dx \\
&= \int_x \int_y f(x,y) e^{-i2\pi(k_x x + 0y)}\, dx\, dy \\
&= F(k_x, k_y = 0)
\end{aligned} \tag{2.18}$$

Because a rotation of coordinate systems does not fundamentally change matters, this result generalizes to other angles. The central section theorem makes clear that projections taken at all angles θ about the 2D object provides sufficient information to fill the 2D Fourier transform space of $f(x,y)$. Hence to reconstruct $f(x,y)$ from its projections, one can simply Fourier transform each projection, fill 2D Fourier transform space, and finally inverse 2D Fourier transform to recover $f(x,y)$.

2.4 Sampling

One-dimensional sampling of a function can be modeled by multiplying the function with a comb (also called *shah*) function $(1/\Delta)\,\text{Ш}(\cdot/\Delta)$ where $\text{Ш}(\cdot/\Delta)$ is an infinite string of equally-spaced delta functions separated by Δ, the sampling period. The $1/\Delta$ factor normalizes each delta function to unit strength. To describe the basic principles, we will consider 1D sampling in this section, although the extension to 2D sampling is straightforward as the 2D function would be multiplied by a 2D array of delta functions (a so-called "bed of nails" function).

Sampling in the time or object domain is a common scenario in many disciplines. In MR imaging however, we will be concerned primarily with the opposite situation of sampling in the frequency domain. Given a function $F(k_x)$, we can express its sampled version, $\hat{F}(k_x)$, as

$$\begin{aligned}
\hat{F}(k_x) &= F(k_x) \cdot \frac{1}{\Delta_{k_x}} \text{Ш}\left(\frac{k_x}{\Delta_{k_x}}\right) \\
&= F(k_x) \cdot \sum_{n=-\infty}^{\infty} \delta(k_x - n\Delta_{k_x}) \\
&= \sum_{n=-\infty}^{\infty} F(n\Delta_{k_x})\delta(k_x - n\Delta_{k_x})
\end{aligned} \tag{2.19}$$

Thus $\hat{F}(k_x)$ consists of a string of delta functions of amplitude given by the sample values $F(n\Delta_{k_x})$. The sampling *period* is Δ_{k_x}, corresponding

to a sampling *rate* of $1/\Delta_{k_x}$. Inverse Fourier transforming Eq. 2.19, the resultant function $\hat{f}(x)$ is

$$\begin{aligned}\hat{f}(x) &= \mathcal{F}^{-1}\{\hat{F}(k_x)\} \\ &= f(x) * \text{Ш}(\Delta_{k_x} x) \\ &= f(x) * \frac{1}{\Delta_{k_x}} \sum_{n=-\infty}^{\infty} \delta\left(x - \frac{n}{\Delta_{k_x}}\right) \\ &= \frac{1}{\Delta_{k_x}} \sum_{n=-\infty}^{\infty} f\left(x - \frac{n}{\Delta_{k_x}}\right) \end{aligned} \tag{2.20}$$

Equation 2.20 represents a function comprised of replicated versions of $f(x)$, where each replication "island" is separated by $1/\Delta_{k_x}$, the sampling rate. Figures 2.4a and 2.4b illustrate the behavior in the two domains.

If $f(x)$ is "space-limited"—that is, $f(x)$ is of finite extent—then the replicated versions of $f(x)$ are nonoverlapping if the sampling rate is sufficiently high. If the sampling rate is too low, then the replication islands overlap, resulting in a condition known as *aliasing*. The minimum sampling rate that avoids aliasing is called the *Nyquist* rate and is equal to the total extent of $f(x)$ (note that if the sampling period is in units of mm^{-1}, then the sampling rate in the frequency domain is in units of mm).

If sampling occurs over a finite extent, then Eq. 2.19 expands to

$$\hat{F}_W(k_x) = F(k_x) \cdot \frac{1}{\Delta_{k_x}} \text{Ш}\left(\frac{k_x}{\Delta_{k_x}}\right) \cdot \sqcap\left(\frac{k_x}{W_{k_x}}\right) \tag{2.21}$$

where W_{k_x} is the total extent sampled in frequency space (Fig. 2.4c). The total extent can be represented as

$$W_{k_x} = 2\left(k_{xmax} + \frac{\Delta_{k_x}}{2}\right) \tag{2.22}$$

where k_{xmax} is the maximum frequency sampled. In this definition of W_{k_x}, we add $\Delta_{k_x}/2$ to each side of the highest frequency sampled so that the borders of the rectangle function lie between sample points. Thus

$$W_{k_x} = \Delta_{k_x} \cdot N_{samples} \tag{2.23}$$

(the convenience of this definition will be appreciated below). The transform of Eq. 2.21 becomes

$$\begin{aligned}\hat{f}_W(x) &= \mathcal{F}^{-1}\{\hat{F}_W(k_x)\} \\ &= f(x) * \text{Ш}(\Delta_{k_x} x) * W_{k_x} \text{sinc}(W_{k_x} x) \end{aligned} \tag{2.24}$$

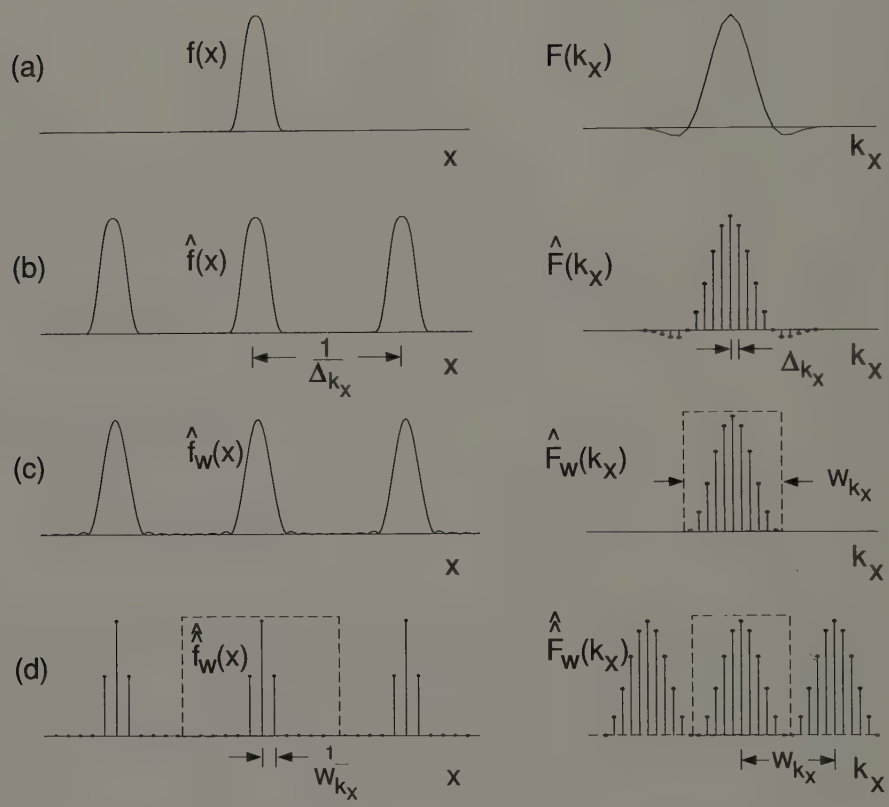

Figure 2.4: Sampling in the Frequency Domain: (a) Original functions. (b) Sampled function $\hat{F}(k_x)$ transforms to replicated version $\hat{f}(x)$ in x domain. (c) Finite sampling results in blurring with sinc function in x domain. (d) If $\hat{f}_W(x)$ is evaluated at discrete points separated by $1/W_{k_x}$, then replication of $\hat{F}_W(k_x)$ occurs every W_{k_x}, giving rise to periodic samples in both domains. One period of sample values in each domain are related by the DFT.

The effect of finite sampling in the frequency domain is to blur in the x domain by a sinc function of approximate width $1/W_{k_x}$ (Fig. 2.4c). Note that as k_{xmax} approaches ∞, $W_{k_x}\mathrm{sinc}(W_{k_x}x)$ approaches $\delta(x)$.

If we now sample $\hat{f}_W(x)$ with a period of $1/W_{k_x}$, the resultant function $\hat{\hat{f}}_W(x)$ is

$$\hat{\hat{f}}_W(x) = \hat{f}_W(x) \cdot W_{k_x} \text{Ш}(W_{k_x}x) \tag{2.25}$$

and its transform $\hat{\hat{F}}_W(k_x)$ is

$$\hat{\hat{F}}_W(k_x) = \hat{F}_W(k_x) * \text{Ш}(\frac{k_x}{W_{k_x}}) \tag{2.26}$$

Because $\hat{F}_W(k_x)$ is of finite extent (width W_{k_x}) sampling $\hat{f}_W(x)$ at a rate of W_{k_x} corresponds to the Nyquist rate and no aliasing occurs (Fig. 2.4d). In addition, both $\hat{\hat{f}}_W$ and $\hat{\hat{F}}_W$ consist of a periodic string of delta functions. One period of sample values in each domain are related by the Discrete Fourier Transform (DFT). Figure 2.4d thus shows the Fourier transform relationship between a finite set of samples and its DFT.

2.5 Rotation Matrices

Rotations in three-dimensional space are specified by two parameters: 1) the axis of rotation and 2) the rotation angle. On 3D vectors, rotations can be described by multiplication with a 3 by 3 rotation matrix. Often the axis of rotation will be about one of the major axes—x, y, or z. For example, a rotation about the z-axis by an angle α is represented by

$$\mathbf{R}_z(\alpha) = \begin{pmatrix} \cos\alpha & \sin\alpha & 0 \\ -\sin\alpha & \cos\alpha & 0 \\ 0 & 0 & 1 \end{pmatrix} \tag{2.27}$$

For convenience in describing MR, we adopt a *left-handed* convention for the rotation.

The inverse matrix corresponds to rotation in the opposite direction. Thus

$$\mathbf{R}_z^{-1}(\alpha) = \mathbf{R}_z(-\alpha) = \mathbf{R}_{-z}(\alpha) \tag{2.28}$$

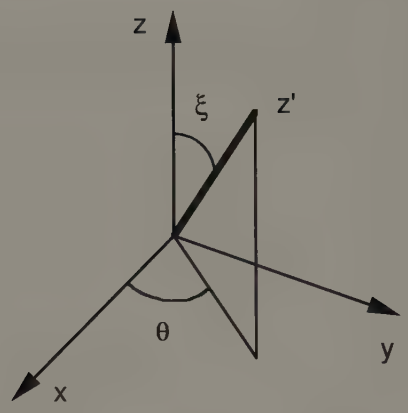

Figure 2.5: Rotation about a general axis z'.

The matrices for rotation about the other major axes are

$$\mathbf{R}_x(\alpha) = \begin{pmatrix} 1 & 0 & 0 \\ 0 & \cos\alpha & \sin\alpha \\ 0 & -\sin\alpha & \cos\alpha \end{pmatrix} \tag{2.29}$$

and

$$\mathbf{R}_y(\alpha) = \begin{pmatrix} \cos\alpha & 0 & -\sin\alpha \\ 0 & 1 & 0 \\ \sin\alpha & 0 & \cos\alpha \end{pmatrix} \tag{2.30}$$

To consider a rotation about a general axis z' specified by angles (θ, ξ) (Fig. 2.5), one approach is to first transform a vector $\mathbf{M}$ into $\mathbf{M}'$, its representation in the primed coordinate system. Using rotations about the major axes,

$$\mathbf{M}' = \mathbf{R}_y(\xi)\mathbf{R}_z(\theta)\mathbf{M} \tag{2.31}$$

Alternatively,

$$\mathbf{M} = \mathbf{R}_z(-\theta)\mathbf{R}_y(-\xi)\mathbf{M}' \tag{2.32}$$

Then, a rotation of $\mathbf{M}'(0)$ about z' by angle α (in time T) gives

$$\begin{aligned}\mathbf{M}'(T) &= \begin{pmatrix} \cos\alpha & \sin\alpha & 0 \\ -\sin\alpha & \cos\alpha & 0 \\ 0 & 0 & 1 \end{pmatrix} \mathbf{M}'(0) \\ &= \mathbf{R}_z(\alpha)\mathbf{M}'(0) \end{aligned} \tag{2.33}$$

Using Eqs. 2.31 and 2.32, we substitute for both $\mathbf{M}'(0)$ and $\mathbf{M}'(T)$, resulting in an expression in the original coordinate system of

$$\mathbf{M}(T) = \mathbf{R}_z(-\theta)\mathbf{R}_y(-\xi)\mathbf{R}_z(\alpha)\mathbf{R}_y(\xi)\mathbf{R}_z(\theta)\mathbf{M}(0) \tag{2.34}$$

Hence, the rotation about a general z'-axis is decomposable as

$$\mathbf{R}_{z'}(\alpha) = \mathbf{R}_z(-\theta)\mathbf{R}_y(-\xi)\mathbf{R}_z(\alpha)\mathbf{R}_y(\xi)\mathbf{R}_z(\theta) \tag{2.35}$$

In the special case where $\theta = 0$, then

$$\mathbf{R}_{z'}(\alpha) = \begin{pmatrix} \cos\alpha\cos^2\xi + \sin^2\xi & \sin\alpha\cos\xi & (1-\cos\alpha)\cos\xi\sin\xi \\ -\sin\alpha\cos\xi & \cos\alpha & \sin\alpha\sin\xi \\ (1-\cos\alpha)\cos\xi\sin\xi & -\sin\alpha\sin\xi & \cos\alpha\sin^2\xi + \cos^2\xi \end{pmatrix} \tag{2.36}$$

In MR, a common rotation is the precession of the magnetization vector about the z-axis at the Larmor frequency ω_0 (left-handed rotation). The rotation matrix that describes such a precession is

$$\mathbf{R}_z(\omega_0 t) = \begin{pmatrix} \cos\omega_0 t & \sin\omega_0 t & 0 \\ -\sin\omega_0 t & \cos\omega_0 t & 0 \\ 0 & 0 & 1 \end{pmatrix} \tag{2.37}$$

2.6 Basic Probability

2.6.1 Random Variables

A random variable X is characterized by its cumulative distribution function $F(x)$, where the probability that X takes on values less than or equal to x is

$$\Pr\{X \le x\} = F(x) \tag{2.38}$$

Relatedly, the probability density function (pdf) $f(x)$ pertaining to X is

$$f(x) = \frac{dF(x)}{dx} \tag{2.39}$$

Therefore the probability that X will take on values between x_1 and x_2 is

$$\Pr\{x_1 \le X \le x_2\} = F(x_2) - F(x_1) = \int_{x_1}^{x_2} f(x)\, dx \tag{2.40}$$

Note that $f(x)$ is a positive-valued function with area equal to 1.

The *expected value* of a random variable X (often called the mean value) is

$$EX = \overline{X} = \int x f(x)\, dx \tag{2.41}$$

the first moment of the pdf. Another quantity of interest is the variance σ^2 of X, defined as

$$\begin{aligned} \sigma^2 &= E[X - \overline{X}]^2 = \int (x - \overline{X})^2 f(x)\, dx \\ &= E[X^2] - \overline{X}^2 \end{aligned} \tag{2.42}$$

The variance equals the second moment of the pdf with respect to the mean, and is indicative of the width of $f(x)$. The standard deviation of X is simply σ, the square root of the variance.

The following are examples of pdfs that are relevant to MR imaging.

Gaussian Density: If X is a Gaussian (normal) random variable of mean μ and variance σ^2, then its pdf is

$$f(x) = \frac{1}{\sqrt{2\pi\sigma^2}} \exp\left[-\frac{(x-\mu)^2}{2\sigma^2}\right] \tag{2.43}$$

Equivalently, we write compactly that $X \sim N(\mu, \sigma^2)$, where $N(\mu, \sigma^2)$ represents the normal distribution of mean μ and variance σ^2. Often, we will deal with a complex-valued random variable $Y = X_1 + iX_2$, where X_1 and X_2 are independent, Gaussian random variables. Y, sometimes termed a bi-variate Gaussian random variable, can be visualized as a random vector in the complex plane. It follows that $EY = EX_1 + iEX_2$ and $\sigma_Y^2 = E|Y - EY|^2$.

Rayleigh Density: Consider $Y = X_1 + iX_2$, where X_1 and X_2 are independent, and $X_1 \sim N(0, \sigma^2)$ and $X_2 \sim N(0, \sigma^2)$. If $Z = |Y| = \sqrt{X_1^2 + X_2^2}$, the magnitude of Y, then Z is called a Rayleigh random variable with a pdf given by

$$f_Z(z) = \frac{z}{\sigma^2} \exp\left(-\frac{z^2}{2\sigma^2}\right) \quad \text{for } z > 0 \tag{2.44}$$

where $\sigma_Z^2 = (2 - \pi/2)\sigma^2$ and $EZ = \sigma\sqrt{\pi/2}$.

Rician Density: Now consider $Y = X_1 + iX_2$ where $X_1 \sim N(\mu_1, \sigma^2)$ and $X_2 \sim N(0, \sigma^2)$, and X_1 and X_2 are independent. If $Z = |Y| = \sqrt{X_1^2 + X_2^2}$, the magnitude of Y, then Z is called a Rician random variable. The Rician density is written as

$$\begin{aligned} f_Z(z) &= \frac{z}{2\pi\sigma^2} \exp\left(-\frac{z^2 + \mu_1^2}{2\sigma^2}\right) \int_0^{2\pi} e^{z\mu_1 \cos\theta/\sigma^2}\, d\theta \\ &= \frac{z}{\sigma^2} \exp\left(-\frac{z^2 + \mu_1^2}{2\sigma^2}\right) I_0\left(\frac{z\mu_1}{\sigma^2}\right) \quad \text{for } z > 0 \end{aligned} \tag{2.45}$$

where I_0 is the modified Bessel function of zero order:

$$I_0(x) = \frac{1}{2\pi} \int_0^{2\pi} e^{x\cos\theta}\, d\theta \tag{2.46}$$

The Rician density arises when one of the Gaussian-distributed components has a non-zero mean whereas the Rayleigh density arises when both of the Gaussian-distributed components have zero means. Figure 2.6 contains plots of $f_Z(z)$ for different values of μ_1. Note that if $\mu_1 \gg 1$, then the Rician density can be approximated by a Gaussian density with mean μ_1 and variance σ^2.

2.6.2 Random Processes

In considering noise in MR imaging, we will deal with random processes $X(t)$ (continuous time) and $X[n]$ (discrete time). An important characterization of a random process is its autocorrelation function, defined as

$$R(t_1, t_2) = E\left[X(t_1)X^*(t_2)\right] \tag{2.47}$$

We will assume that these processes are weakly stationary, meaning that the autocorrelation depends on only $t_2 - t_1$. Therefore, we may write

$$R(\tau) = E\left[X(t)X^*(t + \tau)\right] \tag{2.48}$$

The power spectral density $S(f)$ of a random process is defined to be the Fourier transform of the autocorrelation function; that is,

$$S(f) = \mathcal{F}\{R(t)\} \tag{2.49}$$

If $X(t)$ is passed through a linear time-invariant system with transfer function $H(f)$ to produce output $Y(t)$, then the power spectral density of $Y(t)$ is

$$S_Y(f) = S_X(f)|H(f)|^2 \tag{2.50}$$

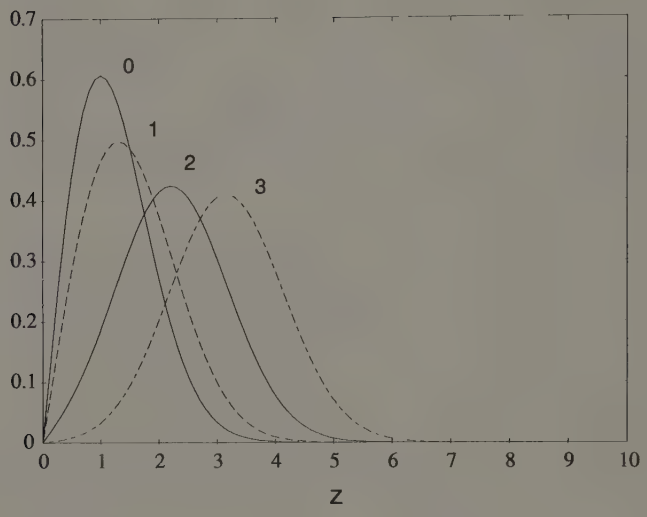

Figure 2.6: Rician density functions $f_Z(z)$ for $\mu_1 = 0, 1, 2, 3$ ($\sigma^2 = 1$). For $\mu_1 = 0$, the function represents a Rayleigh density.

Similar relations exist for a discrete-time random process $X(n)$, where n is an integer (normalizing the sampling rate to unity). The autocorrelation is

$$R(m,n) = E\left[X(m)X^*(n)\right] \tag{2.51}$$

If weakly stationary, then

$$R(m,n) = R(m-n,0) \tag{2.52}$$

and the power spectral density is

$$S(f) = \mathcal{F}\{R(n)\} = \sum_{n=-\infty}^{\infty} R(n)e^{-i2\pi fn} \tag{2.53}$$

If $X(n)$ is a zero-mean input process, then $\overline{X} = 0$ and

$$R(0) = \int_{-1/2}^{1/2} S(f)\,df = \sigma^2 \tag{2.54}$$

the variance of $X(n)$.

2.7 Problems

2.1 If the Fourier transform of $f(x)$ is $F(k_x)$, what is the Fourier transform of the following functions?

(a) $f(ax+b)$

(b) $f(-x)$

(c) $F(x)$

2.2 Find the projection $g_\theta(x')$ of the following 2D functions at the specified projection angles θ.

(a) $e^{-\pi r^2}$ for all θ

(b) ${}^2\sqcap(x,y)$ for $\theta = 45°$

(c) $\text{jinc}(r)$ for all θ

(d) ${}^2\delta(x-x_\circ, y-y_\circ)$ for all θ

2.3 For what projection angles θ is the projection of the following function equal to zero?

$$f(x,y) = \text{sinc}(x)\text{sinc}(y)\cos 2\pi x$$

2.4 A function $f(x)$ is decomposable into the sum of an even function $f_e(x)$ and odd function $f_o(x)$. What is the corresponding decomposition for a two-dimensional function $g(x,y)$?

2.5 If $f(x) = \cos 2\pi f x$ is sampled at a sampling rate of $3f/2$, sketch the resultant spectrum of the sampled function.

2.6 A vector **M** starting at $[0\ 0\ 1]^T$ is rotated about the x axis by 90°, then about z by some angle θ, and finally about x again by 90°. Determine the resulting vector as a function of θ.

2.7 If the **M** vector starts at $[0\ 0\ 1]^T$, specify a rotation axis in the xz-plane and rotation angle α such that the vector is rotated to $[1\ 0\ 0]^T$. Use Eq. 2.36 to verify that the rotation matrix is correct.

Chapter 3

Overview

We will begin by surveying the basic physics and imaging methods of MR. The emphasis in this overview is on providing some acquaintance with the wide variety of physical and instrumental parameters involved in MR imaging. Given the complexity of MR, a qualitative understanding of the main concepts will be useful to have before tackling the more detailed and mathematical descriptions in later chapters.

3.1 Classical Description of MR

This section briefly outlines the basic principles and physics of MR. Although the descriptions in this section are neither complete nor rigorous, the intent is to present only the concepts relevant to understanding the nature and behavior of the MR phenomenon. A rigorous and accurate description of the basic MR physics requires quantum mechanics; however, in most cases, a classical treatment amply describes the macroscopic behavior.

Atoms with an odd number of protons and/or odd number of neutrons possess a nuclear spin angular momentum, and therefore exhibit the MR phenomenon. Qualitatively, these nucleons can be visualized as spinning charged spheres that give rise to a small magnetic moment. We will often refer to these MR-relevant nuclei as simply *spins*. In biological specimens, hydrogen (^{1}H), with a single proton, is the most abundant (the body consists largely of H_2O), the most sensitive (that is, gives rise to the largest signals), and by far the most studied. Other atoms such as phosphorus (^{31}P)—an important indicator of metabolism—are also of interest. Henceforth however, unless noted, we will assume ^{1}H (proton) imaging.

The nature of MR is based on the interaction of these spins with three types of magnetic fields: 1) main field B_0, 2) radiofrequency field B_1, and 3) linear gradient fields G. We will organize our general description of MR around the usages of these fields.

3.1.1 Main Field B_0

In the absence of an external magnetic field, the spins are oriented randomly and the net macroscopic magnetic moment is zero. However, in the presence of an external magnetic field B_0, two notable effects occur. First, the magnetic moment vectors tend to align in the direction of B_0 to create a net magnetic moment. By convention, the direction of the applied field is called the z-direction or *longitudinal* direction. Second, the nuclear spins exhibit resonance at a well-defined frequency called the *Larmor* frequency ω. This Larmor frequency relates to the applied magnetic field by a simple but vastly important expression,

$$\omega = \gamma B \tag{3.1}$$

or

$$f = \frac{\gamma}{2\pi} B \tag{3.2}$$

where γ is called the gyromagnetic ratio, a known constant unique for each type of atom. For ^1H, $\gamma/2\pi = 42.58$ MHz/Tesla (1 Tesla (T) = 10^4 Gauss (G)); hence, at a magnetic field strength of 1.0 T, the Larmor frequency is 42.58 MHz, in the radiofrequency (RF) region. Most whole-body imaging systems operate at a fixed field strength within the range of 0.1 to 3 T.

Macroscopically, the B_0 field polarizes the sample, inducing a net magnetization vector pointed in the z-direction of strength $M_\circ$. Also, the spins exhibit resonance at their Larmor frequency. They will be "excited" by the appropriate radiofrequency magnetic field tuned to the Larmor frequency and they will "oscillate" and produce a signal based on the Larmor frequency as well. As an analogy, the spinning nuclei react to B_0 like a spinning top does in a gravitational field, precessing about the field at a well-defined frequency.

3.1.2 Radiofrequency Field B_1

In the presence of a static magnetic field B_0, the equilibrium state of the magnetization vectors in the body is depicted in Fig. 3.1. To obtain an MR signal, a radiofrequency (RF) magnetic pulse B_1 tuned to the resonant frequency of the spins is applied in the xy (*transverse*) plane to excite these spins out of equilibrium (Fig. 3.2). Effectively, B_1 applies a torque

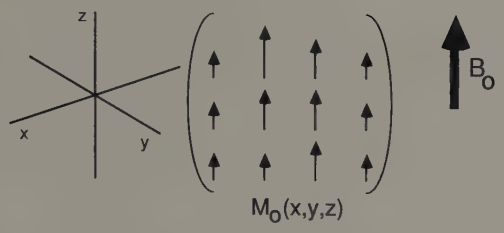

Figure 3.1: Equilibrium condition of magnetization in the presence of the main static magnetic field B_0.

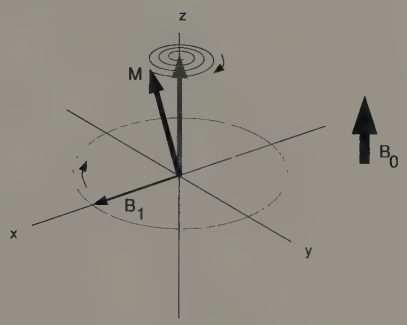

Figure 3.2: B_1 radiofrequency field tuned to Larmor frequency and applied in transverse (xy) plane induces nutation (at Larmor frequency) of magnetization vector as it tips away from z-axis—lab frame of reference.

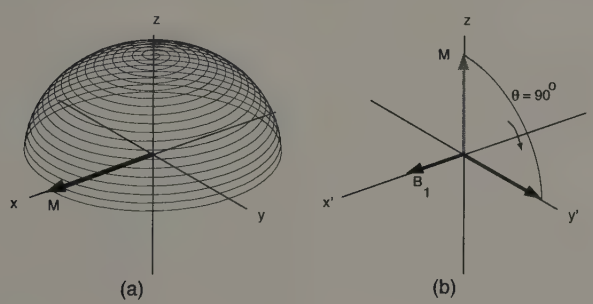

Figure 3.3: B_1 induces rotation of magnetization towards transverse plane—(a) laboratory frame behavior of **M**; (b) rotating frame behavior. Strength and duration of B_1 can be set for a 90° rotation, leaving **M** entirely in the xy plane.

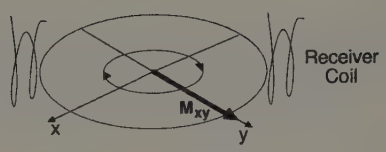

Figure 3.4: After B_1 turns off, **M** precesses in the xy plane at the resonant frequency, generating an EMF signal in the receiver coil.

which rotates the magnetization vectors by a prescribed angle dependent on the strength of B_1 and its duration. On a human imaging system, the strength of B_1 is typically a few microtesla (a small fraction of a Gauss); its duration is usually a few milliseconds. Figure 3.3a depicts the behavior in the laboratory frame of reference while Fig. 3.3b shows the behavior in the frame rotating at the Larmor frequency about the z-axis. If the excitation is set for (say) a 90° tip angle (Fig. 3.3), then upon turning the excitation off, the tipped vectors precess in the xy plane at the Larmor frequency (Fig. 3.4). Relaxation back to equilibrium also occurs in which the length of the magnetization vector does not remain constant over time. The time constant characterizing the return of the magnetization vector along the z-axis (longitudinal axis) is called T_1, while the time constant characterizing the decay of the vector component in the xy plane (transverse plane) is called T_2. In humans, T_1 values of tissues appearing in an image range from about 100–2000 ms while T_2 values range from about 10–300 ms. These relaxation time constants, along with the density ρ of the atoms, are important MR parameters which have distinct values for different tissues.

From Faraday's law of induction, the rotating magnetization vectors induce an electromotive force (EMF) in an RF receiver coil oriented to detect changes of magnetization in the xy plane (Fig. 3.4). Often, the coil generating the RF excitation field will switch modes and receive the signal as well. The generated time signal is called a *free induction decay* (FID); in general, a set of FIDs will be recorded and processed to reconstruct an MR image. Thus, the body can be visualized as an ensemble of tiny oscillators inducing RF signals. The objective of MR imaging then is to map the spatial distribution of their amplitudes. As will be shown, imaging is based on controlling the relative phases and frequencies of these oscillators.

3.1.3 Linear Gradient Fields G

If the applied field is simply the main static field B_0 in the z-direction, then all spins possess the same resonance frequency $\omega_0 = \gamma B_0$ and, if ex-

cited, behave like oscillators inducing signals at that frequency (Fig. 3.5a). Because the excitation/receiver RF coil encompasses the entire region of interest, it is not possible to excite a selected portion of the volume nor is it possible to distinguish the signals generated from different spatial locations if only B_0 exists. The problem lies in the fact that we record the total signal generated by all the oscillators of the excited region in a single time waveform.

In MR imaging, spatial localization is achieved by applying linear *gradient* magnetic fields in addition to B_0. For example, if we apply a gradient G_x in the x-direction (Fig. 3.5b), then the applied field is $B_0 + G_x x$. It is important to note that this gradient field leaves the combined magnetic field still pointing in the z-direction but now the field strength varies with the x-location; hence, $G_x = dB_z/dx$. The frequency of the spins thus becomes a function of their x-location; that is, $\omega(x) = \gamma(B_0 + G_x x) = \omega_0 + \gamma G_x x$. On whole-body imaging systems, the gradient field strength is usually less than 50 mT/m (5 G/cm–although it is proper to use SI units, some find the CGS units of Gauss/centimeter easier to interpret).

The utility of a gradient field can be easily seen if we consider the signal generated when a constant G_x is turned on after an excitation. The time signal contains the contributions of oscillators emitting signals over a range of frequencies. If G_x = 10 mT/m (1 G/cm), then the frequencies vary as 425.8 kHz/m (4.258 kHz/cm) for ^{1}H, amounting to a frequency bandwidth of 42.58 kHz for an object 100 mm (10 cm) wide. Therefore, Fourier transformation of the FID time signal (Fig. 3.5b) determines the contribution from each frequency component which in turn linearly maps to a particular x-position. In this case of a constant x-gradient, a 1D image can be formed since x-position is encoded as temporal frequency.

The idea of purposefully creating an inhomogeneous field with a gradient plays a vital role in MR imaging. By making the magnetic field inhomogeneous, we take advantage of the fact that the resonant frequency of these nuclei is proportional to the applied field strength and that this frequency changes *instantaneously* when the field strength changes.

3.1.4 Bloch Equation

In general, the behavior of the magnetization vector **M** is described phenomenologically by the so-called Bloch equation, given by

$$\frac{d\mathbf{M}}{dt} = \mathbf{M} \times \gamma\mathbf{B} - \frac{M_x\,\mathbf{i} + M_y\,\mathbf{j}}{T_2} - \frac{(M_z - M_\circ)\mathbf{k}}{T_1} \tag{3.3}$$

where **i**, **j**, and **k** are unit vectors in the x, y, and z directions respectively, $M_\circ$ is the equilibrium magnetization arising from the main field B_0, and

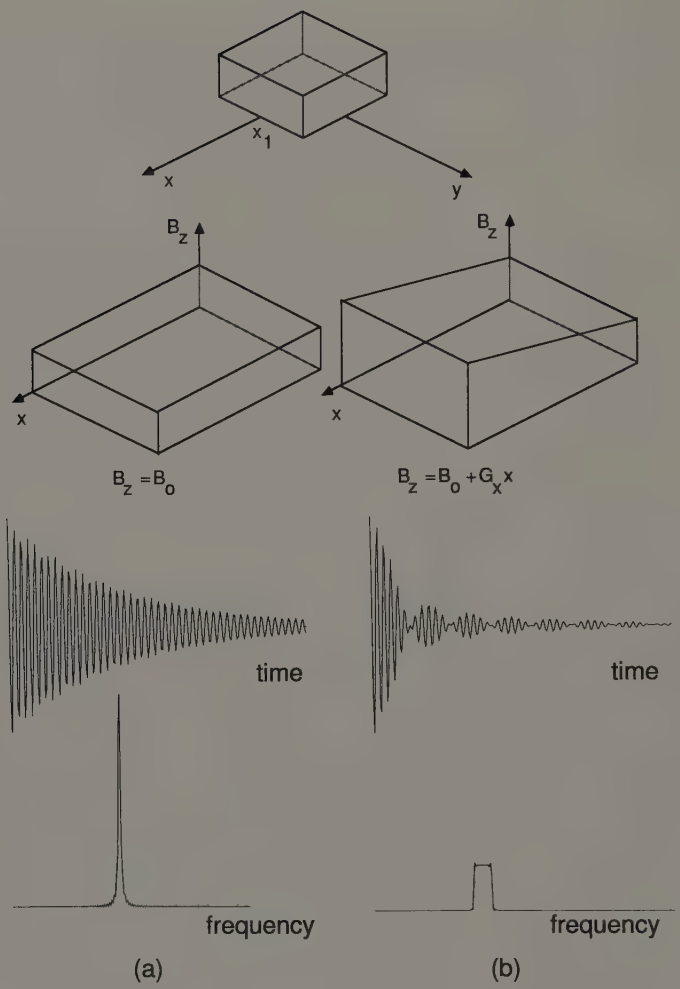

Figure 3.5: Square water object: **(a)** Given only B_0, the FID signal contains contributions from water in the entire square at the same temporal frequency. Fourier transformation of the FID gives a single peak located at the resonant frequency ω_0. The signals from water at different positions are indistinguishable. **(b)** Given B_0 and gradient field G_x, water at a higher x position experiences a higher field than water at a lower x position and therefore generates a signal at a higher frequency. The signal contains contributions over a range of frequencies. Fourier transformation of the FID gives a flat rectangular profile as water at different x-positions contribute at their respective frequencies.

B includes the various magnetic fields applied. In later chapters, we will solve this equation to develop a mathematical description of the different situations just discussed.

3.2 Conventional MR Imaging Methods

MR imaging methods are as diverse as the ways to describe them. However, for conventional methods, the procedure can be organized into basically two parts: excitation and reception. For the methods we will examine in this introductory chapter, each excitation/reception sequence results in a time signal measurement that provides a single spatial projection of the object under study. A typical measurement duration is about 10 ms. After pausing for some time (often 0.1–2.0 s) to allow suitable magnetization recovery, the excitation/reception sequence repeats for collection of the next measurement. A set of measurements is thus collected to provide the appropriate set of projections for image reconstruction.

As described in the previous section, excitation involves the use of a radio-frequency pulse(s) to tip the spins in a specified region so that they become sources of an RF signal. What is important to realize is that the spins generate this recordable RF signal if the tipping results in a vector component rotating in the xy plane (i.e., a 180° excitation leads to no signal). Combinations of excitation pulses are typically employed to make the amplitude of these oscillators become some function of the MR parameters (ρ, T_1, T_2). At this point, we will not be concerned with this issue of image contrast. It suffices to appreciate that after the excitation, we are left with a region of precessing magnetic dipoles with an amplitude distribution $m(x, y, z)$ we would like to reconstruct. As will be described shortly, it is also possible to excite just a thin plane instead of the whole volume by broadening the range of resonant frequencies. If the excited slice is perpendicular to say the z-axis, the imaging problem reduces to that of reconstructing $m(x, y)$.

We will see in the following sections how the various imaging methods use the gradients in different ways to form images. Before elaborating on how gradients are used during the reception portion, we will briefly discuss the use of gradient fields during the excitation portion of the imaging cycle.

3.2.1 Selective Excitation

As discussed in Section 3.1.2, a transverse RF magnetic field B_1, tuned to the Larmor frequency of the nuclear spins, tips the magnetization vectors by some angle, typically 90°. If B_1 is applied in the presence of B_0, then

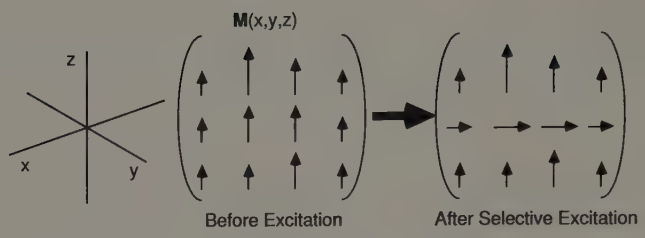

Figure 3.6: Effect of 90° selective excitation on spin distribution.

all spins are at the same resonance frequency and the excitation is *nonselective* because all spins are tipped. In this case where the entire volume contributes signal, some form of 3D imaging must be performed. Unfortunately, 3D imaging is usually a time-consuming endeavor unless image contrast or spatial resolution is compromised.

Hence it is desirable to be able to reduce a 3D imaging task into a manageable 2D one by exciting a plane instead of the entire volume. Such a *selective* excitation is achieved by applying B_1 in the presence of B_0 and a linear gradient field. If we wish to excite a plane, say, perpendicular to the z-axis of thickness Δz (Fig. 3.6), then G_z turns on during the RF excitation. With G_z on, the resonance frequency varies linearly with z-position; intuitively, because B_1 must be tuned to the Larmor frequency for excitation to occur, B_1 must now possess a temporal frequency bandwidth that matches the bandwidth of resonance frequencies of spins in the slice of interest (Fig. 3.7). The desired bandwidth is $\gamma G_z \Delta z$, centered about ω_0 for excitation of the plane at $z = 0$. The B_1 excitation field therefore takes the form of

$$\mathbf{B_1} = B_1(t)(\cos \omega_0 t\, \mathbf{i} - \sin \omega_0 t\, \mathbf{j}) \tag{3.4}$$

giving a field rotating at the center frequency ω_0 with time-varying amplitude $B_1(t)$. Continuing with our intuitive notions, to achieve a slice excitation with a rectangular profile, the frequency content of $B_1(t)$ must be a rectangle function. Thus if the Fourier transform of $B_1(t)$ is to be a rectangle function, then ideally $B_1(t)$ must be a sinc function.

Practically, rectangular slice profiles are difficult to achieve because $B_1(t)$ is of finite duration and because Fourier analysis for determining $B_1(t)$ turns out to be only an approximation—albeit a reasonable one in many cases—as the Bloch equation behaves nonlinearly. In general, for well-defined selective excitations, the waveform $B_1(t)$ is "sinc-like" but should be designed carefully.

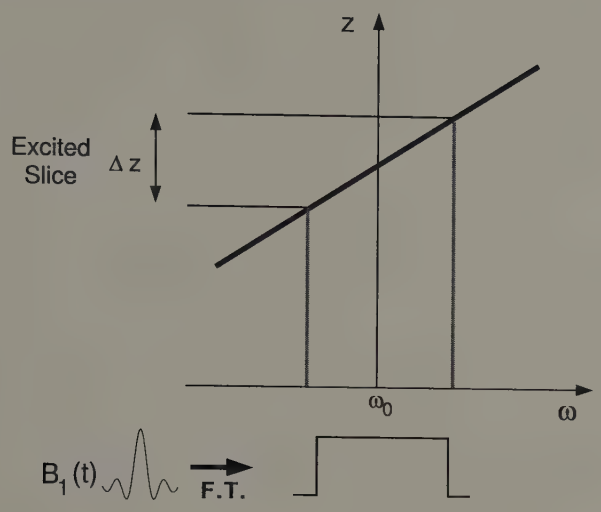

Figure 3.7: Selective Excitation: With G_z, resonant frequency varies linearly with z. A B_1 pulse with a rectangular frequency content excites only those spins in z-locations at the matching frequencies.

3.2.2 2D Imaging Methods

For the ensuing sections which discuss planar (2D) imaging methods, we will simplify matters by considering the following excitation/reception sequence.

1. We apply a selective 90° excitation in the presence of G_z such that the nuclear magnetization vectors in a thin plane at a particular z-location are tipped into the xy plane. We further assume that all of the magnetization vectors in this plane are pointed in the same direction; that is, they are in phase.

2. The excited spins, acting as RF sources, have an amplitude distribution $m(x, y)$ that we wish to image. As the excited spins precess and induce an EMF in the receiver coil, we encode their signals via gradient fields to get spatially dependent information in the FID signal. The methods to be discussed perform this step in different ways.

3. Eventually, the signal decays and the spin vectors return to equilibrium. We then repeat this procedure to acquire the next measurements.

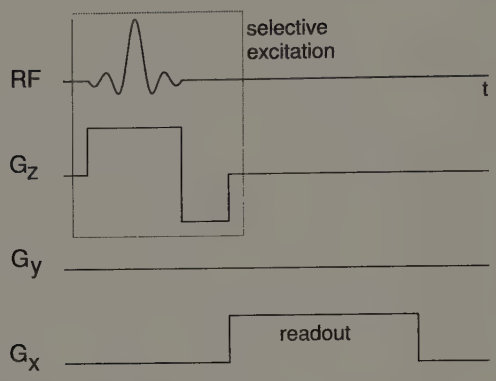

Figure 3.8: Timing diagram for the projection-reconstruction method, projection angle $\theta = 0$.

We now examine the basic principles of two specific imaging methods: projection-reconstruction and 2D Fourier transform. The 2D Fourier transform method dominates the field, but because of the analogy with x-ray CT, it is insightful to discuss the projection-reconstruction method first.

Projection-Reconstruction Method

This method uses the established reconstruction method from x-ray CT by making MR measurements that correspond to the projections of $m(x, y)$ over the required angles. We will give both a qualitative and an analytic description of how a projection at a specific angle is obtained. Generalizing to an arbitrary projection angle will be a straightforward matter.

A timing diagram of the sequence (excitation/reception) is given in Fig. 3.8. Following a selective excitation of a 2D section, the signal readout occurs in the presence of a constant gradient field. (We defer discussion of the negative G_z lobe that follows the RF pulse until Chapter 6). We have already described what happens when a gradient G in the x-direction is applied when the FID is recorded. This sequence corresponds precisely to acquiring a projection in which the line integrals are along the y-direction. The presence of G means that upon Fourier transforming the received FID signal $s_r(t)$, each frequency component corresponds to the contributions from the spins at some x-location. At a particular x-location, all of the spins along y oscillate at the same frequency and therefore sum to give the value at that frequency bin. Thus, the Fourier transform of $s_r(t)$ directly gives the projection of $m(x, y)$ along the y-direction (or projection

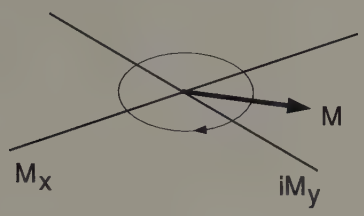

Figure 3.9: Rotating magnetization vector in xy plane with phasor notation.

angle $\theta = 0°$).

To gather a projection at a different angle, we apply a gradient whose field varies along a different direction; that is, we rotate the direction of the gradient (remember though, the applied field remains in the z-direction with B_0) to rotate the angle of the projection. If we want N projection angles, we must repeat the excitation/reception cycle N times, each time with a different gradient direction. We then proceed through the regular reconstruction procedure to form the image of $m(x, y)$.

Mathematically, the Bloch equation can be solved to express the behavior of the magnetization vectors. We will skip directly to the solution and use a more convenient phasor representation of the precessing magnetization vectors. The signal generated by the oscillator at position (x, y) can be written as $m(x, y)\exp(-i\omega t)$ where $m(x, y)$ is a complex quantity given by

$$m(x, y) = m_x(x, y) + im_y(x, y) \tag{3.5}$$

and $\exp(-i\omega t)$, from a phasor point-of-view, represents a rotating vector at frequency ω. Physically, as discussed earlier, the oscillators arise because the magnetization vectors rotate in the xy plane at a frequency ω (Fig. 3.9). In the presence of a gradient G in the x-direction, the frequency is spatially dependent; that is, $\omega(x) = \omega_0 + \gamma G x$. The total received signal $s_r(t)$ can be written by integrating over the entire excited plane. Ignoring relaxation terms,

$$s_r(t) = \int_x \int_y m(x, y) e^{-i\omega_0 t} e^{-i\gamma G x t}\, dx\, dy \tag{3.6}$$

We are interested in the baseband signal, so we will ignore the high-frequency

factor $\exp(-i\omega_0 t)$. Then, the baseband signal $s(t)$ is expressed as

$$\begin{aligned} s(t) &= s_r(t)\, e^{+i\omega_0 t} \\ &= \int_x \int_y m(x,y) e^{-i\gamma G x t}\, dx\, dy, \\ &= \int_x \left[\int_y m(x,y) dy \right] e^{-i\gamma G x t}\, dx \end{aligned} \tag{3.7}$$

If

$$g(x) = \int_y m(x,y)\, dy \tag{3.8}$$

then

$$\begin{aligned} s(t) &= \int_x g(x) e^{-i\gamma G x t}\, dx \\ &= \int_x g(x) \exp\left[-i2\pi \left(\frac{\gamma}{2\pi} G t \right) x \right] dx \\ &= \mathcal{F}\{g(x)\}|_{k_x = (\gamma/2\pi) G t} \end{aligned} \tag{3.9}$$

(x and k_x are space and spatial frequency variables respectively). Because $g(x)$ equals the projection of $m(x,y)$ along the y-direction, $s(t)$ is related to the 1D Fourier transform of this projection. Thus

$$g(x) = \mathcal{F}\{s(t)\}|_{f = -(\gamma/2\pi) G x} \tag{3.10}$$

(t and f are time and temporal frequency variables respectively). The height of each frequency bin in the Fourier spectrum of the FID time signal equals the value of the projection at the appropriate x-position.

This result can be generalized to other projection angles by applying a gradient oriented in a different direction. Applying

$$G_x = G \cos\theta \tag{3.11}$$

$$G_y = G \sin\theta \tag{3.12}$$

leads to a projection at angle θ. Once projections over all angles are obtained, the image is reconstructed by processing the data in the conventional manner used in x-ray CT.

From the central section theorem (Section 2.3.2), the 1D Fourier transform of a projection taken at angle θ provides information along a radial slice of the 2D Fourier transform of the distribution $m(x,y)$ at that angle θ. Each FID therefore gives information along a line as shown in Fig. 3.10.

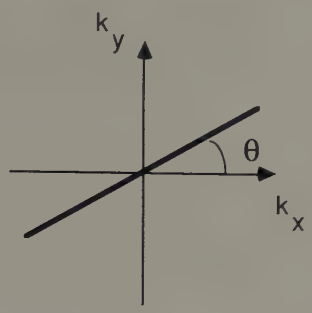

Figure 3.10: From the central section theorem, each FID in the projection-reconstruction method gives a line at the projection angle θ in the 2D Fourier transform of the object.

2D Fourier Transform Method

The projection-reconstruction method just described where projections at different angles are taken is an intuitively pleasing approach. In x-ray imaging, each point in the projection corresponds to the sum of the object distribution along the appropriate ray path. Therefore, a single projection angle does not provide spatial information of the object distribution along the ray path, and it is sensible then that other angles are needed to resolve the ambiguity.

In MR, a method called 2D Fourier transform (2DFT) provides a fresh perspective of the imaging problem. This method operates with a set of projections taken at a *single* projection angle to reconstruct $m(x, y)$. At first, it may not be intuitively obvious that any such method could work based on what was discussed in the previous paragraph. However, the key to the method is that $m(x, y)$ is spatially weighted in some clever way before the projection takes place.

To illustrate the idea, suppose that the projection is always in the y-direction. If, by some means, we were able to apply a weighting factor that was unity at some value of y and zero elsewhere, then the resultant projection of the spatially weighted distribution would give information about the original distribution along y even though we projected along y. Now if, as we obtained subsequent projections along the same direction, we were able to move the y-position of the unity weighting, we would eventually be able to reconstruct $m(x, y)$. In this simple example, no special processing of the projections would be necessary to reconstruct the image because each projection directly determines the value at some y-position.

Another way of decomposing the distribution along the line of projec-

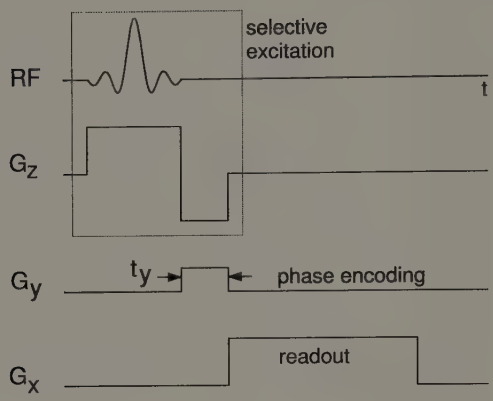

Figure 3.11: Timing diagram for the 2D Fourier transform method.

tion is by its spatial frequency components. If we first weight a distribution $h(x,y)$ by $\cos 2\pi k_i y$ (and $\sin 2\pi k_i y$) and then project along the y-direction, the resultant projection would give information about to what extent $h(x,y)$ contained that particular spatial frequency component k_i. In essence, that projection would give the value of the Fourier transform of $h(x,y)$ for that particular frequency. If we were to vary k_i on subsequent projections, we would eventually assemble the necessary spatial frequency bins to be able to reconstruct $h(x,y)$ by taking the inverse Fourier transform of the accumulated data. This inverse transform operation would amount to a series of 1D transforms, each one reconstructing a distribution along the line of projection at a different x-location.

This Fourier decomposition of $h(x,y)$ is the framework in which the 2DFT method operates. To reconstruct the distribution along the "ray" path, each projection is not of simply $m(x,y)$ but of $m(x,y)$ multiplied by a spatial frequency weighting factor. Subsequent projections are based on $m(x,y)$ multiplied by a different spatial frequency weighting factor. This process continues until the range of spatial frequencies is sufficient to describe the distribution along the line of projection. This capability in MR to induce a weighting distribution with negative values—something not possible in x-ray CT—stems from the availability of phase information. For example, when two magnetization vectors are 180° out of phase, their signal contributions will negate each other.

The timing diagram for the 2DFT method is found in Fig. 3.11. To effectively apply the spatial frequency weighting factor in MR, a gradient G_y in the y direction is turned on for a time t_y before recording the FID.

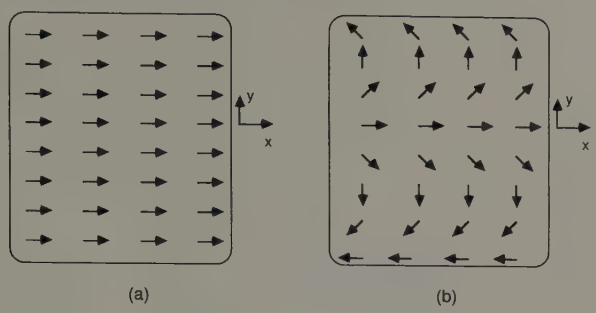

Figure 3.12: (a) Direction of magnetization after excitation but before phase encoding gradient G_y. All vectors have the same phase. (b) Direction of magnetization after phase encoding gradient G_y has been applied. The phase varies linearly with y position. A higher or longer phase encoding gradient creates greater amount of phase warping.

During this gradient interval, spins along y experience a different field strength and therefore rotate at a different frequency (linearly increasing with y). As a result, the spins which were originally in-phase become increasingly out-of-phase with time. The phase of the spins oscillating at $\omega(y) = \omega_0 + \gamma G_y y$ after an interval t_y is $\omega_0 t_y + \gamma G_y t_y y$; in the rotating frame, the phase equals $\gamma G_y t_y y$, a linear function of the y-position. In essence then, the spins are spatially phase-encoded by the time the FID is to be recorded, with the amount of phase-encoding dependent on the amplitude G_y and on the interval t_y. Because $m(x, y)$ is a complex-valued function representing both the M_x and M_y components, the distribution becomes weighted by a complex exponential corresponding to the spatial frequency $(\gamma/2\pi)G_y t_y$; more precisely, the distribution that is projected (at time t_y) is $m(x, y)\exp(-i\gamma G_y t_y y)$.

Physically, the distribution $m(x, y)$ of the magnetization vectors, originally in phase (Fig. 3.12a), are placed out-of-phase along the projection line by the G_y gradient (Fig. 3.12b). This spin warping effectively weights $m(x, y)$ by the complex exponential weighting factor. After this phase-encoding gradient, the usual gradient G_x is applied in the x-direction during the readout of the FID, and the Fourier transform of this time waveform results in the projection as before. For the next projection, t_y (or equivalently G_y) is varied to induce a different spatial frequency weighting factor on $m(x, y)$ and the same readout gradient G_x is used. This procedure repeats until information about enough spatial frequencies is acquired.

Pictorially, each FID (for a given t_y) gives information along a horizontal

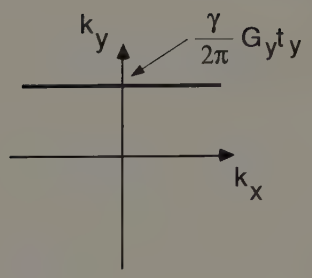

Figure 3.13: Each FID in the 2DFT method gives a horizontal line in the 2D frequency domain of the object.

line in the 2D Fourier space of $m(x, y)$ (Fig. 3.13) in contrast to the radial line that is obtained in the projection-reconstruction method. As we vary t_y, we build the 2D transform space in a Cartesian grid, not a polar one as in projection-reconstruction.

Once all of the FIDs are assembled, a simple 2D Fourier transform is used to reconstruct $m(x, y)$. Effectively, when the Fourier transform is performed in the k_x-direction, the FID time signals transform into projections, each projection corresponding to a particular k_y spatial frequency component. Operating on these projections, a Fourier transform, performed in the k_y-direction, yields the object distribution $m(x, y)$. Figure 3.14 gives an illustrative example.

Describing this method mathematically, the baseband signal is written as

$$s(t; t_y) = \int_x \int_y \left(m(x, y) e^{-i\gamma G_y y t_y} \right) e^{-i\gamma G_x x t} \, dx \, dy \tag{3.13}$$

where for any given FID, t_y is set and t is the running variable. The bracketed term arises from the phase-encoding step, and the $\exp(-i\gamma G_x x t)$ factor results from the presence of the constant G_x gradient during the recording of the FID. Letting

$$g_{t_y}(x) = \int_y m(x, y) e^{-i\gamma G_y y t_y} \, dy \tag{3.14}$$

be the line integral of $m(x, y) \exp(-i\gamma G_y y t_y)$, then

$$s(t; t_y) = \int_x g_{t_y}(x) e^{-i\gamma G_x x t} \, dx \tag{3.15}$$

Thus $s(t; t_y)$ provides information about $g_{t_y}(x)$, the projection of a phase-

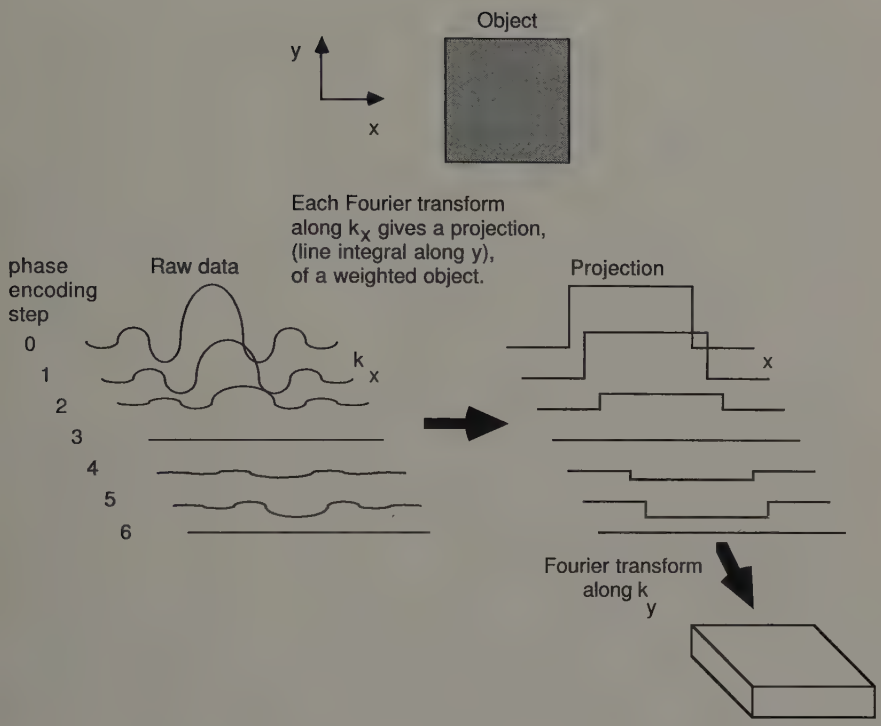

Figure 3.14: 2DFT Example: Square test object and six of its projections with progressively increasing phase-encodings. Assembling the projections (after Fourier transforming each raw data signal) and taking a 2nd Fourier transform results in the reconstructed image.

warped version of $m(x,y)$. More generally, we can write that

$$\begin{aligned} s(t;t_y) &= \int_x \int_y m(x,y) e^{-i\gamma G_x x t} e^{-i\gamma G_y y t_y}\, dx\, dy \\ &= \mathcal{F}_{2D}\{m(x,y)\}\Big|_{\substack{k_x=(\gamma/2\pi)G_x t \\ k_y=(\gamma/2\pi)G_y t_y}} \end{aligned} \tag{3.16}$$

which shows the 2D transform relation between $m(x,y)$ and the FIDs. After assembling all of the FIDs (and therefore all horizontal lines in Fourier transform space), we simply take the inverse 2D transform to reconstruct $m(x,y)$.

The descriptions of projection-reconstruction and 2D Fourier transform imaging just presented give an introductory perspective on gradient fields and the principles of MR imaging, with some emphasis on an object-domain point-of-view. It is clear however that Fourier analysis is intimately involved in the description of MR imaging. We will generalize this Fourier-based treatment of MR imaging in Chapter 5.

3.3 Other Approaches to MR Imaging

One of the interesting aspects of MR imaging is that spatial localization is achieved via the encoding of signals using gradient fields. To appreciate the utility of the gradient field, it is instructive to conceptualize other approaches to MR imaging that rely on the RF or static field for spatial localization.

One possibility is to confine the RF receiver coil sensitivity to a small region near the surface and to move this sensitivity region around to build up an image. This approach would suffer from long scan times and limited spatial resolution. Conceptually, another approach would be to somehow excite a small region. One problem with this idea concerns how to "focus" the RF magnetic field to such a small region without exciting others.

Using the main field for localization, one can imagine confining B_0 to a small region using a local magnet. Among the problems with this approach is poor spatial resolution due to the geometric and continuity constraints in creating such a field. Alternatively, one can shape a field such that the field equals B_0 over a small region as in a saddle-shaped field. An RF excitation at ω_0 therefore produces signal from the B_0 region and image is therefore assembled by moving this saddle point about the object.

All of the above scenarios represent a more geometric approach to MR imaging. In each case though, the scanning procedure is awkward and inefficient as only a small portion of the object produces usable signal at any given time.

3.4 Imaging Considerations

The design and detailed specifications of the imaging sequence depend on an assortment of system and physical factors. These factors play important roles in considerations such as the length of signal readout (and other sequence variables), image contrast, and signal-to-noise ratio (SNR).

There are limits to the duration of signal readout for each time signal. A typical readout duration after each excitation (to give a single projection) is about 5–25 ms. Magnetic field inhomogeneities on the order of a few parts per million create errors in the resonant frequencies across the object and can lead to significant signal loss if long signal readouts are used. In addition, such inhomogeneities cause phase errors in the measurements which result in image distortion. Ultimately, intrinsic T_2 decay determines the duration over which signal is available.

High contrast between various soft tissue in the body has been an important feature of MR imaging. Image contrast depends mainly on the timing and tip angles of the excitation used in signal generation. For example, when a 90° excitation is used for signal generation, the resultant signal depends on the amplitude of the M_z component prior to the excitation, because that component gets rotated into the transverse plane by the radiofrequency pulse. Because of T_1 relaxation, time must elapse after a 90° excitation to yield some M_z recovery before the next 90° excitation can be applied. By setting the interpulse timing appropriately, image contrast based on T_1 differences between tissues can be established. Typically, given T_1 values of around 500–1000 ms, repetition times of about 500–1000 ms are used. This implies that the minimum scan time to acquire sufficient measurements for an image equals N(TR), where N is the number of measurements and TR is the repetition time. If N = 256 and TR = 1000 ms, then the scan time is over 4 min.

The main source of noise in MR imaging is due to thermal fluctuations of electrolytes in the body which are detected by the receiver coil. This additive "body noise" often dominates the noise of the receiver electronics and thermal noise of the coil itself. The resulting image SNR depends on a variety of sequence and image parameters. Generally, the SNR increases by the square root of the acquisition time and linearly with the voxel size.

3.5 Instrumentation

A general drawing of an MR imaging system is shown in Fig. 3.15. Three types of magnetic fields are required for imaging: a static uniform field, gradient fields, and radiofrequency fields.

The main hardware of the system is a large magnet that provides the stable, homogeneous field B_0 in the range typically from 0.1–3.0 T (1.0–30 kG). For clinical use, the magnet must have a sufficiently large bore to allow entry of a torso. Smaller-bore systems, using fields as high as 11 T, exist for animal, small-sample, and microscopic imaging studies. At the other end, less-expensive whole-body imagers using field strengths as low as 0.02 T (200 G) are also available.

Three types of magnets are currently used: permanent magnets, resistive magnets (air-core or iron-core), and superconducting magnets. They each have their advantages and disadvantages with regard to cost, weight, field-strength, stability, homogeneity, and fringe fields. The most popular magnet type is the superconducting magnet, primarily because of its excellent homogeneity, stability, and higher field-strength. However, superconducting magnets require cryogens (liquid helium), are more expensive, and create fringe fields that can extend a large distance, making siting of these magnets more challenging.

The other components in the MR system include gradient coils (for x, y, and z gradients), an RF coil (for excitation and reception), and the associated control and computer hardware. Interestingly, the scanning system involves no moving parts. The cost of a whole-body system ranges from one to over two million dollars.

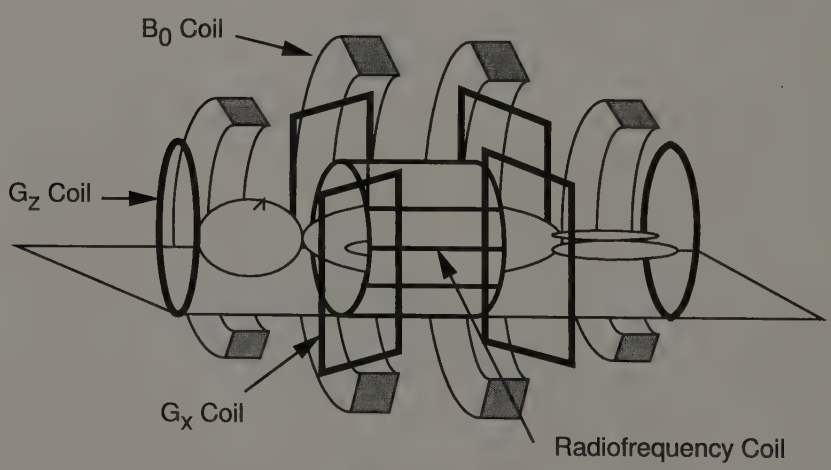

Figure 3.15: Simplified Drawing of Basic Instrumentation. Body lies on table encompassed by coils for static field B_0, gradient fields (two of three shown), and radiofrequency field B_1.

3.6 Problems

3.1 Consider the hypothetical situation of a modified 2DFT imaging sequence in which the 2D object is decomposed in one direction by its Hadamard components and not by its spatial frequency components. Such a weighting factor $W(y)$ is depicted below. Obviously a linear gradient field cannot produce $W(y)$.

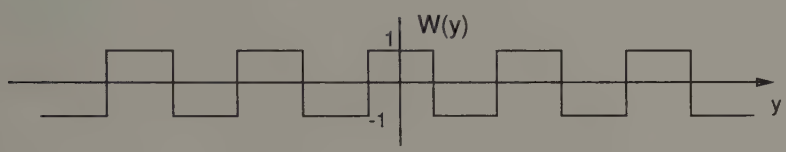

(a) Plot a magnetic field function C(y) (applied in addition to B_0) that will lead to the spatial weighting factor $W(y)$. If C(y) is applied for time t_y, find an expression for the the amplitude of this field. Are there other possible amplitudes?

(b) If imaging hydrogen and $t_y = 1$ ms, find a value for the amplitude of $C(y)$.

3.2 Let $m(x, y)$, in the excited plane at $z = z_\circ$, be $m_\circ{}^2 \sqcap (x/X, y/Y)$.

(a) For the "single-sided" (in Fourier space) projection-reconstruction sequence using FID signals, write a general expression for $s(t)$ when $G_x = G_{x\circ}$, $G_y = G_{y\circ}$. If $X = Y$, predict the FID signal $s(t)$ for $G_x = G\sqrt{2}/2$, $G_y = G\sqrt{2}/2$.

(b) Determine the FID signal $s(t)$ for the 2DFT sequence (single-sided Fourier-space acquisition) when G_y is turned on for t_y seconds before readout. For what value(s) of t_y is $s(t) = 0$? Explain from an object domain perspective why $s(t) = 0$.

3.3 Consider an MR imaging system equipped with only a *radial* gradient $G_r = \dfrac{dB_z}{dr}$ where $r = \sqrt{x^2 + y^2} \geq 0$, the radial distance in the xy plane. We desire to use this system to image 2D circularly symmetric objects $m(r)$.

(a) For a general $G_r(t)$ and $m(r)$, determine the baseband signal equation s(t) for this system.

(b) Find an expression for the baseband signal $s(t)$ if the 2D circularly symmetric object is a delta ring $\delta(r - R)$ and $G_r(t) = G_r$, a constant for $t > 0$.

(c) If the object is a circular pillbox of unit amplitude and diameter D, as shown below, sketch $|S(f)|$, the Fourier transform magnitude of the recorded baseband signal $s(t)$. Describe a strategy for image reconstruction of $m(r)$.

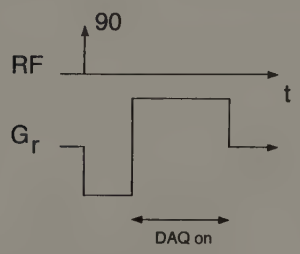

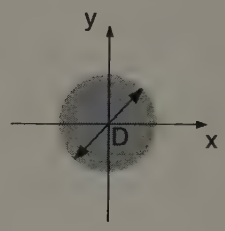

(d) Given the imaging situation of part (c), if $G_r = 2$ mT/m (0.2 G/cm) during signal readout and $D = 100$ mm (10 cm), what is the bandwidth of the recorded signal?

Chapter 4

Physics

We will briefly cover the basic physics of magnetic resonance (MR) at a level suitable for understanding imaging. Although the focus will be largely on a classical descriptions of MR, some quantum mechanical descriptions are included when appropriate. For a more complete background of MR physics, there are several excellent texts on this subject (for example, see [Abr61, FB71, Gol88, Sli80, Gad82]).

4.1 Nuclear Spins

The phenomenon of nuclear magnetic resonance arises in atoms with an odd number of protons and/or an odd number of neutrons. These atoms possess a property known as spin angular momentum. Spin angular momentum is a vector quantity expressed as

$$\mathbf{S} = \hbar \mathbf{I} \tag{4.1}$$

where $\hbar$ is Planck's constant (divided by 2π) and $\mathbf{I}$ is called the spin operator in quantum mechanics. Associated with $\mathbf{S}$ is a magnetic dipole moment $\boldsymbol{\mu}$, where

$$\boldsymbol{\mu} = \gamma \mathbf{S} = \gamma \hbar \mathbf{I} \tag{4.2}$$

and γ is the gyromagnetic ratio, a known constant unique for different nuclear species. As a classical picture, one can imagine a charged sphere spinning about its axis, thereby giving rise to a current loop that creates the magnetic dipole moment. Several atoms such as ^{1}H, ^{31}P, and ^{23}Na fit this category and therefore exhibit the MR phenomenon. However, because ^{1}H is by far the most abundant in the body (mainly in H_2O), imaging based on the proton is the most practiced case. To appreciate the source of the

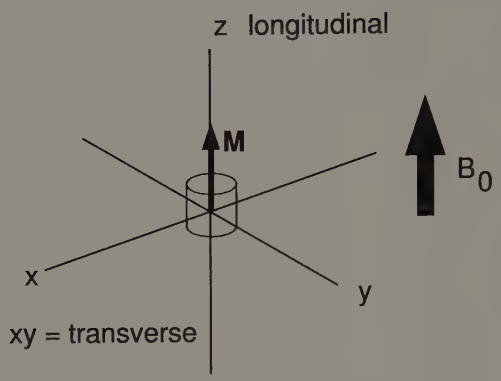

Figure 4.1: Applied B_0 field in z-direction (longitudinal) creates magnetization **M**.

MR signal, we will need to consider the interaction of these nuclei with two types of magnetic fields: a static magnetic field and a radiofrequency (RF) field.

4.2 Interaction with a Static Magnetic Field

When nuclear spins are subjected to a static magnetic field, (say) B_0 in the z direction, two important effects arise. First, there occurs a tendency of the spins to align in the direction of B_0, giving rise to a net magnetization moment **M**. Second, the spins exhibit resonance which is manifested by precessional behavior at a well-defined frequency.

4.2.1 Magnetization

In the presence of B_0, a magnetization moment **M** is produced in the direction of B_0. From a classical viewpoint, one can imagine that $\boldsymbol{\mu}$ aligns in the direction of the applied field; therefore, per unit volume, $\mathbf{M} = \sum \boldsymbol{\mu}$. Figure 4.1 shows the conventions. The z direction is called the longitudinal direction while the xy direction is called the transverse direction.

A quantum mechanical description helps put this polarization into some perspective however. The potential energy E of a magnetic moment $\boldsymbol{\mu}$ in the presence of a **B** field is

$$E = -\boldsymbol{\mu} \cdot \mathbf{B} = -\mu_z B_0 = -\gamma S_z B_0 \tag{4.3}$$

However from quantum mechanics, S_z is quantized to $\hbar I_z$. For hydrogen, $I_z = \pm 1/2$, leading to two energy states separated by

$$\Delta E = \gamma \hbar B_0 = h \frac{\gamma}{2\pi} B_0 \tag{4.4}$$

Thus two populations of nuclei arise, one parallel (n_+) and the other anti-parallel (n_-). Although the n_+ population is of lower energy and the tendency is to occupy the minimum energy state, thermal energy is sufficient to exceed the energy separation. Hence the ratio of the two populations is dependent on the Boltzmann distribution:

$$\frac{n_-}{n_+} = e^{-\Delta E/kT} \tag{4.5}$$

where k is Boltzmann's constant and T is absolute temperature. Typically, this ratio is about 0.999993, implying an excess of only 4 out of 10^6 in the parallel state. Macroscopically however, this excess accounts for the polarization (albeit a weak one).

We can compute the equilibrium nuclear magnetization $M_\circ$. In general, it can be shown that

$$\begin{aligned} M_\circ &= \mu(n_+ - n_-) \\ &= \frac{N\gamma^2\hbar^2 I_z(I_z+1)B_0}{3kT} \end{aligned} \tag{4.6}$$

where $N = n_+ + n_-$, the number of nuclear spins per unit volume. Thus the magnetization is proportional to the applied field B_0. At 37° C = 310 K, $M_\circ$ for protons in H_2O is $3.25 \times 10^{-3} B_0$ A/m.

4.2.2 Precession

At thermal equilibrium, **M** and **B** will be pointed in the same direction. If **M** is made to point in a different direction than **B**, precessional behavior of the magnetization will occur. From classical mechanics, the torque applied to a dipole moment $\boldsymbol{\mu}$ in the presence of **B** is $\boldsymbol{\mu} \times \mathbf{B}$. However, while force equals the rate of change of linear momentum, torque equals the rate of change of angular momentum. Therefore

$$\frac{d\mathbf{S}}{dt} = \boldsymbol{\mu} \times \mathbf{B} \tag{4.7}$$

Multiplying both sides by γ,

$$\frac{d\boldsymbol{\mu}}{dt} = \boldsymbol{\mu} \times \gamma\mathbf{B} \tag{4.8}$$

Nucleus	$\frac{\gamma}{2\pi}$ MHz/T	Relative Sensitivity
^{1}H	42.577	1.000
^{13}C	10.705	0.016
^{19}F	40.054	0.830
^{23}Na	11.262	0.093
^{31}P	17.235	0.066

Table 4.1: Gyromagnetic ratios and relative sensitivities.

Finally, if we consider the summation of $\boldsymbol{\mu}$ over a unit volume,

$$\frac{d\mathbf{M}}{dt} = \mathbf{M} \times \gamma \mathbf{B} \tag{4.9}$$

The solution to this equation is for $\mathbf{M}$ to precess (nutate) about $\mathbf{B}$ at a frequency given by

$$\omega = \gamma B \text{ rad/s} \tag{4.10}$$

$$f = \frac{\gamma}{2\pi} B \text{ Hz} \tag{4.11}$$

This frequency is an important quantity known as the *Larmor* frequency. The magnetization is resonant at that well-defined frequency. As noted earlier, γ, the gyromagnetic ratio, is a unique constant. Table 4.1 lists the value of γ for relevant nuclei along with their relative sensitivities. (The sensitivity depends on γ, I_z and the natural abundance of the isotope). As described in the next section, a radiofrequency field can perturb the magnetization and following this perturbation, the magnetization will precess at the Larmor frequency.

Note that this behavior is analogous to the nutation of a spinning top in a gravitational field. The angular momentum of the top is analogous to the magnetic moment while the gravitation field is analogous to the magnetic field. The gravitational field applies a torque to the top, causing it to precess about the direction of the gravitational field.

4.3 Interaction with a Radiofrequency Field

A magnetic field $\mathbf{B_1}$ applied in the transverse direction and rotating at the resonant frequency of the magnetization will "excite" the magnetization.

Classically, excitation implies a rotation of **M** by some angle. From a classical description, the rotating magnetic field B_1 induces a torque on the magnetization, causing **M** to rotate away from its equilibrium position along z while precessing about the z-axis. As discussed later in Chapter 6, this behavior is describable by solving Eq. 4.9. The frequency of rotation away from the z-axis is $\omega_1 = \gamma B_1$, an analogous result to the Larmor relationship.

Referring back to the quantum mechanical description, another perspective is that the application of RF energy at a frequency $f = (\gamma/2\pi)B_0$ stimulates energy exchange between the two populations that are separated by

$$\Delta E = h\frac{\gamma}{2\pi}B_0 \tag{4.12}$$

This description suffices for describing the behavior of the longitudinal component but does not suffice for describing the resulting transverse component. For the transverse component, we will rely on the classical description.

Following this excitation, the magnetization will continue to precess about the z-axis at a precessional frequency proportional to the applied field. Given a transverse component to the magnetization, detection of the magnetization becomes possible via Faraday's law of induction. The same RF coil used to generate the rotating B_1 field can be used to detect the precessing magnetization. This detection occurs because the precessing magnetization causes a change in flux Φ in the coil, thereby inducing a small electromotive force (EMF) ϵ, where

$$\epsilon = -\frac{\partial \Phi}{\partial t} \tag{4.13}$$

The resulting time signal is commonly called a *free induction decay* (FID) and represents the basic MR signal that is recorded.

A common excitation angle is 90° in which the magnetization is rotated to lie completely in the xy plane with no M_z component. For a single excitation, a 90° excitation leads to the largest possible signal. However, **M** eventually returns to its equilibrium state along z. This implies that the transverse component M_{xy} must decay away while the longitudinal component M_z must regrow. Two important MR parameters, T_1 and T_2, characterize this return to equilibrium and are called relaxation time constants.

4.4 Relaxation

Following an excitation, the transverse component of the magnetization decays away while the longitudinal component returns to its thermal equilibrium state. The mechanisms by which these relaxation events occur are diverse and complex, but can be appreciated from a classical description. We will consider only the dominant mechanism relevant to biological tissues—magnetic dipole-dipole interactions.

4.4.1 Longitudinal Relaxation

The longitudinal component of the magnetization behaves according to

$$\frac{dM_z}{dt} = -\frac{M_z - M_\circ}{T_1} \tag{4.14}$$

The solution of this equation is

$$M_z = M_\circ + (M_z(0) - M_\circ)e^{-t/T_1} \tag{4.15}$$

Following a 90° excitation, $M_z(0) = 0$; hence,

$$M_z = M_\circ(1 - e^{-t/T_1}) \tag{4.16}$$

T_1 is called the spin-lattice time constant and characterizes the return to equilibrium along the z-direction (direction of B_0 field). Physically, T_1 involves the exchange of energy between the nuclei and the surrounding lattice. Thermal equilibrium occurs when M_z is restored to $M_\circ$; that is, when the lowest energy state is reached. At a microscopic level, randomly fluctuating magnetic fields caused by motion of surrounding magnetic dipoles enhance energy exchange and therefore enhance longitudinal relaxation (shortens T_1). The pertinent field fluctuations are those with an xy-component at the spins' resonant frequency, inducing transitions between the populations n_+ and n_-. Note therefore that T_1 will be dependent on field-strength. Because greater energy exchange is required at higher frequencies, this relaxation effect will take longer at higher fields. Hence T_1 values lengthen with increasing B_0.

4.4.2 Transverse Relaxation

The behavior of the transverse component of the nuclear magnetization is describable by

$$\frac{dM_{xy}}{dt} = -\frac{M_{xy}}{T_2} \tag{4.17}$$

The solution (after a 90° excitation—$M_{xy}(0) = M_\circ$) is simply

$$M_{xy} = M_\circ e^{-t/T_2} \tag{4.18}$$

T_2 is called the spin-spin time constant and characterizes the decay of the transverse magnetization. Because the magnetization must eventually return to its equilibrium position along z, the same xy-component field fluctuations that account for T_1 relaxation also account for T_2 relaxation. However, T_2 relaxation processes also depend on z-component field fluctuations; therefore $T_2 \leq T_1$. The z-component fluctuations often dominate the T_2 relaxation process. Microscopically, the interactions between dipoles of their field components in z lead to a broadening of the spins' resonant frequencies. Macroscopically, this spread in resonant frequencies manifests as transverse decay owing to the loss of phase coherence (dephasing) of the transverse component. The pertinent frequency components of the fluctuating z fields are those near zero. These components contribute only to the T_2 relaxation process and not to T_1. Therefore T_2 is largely independent of field strength.

In solids, the presence of relatively slow fluctuations creates a large resonant frequency broadening effect and thus extremely rapid T_2 decay. In biological tissue, spins bound to lumbering macromolecules also experience rapid T_2 decay while relatively mobile spins (e.g., those in water) exhibit much slower decay. However, because of rapid exchange of protons between these two types of environments, the effective T_2 is some average of the two relaxation rates.

4.4.3 Relaxation Times of Biological Tissue

Figure 4.2 plots typical values of T_1 versus field strength for various normal tissue types. Correspondingly, Table 4.2 lists their approximate T_2 values along with approximate values of their relative spin density [BHAAM87, EKH+85, EMB94].

4.5 Bloch Equation

Combining Eq. 4.9 with Eqs. 4.14 and 4.17, the dynamics of the nuclear magnetization are described phenomenologically by the Bloch equation:

$$\boxed{\frac{d\mathbf{M}}{dt} = \mathbf{M} \times \gamma\mathbf{B} - \frac{M_x\,\mathbf{i} + M_y\,\mathbf{j}}{T_2} - \frac{(M_z - M_\circ)\,\mathbf{k}}{T_1}} \tag{4.19}$$

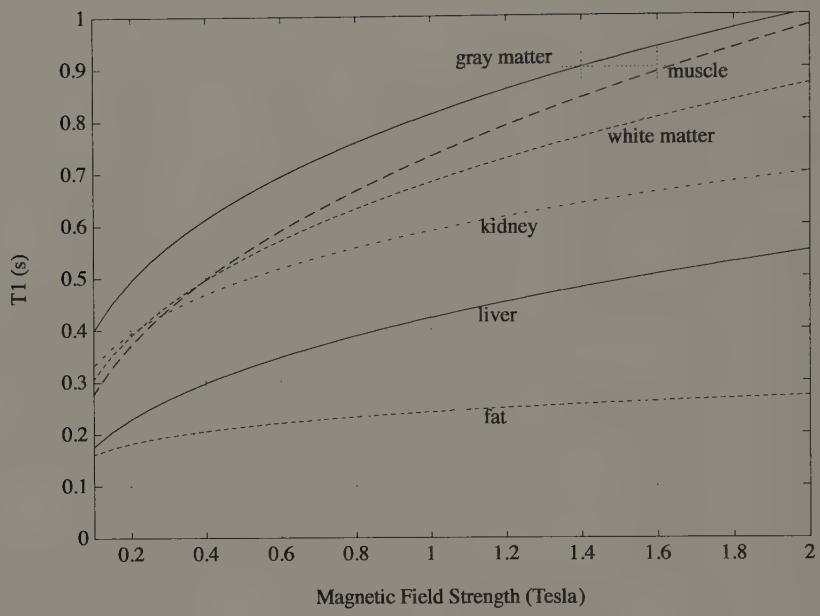

Figure 4.2: Approximate T_1 values as a function of B_0.

Tissue	T_2 (ms)	relative spin density
gray matter	100	0.75
white matter	92	0.65
muscle	47	0.61
fat	85	0.90
kidney	58	0.60
liver	43	0.60

Table 4.2: T_2 and relative spin density (water spin density = 1) of some normal tissue types.

where

γ	=	gyromagnetic ratio
T_1	=	spin-lattice (longitudinal-z) relaxation time constant
T_2	=	spin-spin (transverse-xy) relaxation time constant
$M_\circ$	=	equilibrium sample magnetization due to B_0 field
$\mathbf{i}, \mathbf{j}, \mathbf{k}$	=	unit vectors in x, y, z – directions respectively

The cross-product relation describes a precessional behavior while the relaxation terms describe the exponential behavior of both the longitudinal and transverse components. It should be noted that this exponential behavior is an approximation, given the phenomenological nature of the equation. Although precession does not change the magnitude of $\mathbf{M}$, T_1 and T_2 relaxation effects do change the magnitude. Hence the length of the magnetization does not remain constant as a function of time. For example, in species where T_2 is considerably shorter than T_1, the magnetization can temporarily decay to zero prior to its regrowth along the longitudinal direction.

4.6 Chemical Shift

Chemical shift is a small displacement of the resonant frequency due to shielding created by the orbital motion of the surrounding electrons in response to the main B_0 field. In the presence of B_0, the effective field experienced by the nucleus is

$$B_{\text{eff}} = B_0 - B_{0\sigma} = B_0(1 - \sigma) \tag{4.20}$$

where σ equals a shielding constant that is dependent on the chemical environment. From the Larmor relationship,

$$\omega_{\text{eff}} = \omega_0 - \omega_{0\sigma} = \omega_0(1 - \sigma) \tag{4.21}$$

$\omega_{0\sigma}$ is therefore the displacement of the resonant frequency. Thus the change in frequency is proportional to the magnetic field B_0. The chemical shift is defined with respect to a reference frequency ω_R. If the resonant frequency of our sample is ω_S, then the chemical shift δ, in parts per million, is

$$\begin{aligned} \delta &= \frac{\omega_S - \omega_R}{\omega_R} \times 10^6 \\ &= \frac{\sigma_R - \sigma_S}{1 - \sigma_R} \times 10^6 \\ &\approx (\sigma_R - \sigma_S) \times 10^6 \quad \text{because } \sigma_R \ll 1 \end{aligned} \tag{4.22}$$

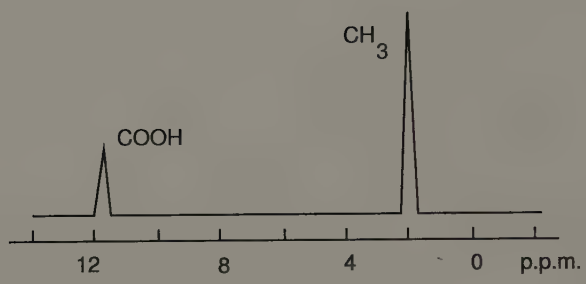

Figure 4.3: ^{1}H NMR spectrum of acetic acid (CH_3COOH).

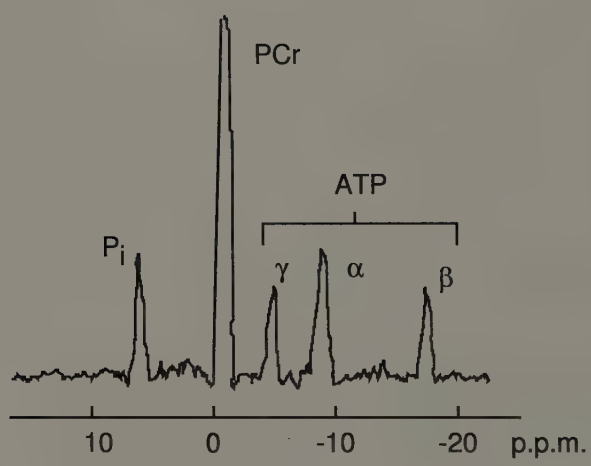

Figure 4.4: ^{31}P NMR spectrum showing the lines from inorganic phosphate P_i, phosphocreatine (PCr), and the three lines from the high-energy compound adenosine triphosphate (ATP).

By placing a sample of some material in a uniform magnet, exciting it, recording its FID, and then Fourier transforming the FID, the resultant NMR spectrum shows lines at different frequencies corresponding to different chemical shifts. An example of such a spectrum is given in Fig. 4.3, which is the ^{1}H spectrum of acetic acid (CH_3COOH). The three protons in the CH_3 group experience a different chemical shift than the proton in the COOH group. Because the valency of the oxygen in the COOH group leads to an attraction of the electron away from the proton, there is less shielding for the proton in the COOH group compared to the protons in the CH_3 group.

For historical reasons, the chemical shift axis in NMR spectroscopy is such that the frequency *decreases* from left to right. Note too that the area under the CH_3 line is three times the area under the COOH line, reflecting the presence of three times more protons. The characteristic lineshape is a Lorentzian owing to the T_2 exponential decay of the signal. For a line centered about ω_0, the Lorentzian lineshape is

$$G(\omega) = \frac{T_2}{1 + (\omega - \omega_0)^2 T_2{}^2} \tag{4.23}$$

which has a linewidth at half height of $2/T_2$. Because T_2 varies little with B_0 while the absolute frequency difference between two lines increases linearly with B_0, higher field strengths are employed to obtain greater line separation (also to improve SNR).

In humans, the most abundant ^{1}H species with different chemical shifts are water (H_2O) and fat (lipids) (many CH_2 groups). We will often assume that the resonant frequency of fat with respect to water's is about 3.5 ppm lower. In general however, fat contains several spectral lines.

A second example of an NMR spectrum is given in Fig. 4.4 which shows a ^{31}P spectrum. PCr is phosphocreatine, P_i is inorganic phosphate, and ATP is adenosine triphosphate. The compounds identified in the ^{31}P spectrum are of physiological interest as the metabolic state of tissue can be inferred by analyzing the relative heights of these lines. For example, an increase in the P_i peak and corresponding decrease in the PCr peak indicates a state of high energy demand or an anaerobic condition, perhaps due to some pathology. Also, the P_i line shifts depend on the pH level, providing additional information such as the level of lactic acid (a byproduct of anaerobic metabolism) which reduces the pH level. Correlation of these peaks with pathology remains an area of research.

Overall NMR spectroscopy is a powerful tool that can be used to probe molecular structure, analyze chemical exchange rates, and follow metabolic processes. Other phenomena exist that complicate the spectrum and add even more subtle but useful information.

4.7 Problems

4.1 Let the total number of spins per unit volume be $N = n_+ + n_-$.

(a) Use Eqn. 4.5 to find an expression for $n_+ - n_-$ in terms of N and the physical parameters.

(b) If $I_z = 1/2$ and kT is large compared to the energy difference between n_+ and n_-, simplify your expression from part (a).

4.2 A material has equilibrium magnetization $M_\circ$ and relaxation time constants T_1 and T_2. If a 90° excitation is applied, find an expression for $|\mathbf{M}(t)|$, the magnitude of the magnetization as a function of time. Show that if $T_2 < T_1$, $|\mathbf{M}(t)|$ can never exceed $M_\circ$.

4.3 Solve equation 4.14 for $M_z(t)$, assuming a general initial condition $M_z(0)$.

4.4 Consider two materials A and B with the same $M_\circ$ but with relaxation time constants (T_{1A}, T_{2A}) and (T_{1B}, T_{2B}) respectively. Let $\Delta S_{xy}(t) = M_{xyA}(t) - M_{xyB}(t)$ be the difference in transverse magnetization, and $\Delta S_z(t) = M_{zA}(t) - M_{zB}(t)$ be the difference in longitudinal magnetization. Assume a 90° excitation.

(a) Find an expression for the time that maximizes $|\Delta S_{xy}|$.

(b) Find an expression for the time that maximizes $|\Delta S_z|$.

(c) Evaluate the expressions from parts (a) and (b) if the two materials are white brain matter and gray brain matter (at $B_0 = 1$ T).

Chapter 5

Imaging Principles

In this chapter, we will derive the equations for the MR signals that will allow us to describe the basic principles of MR image formation. From these analyses, an elegant Fourier interpretation of the signals will emerge that lends powerful insight into the structure of MR imaging. We will show that the received signal directly gives information about the Fourier transform of the object that we wish to image. The ramifications of this result on parameters such as spatial resolution and image field-of-view will also be discussed.

5.1 Bloch Equation

We begin with the Bloch equation,

$$\frac{d\mathbf{M}}{dt} = \mathbf{M} \times \gamma\mathbf{B} - \frac{M_x\,\mathbf{i} + M_y\,\mathbf{j}}{T_2} - \frac{(M_z - M_\circ)\,\mathbf{k}}{T_1} \tag{5.1}$$

a phenomenological equation that governs the behavior of the nuclear magnetization, $\mathbf{M}(t)$, in the presence of a magnetic field $\mathbf{B}(t)$. In MR imaging, $\mathbf{B}$ consists of three types of magnetic fields: 1) $\mathbf{B}_0$, the main static field; 2) $\mathbf{B}_1(t)$, radiofrequency fields which are used for excitation (discussed in Chapter 6); and 3) $\mathbf{G}(t)$, gradient fields which are essential for spatial localization.

We first present a brief qualitative description of the solution to the Bloch equation. Ignoring the relaxation terms, the Bloch equation states that the time rate of change of $\mathbf{M}$ is proportional to the cross-product of $\mathbf{M}$ with $\gamma\mathbf{B}$. Because this cross-product is perpendicular to the plane defined by $\mathbf{M}$ and $\mathbf{B}$, the time rate of change of $\mathbf{M}$ will be perpendicular to the

direction of **M**, implying that the angle between **M** and **B** does not change. Hence if **B** is static, this motion corresponds to a precession of **M** about **B** at an angular frequency of $\gamma|\mathbf{B}|$. If **B** is time-varying in amplitude, then the precessional frequency becomes time-varying. Also if **B** changes directions, the axis of precession will change accordingly.

Example: If **B** points in the z-direction and **M** points as shown in Fig. 5.1, then the precession of **M** will be in the xy plane at angular frequency $\gamma|\mathbf{B}|$. The 90° angle between **B** and **M** will not change.

We now proceed to present mathematical solutions to the Bloch equation for a variety of conditions.

5.1.1 Homogeneous Object, Uniform Field

In the simplest case, we consider a homogeneous sample in a static, uniform field; that is, $\mathbf{B}(t) = B_0\mathbf{k}$. If we ignore both T_1 and T_2 effects, the Bloch equation is

$$\frac{d\mathbf{M}}{dt} = \mathbf{M} \times \gamma B_0 \mathbf{k} \tag{5.2}$$

which in matrix form is

$$\begin{pmatrix} \frac{dM_x}{dt} \\ \frac{dM_y}{dt} \\ \frac{dM_z}{dt} \end{pmatrix} = \begin{pmatrix} 0 & \gamma B_0 & 0 \\ -\gamma B_0 & 0 & 0 \\ 0 & 0 & 0 \end{pmatrix} \begin{pmatrix} M_x \\ M_y \\ M_z \end{pmatrix} \tag{5.3}$$

The cross-coupling of the M_x and M_y components leads to a solution of

$$\begin{aligned} \mathbf{M}(t) &= \begin{pmatrix} M_x(t) \\ M_y(t) \\ M_z(t) \end{pmatrix} = \begin{pmatrix} \cos\omega_0 t & \sin\omega_0 t & 0 \\ -\sin\omega_0 t & \cos\omega_0 t & 0 \\ 0 & 0 & 1 \end{pmatrix} \mathbf{M}^\circ \\ &= \mathbf{R}_z(\omega_0 t)\mathbf{M}^\circ \end{aligned} \tag{5.4}$$

where

$$\begin{aligned} \mathbf{M}^\circ &= \text{initial conditions} \\ \omega_0 &= \gamma B_0 = \text{Larmor frequency} \end{aligned} \tag{5.5}$$

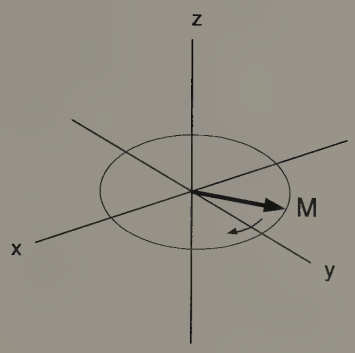

Figure 5.1: Precessing Magnetization Vector about the z-axis.

Equation 5.4 describes a magnetization vector precessing about z, the direction of the applied field, at an angular frequency of ω_0 (Fig. 5.1).

If we include the terms containing T_1 and T_2, the Bloch equation written in matrix form becomes

$$\frac{d\mathbf{M}}{dt} = \begin{pmatrix} -1/T_2 & \gamma B_0 & 0 \\ -\gamma B_0 & -1/T_2 & 0 \\ 0 & 0 & -1/T_1 \end{pmatrix} \mathbf{M} + \begin{pmatrix} 0 \\ 0 \\ \frac{M_\circ}{T_1} \end{pmatrix} \tag{5.6}$$

and the solution is

$$\mathbf{M}(t) = \begin{pmatrix} e^{-t/T_2} & 0 & 0 \\ 0 & e^{-t/T_2} & 0 \\ 0 & 0 & e^{-t/T_1} \end{pmatrix} \mathbf{R}_z(\omega_0 t)\mathbf{M}^\circ + \begin{pmatrix} 0 \\ 0 \\ M_\circ(1 - e^{-t/T_1}) \end{pmatrix} \tag{5.7}$$

The solution for M_x and M_y now contains the factor $\exp(-t/T_2)$, indicating the existence of decay of the precessing magnetization in the transverse (xy) plane with time constant T_2. Simultaneous with this transverse decay, there occurs a return to the equilibrium position along the longitudinal axis (z) at a rate determined by time constant T_1. Figure 5.2 plots the transverse and longitudinal behavior of $\mathbf{M}$ when $\mathbf{M}^\circ = M_\circ \mathbf{i}$.

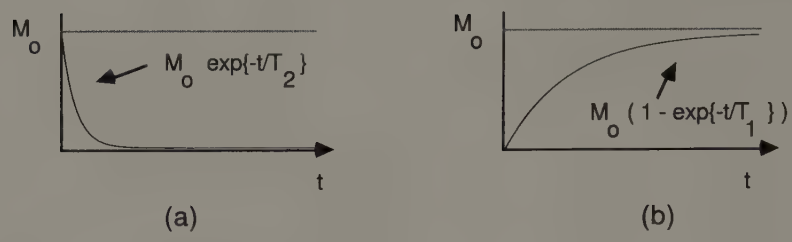

Figure 5.2: Relaxation Behavior: (a) Transverse relaxation characterized by time constant T_2. (b) Longitudinal relaxation characterized by time constant T_1.

We often examine the behavior of the transverse component M_{xy}, because it determines the time signals recorded. Because vectors rotating at frequency ω_0 are conveniently described by the complex exponential $\exp(-i\omega_0 t)$, we will make a slight notational change by representing the transverse component as a complex quantity,

$$M \triangleq M_x + iM_y \tag{5.8}$$

with an initial condition of

$$M^\circ = M_x^\circ + iM_y^\circ \tag{5.9}$$

Using this complex representation, the Bloch equation for this case is now written as

$$\frac{dM}{dt} = \frac{dM_x}{dt} + i\,\frac{dM_y}{dt} = -\left(\frac{1}{T_2} + i\omega_0\right)M \tag{5.10}$$

$$\frac{dM_z}{dt} = -\frac{M_z - M_\circ}{T_1} \tag{5.11}$$

Equation 5.10 for the transverse component is a simple first-order differential equation with a compact solution of

$$\begin{aligned} M &= M^\circ e^{-t/T_2} e^{-i\omega_0 t} \\ &= M^\circ e^{-t/T_2} e^{-i2\pi f_0 t} \end{aligned} \tag{5.12}$$

representing a decaying complex exponential of frequency f_0. The original components' values are related to M by

$$Re\{M\} = M_x \tag{5.13}$$

$$Im\{M\} = M_y \tag{5.14}$$

5.1.2 Inhomogeneous Object, Nonuniform Field

We now generalize from a homogeneous sample to an inhomogeneous sample. Therefore $M(t)$ and T_2 become $M(\mathbf{r},t)$ and $T_2(\mathbf{r})$, now functions of space ($\mathbf{r} = [x\ y\ z]$). Note here that it is important to keep track of whether (x,y,z) is being used to designate spatial position or magnetization component. In general, the quantities we deal with are $M_x(x,y,z)$, $M_y(x,y,z)$, and $M_z(x,y,z)$.

We will also generalize the situation from a uniform static magnetic field $B_0\mathbf{k}$ to a nonuniform magnetic field but one still pointed in the z-direction. This nonuniform field can be static $\mathbf{B}(\mathbf{r})$ or, more generally, time-varying $\mathbf{B}(\mathbf{r},t)$ where

$$\mathbf{B}(\mathbf{r},t) = [B_0 + \Delta B(\mathbf{r},t)]\mathbf{k} \tag{5.15}$$

The term $\Delta B(\mathbf{r},t)$ accounts for both the spatial and time dependences.

Using this expression for $\mathbf{B}$, we write the Bloch equation for the transverse component as

$$\frac{dM}{dt} = -\left\{\frac{1}{T_2(\mathbf{r})} + i[\omega_0 + \Delta\omega(\mathbf{r},t)]\right\} M \tag{5.16}$$

where

$$\begin{aligned} \omega_0 &= \gamma B_0 \\ \Delta\omega(\mathbf{r},t) &= \gamma \Delta B(\mathbf{r},t) \end{aligned} \tag{5.17}$$

The general solution for the transverse component is

$$M(\mathbf{r},t) = M^\circ(\mathbf{r}) e^{-t/T_2(\mathbf{r})} e^{-i\omega_0 t} \exp\left(-i\int_0^t \Delta\omega(\mathbf{r},\tau)\, d\tau\right) \tag{5.18}$$

We now consider specific cases of nonuniform fields.

Static Gradient Field

The simplest but most common and important case of a nonuniform field is a *static gradient field.* This is a field pointing in the z direction (as is B_0) but with an amplitude that varies with position. For example, an x-gradient G_x is the slope in the x-direction of the z-component of the applied field; that is,

$$\frac{dB_z}{dx} = G_x \tag{5.19}$$

With a static x-gradient,

$$\Delta\omega(\mathbf{r}) = \gamma G_x x \tag{5.20}$$

Note that with only B_0 present, the Larmor frequency is $\omega = \omega_0 = \gamma B_0$, but with an x-gradient turned on in addition, the Larmor frequency varies with x-position:

$$\omega(x) = \omega_0 + \Delta\omega(\mathbf{r}) = \gamma(B_0 + G_x x) \tag{5.21}$$

The solution to the Bloch equation is

$$M(\mathbf{r}, t) = M^\circ(\mathbf{r}) e^{-t/T_2(\mathbf{r})} e^{-i\omega_0 t} e^{-i(\gamma G_x x)t} \tag{5.22}$$

This equation implies that planes at different x-locations produce signals at different frequencies. The variation in frequency with x-position is linear, corresponding to the use of a linear gradient field.

Static Gradient Field—Arbitrary Orientation

A more general case than an x-gradient is a static gradient at a general orientation in 3D. This gradient can be expressed as a vector $\mathbf{G} = G_x\,\mathbf{i} + G_y\,\mathbf{j} + G_z\,\mathbf{k}$. With all three gradients turned on, the resultant field is a gradient of magnitude $(G_x^2 + G_y^2 + G_z^2)^{1/2}$ and sloped in a direction dependent on their relative amplitudes.

The total magnetic field is

$$\begin{aligned} \mathbf{B}(\mathbf{r}) &= (B_0 + G_x x + G_y y + G_z z)\mathbf{k} \\ &= (B_0 + \mathbf{G}\cdot\mathbf{r})\mathbf{k} \end{aligned} \tag{5.23}$$

Thus

$$\Delta\omega(\mathbf{r}) = \gamma\mathbf{G}\cdot\mathbf{r} \tag{5.24}$$

and

$$M(\mathbf{r}, t) = M^\circ(\mathbf{r}) e^{-t/T_2(\mathbf{r})} e^{-i\omega_0 t} e^{-i\gamma\mathbf{G}\cdot\mathbf{r}\,t} \tag{5.25}$$

Time-Varying Gradient Fields

Most generally, we will deal with *time-varying gradients* in which

$$\mathbf{B}(\mathbf{r}, t) = [B_0 + \mathbf{G}(t)\cdot\mathbf{r}]\mathbf{k} \tag{5.26}$$

The solution is

$$M(\mathbf{r}, t) = M^\circ(\mathbf{r}) e^{-t/T_2(\mathbf{r})} e^{-i\omega_0 t} \exp\left(-i\gamma \int_0^t \mathbf{G}(\tau)\cdot\mathbf{r}\,d\tau\right) \tag{5.27}$$

For example, with a time-varying x-gradient $G_x(t)$,

$$M(\mathbf{r}, t) = M^\circ(\mathbf{r}) e^{-t/T_2(\mathbf{r})} e^{-i\omega_0 t} \exp\left(-i\gamma x \int_0^t G_x(\tau)\,d\tau\right) \tag{5.28}$$

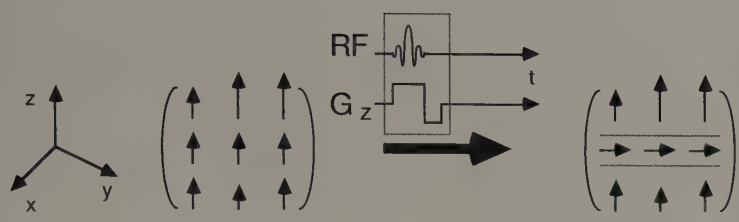

Figure 5.3: Selective excitation results in transverse magnetization from a plane.

5.2 Signal Equation

Thus far, we have solved the Bloch equation for several important cases involving gradient fields. We now use these solutions to show how these gradients enable imaging of the nuclear magnetization. In MR imaging systems, the receiver coil encompasses and is (ideally) uniformly sensitive over the entire volume-of-interest. Also the receiver coil is designed to detect flux changes in the transverse direction. Therefore, the received time signal $s_r(t)$ is derived from the contributions of all precessing transverse magnetization in the volume. Simplistically, we may write then that

$$\begin{aligned} s_r(t) &= \int_{\text{vol}} M(\mathbf{r},t)\, dV \\ &= \int_x \int_y \int_z M(x,y,z,t)\, dx\, dy\, dz \end{aligned} \tag{5.29}$$

ignoring constant gain factors and constant phase factors (see next section). Using the result for a general time-varying gradient (Eq. 5.27),

$$s_r(t) = \int\int\int M^\circ(x,y,z) e^{-t/T_2(\mathbf{r})} e^{-i\omega_0 t} \exp\left(-i\gamma \int_0^t \mathbf{G}(\tau)\cdot \mathbf{r} d\tau\right) dx\, dy\, dz \tag{5.30}$$

At this point, we will use the following simplifications to facilitate our discussion on imaging methods.

- We will ignore the relaxation term $\exp(-t/T_2)$.
- We will deal with 2D (planar) imaging methods (3D imaging is discussed in Chapter 8). We assume then that a plane centered at $z = z_\circ$ and of thickness Δz has been selectively excited (we defer a detailed discussion on selective excitation until Chapter 6) so that signals from only that plane are received (Fig. 5.3). Examining Fig. 5.4, we

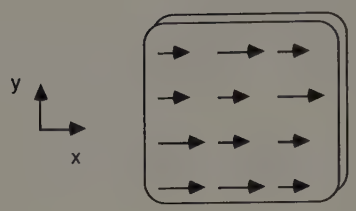

Figure 5.4: Distribution of transverse magnetization in the excited plane.

see that the length of each vector represents the magnitude of magnetization at a particular (x, y) position and the direction of each vector represents its relative phase.

The 2D function that we are interested in imaging is based on the integral over the slice width. Therefore

$$m(x,y) \triangleq \int_{z_\circ-\Delta z/2}^{z_\circ+\Delta z/2} M^\circ(x,y,z)\, dz \tag{5.31}$$

and

$$s_r(t) = \int_x \int_y m(x,y) e^{-i\omega_0 t} \exp\left(-i\gamma \int_0^t \mathbf{G}(\tau)\cdot\mathbf{r}\, d\tau\right) dx\, dy \tag{5.32}$$

- We will drop the $\exp(-i\omega_0 t)$ factor. This simplification is completely justified because $s_r(t)$ is typically demodulated in frequency by ω_0 using phase sensitive detection as described in the next section. The resultant *baseband* (or envelope) signal, $s(t)$, is therefore

$$\begin{aligned} s(t) &= s_r(t)\, e^{+i\omega_0 t} \\ &= \int_x \int_y m(x,y) \exp\left(-i\gamma \int_0^t \mathbf{G}(\tau)\cdot\mathbf{r}\, d\tau\right) dx dy \end{aligned} \tag{5.33}$$

Via this planar integral, $s(t)$ provides information about $m(x,y)$, the transverse nuclear magnetization distribution of interest. Ultimately, we wish to acquire an appropriate set of time signals $\{s(t)\}$ to reconstruct an image $I(x,y)$ that most closely approximates $m(x,y)$. In general, $m(x,y)$ is a function of the NMR parameters $\rho(x,y)$ (density), $T_1(x,y)$, and $T_2(x,y)$. The precise functional form depends on various timing and excitation parameters. We defer this issue of image contrast until Chapter 7 and instead concentrate first on the mechanisms of image formation.

Because spatial localization is required in only the x and y directions, Eq. 5.33 simplifies further by considering only the x and y gradient fields

$G_x(t)$ and $G_y(t)$. Thus, our equation for the received time signal from an excited plane becomes

$$s(t) = \int\int m(x,y) \exp\left[-i\gamma\left(\int_0^t G_x(\tau)d\tau\right)x\right] \cdot \exp\left[-i\gamma\left(\int_0^t G_y(\tau)d\tau\right)y\right] dx\,dy \tag{5.34}$$

or

$$\boxed{s(t) = \int_x \int_y m(x,y) e^{-i2\pi[k_x(t)x + k_y(t)y]}\, dx\,dy} \tag{5.35}$$

where

$$\begin{aligned} k_x(t) &= \frac{\gamma}{2\pi}\int_0^t G_x(\tau)\, d\tau \\ k_y(t) &= \frac{\gamma}{2\pi}\int_0^t G_y(\tau)\, d\tau \end{aligned} \tag{5.36}$$

the time integrals of the gradient waveforms.

We will refer to Eq. 5.35 as the *signal equation.* This equation is extremely important as it will enable us to describe almost every imaging method. The imaging problem becomes one of acquiring the appropriate set of signals $\{s(t)\}$ to enable inversion of Eq. 5.35 to determine $m(x,y)$.

5.2.1 Other Considerations of the Signal Equation

This simplified form of the signal equation is convenient and will not impede our discussion on the basic imaging principles. However we ignored two complicating issues in the derivation of $s(t)$. The first issue concerns Faraday's law of induction which is the physical law that dictates signal detection. The second issue deals with the real-valued nature of the received signal and how demodulation occurs. Before proceeding then, we will address these issues to provide a more accurate description. However we will show that the same expression results for $s(t)$.

Faraday's Law and the Signal Equation

The precessing magnetization gives rise to an electromotive force (EMF) in the neighboring receiver coil. From Faraday's law of induction, the electromotive force (ϵ) generated in a receiver coil depends on the rate of change of flux (Φ) in the coil; specifically,

$$\epsilon = -\frac{\partial \Phi}{\partial t} \tag{5.37}$$

If $\mathbf{B}_1(x, y, z)$ is the magnetic field produced at point (x, y, z) per unit current in the coil, then from the principle of reciprocity [HL79], it can be shown that the incremental EMF produced in the coil is

$$d\epsilon = -\frac{\partial}{\partial t}[\mathbf{B}_1(x, y, z) \cdot \mathbf{M}(x, y, z, t)]\, dV \tag{5.38}$$

Hence $\mathbf{B}_1(x, y, z)$ is indicative of the receiver coil's sensitivity within the volume. The units are as follows:

$$\begin{aligned}
B_1 : &\quad \frac{T}{A} = \frac{\mathrm{Wb/m^2}}{A} \\
M : &\quad \frac{A\,\mathrm{m}^2}{\mathrm{m}^3} = \frac{\text{magnetic moment}}{\text{unit volume}} = \text{magnetization} \\
\frac{\partial}{\partial t}\{\mathbf{B_1} \cdot \mathbf{M}\, dV\} : &\quad \frac{1}{s} \cdot \frac{\mathrm{Wb/m^2}}{A} \cdot \frac{A}{\mathrm{m}} \cdot \mathrm{m}^3 = \frac{\mathrm{Wb}}{s} = \text{Volts}
\end{aligned}$$

Integrating over the volume, we derive the total EMF signal $s_r(t)$.

$$\int_{vol} d\epsilon = s_r(t) = -\int_{vol} \frac{\partial}{\partial t}[\mathbf{B}_1(x, y, z) \cdot \mathbf{M}(x, y, z, t)]\, dV \tag{5.39}$$

Assuming that $\mathbf{B}_1$ is directed in the transverse direction and is homogeneous ($= B_{1xy}$) over the volume of interest, then the EMF depends on the time-variation of the transverse component of the magnetization. Ignoring T_2 decay,

$$\begin{aligned}
s_r(t) &= -\int_{vol} B_{1xy} \frac{\partial}{\partial t} M(x, y, z, t)\, dV \\
&= -\int_{vol} B_{1xy}\, M^\circ(x, y, z) \frac{\partial}{\partial t}\left[e^{-i\omega_0 t} \exp\left(-i\gamma \int \mathbf{G}(\tau) \cdot \mathbf{r}\, d\tau\right)\right] dV \\
&= -\int_{vol} B_{1xy}\, M^\circ(x, y, z) \\
&\qquad \left[-i(\omega_0 + \gamma \mathbf{G}(t) \cdot \mathbf{r}) e^{-i\omega_0 t} \exp\left(-i\gamma \int \mathbf{G}(\tau) \cdot \mathbf{r}\, d\tau\right)\right] dV
\end{aligned} \tag{5.40}$$

This relation helps explain the rationale for having the receiver coil designed to detect changes in the transverse component of the magnetization rather than the longitudinal component. The presence of B_0 along z, the longitudinal axis, establishes a high-frequency precession in the transverse direction, lending itself to convenient detection by induction.

Because the main field dominates the gradient field on most systems, the center frequency $\omega_0 \gg \gamma \mathbf{G}(t) \cdot \mathbf{r}$, and the signal equation reduces to

$$s_r(t) = i\omega_0 B_{1xy} \int_{vol} M^\circ(x,y,z) e^{-i\omega_0 t} \exp\left(-i\gamma \int \mathbf{G}(\tau) \cdot \mathbf{r}\, d\tau\right) dV \tag{5.41}$$

At this point, we note that the strength of the signal is proportional to ω_0 which is also proportional to B_0. This is one factor in the B_0-dependence of signal-to-noise considerations.

Henceforth we will ignore the constant $i\omega_0 B_{1xy}$ and write the signal equation as simply

$$s_r(t) = \int\int\int M^\circ(x,y,z) e^{-i\omega_0 t} \exp\left(-i\gamma \int \mathbf{G}(\tau) \cdot \mathbf{r}\, d\tau\right) dx\, dy\, dz \tag{5.42}$$

Demodulation

For our analysis, we have described a complex-valued received signal $s_r(t)$ and a complex-valued baseband signal $s(t)$, related by

$$s_r(t) = s(t) e^{-i\omega_0 t} = \alpha(t) e^{-i[\omega_0 t + \phi(t)]} \tag{5.43}$$

where $\alpha(t)$ and $\phi(t)$ are the amplitude and phase modulation of the baseband signal. The received signal corresponds to the laboratory frame behavior while the baseband signal corresponds to the rotating frame behavior.

The demodulation of $s_r(t)$ down to $s(t)$ is described by

$$s(t) = s_r(t) e^{+i\omega_0 t} = \alpha(t) e^{-i\phi(t)} \tag{5.44}$$

It is important to realize that the complex-valued $s_r(t)$ serves as a useful quantity for the sake of analysis but in practice, a single time signal is usually recorded. If we call this real-valued physical signal $s_p(t)$, then

$$s_p(t) = Re\{s_r(t)\} = \alpha(t) \cos[\omega_0 t + \phi(t)] \tag{5.45}$$

However from this real-valued $s_p(t)$, we can still demodulate down to the desired complex-valued $s(t)$ through a process known as *quadrature phase-sensitive detection* (PSD).

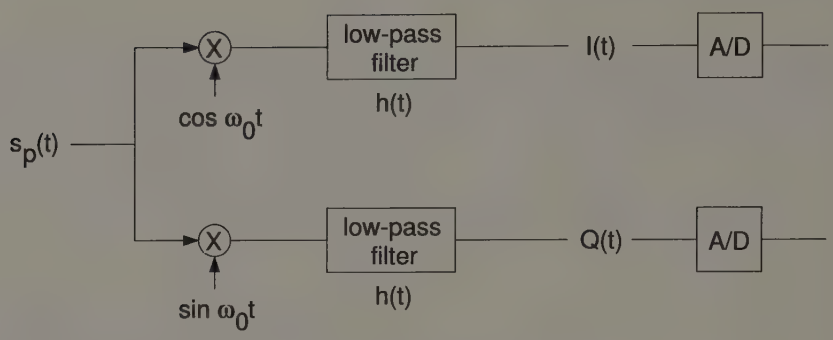

Figure 5.5: Quadrature Detection: The incoming RF signal is split into two channels, one multiplied by $\cos\omega_0 t$ and and the other by $\sin\omega_0 t$. Subsequent low-pass filtering retains the baseband component. The output consists of $I(t)$ (the in-phase signal) and $Q(t)$ (the quadrature signal) which are then digitized.

Figure 5.5 is a block diagram of quadrature PSD which leads to two output signals: $I(t)$ (for in-phase) and $Q(t)$ (for quadrature). Equivalently, they are often called the real and imaginary components of the baseband signal.

The expression for $I(t)$ is

$$\begin{aligned} I(t) &= \{\alpha(t)\cos[\omega_0 t + \phi(t)] \cdot \cos\omega_0 t\} * h(t) \\ &= \left\{\frac{\alpha(t)}{2}\{\cos[2\omega_0 t + \phi(t)] + \cos\phi(t)\}\right\} * h(t) \\ &= \alpha(t)\cos\phi(t) \end{aligned} \tag{5.46}$$

where $h(t)$ is the impulse response of the low-pass filter that removes the $2\omega_0$ frequency component. For Q, the expression is

$$\begin{aligned} Q(t) &= \{\alpha(t)\cos[\omega_0 t + \phi(t)] \cdot \sin\omega_0 t\} * h(t) \\ &= \left\{\frac{\alpha(t)}{2}\{\sin[2\omega_0 t + \phi(t)] - \sin\phi(t)\}\right\} * h(t) \\ &= -\alpha(t)\sin\phi(t) \end{aligned} \tag{5.47}$$

Hence the baseband signal is realized by

$$\begin{aligned} s(t) &= I(t) + iQ(t) \\ &= \alpha(t)e^{-i\phi(t)} \end{aligned} \tag{5.48}$$

as desired.

5.3 Alternate Derivation: Signal Equation

The baseband signal equation, derived explicitly by solving the Bloch equation, can be also derived by using a simple physical model. We can imagine a tiny "magnetic oscillator" rotating at frequency $\omega = \gamma B$ at each position (x, y) in the plane-of-interest. The oscillator possesses some amplitude $m(x, y)$ (which we will assume is time-invariant) and some phase $\phi(x, y, t)$ (which is in general time-varying). Hence we express the signal from the oscillator at (x, y) as $m(x, y)\exp[-i\phi(x, y, t)]$. If the receiver coil is uniformly sensitive over the plane, then the total received signal is the sum of signals from every point in the plane. The expression becomes

$$s_r(t) = \int_x \int_y m(x, y) e^{-i\phi(x,y,t)}\, dx\, dy \tag{5.49}$$

What is $\phi(x, y, t)$? By definition, frequency equals the time rate of change in phase, and from the solution to the Bloch equation, frequency is also proportional to the applied field $B(x, y, t)$ from the Larmor relation. Therefore

$$\frac{d\phi(x, y, t)}{dt} = \omega(x, y, t) = \gamma B(x, y, t) \tag{5.50}$$

and

$$\phi(x, y, t) = \int_0^t \omega(x, y, \tau)\, d\tau = \gamma \int_0^t B(x, y, \tau)\, d\tau \tag{5.51}$$

assuming an initial phase of zero. If

$$B(x, y, t) = B_0 + G_x(t)x + G_y(t)y \tag{5.52}$$

then

$$\begin{aligned} \phi(x, y, t) &= \gamma \int_0^t B_0\, d\tau + \gamma \left(\int_0^t G_x(\tau)\, d\tau \right) x + \gamma \left(\int_0^t G_y(\tau)\, d\tau \right) y \\ &= \omega_0 t + 2\pi k_x(t)x + 2\pi k_y(t)y \end{aligned} \tag{5.53}$$

The gradient fields thus enable control of the phase of the precessing magnetization.

Demodulating to remove the carrier frequency factor $\exp(-i\omega_0 t)$, we get

$$s(t) = \int_x \int_y m(x, y) e^{-i2\pi[k_x(t)x + k_y(t)y]}\, dx\, dy \tag{5.54}$$

the same as Eq. 5.35 as derived earlier from first principles with the Bloch equation. This derivation, which avoids an explicit use of the Bloch equation, illustrates a convenience of relying on the basic Larmor relationship

(that is implicit with the Bloch equation) when considering the transverse component.

Example: Given an MR sequence, the Bloch equation need not be solved explicitly to determine the resultant signal; instead, only the expression for the phase ϕ of the baseband signal need be determined. Hence,

$$\phi = \gamma \int_0^t \mathbf{G}(\mathbf{r}, \tau) \cdot \mathbf{r}\, d\tau \tag{5.55}$$

Often, the analysis will center on just this expression for the phase.

If, for example, we apply $G_x(t) = A \sin \Omega t$ (a gradient whose amplitude varies sinusoidally with time), then we can immediately write the expression for the resultant phase as

$$\begin{aligned} \phi(x,t) &= \gamma \int_0^t A(\sin \Omega\tau) x\, d\tau \\ &= \gamma \frac{A}{\Omega}(1 - \cos \Omega t) x \end{aligned} \tag{5.56}$$

The signal equation becomes

$$s(t) = \int_x \int_y m(x,y) \exp\left[-i\gamma \frac{A}{\Omega}(1 - \cos \Omega t) x\right] dx\, dy \tag{5.57}$$

5.4 Fourier Interpretation of the Signal Equation

The signal equation states that the baseband signal is the planar integral of the magnetization multiplied by a spatially-dependent phase factor. Because linear gradient fields are applied, the resultant phase modulation factor will also vary linearly with spatial position. Comparing the signal equation,

$$s(t) = \int_x \int_y m(x,y) e^{-i2\pi[k_x(t)x + k_y(t)y]}\, dx\, dy \tag{5.58}$$

with the 2D Fourier transform of $m(x,y)$,

$$\mathcal{M}(k_x, k_y) = \int_x \int_y m(x,y) e^{-i2\pi(k_x x + k_y y)}\, dx\, dy \tag{5.59}$$

and doing a one-to-one correspondence, we see immediately that the baseband signal can be expressed as

$$s(t) = \mathcal{M}\big(k_x(t),\ k_y(t)\big) \tag{5.60}$$

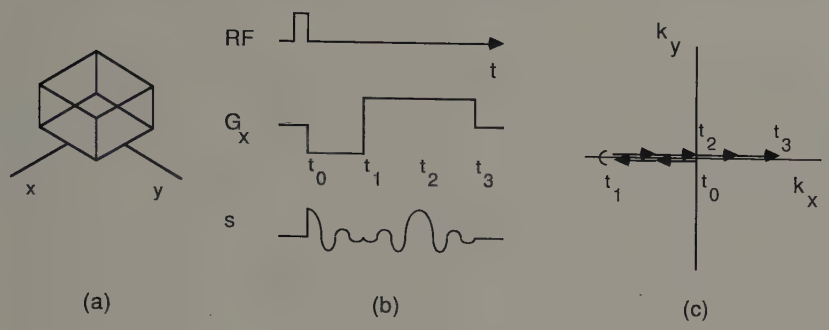

Figure 5.6: Square Object Example: (a) $m(x,y) = {}^2\sqcap(x,y)$. (b) Pulse Sequence with plot of baseband signal generated. (c) k-Space trajectory of pulse sequence.

or

$$\boxed{s(t) = \mathcal{M}\left(\frac{\gamma}{2\pi}\int_0^t G_x(\tau)\,d\tau\,,\ \frac{\gamma}{2\pi}\int_0^t G_y(\tau)\,d\tau\right)} \tag{5.61}$$

Thus k_x and k_y are in units of spatial-frequency, typically cycles/mm or cycles/cm.

This is the most important relationship in MR imaging. At any given time t, $s(t)$ equals the value of the 2D Fourier transform of $m(x,y)$ at some spatial frequency. The total recorded signal $s(t)$ therefore maps directly to a trajectory through spatial-frequency (Fourier) space as determined by the time integrals of the applied gradient waveforms $G_x(t)$ and $G_y(t)$. In the MR literature [Lju83, Twi83], 2D Fourier transform space is often called "k-space," where k represents the spatial-frequency variable. To form an image, the required set of signals $\{s(t)\}$ is obvious. The trajectories given by $\{s(t)\}$ should cover a sufficient part of k-space to allow reconstruction of $m(x,y)$. This elegant Fourier-space interpretation greatly facilitates the design and analysis of imaging methods. It is particularly useful for analyzing sequences employing time-varying gradients, which are more difficult to appreciate from an object-domain perspective because the mapping between temporal frequency and spatial position breaks down.

Example: Consider a square object (see Fig. 5.6a) where $m(x,y) = {}^{2}\sqcap(x,y)$. When the pulse sequence of Fig. 5.6b is applied, the resultant signal $s(t)$ appears as plotted. Figure 5.6c shows the k-space trajectory of this particular pulse sequence. The trajectory starts at the origin and, with the negative gradient on, moves along the negative k_x-axis. When the gradient reverses at time t_1, the trajectory, being the time-integral of the gradient waveform, begins to move in the positive k_x direction, eventually crossing the origin at time t_2 (when the gradient area becomes zero) and stopping at time t_3 at some positive k_x-position. With a square object, its Fourier transform will be a centered sinc function along the k_x axis. Therefore, from the k-space interpretation of the signal equation, we know that $s(t)$ will also be a sinc function, as depicted in Fig. 5.6b. Because the trajectory retraces itself over the negative k_x region, the signal from t_0 to t_1 will be the time reflection of the signal from t_1 to t_2.

5.5 Illustration of the k-Space Perspective

Before discussing specific imaging methods, we elaborate in this section on why the value of the signal $s(t)$ at a given time equals the 2D Fourier transform of $m(x,y)$ at a particular spatial frequency (k_x, k_y). This section presents plots illustrating the phase behavior of the nuclear magnetization vectors in a plane under the influence of gradient fields (which determine k_x and k_y). Each plot presents a top-view "snapshot" of the excited slice at a given time. Each vector in the plot represents the transverse magnetization at a position (x,y) in the slice (in the case considered, 23 by 23 different elements are depicted), with the vector length indicating magnitude and the vector direction indicating phase. Because all vectors shown possess the same length, the assumed object is uniform.

The first plot (Fig. 5.7, position 1) shows the state of the vectors immediately following the excitation. An ideal excitation leaves each vector pointed in the same direction as shown. Because the vectors are in phase, they sum coherently and the resultant signal at this moment in time equals the "magnetization volume" of the slice. Because the volume under a 2D function $m(x,y)$ equals the value of its 2D Fourier transform at $(k_x = 0, k_y = 0)$, $s(t = 0)$ is exactly equal to the value at the origin of k-space. Therefore, the trajectory begins at the origin.

Continuing with the sequence, the y-gradient is switched on, causing spins at higher y-positions to precess faster than those at lower y-positions. After leaving G_y on for some time, the snapshot taken of the

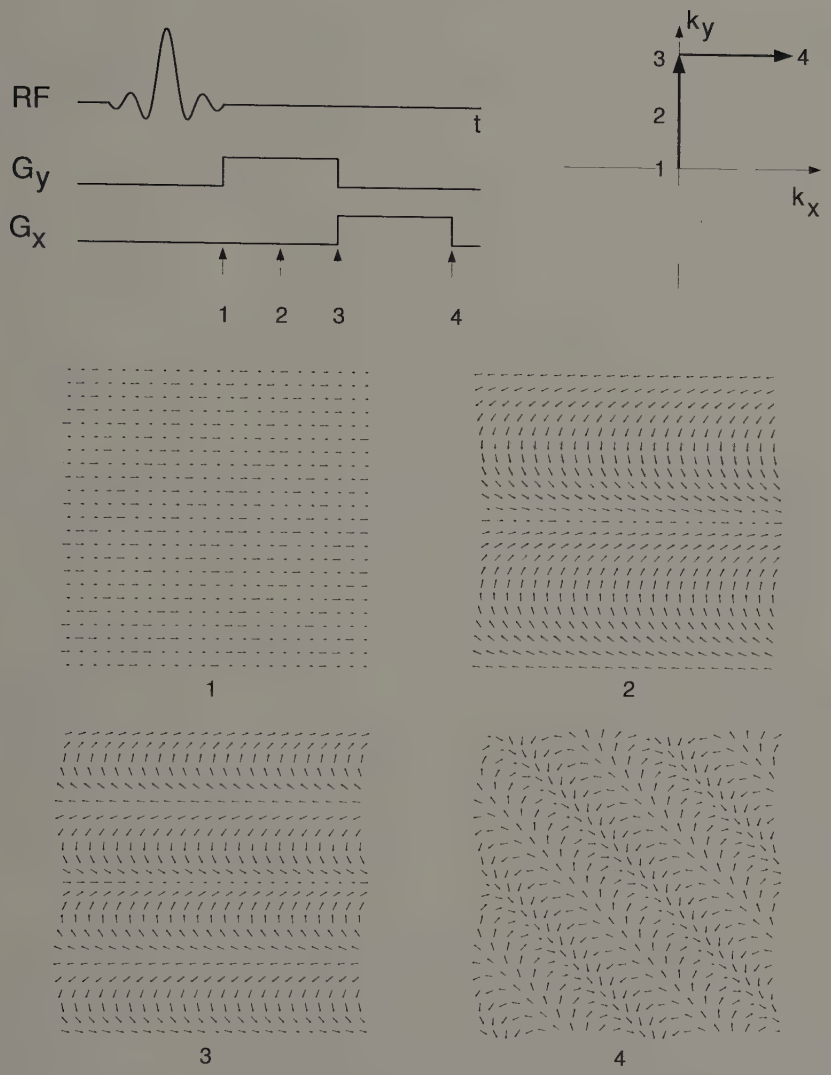

Figure 5.7: (Top) Timing diagram and k-space trajectory. (Bottom) Spin distribution corresponding to the four labelled time points: (1) immediately after excitation; (2) midway after the y gradient has been turned on; (3) just prior to turning off the y gradient; and (4) after the x gradient has been left on.

slice (Fig. 5.7, position 2) shows the phase progressively increasing as one moves along the y-direction (the vectors rotate clockwise as one scans from bottom to top). In fact, the phase varies linearly with y-position. Such a linear phase variation with spatial position implies a particular spatial frequency, analogous to the linear phase variation with time that exists for $\cos 2\pi f t$, a sinusoid at a particular temporal frequency f. Examination of Fig. 5.7 (position 2) reveals that the x-component of each vector is weighted by a cosine as a function of the vectors' y-position; the y-component of each vector is weighted by a sine as a function of the vectors' y-position. Because the vectors are representable as complex-valued quantities, they are thus being multiplied by a complex exponential of some frequency k_{y1}. The signal at this instant in time therefore equals the planar integral of $m(x, y)$ multiplied by $\exp(-i2\pi k_{y1} y)$. This integral (and hence the signal value) is precisely equal to the 2D Fourier transform of $m(x, y)$ at k-space position $(0, k_{y1})$.

After leaving G_y on longer, the phase varies even faster as one scans in the y-direction, effectively weighting the complex-valued distribution by a complex exponential of a higher spatial frequency k_{y2}. Thus at this moment in time (Fig. 5.7, position 3), the signal equals the k-space value at a higher spatial-frequency position $(0, k_{y2})$.

We now turn off the G_y gradient and turn on the G_x gradient. The x-gradient creates phase variations in x because those vectors located at higher x-positions precess faster. The trajectory through k-space takes a right-hand turn and moves parallel to the k_x-axis. The resultant snapshot of the magnetization vectors (Fig. 5.7, position 4) resembles the cosinusoidal function of Fig. 2.1, oriented at some angle between 0° and 90°. The signal at this moment, being the sum of all the vectors, equals the k-space value at the appropriate (k_{x1}, k_{y2}) position.

5.6 Basic 2D Imaging Methods

We now discuss some specific 2D MR imaging sequences from both spatial-frequency domain and object-domain perspectives.

5.6.1 2D Projection Reconstruction

This method is similar to that used in x-ray computed tomography (CT). The timing diagram of the basic 2D projection reconstruction (2DPR) sequence is given in Fig. 5.8a. Following the excitation, the x and y gradients turn on and the FID signal is read out. The amplitudes of the two gradients are incremented appropriately on subsequent excitations.

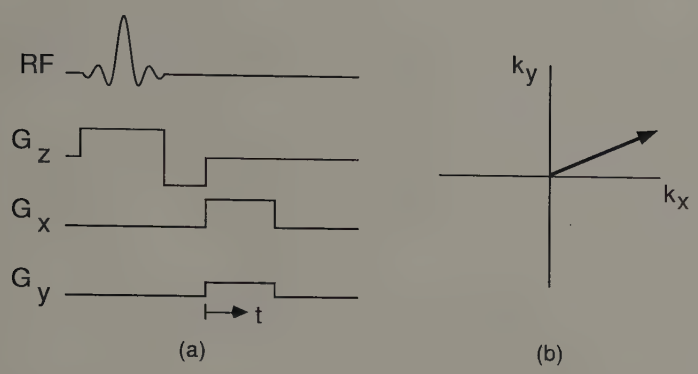

Figure 5.8: 2D Projection Reconstruction Sequence: (a) Timing Diagram: Readout begins immediately after selective excitation in the presence of a gradient. (b) *k*-Space trajectory begins at the origin and extends outwards.

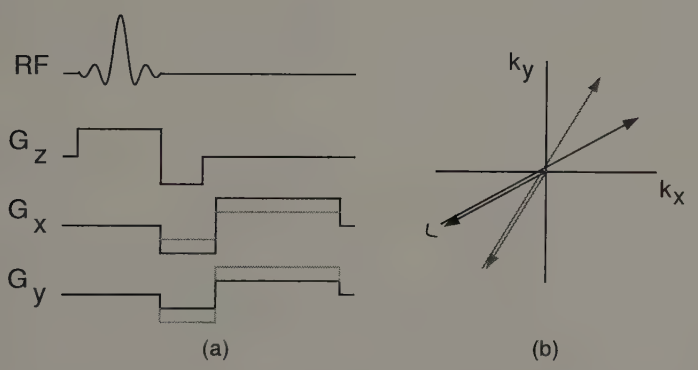

Figure 5.9: Modified 2D Projection Reconstruction Sequence: (a) Timing Diagram: A negative gradient lobe precedes the positive lobe; The signal is read out during the positive lobe. (b) *k*-Space trajectory extends outwards and then retraces itself. Information in two quadrants is acquired.

Fourier-Domain Perspective

The k-space trajectory of this sequence is a set of radial lines ("spokes") emanating from the origin of k-space, one from each excitation. Each line starts at the origin (because $k_x(0) = k_y(0) = 0$) and moves out at an angle θ where $\theta = \tan^{-1}(G_y/G_x)$ (Fig. 5.8b). Because data from only one quadrant is obtained after each excitation, the angular extent of the measurement set must range from 0 to 360 degrees.

Theoretically, if $m(x, y)$ is a real function, then $\mathcal{M}(k_x, k_y)$ is Hermitian; that is,

$$\mathcal{M}(-k_x, -k_y) = \mathcal{M}^*(k_x, k_y) \tag{5.62}$$

Thus the line in quadrant I can be used to determine the corresponding line in quadrant III and only half of k-space need be acquired. Practically however, $m(x, y)$ is usually not real-valued (due to phase shifts from a variety of sources) and the Hermitian assumption breaks down.

Alternatively, to traverse the entire line, the gradient waveforms of Fig. 5.9a can be applied during the signal readout. In this case, the k-space trajectory begins at the origin, initially moves left, turns around when the gradient reverses, moves right, passes through the origin again, and continues to move right (Fig. 5.9b). Hence information from two quadrants is obtained for each readout, and so an angular extent from 0 to 180 degrees suffices to fill k-space. As depicted by the dotted lines in Fig. 5.9, the relative amplitudes of the two gradient components are varied to acquire a line at a different angle in k-space.

Object-Domain Perspective

Whenever a constant gradient is used during signal readout, temporal frequency maps conveniently to spatial position, and a clear object-domain perspective emerges. If (say) an x-gradient is on, then all spins located at a particular x-position will contribute signal at a single frequency. Each frequency bin is based therefore on the integration over y of spins with the same x-position. This relationship implies that the frequency spectrum of the recorded signal represents a 1D projection of the object. Because the gradient during readout is applied at different angles in a 2DPR sequence, the measurement set provides 1D projections at different angles as in the x-ray CT situation.

The relationship between the measurements and the projections can be

derived from the signal equation, as

$$\begin{aligned} s(t) &= \int_x \int_y m(x,y) e^{-i\gamma G_x t x}\, dx\, dy \\ &= \int_x \left(\int_y m(x,y)\, dy \right) \exp\left[-i2\pi \left(\frac{\gamma}{2\pi} G_x t \right) x \right] dx \\ &= \mathcal{F}_{1D}\{g_{\theta=0^\circ}(x)\}|_{k_x=(\gamma/2\pi)G_x t} \end{aligned} \tag{5.63}$$

where

$$g_{0^\circ}(x) = \int_y m(x,y)\, dy \tag{5.64}$$

the projection of $m(x,y)$ along the y-direction. As noted, each frequency bin of the temporal Fourier transform of $s(t)$ corresponds to the summation of $m(x,y)$ at a particular x–location. To compute this projection, we simply Fourier transform $s(t)$; that is,

$$g_{0^\circ}(x) = \mathcal{F}_{1D}\{s(t)\}|_{f=-(\gamma/2\pi)G_x x} \tag{5.65}$$

More generally, to generate a gradient oriented at an angle θ,

$$\begin{aligned} G_x &= G\cos\theta \\ G_y &= G\sin\theta \end{aligned} \tag{5.66}$$

Then using rotated coordinates, where

$$\begin{aligned} x &= u\cos\theta - v\sin\theta \\ y &= u\sin\theta + v\cos\theta \end{aligned} \tag{5.67}$$

we can write the signal expression as

$$\begin{aligned} s_\theta(t) &= \int_u \int_v m_\theta(u,v) e^{-i\gamma G t u}\, du\, dv \\ &= \int_u \exp\left[-i2\pi \left(\frac{\gamma}{2\pi} G t \right) u \right] du \left(\int_v m_\theta(u,v)\, dv \right) \\ &= \mathcal{F}_{1D}\{g_\theta(u)\}|_{k_u=(\gamma/2\pi)Gt} \end{aligned} \tag{5.68}$$

From the central section theorem, the 1D Fourier transform of a projection taken at angle θ gives us the radial slice of the 2D Fourier transform of the object at that angle θ. Hence each measurement provides information in the 2D Fourier transform plane along the line at angle θ.

Note that the reasoning in this section involved two 1D Fourier transforms, one relating $s(t)$ to the 1D projection, and the other relating the 1D projection to the radial line in 2D Fourier transform space via the central section theorem. Given these back-to-back Fourier transforms, we have

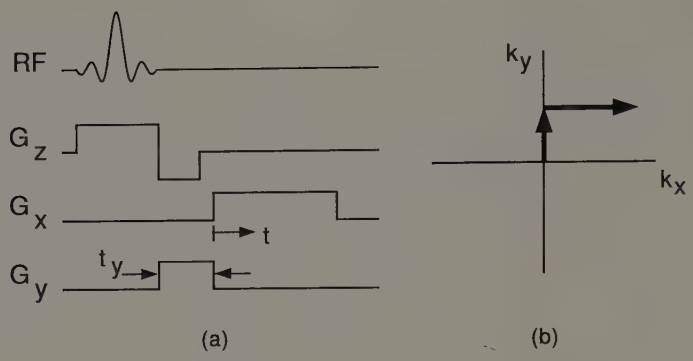

Figure 5.10: 2D Fourier Transform Sequence: (a) Timing Diagram (b) k-Space Trajectory.

another indication that $s(t)$ resides in the 2D Fourier transform domain of $m(x,y)$. Therefore, we have obtained the k-space perspective of the signal equation from a different point of view—that is, by using physical reasoning to derive projections, and invoking the central section theorem to relate the projections to k-space.

To summarize the 2D projection-reconstruction method:

1. record N k-space lines (projections), each line (projection) at a different angle θ by changing the gradient orientation each time;

2. reconstruct $m(x,y)$ by processing the data set with established CT reconstruction algorithms (for example, convolution back-projection) on the projections or by 2D Fourier transformation of the k-space data after interpolation onto a 2D grid.

5.6.2 2D Fourier Transform

This method has no analog in x-ray imaging. Figure 5.10a shows the timing diagram of the basic 2D Fourier transform (2DFT) sequence. A selective excitation pulse excites the slice and the y-gradient turns on for a time t_y. Once G_y turns off, the signal is read out in the presence of a constant x-gradient. On subsequent excitations, the amplitude of the y-gradient lobe is incremented but the x-gradient remains the same.

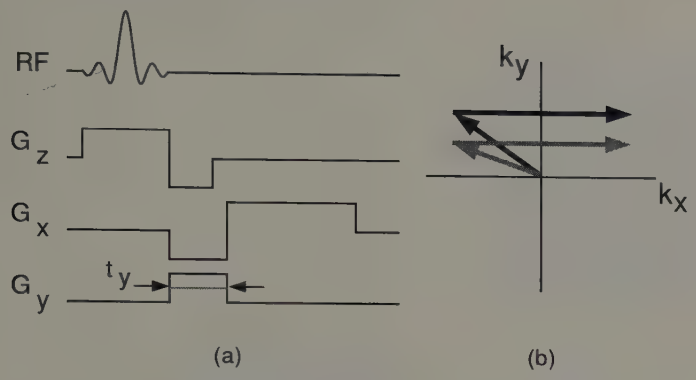

Figure 5.11: Modified 2D Fourier Transform Sequence: (a) Timing Diagram (b) k-Space Trajectory.

Fourier-Domain Perspective

Beginning at the origin, the k-space trajectory moves along the k_y-axis during the G_y interval and then takes a right turn, moving along the k_x direction as the signal is read out (Fig. 5.10b).

To obtain the entire horizontal line in k-space, the sequence is modified as shown in Fig. 5.11a. The timing of the data acquisition is adjusted accordingly to record during the full-length horizontal traversal in k-space (Fig. 5.11b). A change in the amplitude of the G_y gradient leads to a different line in k-space (see dotted lines in Fig. 5.11). In comparison with 2DPR, where sampling in k-space falls on a polar grid, the 2DFT method samples k-space in a rectilinear (Cartesian) grid. By indexing to a set of k_y-positions, we can assemble sufficient measurements to fill 2D transform space and simply perform an inverse 2D transform to reconstruct $m(x, y)$.

Object-Domain Perspective

The signal equation for the one-sided sequence is

$$s(t) = \int_x \int_y m(x, y) e^{-i\gamma(G_x x t + G_y y t_y)} \, dx \, dy \tag{5.69}$$

For each measurement, $G_y t_y$ is fixed and t is the "running" variable. We can rewrite the signal equation as

$$\begin{aligned} s(t) &= \int_x \exp\left[-i2\pi\left(\frac{\gamma}{2\pi}G_x t\right)x\right]dx \cdot \\ &\qquad \left\{\int_y m(x,y)\exp\left[-i2\pi\left(\frac{\gamma}{2\pi}G_y t_y\right)y\right]dy\right\} \\ &= \mathcal{F}_{1D}\{\text{Projection along y of} \\ &\qquad m(x,y)\exp\left[-i2\pi\left(\frac{\gamma}{2\pi}G_y t_y\right)y\right]\}|_{k_x=(\frac{\gamma}{2\pi})G_x t} \end{aligned} \tag{5.70}$$

Because the same constant G_x gradient is on during each signal acquisition, we can view the set of measurements as giving projections with line-integration always along the y-direction. However, the application of a y-gradient prior to signal readout implies that the projection is of $m(x,y)$ multiplied by a complex weighting factor $\exp\{-i2\pi[(\gamma/2\pi)G_y t_y]y\}$. This complex weighting factor varies with y-position and corresponds to spatial frequency $k_y = (\gamma/2\pi)G_y t_y$. In interpreting this complex weighting (or phase) factor, we observe that the y-gradient "warps" the phases of the spins prior to the signal readout—hence 2DFT imaging is sometimes referred to as *spin-warp* imaging. Each measurement is based on a different $G_y t_y$ product which implies a different amount of phase warping. Typically we hold t_y fixed and vary the amplitude of G_y, although in principle, G_y and/or t_y can be varied. What matters is the area under the y-gradient waveform.

Because of the specific roles that these gradients play, the indexed G_y gradient is often referred to as the *phase-encoding* gradient while the G_x gradient, which is on during the data acquisition, is called the *readout* gradient. The third gradient G_z is appropriately called the *slice-select* gradient.

To summarize the 2D Fourier Transform Method:

1. record N k-space lines at different k_y-positions by changing the area under the y-gradient for each measurement.

2. reconstruct $m(x,y)$ by 2D Fourier transformation of the k-space data which already resides on a Cartesian grid.

Figure 5.12 displays some of the baseband time signals from a typical 2DFT scan. These time signals correspond to the readouts of some of the 256 phase encoding steps taken during the scan. The image is reconstructed by mapping this raw data appropriately in Fourier space and then Fourier transforming.

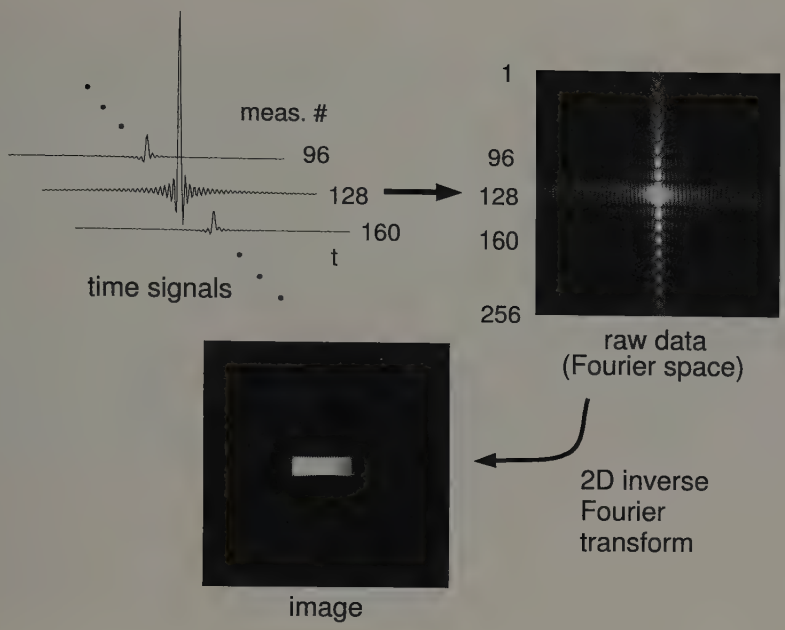

Figure 5.12: A collection of time signals maps to Fourier space (raw data space). Inverse Fourier transformation of the raw data reconstructs the image. Not surprisingly, the time signals resemble sinc functions because the object is rectangular.

2DFT Examples

Imaging with 2DFT sequences predominates in MR. One reason is the convenience and efficiency in image reconstruction afforded by the Cartesian sampling in k-space (other reasons are discussed in Chapter 7). In this section, we show images and the corresponding k-space data which will illustrate the Fourier transform relationship. Figure 5.13a is the "raw" data (actually the magnitude of raw data), displayed in an image format. This data, collected with a 2DFT sequence, consists of 256 by 256 data points, where each of the 256 rows corresponds to a particular time signal acquired at one of the phase-encoding levels. The 256 points in each row implies that each time signal was sampled to 256 points. The brightness at each point indicates the amplitude of the time-signal sample. Figure 5.13b is the resultant image produced after a 2D FFT of the raw data. Not surprisingly, the object is a circle which corresponds to the jinc function appearance in the raw data.

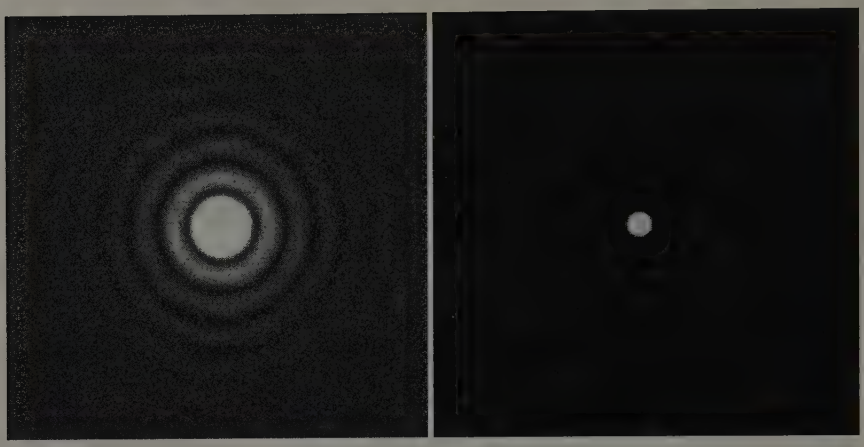

Figure 5.13: Test Tube of Water—2DFT sequence: (a) Raw Data (magnitude) displayed in image format; 256 phase encodes (vertical direction) x 256 time samples (horizontal direction). Raw data, being in k-space, is a jinc function. (b) Image after 2D FFT of (a).

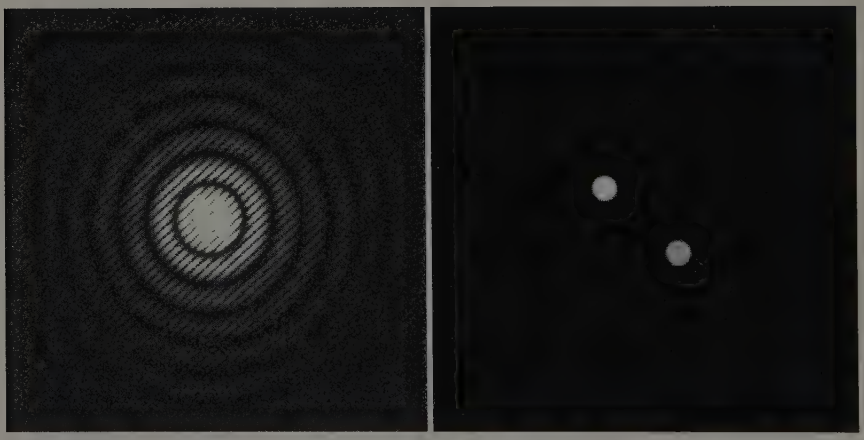

Figure 5.14: Two Test Tubes of Water—2DFT sequence: (a) Raw Data (magnitude): This example illustrates the modulation theorem of Fourier transforms as the raw data shows a modulation in the 45° direction. (b) Image shows two test tubes separated in the modulation direction.

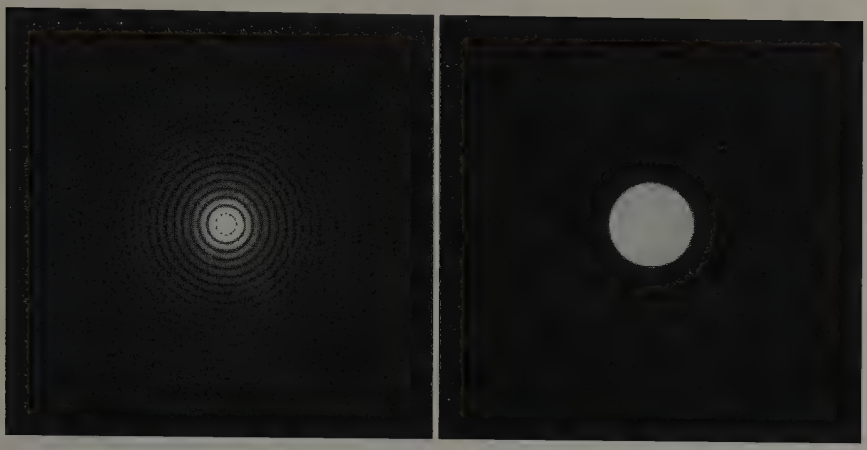

Figure 5.15: Larger Test Tube: (a) Raw Data (magnitude): This example illustrates the stretch theorem of Fourier transforms. The raw data is a compressed version of the raw data from the small test tube. (b) Image is of a correspondingly larger test tube.

Figures 5.14 and 5.15 show related raw data/image pairs. Based on Fig. 5.13a, one can predict the resultant images in Figs. 5.14 and 5.15 by invoking Fourier transform theorems. The modulation theorem applies for the case of Fig. 5.14 because the raw data of Fig. 5.14a equals the raw data of Fig. 5.13a multiplied a cosinusoidal weighting factor. Therefore the image, Fig. 5.14b, consists of two small vials separated along the direction of modulation. At larger separations, the modulation frequency will be increased. Figure 5.15 exemplifies the stretch theorem as the narrower jinc function behavior in k-space (Fig. 5.15a) leads to a circular object of larger radius (Fig. 5.15b).

Magnitude Display of MR Images: All of the MR images shown are based on the magnitude of the complex-valued reconstruction. In an ideal situation, $I(x,y) = m(x,y)$, a real-valued function, and a magnitude display is unnecessary. In practice however, $I(x,y)$ will be complex-valued for a variety of reasons (e.g., the data acquisition is not precisely centered at the k-space origin, the spatial sensitivity of the RF coil is not uniform in phase). Typically, if $m(x,y)$ represents the ideal magnetization distribution, then we can model the actual image reconstruction as $m(x,y)\exp(-i\phi(x,y))$, where $\phi(x,y)$ represents the phase variation across the image.

5.7 Sampling Requirements: 2DFT Imaging

Proper image formation depends on the appropriate coverage in k-space. In 2DFT imaging, the raster nature of the k-space trajectory corresponds to rectangular coverage on a Cartesian grid, allowing convenient image reconstruction with a 2D DFT. Thus far, our analysis has been with continuous time signals but in practice, the baseband signal, and thus k-space, is sampled as shown in Fig. 5.16a. The sampling periods are Δ_{k_x} and Δ_{k_y} while the highest spatial frequencies sampled are k_{xmax} and k_{ymax}. With 2DFT imaging, an asymmetry exists in the k-space acquisition as samples along the k_x direction accumulate during a single readout while samples along the k_y direction accumulate by repeating the excitation for different phase encodes. As discussed in Section 2.4, we can express the sampled k-space data $\widehat{\mathcal{M}}(k_x, k_y)$ as

$$\widehat{\mathcal{M}}(k_x, k_y) = \mathcal{M}(k_x, k_y) \cdot \left(\frac{1}{\Delta_{k_x}\Delta_{k_y}}\right) {}^2\text{Ш}\left(\frac{k_x}{\Delta_{k_x}}, \frac{k_y}{\Delta_{k_y}}\right) \cdot {}^2\sqcap\left(\frac{k_x}{W_{k_x}}, \frac{k_y}{W_{k_y}}\right) \tag{5.71}$$

where

$$\begin{aligned} W_{k_x} &= 2\left(k_{xmax} + \frac{\Delta_{k_x}}{2}\right) \\ W_{k_y} &= 2\left(k_{ymax} + \frac{\Delta_{k_y}}{2}\right) \end{aligned} \tag{5.72}$$

are the widths traversed in k-space in each direction (note the extra Δ term above, which makes the width W equal the product of Δ and the number of samples; the boundaries of the rectangle function thus lie a half sample period past the highest spatial frequency sample on each side).

The resultant Fourier transform into the object domain relates the image $\widehat{m}(x, y)$ to the actual distribution $m(x, y)$.

$$\widehat{m}(x, y) = m(x, y) ** {}^2\text{Ш}(\Delta_{k_x}x, \Delta_{k_y}y) ** W_{k_x}W_{k_y}\,\text{sinc}(W_{k_x}x)\,\text{sinc}(W_{k_y}y) \tag{5.73}$$

where $**$ denotes 2D convolution. We now analyze Eq. 5.73 to discuss how the image field of view (FOV) and spatial resolution relate to the k-space sampling periods $(\Delta_{k_x}, \Delta_{k_y})$ and k-space widths (W_{k_x}, W_{k_y}).

5.7.1 Field of View

In general, sampling in one domain (object or spatial frequency) amounts to replication in the corresponding transform domain. In MR, sampling

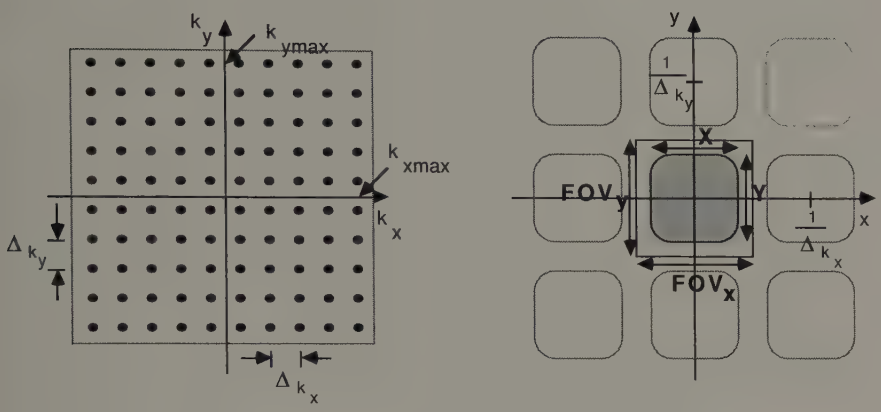

Figure 5.16: (a) Sampling in k-space. (b) Corresponding replication in object domain.

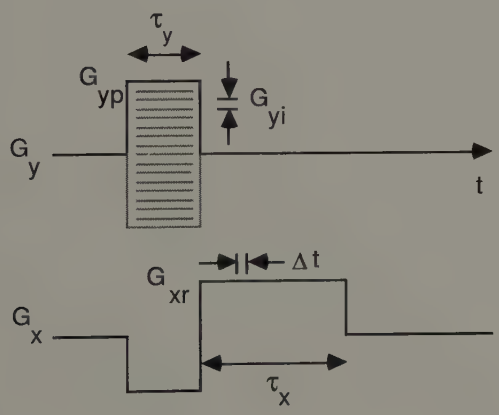

Figure 5.17: Timing and Amplitude Parameters: Phase Encoding: G_{yi} = incremental gradient amplitude; G_{yp} = maximum gradient amplitude; τ_y = phase-encoding interval. Readout: G_{xr} = gradient amplitude; Δt = interval between data samples; τ_x = total readout interval.

takes place in the spatial frequency domain; hence replication in the object domain must be considered. If we assume sampling that is infinite in extent, then from Eq. 5.73 the resultant object is

$$\widehat{m}(x,y) = m(x,y) * *^2\text{Ш}(\Delta_{k_x}x, \Delta_{k_y}y) \tag{5.74}$$

The next section on spatial resolution discusses the effect of finite-extent sampling.

The convolution of $m(x,y)$ with ${}^2\text{Ш}(\Delta_{k_x}x, \Delta_{k_y}y)$ implies a replication of $m(x,y)$ at intervals of $1/\Delta_{k_x}$ in the x direction and by $1/\Delta_{k_y}$ in the y direction (Fig. 5.16b). The separation of these replication islands determines the effective FOV in the image. From Eq. 5.74 and Fig. 5.16b, we can write that

$$\begin{aligned} \text{FOV}_x &= \frac{1}{\Delta_{k_x}} = \text{sampling rate along } k_x \\ \text{FOV}_y &= \frac{1}{\Delta_{k_y}} = \text{sampling rate along } k_y \end{aligned} \tag{5.75}$$

To relate FOV to the parameters of 2DFT imaging, we refer to Fig. 5.17. Because the k-space position is a function of the gradient areas, the k-space sampling period is a function of the incremental area under each gradient. Thus the sampling period along the readout direction depends on the readout gradient amplitude G_{xr} and the sampling period Δt of the A/D converters. Along the phase-encoding direction, the sampling period depends on the incremental gradient area, as determined by the incremental gradient amplitude G_{yi} and the fixed phase-encoding duration τ_y. The expressions for these periods are

$$\begin{aligned} \Delta_{k_x} &= \frac{\gamma}{2\pi} G_{xr} \Delta t \\ \Delta_{k_y} &= \frac{\gamma}{2\pi} G_{yi} \tau_y \end{aligned} \tag{5.76}$$

From this, we can write the expressions for FOV as

$$\boxed{\text{FOV}_x = \frac{1}{\Delta_{k_x}} = \frac{1}{\frac{\gamma}{2\pi} G_{xr} \Delta t}} \tag{5.77}$$

and

$$\boxed{\text{FOV}_y = \frac{1}{\Delta_{k_y}} = \frac{1}{\frac{\gamma}{2\pi} G_{yi} \tau_y}} \tag{5.78}$$

Note that we can rearrange Eqs. 5.77 and 5.78 as

$$\begin{aligned} \gamma G_{xr} \Delta t (\mathrm{FOV}_x) &= 2\pi \\ \gamma G_{yi} \tau_y (\mathrm{FOV}_y) &= 2\pi \end{aligned} \tag{5.79}$$

From an object-domain perspective, these equations imply that the incremental gradient area in going from one phase encode to the next amounts to applying an additional cycle of phase warp over the FOV.

Aliasing

Aliasing arises in a sampled system if the sampling rate is not sufficient. In MR, sampling in spatial frequency domain means that aliasing will occur in the object domain. Because objects are spatially bounded, aliasing can be avoided in MR imaging by adjusting the sequence to give smaller incremental gradient areas between samples in both the readout and phase-encoding directions, thereby increasing the FOV in both directions. Figure 5.18a shows a 480 mm (48 cm) FOV 2DFT image of a circular object with a diameter of about 280 mm (28 cm). If the phase-encoding and readout gradients are *doubled*—thereby doubling the sampling period and halving the FOV to 240 mm (24 cm)—the resultant image is Fig. 5.18b. The "wrap-around" apparent in both directions of Fig. 5.18b is a result of the adjacent replicated object islands aliasing into the FOV (readout = horizontal direction, phase encoding = vertical direction). Anti-aliasing measures are possible in 2DFT imaging, but they are different for the readout and phase-encoding directions.

To avoid aliasing in the phase-encoding direction, the incremental area under the phase-encoding lobe must be reduced to increase the FOV (as in Fig. 5.18a). However, for a fixed scan time, the number of phase encodes remains fixed and thus the highest spatial frequency sampled along k_y is reduced. This worsens the spatial resolution, as will be discussed in the next section. To maintain the same spatial resolution, additional phase encodes must be acquired which increases the scan time. Hence an increase in scan time or a reduction in spatial resolution are the trade-offs for avoiding aliasing in the phase-encoding direction.

In the readout direction, k-space samples are acquired rapidly after each excitation in the presence of a constant readout gradient. The amplitude of this gradient dictates the temporal frequency bandwidth of the recorded signal, which in 2DFT imaging is $(\gamma/2\pi)G_{xr}X$, where X is the width of the object in the readout direction. If X exceeds FOV_x, then the Nyquist sampling criterion is violated and aliasing in the object domain occurs. One means of avoiding aliasing in the readout direction is to pass

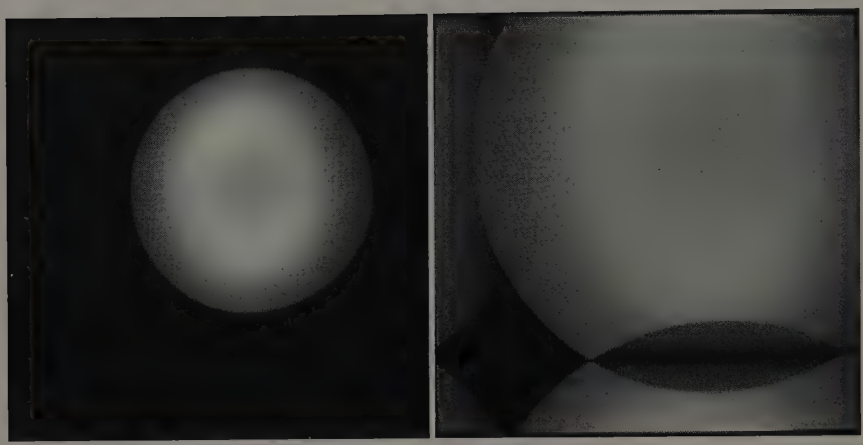

Figure 5.18: (a) 480 mm (48 cm) FOV; (b) 240 mm (24 cm) FOV shows aliasing in both directions.

Figure 5.19: (a) 240 mm (24 cm) FOV with reduced filter bandwidth; (b) 240 mm (24 cm) FOV with oversampling in the readout direction.

the signal through an anti-aliasing filter with a bandwidth commensurate with the sampling frequency of the A/D converters. Although such a filter was used for Fig. 5.18b, aliasing effects remained because of tails in the filter's frequency response. Figure 5.19a demonstrates the use of a narrower bandwidth filter, which eliminates aliasing in the readout direction, but is often undesirable because part of the usable image is filtered away. Alternatively, a filter with a better frequency response at the proper bandwidth is preferable. A second means of eliminating aliasing is to simply sample the time signal at a higher rate. For example, by doubling the A/D sampling rate, FOV_x doubles with no penalty in scan time or readout time. Figure 5.19b shows an image with the same parameters as in Fig. 5.18b except that the A/D sampling rate was doubled. FOV_x is therefore 480 mm (48 cm) for Fig. 5.19b and only the center 240 mm (24 cm) is displayed. Aliasing in the phase-encoding direction remains.

5.7.2 Spatial Resolution

As shown in Fig. 5.16a, the k-space sampling is finite, extending a distance $(2k_{xmax} + \Delta_{k_x})$ and $(2k_{ymax} + \Delta_{k_y})$ in the readout and phase-encoding directions respectively. Therefore, from Eq. 5.73, the replicated object is not $m(x, y)$, rather it is

$$m(x, y) * * W_{k_x} W_{k_y} \operatorname{sinc}(W_{k_x} x) \operatorname{sinc}(W_{k_y} y) \tag{5.80}$$

This 2D sinc blur function limits the ability to resolve detailed structures. Given an FOV and number of sample points, one appealing definition of spatial resolution is FOV/(number of sample points). Thus if δ_x and δ_y represent the spatial resolution in the x and y directions respectively, then using this definition,

$$\begin{aligned} \delta_x &= \frac{\text{FOV}_x}{N_{read}} = \frac{1}{\Delta_{k_x} N_{read}} = \frac{1}{W_{k_x}} \\ \delta_y &= \frac{\text{FOV}_y}{N_{pe}} = \frac{1}{\Delta_{k_y} N_{pe}} = \frac{1}{W_{k_y}} \end{aligned} \tag{5.81}$$

where N_{read} is the number of readout samples and N_{pe} is the number of phase encodes (the benefit of the extra Δ in the definition of W is now evident). Thus while FOV depends on the k-space sampling periods, spatial resolution depends on the widths of the k-space coverage.

Referring again to the 2DFT sequence of Fig. 5.17, k_{xmax} and k_{ymax} are functions of the maximum gradient areas attained by the readout and phase-encoding gradients. For the readout, the maximum gradient area is

$G_{xr}\tau_x/2$ while for the phase encoding, it is $G_{yp}\tau_y$. We can write then that

$$\begin{aligned} k_{xmax} &= \frac{\gamma}{2\pi} G_{xr} \frac{\tau_x}{2} \\ k_{ymax} &= \frac{\gamma}{2\pi} G_{yp} \tau_y \end{aligned} \tag{5.82}$$

Combining Eq. 5.82 with Eqs. 5.72and 5.76, the expression for the spatial resolution is

$$\delta_x = \frac{1}{W_{k_x}} = \frac{1}{\frac{\gamma}{2\pi} G_{xr}(\tau_x + \Delta t)} \tag{5.83}$$

and

$$\delta_y = \frac{1}{W_{k_y}} = \frac{1}{\frac{\gamma}{2\pi}(2G_{yp} + G_{yi})\tau_y} \tag{5.84}$$

These expressions for the spatial resolution are slightly cumbersome because of the two terms in the denominator. The expressions are most useful when N is small. In most cases however, N is large (N > 100) and

$$\begin{aligned} W_{k_x} &\approx 2k_{xmax} \\ W_{k_y} &\approx 2k_{ymax} \end{aligned} \tag{5.85}$$

Then, the spatial resolution expressions simplify to

$$\boxed{\delta_x \approx \frac{1}{2k_{xmax}} = \frac{1}{\frac{\gamma}{2\pi} G_{xr}\tau_x}} \tag{5.86}$$

and

$$\boxed{\delta_y \approx \frac{1}{2k_{ymax}} = \frac{1}{\frac{\gamma}{2\pi} 2G_{yp}\tau_y}} \tag{5.87}$$

To gain an object-domain perspective, we can rearrange Eqs. 5.86 and 5.87 as

$$\begin{aligned} \gamma G_{xr} \frac{\tau_x}{2} \delta_x &= \pi \\ \gamma G_{yp} \tau_y \delta_y &= \pi \end{aligned} \tag{5.88}$$

These equations imply that the resolution size δ is the half-cycle width of the highest spatial frequency recorded in each direction.

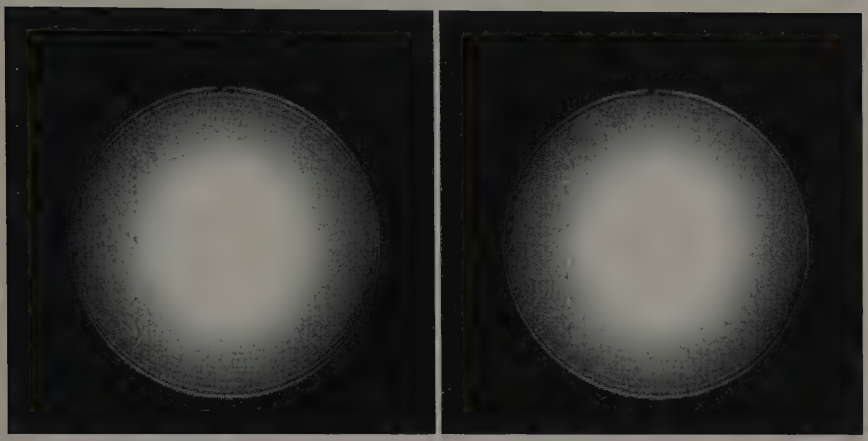

Figure 5.20: 2DFT Images (a) 128 phase encodes, no apodization (b) 128 phase encodes with apodization.

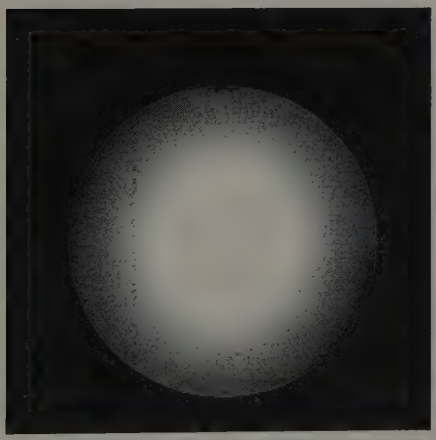

Figure 5.21: 2DFT Image: 256 phase encodes, no apodization.

Truncation Artifact

Whereas a low sampling rate can create image artifacts from aliasing, a low sampling extent can create artifacts from truncation in the spatial-frequency domain. With truncation, the high spatial frequencies are not sampled, leading to an effect commonly known as the Gibb's ringing artifact [Bra00]. Figure 5.20a, an image of a circular test object, illustrates this artifact. This image is based on a scan using 256 readout samples per excitation and only 128 phase encodes. Because the FOV is the same in both directions, the spatial resolution along y is poorer than along x. Figure 5.20a shows the ripples characteristic of Gibb's ringing, emanating in the phase-encoding (vertical) direction near the step transition to the high-contrast object. To soften the amount of ringing, a common practice is to multiply the raw data with an apodization function prior to image reconstruction, accepting the concomitant blur. The result of this approach is shown in Fig. 5.20b. Alternatively, the Gibb's ringing can be reduced by acquiring more phase encodes, as illustrated by Fig. 5.21, an image based on 256 phase encodes and no apodization. Because Figs. 5.20a and 5.21 have the same FOV_y (that is, the same k_y sampling period), Fig. 5.21 possesses better spatial resolution because the k-space coverage extends twice as far in the k_y direction.

Example: Given a desired $\text{FOV}_x = \text{FOV}_y = 256$ mm (25.6 cm) and desired resolution $\delta_x = \delta_y = 1$ mm (0.1 cm), we can compute the values of the sequence parameters (using Eqs. 5.86 and 5.87). The resultant k-space data matrix will consist of 256 by 256 points.

$$\text{FOV}_x = 256 \text{ mm} \Rightarrow G_{xr}\Delta t = 91.75 \times 10^{-6} \text{ (mT/m)} \cdot \text{s} \tag{5.89}$$

If $G_{xr} = 3$ mT/m (0.3 G/cm), then $\Delta t = 30.58$ μs (sampling rate = 32.7 kHz).

$$\delta_x = 1 \text{ mm} \Rightarrow G_{xr}\tau_x = 23.49 \times 10^{-3} \text{ (mT/m)} \cdot \text{s} \tag{5.90}$$

If $G_{xr} = 3$ mT/m (0.3 G/cm), then $\tau_x = 7.83$ ms.

$$\text{FOV}_y = 256 \text{ mm} \Rightarrow G_{yi}\tau_y = 91.75 \times 10^{-6} \text{ (mT/m)} \cdot \text{s} \tag{5.91}$$

If $\tau_y = 4$ ms, then $G_{yi} = 0.023$ mT/m (0.0023 G/cm).

$$\delta_y = 1 \text{ mm} \Rightarrow G_{yp}\tau_y = 11.74 \times 10^{-3} \text{ (mT/m)} \cdot \text{s} \tag{5.92}$$

If $\tau_y = 4$ ms, then $G_{yp} = 2.9$ mT/m (0.29 G/cm).

5.7.3 DFT Image Reconstruction

Given a 2DFT imaging sequence, an inverse 2D DFT of the finite sample values of $\widehat{M}(k_x, k_y)$ reconstructs the image. Let the 2D discrete signal representing the collected data samples be

$$M(u,v) = \mathcal{M}(u\Delta_{k_x}, v\Delta_{k_y}) \tag{5.93}$$

where $u \in [-N_{read}/2+1, N_{read}/2]$ and $v \in [-N_{pe}/2+1, N_{pe}/2]$. For convenience, we assume here that the samples include the origin of k-space. In practice however, it is likely (by choice or due to system imperfections) that the samples will be offset by a fraction of a sample width in one or both directions.

The resultant reconstructed image $I(a,b)$ is computed by taking the inverse 2D DFT of $M(u,v)$:

$$I(a,b) = \sum_{u=-N_{read}/2+1}^{N_{read}/2} \sum_{v=-N_{pe}/2+1}^{N_{pe}/2} M(u,v) \exp\left(i\frac{2\pi}{N_{read}}au\right) \exp\left(i\frac{2\pi}{N_{pe}}bv\right) \tag{5.94}$$

where $a \in [-N_{read}/2+1, N_{read}/2]$ and $b \in [-N_{pe}/2+1, N_{pe}/2]$.

How does this output $I(a,b)$ relate to our Fourier transform analysis? As discussed in Section 2.4, the resultant discrete image is simply a sampled version of $\widehat{m}$, where

$$\widehat{m}(x,y) = m(x,y) ** {}^2\text{Ш}(\Delta_{k_x}x, \Delta_{k_y}y) ** W_{k_x}W_{k_y}\,\text{sinc}(W_{k_x}x)\,\text{sinc}(W_{k_y}y) \tag{5.95}$$

Hence

$$I(a,b) = \widehat{m}(a\delta_x, b\delta_y) \tag{5.96}$$

As mentioned earlier $\widehat{m}(x,y)$ is often regarded as a real-valued function for analysis purposes but in practice, the image will be complex-valued due to a variety of factors that create spurious phase shifts. Thus the displayed image is usually based on the magnitude $|I(a,b)|$, although in certain applications (such as flow imaging), the phase information can provide important information.

If the raw data is apodized with a weighting function W(u,v), then

$$I(a,b) = \sum_u \sum_v M(u,v)W(u,v) \exp\left(i\frac{2\pi}{N_{read}}au\right) \exp\left(i\frac{2\pi}{N_{pe}}bv\right) \tag{5.97}$$

5.8 Problems

5.1 (a) Draw the timing diagram for the MR imaging sequence that produces the k-space trajectory shown below (the trajectory starts at the origin). Specify how the waveforms change between measurements. Note that two excitations are required, one to cover the top half of k-space and the other to cover the bottom half.

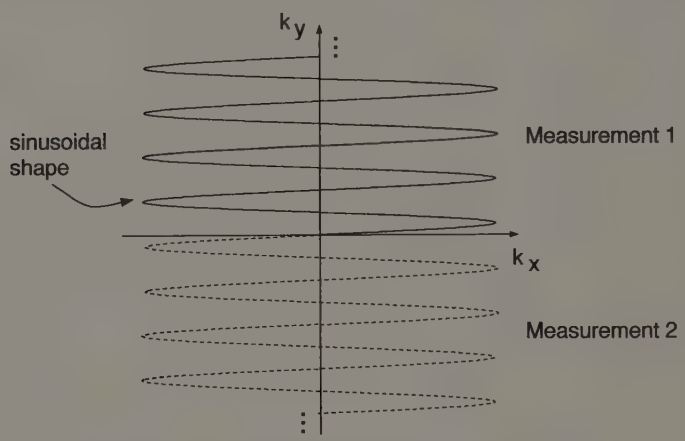

(b) Determine the parameters (amplitudes, timing intervals, etc...) of the gradient waveforms from part (a) that will approximately achieve $\text{FOV}_y = 192$ mm (19.2 cm) and $\delta_x = \delta_y = 3$ mm (0.3 cm) (do not worry about FOV_x). Assume that δ_y and FOV_y are based on the k-space coverage along the k_y axis. Also assume a maximum available gradient amplitude of 10 mT/m (1 G/cm).

5.2 Design a 2D imaging sequence that uses a k-space trajectory entirely different from 2DPR and 2DFT. Draw a labeled timing diagram showing the gradient waveforms applied and the resultant k-space trajectories. Assume idealized excitations. If a set of FID signals are acquired, indicate how the pulse sequence varies from measurement to measurement. Discuss strategies for image reconstruction with your measurement set.

5.3 Examine the region of overlap in the aliased image of Fig. 5.18b. Offer an explanation for why the signals in the region of overlap sum to give a lower signal intensity. Your explanation should be based on only sequence-dependent factors.

5.4 Dr. C designs a 2DFT imaging sequence in which the amplitude of the y gradient is varied from measurement to measurement for phase

encoding. The phase-encoding lobe is a rectangular waveform of duration t_y. While Dr. C thinks a linear G_y gradient is being applied, the actual field experienced by the spins is $G_y y + G_{y3} y^3$ (i.e., it contains a nonlinear component).

(a) Rewrite the signal equation for $s(t)$ given the nonlinearity in the y gradient.

(b) If the object is an impulse at $(x_\circ, y_\circ)$ (i.e., ${}^2\delta(x - x_\circ, y - y_\circ)$), at what position will this object be reconstructed? Assume that the ratio G_y/G_{y3} remains fixed as one changes the current through the gradient coil to obtain the next phase encode.

5.5 Consider an impulse object at the origin that is precessing at a slightly higher frequency than expected; i.e., at frequency $f_0 + \Delta f$. However the demodulation of this signal down to baseband is still based on f_0.

(a) If using a double-sided 2DFT sequence (Fig. 5.11), describe the nature of the resultant measurements in k-space. At what position will the impulse be reconstructed if the readout gradient amplitude is G_x? For comparison, it may help to consider first the case where the impulse is precessing at f_0.

(b) If using the single-sided projection-reconstruction sequence, find an expression for the resulting $s(t)$. Explain qualitatively what the reconstructed image will look like.

5.6 An object consists of two impulses separated in the y-direction by distance L. This object is imaged using a 2DFT sequence with a k-space trajectory as shown below.

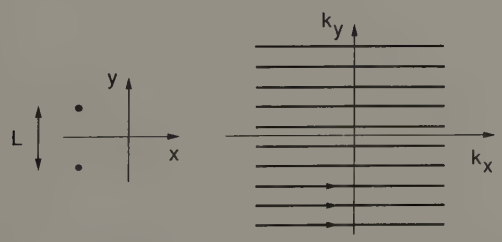

(a) At what FOV_y will the image equal zero?

(b) At what FOV_y will the image be a single impulse?

(c) For parts (a) and (b), does it matter that the two impulses are centered about the x axis?

5.7 A 2DFT imaging sequence is executed in which k-space is acquired in a raster-line fashion, beginning with the most negative k_y phase encode and moving progressively to the adjacent phase encode. 256 phase encodes symmetrically spaced about the origin are collected, with each readout time signal sampled to 256 points after passing through a low-pass filter appropriate for the sampling rate. The "dumb" (inflexible) computer is programmed to simply take the incoming data, fill a 256 by 256 matrix from the bottom row to the top row, and then perform a 2D Inverse FFT of this matrix to reconstruct the 256 by 256 magnitude image matrix as shown below.

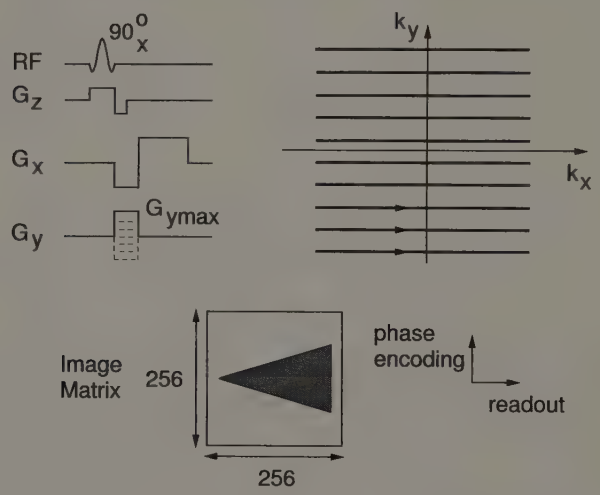

For each of the following modifications (a–g) to the 2DFT sequence described above, sketch the resultant 256 by 256 magnitude image matrix. You may clarify your answer with words if you wish.

(a) Replace G_y with (still 256 phase encodes)

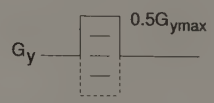

(b) Replace G_x with

(c) Cut the low-pass filter bandwidth in half but keep the same time sampling rate.

(d) Apply 90°_x, -90°_x, 90°_x, -90°_x, $\cdots$ excitations as we progress through the phase encodes (see the end of Section 6.1 to understand how these excitations affect the signal).

(e) Apply 90°_x, 90°_y, -90°_x, -90°_y, $\cdots$ excitations as we progress through the phase encodes.

(f) Multiply the G_x amplitude by 2.

(g) Reconstruct by using a 2D FFT instead of a 2D inverse FFT.

Chapter 6

Excitation

In the previous chapter, which focused on the nature of the received signal, we assumed that the magnetization vectors had somehow been excited—rotated away from the z-axis to produce some transverse component. We will now examine the mechanisms of the excitation portion of the imaging sequence. The general approach to excitation involves the application of a radiofrequency (RF) magnetic field in the transverse direction. In the most basic case, this RF field is turned on with only B_0 present, exciting all spins in the volume similarly. This type of excitation is commonly referred to as *nonselective*. In a more general case, a gradient field is turned on with the RF field, exciting spins in only a restricted region of the volume, typically a plane. Such an excitation is called *selective*. Selective excitation of a plane is important because it provides one level of spatial localization, thereby reducing the imaging task to a (more manageable) two-dimensional one. Functionally, excitations are commonly categorized as being either nonselective or selective, as illustrated in Fig. 6.1, but such a sharp distinction is hardly necessary since the same mechanisms apply for both.

We will present both graphical and analytical descriptions of the behavior of the spins during excitation. Both descriptions are valuable to understand although each will lend different amounts of insight, depending on the conditions. We first consider the basic nonselective case where an RF pulse is applied in the presence of B_0 to illustrate the basic principles of excitation. We follow this analysis with a treatment of the more general case of selective excitation. As in the receive portion of the imaging sequence, the excitation portion will have a powerful Fourier-domain relationship.

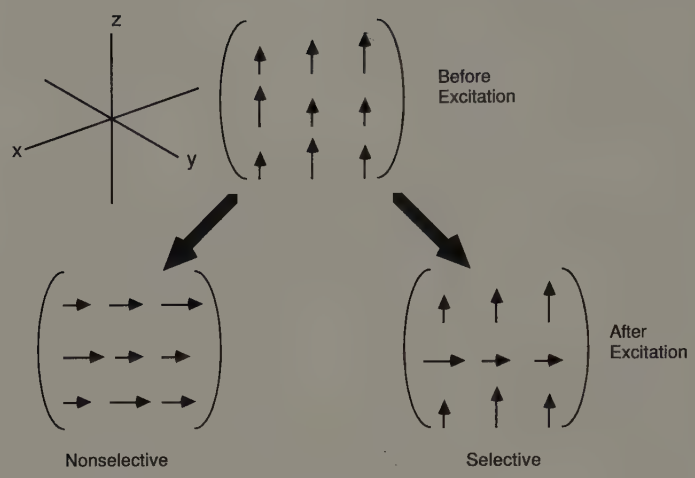

Figure 6.1: Effect of Nonselective and Selective Excitations on Spin Distribution.

6.1 Basic Excitation Principles

6.1.1 General Formulation

A mathematical description of excitation begins with the governing Bloch equation:

$$\frac{d\mathbf{M}}{dt} = \mathbf{M} \times \gamma \mathbf{B} - \frac{M_x \mathbf{i} + M_y \mathbf{j}}{T_2} - \frac{(M_z - M_\circ)\,\mathbf{k}}{T_1} \tag{6.1}$$

The form of excitation we will consider is an amplitude-modulated RF pulse $\mathbf{B}_1(t)$ applied in the transverse direction. Let $\mathbf{B}_1(t)$ be a linearly polarized magnetic field (Fig. 6.2) generated by the RF coil, where

$$\mathbf{B}_1(t) = 2B_1(t)\cos\omega t\,\mathbf{i} \tag{6.2}$$

$B_1(t)$ is an amplitude modulation function and ω is the carrier frequency of the excitation. This linearly polarized field decomposes into two circularly polarized fields, one a left-handed rotating field and the other a right-handed rotating field (Fig. 6.3), as seen mathematically by rewriting Eq. 6.2 as

$$\mathbf{B}_1(t) = B_1(t)\,(\cos\omega t\,\mathbf{i} - \sin\omega t\,\mathbf{j}) + B_1(t)\,(\cos\omega t\,\mathbf{i} + \sin\omega t\,\mathbf{j}) \tag{6.3}$$

The first bracketed term represents the left-handed field while the second bracketed term represents the right-handed field. One interpretation of this decomposition is that the circularly polarized fields possess

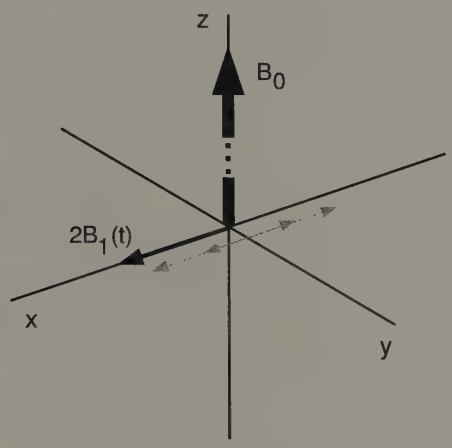

Figure 6.2: Linearly polarized excitation field applied in transverse plane at frequency ω.

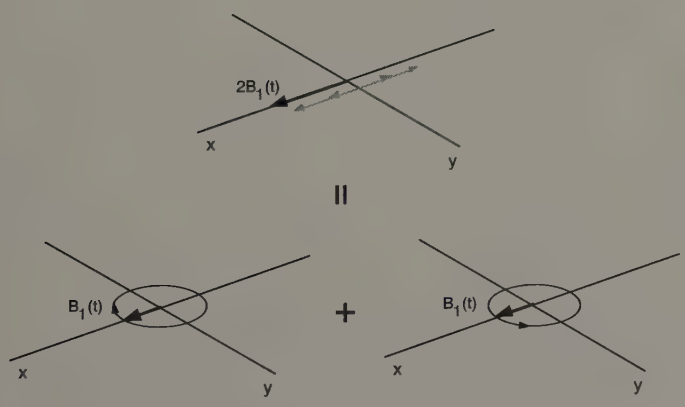

Figure 6.3: Decomposition of a linearly polarized field into the sum of two counter-rotating circularly polarized fields.

single-sided spectra—one at negative frequencies and the other at positive frequencies—the sum of which comprise the double-sided spectrum of the "real-valued" linearly polarized field.

Having made this decomposition, we will neglect the right-handed field, which has negligible effect on the spins, and consider only the left-handed field, which gives rise to the dominant effect. The left-handed field, which rotates in the same direction as the precessing spins, is more resonant with the spins.

Most MR imaging systems now use RF coils that generate circularly polarized fields. Such coils (often called quadrature coils) offer the advantages of lower RF power deposition into the body (no unnecessary right-handed field applied) and an SNR improvement factor of $\sqrt{2}$ (from basically the signal summation of two orthogonal receive channels).

With $\mathbf{B}_1$ turned on, the dynamics of the magnetization is described by the Bloch equation with

$$\mathbf{B} = B_1(t)\,(\cos\omega t\,\mathbf{i} - \sin\omega t\,\mathbf{j}) + B_0\,\mathbf{k} \tag{6.4}$$

We will ignore the relaxation terms and assume that the B_1 field is a pulse of short duration compared to T_1 and T_2 (an accurate assumption in most situations).

We must therefore solve

$$\frac{d\mathbf{M}}{dt} = \mathbf{M} \times \gamma\,[B_1(t)\,(\cos\omega t\,\mathbf{i} - \sin\omega t\,\mathbf{j}) + B_0\,\mathbf{k}] \tag{6.5}$$

Letting $\omega_0 = \gamma B_0$ and $\omega_1(t) = \gamma B_1(t)$, Eq. 6.5 can be written in matrix form as

$$\frac{d\mathbf{M}}{dt} = \begin{pmatrix} 0 & \omega_0 & \omega_1(t)\sin\omega t \\ -\omega_0 & 0 & \omega_1(t)\cos\omega t \\ -\omega_1(t)\sin\omega t & -\omega_1(t)\cos\omega t & 0 \end{pmatrix} \begin{pmatrix} M_x \\ M_y \\ M_z \end{pmatrix} \tag{6.6}$$

6.1.2 Rotating Frame Transformation

For convenience, we will now transform to a frame of reference rotating about z at the frequency ω of the B_1 excitation field. If we let

$$\mathbf{M}_{\text{rot}} = \begin{pmatrix} M_{x'} \\ M_{y'} \\ M_z \end{pmatrix}, \quad \mathbf{B}_{\text{rot}} = \begin{pmatrix} B_{x'} \\ B_{y'} \\ B_z \end{pmatrix} \tag{6.7}$$

be vectors of the components as viewed in the rotating frame, then the lab and rotating-frame components are related by

$$\mathbf{M} = \mathbf{R}_z(\omega t)\mathbf{M}_{\text{rot}} \tag{6.8}$$

and

$$\mathbf{B} = \mathbf{R}_z(\omega t)\mathbf{B}_{\text{rot}} \tag{6.9}$$

We will define the complex representation of the transverse component in the rotating frame as

$$M_r(t) \triangleq M_{x'}(t) + iM_{y'}(t) \tag{6.10}$$

Because

$$M(t) = M_x(t) + iM_y(t) \tag{6.11}$$

the lab and rotating frame components are related by

$$M(t) = M_r(t)e^{-i\omega t} \tag{6.12}$$

If ω equals the Larmor frequency of the magnetization of interest, then the time-varying expressions for M_x and M_y become constants for $M_{x'}$ and $M_{y'}$. Figure 6.4, which compares the behaviors in the lab and rotating frames, illustrates the simplification afforded by the rotating frame representation.

We can also relate the lab-frame components to the rotating-frame components by choosing rotating unit vectors $\mathbf{i}'$ and $\mathbf{j}'$ such that

$$\begin{aligned} \mathbf{i}' &= \mathbf{i}\cos\omega t - \mathbf{j}\sin\omega t \\ \mathbf{j}' &= \mathbf{i}\sin\omega t + \mathbf{j}\cos\omega t \end{aligned} \tag{6.13}$$

Then,

$$M_x(t)\,\mathbf{i} + M_y(t)\,\mathbf{j} = M_{x'}(t)\,\mathbf{i}' + M_{y'}(t)\,\mathbf{j}' \tag{6.14}$$

Using this transformation into the rotating frame, the Bloch equation becomes (see Appendix I for details)

$$\boxed{\frac{d\mathbf{M}_{\text{rot}}}{dt} = \mathbf{M}_{\text{rot}} \times \gamma\mathbf{B}_{\text{eff}}} \tag{6.15}$$

where

$$\mathbf{B}_{\text{eff}} = \mathbf{B}_{\text{rot}} + \frac{\boldsymbol{\omega}_{\text{rot}}}{\gamma}; \quad \boldsymbol{\omega}_{\text{rot}} = \begin{pmatrix} 0 \\ 0 \\ -\omega \end{pmatrix} \tag{6.16}$$

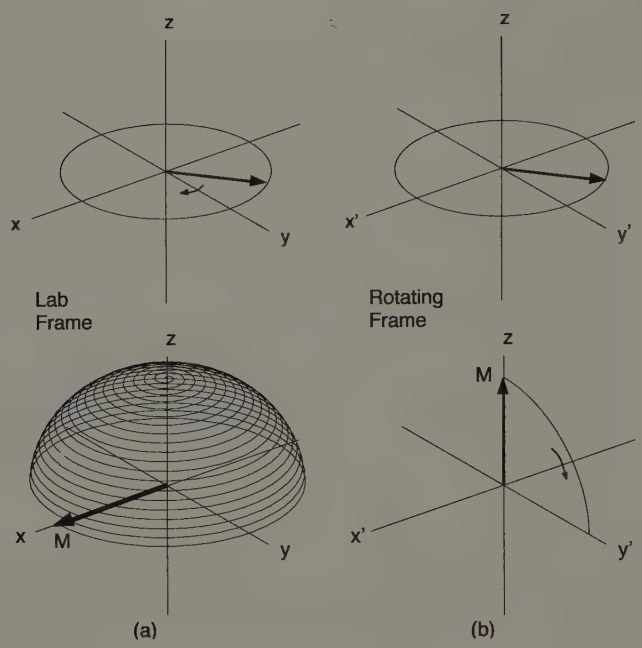

Figure 6.4: Comparison of magnetization behavior in laboratory and rotating frames of reference.

In the rotating frame, the equation describing the behavior of $\mathbf{M}_{\text{rot}}$ takes the same form as the original Bloch equation but now influenced by an effective field $\mathbf{B}_{\text{eff}}$. Hence the form of the solution remains the same; that is, $\mathbf{M}_{\text{rot}}$ precesses about the direction of $\mathbf{B}_{\text{eff}}$ at precessional frequency $\gamma|\mathbf{B}_{\text{eff}}|$. This simplifies the solution to the excitation case because in many cases, $\mathbf{B}_{\text{eff}}$ is more convenient and easier to visualize than $\mathbf{B}$.

6.1.3 Graphical and Analytical Solutions

For the excitation case, if the lab-frame magnetic field is given by Eq. 6.4, then the effective field for the rotating frame is

$$\mathbf{B}_{\text{eff}} = B_1(t)\,\mathbf{i} + \left(B_0 - \frac{\omega}{\gamma}\right)\mathbf{k} \tag{6.17}$$

where

$$\mathbf{B}_{\text{rot}} = B_1(t)\,\mathbf{i} + B_0\,\mathbf{k} \tag{6.18}$$

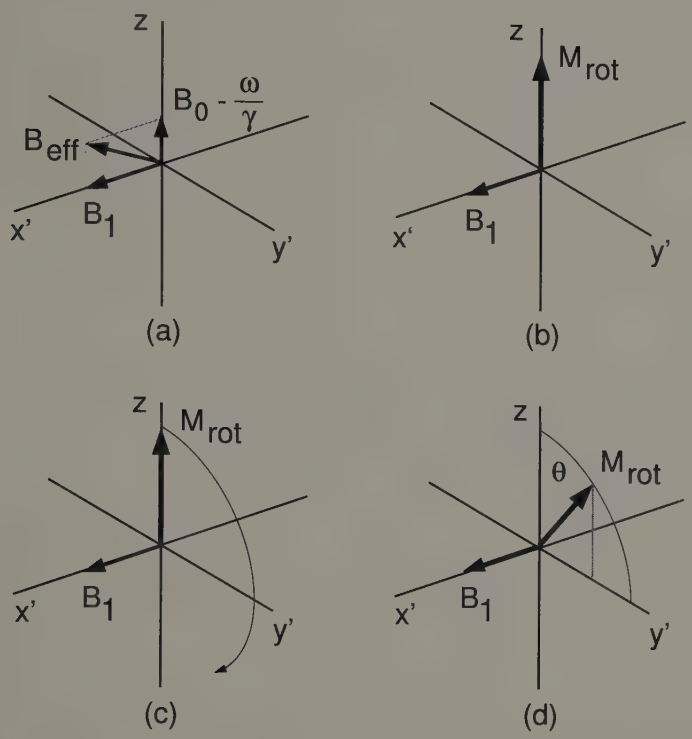

Figure 6.5: Graphical View of Excitation: (a) $\mathbf{B}_{\text{eff}}$ field consisting of $B_1(t)$ along x' and $B_0 - \omega/\gamma$ along z. (b) If $\omega = \omega_0$, then $\mathbf{B}_{\text{eff}}$ points along x'. (c) From the Bloch equation, $\mathbf{M}_{\text{rot}}$ precesses about $\mathbf{B}_{\text{eff}}$ in $y'z$ plane. (d) $\mathbf{M}_{\text{rot}}$ rotates by tip angle θ.

(Fig. 6.5a). By moving to a rotating frame, $\mathbf{B}_{\text{eff}}$ possesses a significantly reduced z-component, corresponding to the fact that the amount of precession about z seen in this rotating frame is greatly reduced. The Bloch equation (Eq. 6.6) is now

$$\frac{d\mathbf{M}_{\text{rot}}}{dt} = \begin{pmatrix} 0 & \omega_0 - \omega & 0 \\ -(\omega_0 - \omega) & 0 & \omega_1(t) \\ 0 & -\omega_1(t) & 0 \end{pmatrix} \mathbf{M}_{\text{rot}} \tag{6.19}$$

If $\omega = \omega_0$, then the excitation is said to be exactly *on resonance*, $\mathbf{B}_{\text{eff}} =$

$B_1(t)\,\mathbf{i}$, and (Fig. 6.5b)

$$\frac{d\mathbf{M}_{\text{rot}}}{dt} = \begin{pmatrix} 0 & 0 & 0 \\ 0 & 0 & \omega_1(t) \\ 0 & -\omega_1(t) & 0 \end{pmatrix} \mathbf{M}_{\text{rot}} \tag{6.20}$$

When $\omega_1(t) = \omega_1 = \gamma B_1$, a constant, the solution to the Bloch equation becomes

$$\mathbf{M}_{\text{rot}}(t) = \mathbf{R}_x(\omega_1 t)\mathbf{M}_{\text{rot}}(0) \tag{6.21}$$

corresponding to a rotation about x', the direction of the applied B_1 field at an angular frequency of $\omega_1 = \gamma B_1$.

If the initial condition is $\mathbf{M}_{\text{rot}}(0) = [0\ 0\ M_\circ]^T$ (at equilibrium),

$$\mathbf{M}_{\text{rot}}(t) = \begin{pmatrix} 0 \\ M_\circ \sin \omega_1 t \\ M_\circ \cos \omega_1 t \end{pmatrix} \tag{6.22}$$

Analogous to $\mathbf{M}$ precessing about B_z, the effect of the excitation field $\mathbf{B}_{\text{eff}}$ is to rotate $\mathbf{M}_{\text{rot}}$ in the $y'z$ plane at angular frequency γB_1 (Fig. 6.5c). Figuratively the excitation field B_1 acts like a *screwdriver* in rotating $\mathbf{M}$.

For general $B_1(t)$, the instantaneous angular frequency becomes $\omega_1(t) = \gamma B_1(t)$ and the solution to the Bloch equation is

$$\mathbf{M}_{\text{rot}}(t) = \mathbf{R}_x\left(\int_0^t \omega_1(s)\,ds\right)\mathbf{M}_{\text{rot}}(0) \tag{6.23}$$

If B_1 is on for a time τ, then the *tip angle* θ (Fig. 6.5d) (also called *flip angle* and *rotation angle*) (in radians) is

$$\begin{aligned} \theta &= \omega_1 \tau && \text{for constant } B_1 \\ &= \int_0^\tau \omega_1(s)\,ds && \text{for general time-varying } B_1(t) \end{aligned} \tag{6.24}$$

Excitation pulses are often referred to as (say) $\pi/2$ (90°) or π (180°) pulses. This means that the tip angle θ is $\pi/2$ (90°) or π (180°). The axis of rotation in the rotating frame may also be specified although for convenience, it is common to refer to the axis as simply x or y (instead of x' or y'). Thus a 90°_x pulse specifies a rotation of 90° about the x-axis in the rotating frame.

The axis of rotation amounts to the "phase" of the RF excitation. The RF phase is an important parameter that can be used to control the phase of the resultant signal. For example, a 90°_y pulse, which is 90° out of phase with a 90°_x pulse, will drive the magnetization to the $-x$ axis (or $-x'$ axis if you wish). Such an excitation will produce a signal that is 90° out of phase with that produced by a 90°_x pulse, which drives the magnetization to the $+y$ axis. This difference in phase between the two signals occurs because the signal demodulation operation is typically kept the same for both excitations.

Example: For a 90° pulse ($\gamma = 267.52 \times 10^3$ rad/s/mT = 26752 rad/s/G for ^{1}H),

$$\frac{\pi}{2} = \omega_1 \tau \Longrightarrow \tau = \frac{\pi/2}{\gamma B_1} \tag{6.25}$$

If $B_1 = 0.01$ mT (0.1 G), then $f_1 = \omega_1/2\pi = 426$ Hz and $\tau \cong 0.6$ ms, justifying the assumption of a brief pulse.

6.2 Selective Excitation

We have just shown that an RF field B_1 tuned to the Larmor frequency of the magnetization induces a rotation about the axis of the applied RF field. In the presence of only B_0, B_1 excites all spins in the volume sensitive to the excitation coil. In this section, we consider the case of excitation of just a selectable plane in the volume. The basic approach to such selective excitation is to apply an RF pulse with modulation function $B_1(t)$ in the presence of a static gradient, say G_z [GGM74]. Intuitively, if $B_1(t)$ is on in the presence of G_z, then only those spins residing in z-locations with resonant frequencies matching the (temporal) frequencies of $B_1(t)$ will be excited. Spins residing in z-locations with resonant frequencies outside the bandwidth of $B_1(t)$ will remain unexcited. Thus the excited plane will be perpendicular to the z-axis. Figure 6.6 summarizes this important concept.

A common and insightful way to evaluate the performance of a selective excitation pulse is to plot the resultant magnetization components ($M_{x'}$, $M_{y'}$, M_z) as a function of z-position, providing a side view of the excited region. From these profiles, one can examine the slice width and definition. For example, an ideal 90° selective excitation slice profile will resemble a rectangle function with no ringing in the in-slice and out-of-slice regions (Fig. 6.7).

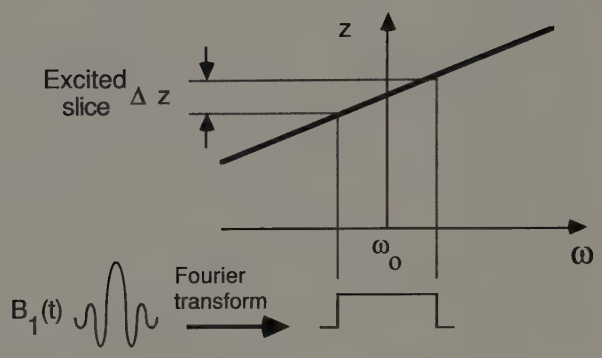

Figure 6.6: Selective Excitation: B_1 applied in the presence of G_z excites a plane perpendicular to z. The Fourier transform of $B_1(t)$ approximates the slice profile.

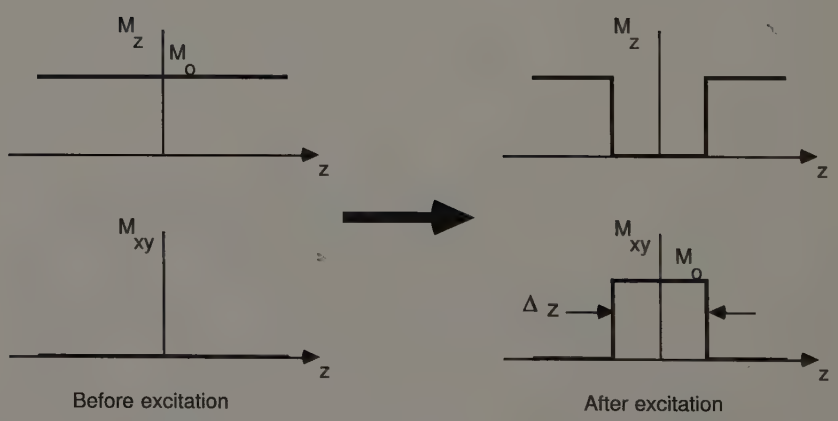

Figure 6.7: Ideal slice profiles for a 90° excitation (slice thickness = Δz).

6.2.1 General Formulation

The Bloch equation to be evaluated is (continuing to ignore relaxation)

$$\frac{d\mathbf{M}_{\text{rot}}}{dt} = \mathbf{M}_{\text{rot}} \times \gamma \mathbf{B}_{\text{eff}} \tag{6.26}$$

with

$$\mathbf{B}_{\text{eff}} = B_1(t)\,\mathbf{i} + \left(B_0 + G_z z - \frac{\omega}{\gamma}\right)\mathbf{k} \tag{6.27}$$

or

$$\frac{d\mathbf{M}_{\text{rot}}}{dt} = \begin{pmatrix} 0 & \omega_0 + \gamma G_z z - \omega & 0 \\ -(\omega_0 + \gamma G_z z - \omega) & 0 & \omega_1(t) \\ 0 & -\omega_1(t) & 0 \end{pmatrix} \mathbf{M}_{\text{rot}} \tag{6.28}$$

Notice that the above equation is similar to Eq. 6.19 from the previous section except that $(\omega_0 - \omega + \gamma G_z z)$ replaces $(\omega_0 - \omega)$ in the off-diagonal position. Clearly selective excitation simplifies to nonselective excitation if $G_z = 0$ or $z = 0$.

If the excitation frequency is tuned to the central Larmor frequency, then $\omega = \omega_0 = \gamma B_0$ and

$$\frac{d\mathbf{M}_{\text{rot}}}{dt} = \begin{pmatrix} 0 & \omega(z) & 0 \\ -\omega(z) & 0 & \omega_1(t) \\ 0 & -\omega_1(t) & 0 \end{pmatrix} \mathbf{M}_{\text{rot}} \tag{6.29}$$

where $\omega(z) = \gamma G_z z$. The term $\gamma G_z z$ equals the amount to which the nuclear spins are *off resonance* from the excitation carrier frequency. Note that in the previous section, an equivalent off-resonance condition occurs if $\omega_0 - \omega \neq 0$. From the perspective of the spin, the source of the off-resonance condition—be it from a gradient field or from the excitation frequency being improperly tuned—does not matter. Hence the amount of resonant frequency offset in the selective excitation case when $z = z_\circ$ and $\omega = \omega_0$ is the same as in the nonselective case when $\omega = \omega_0 - \gamma G_z z_\circ$. In principle then, we could solve the selective excitation case by solving the nonselective excitation equation simultaneously for many z-positions, each corresponding to a different offset frequency. A graphical representation of this approach is in Fig. 6.8. At different z-positions, the z-component of $\mathbf{B}_{\text{eff}}$ is different. At $z = 0$ (on-resonance), $\mathbf{B}_{\text{eff}}$ consists of

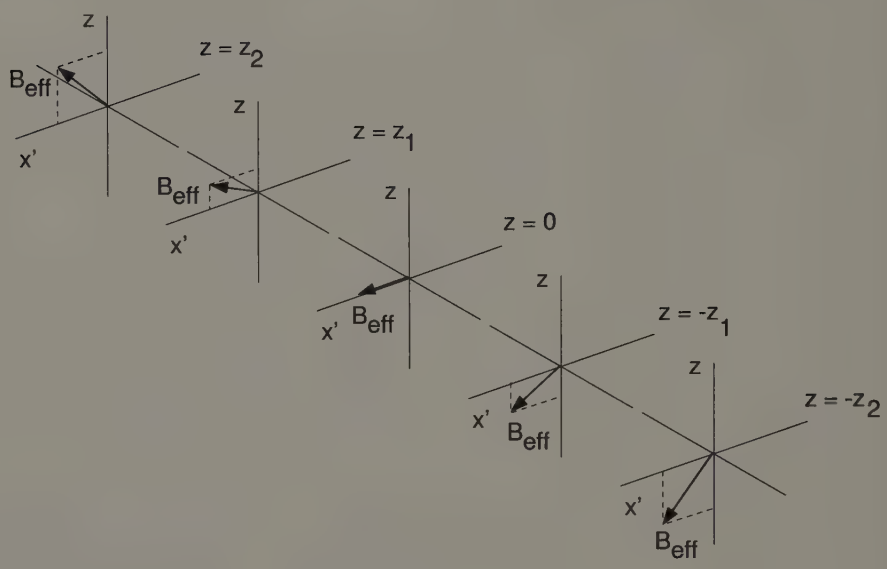

Figure 6.8: Graphical Solution: Selective Excitation.

solely B_1 and the picture is identical to Fig. 6.5b considered in the nonselective case without a gradient. As the magnitude of z gets larger, the length of $\mathbf{B}_{\text{eff}}$ grows and its direction becomes more aligned with the z-axis (if highly offset in frequency, then $\mathbf{B}_{\text{eff}}$ is essentially along z and no excitation occurs). As B_1 varies with time, $\mathbf{B}_{\text{eff}}$ hovers above (or below) the $x'y'$ plane. Although the pictorial representation of the nonselective excitation solution provides a useful physical picture, this representation is cumbersome because of the (infinitely) many offset frequencies to consider (corresponding to different z-positions). What is more desirable in the selective excitation case is an analytic solution to the Bloch equation that will predict the resultant $\mathbf{M}_{\text{rot}}(z)$.

Before we attempt such a solution, we summarize the assumptions and conditions:

- T_1 and T_2 effects ignored because the B_1 pulse is short
- z-gradient G_z applied
- a circularly polarized RF pulse $B_1(t)$ applied at frequency $\omega = \omega_0$

6.2.2 Small Tip-Angle Approximation

Equation 6.29 is not easily solved in the general case. However we will simplify matters and gain insight into the behavior of the spin distribution if we make further assumptions:

- initial condition is $\mathbf{M}_{\text{rot}} = [0\ 0\ M_\circ]^T$ (at equilibrium)
- RF pulse is "weak," leading to a small tip angle $\theta < 30°$

Assuming a small tip-angle excitation, we use the approximations $M_z \cong M_\circ$ and $dM_z/dt \cong 0$ to simplify the Bloch equation from Eq. 6.29 to

$$\begin{pmatrix} \dfrac{dM_{x'}}{dt} \\ \\ \dfrac{dM_{y'}}{dt} \\ \\ \dfrac{dM_z}{dt} \end{pmatrix} = \begin{pmatrix} 0 & \omega(z) & 0 \\ \\ -\omega(z) & 0 & \omega_1(t) \\ \\ 0 & 0 & 0 \end{pmatrix} \begin{pmatrix} M_{x'} \\ \\ M_{y'} \\ \\ M_\circ \end{pmatrix} \tag{6.30}$$

The equations for the transverse components are no longer coupled to the equation for the longitudinal component. We can write the equation for the transverse component as

$$\frac{dM_r}{dt} = -i\omega(z)M_r + i\omega_1(t)M_\circ \tag{6.31}$$

a first-order linear differential equation whose solution is (see Appendix II)

$$\boxed{M_r(t,z) = iM_\circ e^{-i\omega(z)t} \int_0^t e^{i\omega(z)s}\omega_1(s)\, ds} \tag{6.32}$$

If $B_1(t)$ is on from $t = 0$ to τ, then at $t = \tau$,

$$\begin{aligned} M_r(\tau,z) &= iM_\circ e^{-i\omega(z)\tau} \int_0^\tau e^{i\omega(z)s}\omega_1(s)\, ds \\ &= iM_\circ e^{-i\omega(z)\tau} \int_0^\tau e^{i2\pi f(z)s}\omega_1(s)\, ds \end{aligned} \tag{6.33}$$

where $f(z) = (\gamma/2\pi)G_z z$, the frequency at each z-plane. Because $B_1(t)$ is typically symmetric about $\tau/2$, we will let $s' = s - \tau/2$, which leads to

$$\begin{aligned} M_r(\tau,z) &= iM_\circ e^{-i\omega(z)\tau/2} \int_{-\tau/2}^{\tau/2} e^{i2\pi f(z)s'}\omega_1\left(s' + \frac{\tau}{2}\right) ds' \\ &= iM_\circ e^{-i\omega(z)\tau/2} \mathcal{F}_{1D}\left\{\omega_1\left(t + \frac{\tau}{2}\right)\right\}\Big|_{f=-f(z)=-(\gamma/2\pi)G_z z} \end{aligned} \tag{6.34}$$

The magnitude of the transverse component after the excitation (we will later address the phase factor, $\exp[-i\omega(z)\tau/2]$), as a function of z-position, is therefore

$$|M_\gamma(\tau, z)| = M_\circ \mathcal{F}_{1D}\left\{\omega_1\left(t + \frac{\tau}{2}\right)\right\}\Big|_{f=-(\gamma/2\pi)G_z z} \tag{6.35}$$

Conforming to our intuitive notions, this relation directly shows the Fourier transform relationship between $B_1(t)$ and $M_\gamma(z)$. Therefore, in the small tip-angle case, the temporal frequency content of $B_1(t)$ predicts the resultant slice profile—the amount and spatial extent of excitation as a function of z-position. The temporal frequency content of the excitation pulse should match the resonant frequencies of the spins in the desired slice.

Note that with $z = 0$ or $G_z = 0$, the excitation is exactly on resonance and Eq. 6.33 simplifies to

$$M_\gamma(\tau, z = 0) = iM_\circ \int_0^\tau \omega_1(s)\, ds = iM_\circ\theta \cong iM_\circ \sin\theta \tag{6.36}$$

where $\theta = \int_0^\tau \omega_1(s)\, ds$. In the small tip-angle regime, the solution reduces to the nonselective excitation solution. Note too that $M_\gamma(\tau)$ is imaginary, implying only a $M_{y'}$-component because **M** rotates about x', the direction of B_1.

Although this Bloch equation solution assumes a small tip-angle excitation, the Fourier transform relation between $B_1(t)$ and the resultant slice profile $M_\gamma(z)$ provides powerful insight into the design of $B_1(t)$. To achieve a sharply defined slice profile, an excitation function such as a sinc or a Gaussian can be used for $B_1(t)$. As demonstrated later, Fourier analysis remains a reasonable predictor even out to excitations of 90°. Only when considering excitations above 90° does it begin to suffer a significant loss of accuracy.

6.2.3 Refocusing

If one were to sample the signal immediately after the selective excitation pulse, the signal would be relatively weak. The reason for the signal loss is dephasing stemming from phase dispersion across the finite slice width and represented by the phase factor $\exp(-i\omega(z)\tau/2)$ of Eq. 6.34. Because the signal is based on the integral of $M_\gamma(z)$ over z, significant destructive interference results.

Fortunately, the phase dispersion factor is a linear function of z and can be removed by the application of a linear z-gradient that produces a phase factor of $\exp(+i\omega(z)\tau/2)$, exactly cancelling $\exp(-i\omega(z)\tau/2)$. The necessary z-gradient waveform is thus of opposite polarity to that used

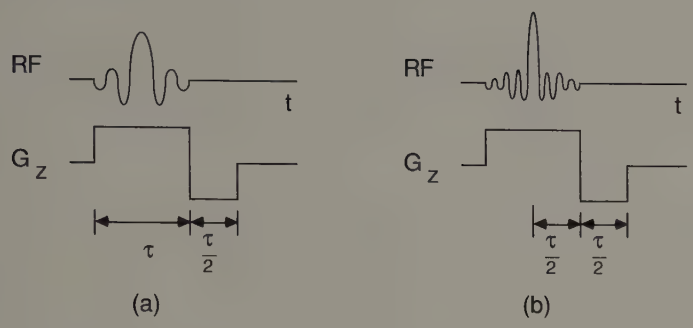

Figure 6.9: (a) Selective Excitation with Refocusing: A negative gradient is applied after the RF pulse is turned off to unwind the linear phase that has accrued over the slice width. (b) Narrow sinc pulse excitation: The bulk of the rotation occurs at time $\tau/2$ and phase shift accrues for the remainder of the pulse duration, $\tau/2$. For maximum refocusing, the negative gradient must undo this phase shift by having an area of $-G_z\tau/2$. If the negative gradient is the same magnitude as the positive gradient, then the duration of the negative gradient must be $\tau/2$.

during the RF pulse and of area $-G_z\tau/2$. An example of the resultant selective excitation sequence is shown in Fig. 6.9a. At the conclusion of the negative gradient lobe ($t = 3\tau/2$), the resultant transverse distribution is

$$\begin{aligned} M_r\left(\frac{3\tau}{2}, z\right) &= e^{+i\omega(z)\tau/2} M_r(\tau, z) \\ &= e^{+i\omega(z)\tau/2} i M_\circ e^{-i\omega(z)\tau/2} \mathcal{F}_{1D}\left\{\omega_1\left(t + \frac{\tau}{2}\right)\right\}\Big|_{f=-(\gamma/2\pi)G_z z} \\ &= i M_\circ \mathcal{F}_{1D}\left\{\omega_1\left(t + \frac{\tau}{2}\right)\right\}\Big|_{f=-(\gamma/2\pi)G_z z} \end{aligned} \tag{6.37}$$

With $B_1(t)$ typically symmetric about $\tau/2$, the Fourier transform of $\omega_1(t + \tau/2)$ will have zero phase distribution. Hence the integral of $M_r(3\tau/2, z)$ over z no longer encounters phase cancellation and the excitation is said to be refocused.

At first thought, it may seem odd that the negative lobe corresponds to only half the area under the positive lobe when the RF pulse was on, not the full area. This effect can be better appreciated by considering a more extreme case in which the RF pulse is a narrow sinc pulse centered in the excitation interval as seen in Fig. 6.9b. Physically, most of the spin rotation happens when B_1 is large, which occurs at time $\tau/2$. As an approximation, we can assume that the RF pulse does all of its work at time $\tau/2$. After

that moment, the z-gradient remains on, creating a phase dependence on z for a period of $\tau/2$. This accounts for the phase factor $\exp(-i\omega(z)\tau/2)$ of Eq. 6.34. The negative refocusing lobe in Fig. 6.9b eliminates this phase factor since the net area under the gradient lobe from time $\tau/2$ to $3\tau/2$ is zero.

Small Tip Angle Excitation Example: Consider a rectangular RF pulse of duration τ given by

$$B_1(t) = B_1 \sqcap \left(\frac{t-\tau/2}{\tau}\right) \tag{6.38}$$

Substituting this function into Eq. 6.33, we get

$$\begin{aligned} M_r(\tau, z) &= iM_\circ e^{-i\omega(z)\tau} \int_0^\tau e^{i\omega(z)s} \omega_1 \sqcap \left(\frac{s-\tau/2}{\tau}\right) ds \\ &= iM_\circ e^{-i\omega(z)\frac{\tau}{2}} \mathcal{F}_{1D} \left\{\omega_1 \sqcap \left(\frac{t}{\tau}\right)\right\} \Big|_{f=-(\gamma/2\pi)G_z z} \\ &= iM_\circ e^{-i\omega(z)\tau/2} (\omega_1 \tau) \mathrm{sinc}\left[\frac{\omega(z)\tau}{2\pi}\right] \end{aligned} \tag{6.39}$$

With refocusing, we eliminate the $\exp(-i\omega(z)\tau/2)$ phase term, leaving

$$M_r(z) = iM_\circ(\omega_1\tau)\mathrm{sinc}\left(\frac{\gamma G_z \tau z}{2\pi}\right) \tag{6.40}$$

This sinc-shaped slice profile is plotted in Fig. 6.10. Overall, the narrow bandwidth of the rectangle pulse gives a slice profile of narrow width; however this slice definition is poor owing to the significant sidelobes out of slice and rounded nature in-slice. Given the arguments of the sinc function, the slice width is proportional to $1/\gamma G_z \tau$.

6.2.4 General Selective Excitation Example

In this section, we present an example of selective excitation to illustrate the behavior of the spin system. As a representative RF pulse $B_1(t)$, we consider a Hamming-windowed sinc pulse, Fig. 6.11a, given by

$$B_1\left(t+\frac{\tau}{2}\right) = A\mathrm{sinc}\left(\frac{8t}{\tau}\right)\left[0.54 + 0.46\cos\left(\frac{2\pi t}{\tau}\right)\right] \quad -\frac{\tau}{2} < t < \frac{\tau}{2} \tag{6.41}$$

where the amplitude A can be varied to change the tip angle of the pulse. This symmetric pulse is assumed to be truncated at the fourth zero crossing at each end, and a Hamming window softens the ringing effects of truncation in the frequency spectrum.

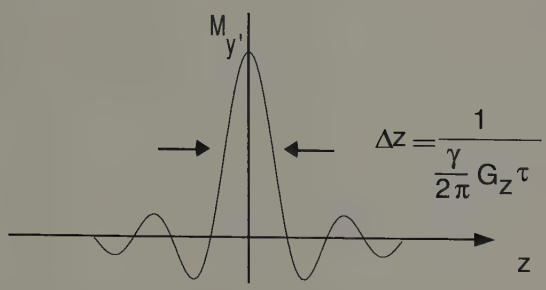

Figure 6.10: Small Tip Angle Solution to a Rectangular Excitation Pulse: Sinc-shaped slice profile of width $1/(\gamma/2\pi)G_z\tau$.

For selective excitation, we assume that the RF pulse is applied in the presence of a z-gradient. We also assume that the normalized initial condition is $\mathbf{M}(z) = [0\ 0\ 1]^T$; that is, the spins are at equilibrium over the entire volume. By numerical integration of the Bloch equation, the slice profile can be computed for different tip-angle excitations. In the small tip-angle case of 30°, we expect the transverse magnetization profile to resemble the temporal Fourier transform of $B_1(t)$, shown in Fig. 6.11b. This slice profile, corresponding to that immediately after the pulse, is given in Fig. 6.11c. Following a refocusing interval in which the z-gradient is reversed, the profile appears as in Fig. 6.11d. The linear phase distribution that appears across the slice in Fig. 6.11c has been unwound to produce a distribution with virtually no phase difference across the slice. The magnitude of the transverse component does not change because only the phase as a function of z is altered. As noted earlier, this phase coherence leads to the strongest signals. Comparison of Fig. 6.11b with Fig. 6.11d reveals the high accuracy to which Fourier analysis of $B_1(t)$ predicts the slice profile. The longitudinal component $M_z(z)$ is plotted along with the transverse components $M_x(z)$ and $M_y(z)$. Note that because we ignored relaxation during the pulse, $M_x^2(z) + M_y^2(z) + M_z^2(z) = 1$, which implies that the length of the normalized magnetization remains unity.

Figure 6.11e displays the slice profile (after refocusing) for a 90° tip angle excitation. Although the excitation no longer resides in the small tip-angle range, the shape of the transverse magnetization continues to resemble that of the Fourier transform. However, the magnitude of the transverse profile deviates slightly from the Fourier transform prediction; in addition, as evidenced by the non-zero $M_x(z)$ component, nonlinear phase now appears across the slice. This phase dispersion is not refocusable with a linear gradient field and creates signal loss when the signal is

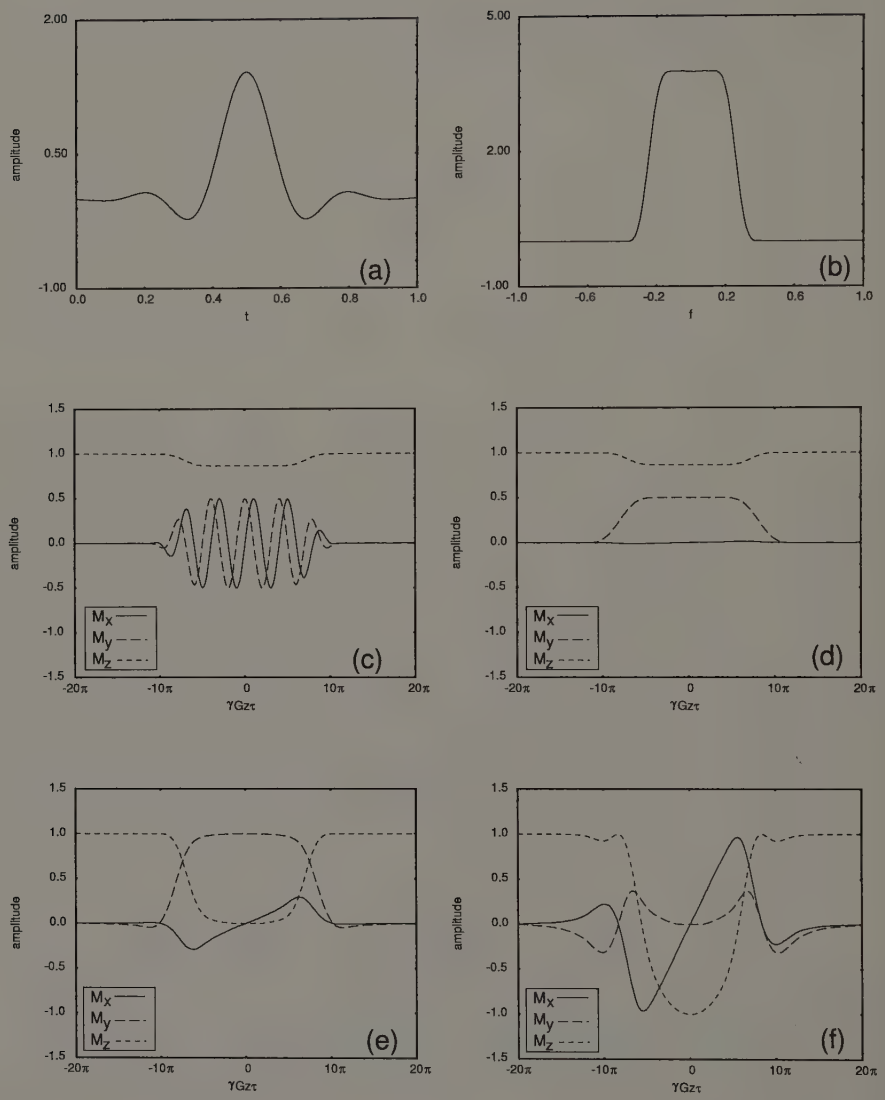

Figure 6.11: Selective Excitation Example: (a) $B_1(t)$: Hamming-windowed sinc pulse; (b) Fourier transform of $B_1(t)$; (c) 30° slice profile—unrefocused; (d) 30° slice profile after refocusing; (e) 90° slice profile after refocusing; (f) 180° slice profile.

integrated over the z-profile. Although undesirable, the extent of profile distortion shown in Fig. 6.11e is tolerable in most circumstances.

By doubling the amplitude of $B_1(t)$, the 90° excitation becomes a 180° excitation. The 180° slice profile is shown in Fig. 6.11f. When the initial conditions are along z, the profile of interest for a 180° pulse is $M_z(z)$, the longitudinal component. The shape of $M_z(z)$ in this large tip-angle case no longer resembles the Fourier transform of $B_1(t)$ as the nonlinear behavior of the spin system becomes appreciable. One may argue though that examination of $M_z(z)$ is deceptive because the linear Fourier relation was based on the output being the transverse component. Obviously the transverse component cannot become arbitrarily large since the magnetization vectors are constrained to rotate in a sphere. Perhaps a less misleading way to judge nonlinearity is to define the output to be the rotation angle as a function of z, $\theta(z)$. However, even with this definition, $\theta(z)$ exhibits nonlinear behavior not predicted by Fourier analysis.

Practical Considerations: In Fig. 6.11e, we labelled the abscissa as $\gamma G z \tau$, a quantity that takes into account the duration and gradient amplitude of the excitation. The slice thickness Δz is therefore proportional to $1/\gamma G \tau$. By doubling the gradient strength G or the duration τ, Δz is halved. We can compute the gradient and timing requirements for achieving a desired slice width. From Fig. 6.11e, $\gamma G \tau \Delta z \approx 16\pi$; hence to achieve a slice width of 0.01 m (1 cm),

$$\begin{aligned} G\tau &= \frac{16\pi}{(267.52 \times 10^3)(0.01)} = 0.0188 \ \text{(mT/m)} \cdot \text{s} \\ &= \frac{16\pi}{(26752)(1)} = 0.00188 \ \text{(G/cm)} \cdot \text{s} \end{aligned} \tag{6.42}$$

If $\tau = 4$ ms, then $G = 4.7$ mT/m (0.47 G/cm) and the bandwidth of the RF pulse is 2 kHz.

Hardware and physical limitations preclude arbitrarily thin slice excitations. Gradient amplifier power constraints limit the gradient amplitude G, while RF amplifier power constraints as well as spin relaxation and other considerations (such as chemical shift) limit the duration τ. If G and τ are fixed, then thinner slices may be achieved by reducing the intrinsic bandwidth of $B_1(t)$ although at the expense of the slice definition. For example, a broader (in the time-domain) sinc pulse possesses a narrower bandwidth, but because τ is fixed, the truncation of the sinc pulse will be worse, leading to greater out-of-slice ringing in the slice profile.

6.3 Excitation k-Space Interpretation

With $B_1(t)$ applied in the presence of a constant gradient, the small-tip approximation gave a Fourier relationship between $B_1(t)$ and the slice profile. This result parallels the Fourier relationship between the received signal $s(t)$ and the object domain when a constant readout gradient is applied. A parallel structure also exists from a general Fourier-domain perspective. The k-space structure that provides insight into the reception phase of MR also applies to the excitation phase [PNM89].

Generalizing the small-tip solution (Eq. 6.32) for the case of a time-varying gradient $\mathbf{G}(t)$, the equation for the transverse magnetization becomes

$$M_r(\tau, \mathbf{r}) = iM_\circ \int_0^\tau \omega_1(s) \exp\left(-i\gamma \int_s^\tau \mathbf{G}(t') \cdot \mathbf{r}\, dt'\right) ds \tag{6.43}$$

Defining

$$\mathbf{k}(s) = \frac{\gamma}{2\pi} \int_s^\tau \mathbf{G}(t')\, dt' \tag{6.44}$$

Eq. 6.43 becomes

$$M_r(\tau, \mathbf{r}) = iM_\circ \int_0^\tau \omega_1(s) e^{-i2\pi \mathbf{k}(s)\cdot \mathbf{r}}\, ds \tag{6.45}$$

We interpret Eq. 6.45 from a Fourier-domain (k-space) perspective as follows. The applied gradients during the RF pulse map a trajectory through excitation k-space. As the trajectory is being mapped out, $B_1(t)$ provides a weighting function to the trajectory. The resulting slice profile is based on the Fourier transform of the weighted k-space distribution. One important nuance however, relates to the manner in which k-space is traversed as indicated by Eq. 6.44. Because the limits of the integral are from s to τ, then at $s = \tau$, $\mathbf{k}(\tau) = 0$. This implies that the trajectory always terminates at the *origin* of excitation k-space. Therefore, one way to trace the trajectory is to begin at the origin at time τ and work backwards in time. The refocusing interval should also be considered in determining the k-space trajectory but because $B_1(t)$ is turned off, no weighting in k-space is applied during that interval. Hence the purpose of the refocusing gradient lobe may be viewed as shifting the origin of k-space.

For example, in the 1D case already considered in which a constant G_z gradient is applied (Fig. 6.12a),

$$M_r(\tau, \mathbf{r}) = iM_\circ \int_0^\tau \omega_1(s) e^{-i\gamma G_z z(\tau - s)}\, ds \tag{6.46}$$

where

$$k_z(s) = \frac{\gamma}{2\pi} G_z(\tau - s) \tag{6.47}$$

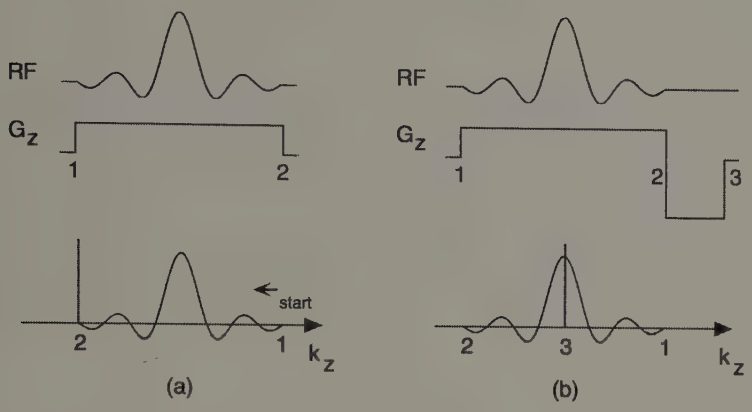

Figure 6.12: 1D selective excitation example with k-space interpretation. (a) A sinc-like pulse weights the k_z-axis as a constant G_z gradient is on. The location upon termination of the gradient and pulse defines the k-space origin. (b) With a refocusing lobe, the origin is shifted with respect to case (a) so that the k-space weighting become symmetric.

By time τ, a "sinc-like" weighting has been laid down in k-space with the tail of the pulse located at the origin. The slice profile will be based on the Fourier transform of this weighting function. Because the weighting distribution is not symmetric along the k_z-axis, the shift theorem of Fourier transforms dictates that the slice profile will resemble a rectangle function multiplied by a linear phase factor, the same result as derived earlier. Using this k-space perspective, the purpose of the refocusing lobe becomes clear. By adding a negative gradient lobe (Fig. 6.12b), the trajectory partially retraces itself (but no weighting is being applied) so that the sinc-weighting becomes symmetric about the origin.

The excitation k-space perspective lends powerful insight into more elaborate selective excitation schemes with time-varying gradients in one or more dimensions. A non-constant gradient waveform implies that the velocity trajectory becomes variable during the pulse. Hence, $B_1(t)$ must be adjusted accordingly for proper weighting. Two-dimensional excitation is possible by applying two gradients during the B_1 pulse to traverse an appropriate 2D region in excitation k-space.

6.4 Selective Excitation Pulse Design

For small tip-angle excitation situations, Fourier analysis accurately designs the RF envelope $B_1(t)$. In general, because there does not exist a closed form solution for $B_1(t)$ given some desired $M_r(z)$ (or $M_z(z)$), the design of $B_1(t)$ remains an active research area, drawing from many disciplines. Among the possibilities considered for improved excitation pulse design are Fourier-based methods (e.g., windowing), digital filter design methods, perturbation analysis, parametric optimization, and optimal control theory.

Appendix I: Bloch Equation in the Rotating Frame

We define vectors $\mathbf{M}_{\text{rot}} = [M_{x'}\ M_{y'}\ M_{z'}]^T$ and $\mathbf{B}_{\text{rot}} = [B_{x'}\ B_{y'}\ B_{z'}]^T$, representing the components of $\mathbf{M}$ and $\mathbf{B}$ in the rotating frame.

Beginning with expressions based in the laboratory frame, we can relate the lab frame components to the rotating frame components. First,

$$\begin{aligned} \mathbf{M} &= M_x\,\mathbf{i} + M_y\,\mathbf{j} + M_z\,\mathbf{k} \\ &= M_{x'}\,\mathbf{i}' + M_{y'}\,\mathbf{j}' + M_{z'}\,\mathbf{k}' = \mathbf{M}_{\text{rot}} \cdot \mathbf{n}' \end{aligned} \tag{6.48}$$

and

$$\begin{aligned} \mathbf{B} &= B_x\,\mathbf{i} + B_y\,\mathbf{j} + B_z\,\mathbf{k} \\ &= B_{x'}\,\mathbf{i}' + B_{y'}\,\mathbf{j}' + B_{z'}\,\mathbf{k}' = \mathbf{B}_{\text{rot}} \cdot \mathbf{n}' \end{aligned} \tag{6.49}$$

where $\mathbf{n}' = [\mathbf{i}'\ \mathbf{j}'\ \mathbf{k}']^T$. ($\mathbf{i}', \mathbf{j}', \mathbf{k}'$ are unit vectors rotating about some vector $\boldsymbol{\omega}$).

Differentiating Eq. 6.48 gives

$$\dot{\mathbf{M}} = (\dot{\mathbf{M}}_{\text{rot}} \cdot \mathbf{n}') + (\mathbf{M}_{\text{rot}} \cdot \dot{\mathbf{n}}') \tag{6.50}$$

Note that the rotation of unit vectors $\mathbf{i}', \mathbf{j}', \mathbf{k}'$ about $\boldsymbol{\omega}$ can be described by the equations

$$\frac{d\mathbf{i}'}{dt} = -\mathbf{i}' \times \boldsymbol{\omega}\ ;\ \frac{d\mathbf{j}'}{dt} = -\mathbf{j}' \times \boldsymbol{\omega}\ ;\ \frac{d\mathbf{k}'}{dt} = -\mathbf{k}' \times \boldsymbol{\omega} \tag{6.51}$$

Equation 6.50 becomes

$$\dot{\mathbf{M}} = (\dot{\mathbf{M}}_{\text{rot}} \cdot \mathbf{n}') - (\mathbf{M}_{\text{rot}} \cdot \mathbf{n}' \times \boldsymbol{\omega}) \tag{6.52}$$

Substituting the Bloch equation into the left-hand side of Eq. 6.52, we get

$$\mathbf{M} \times \gamma\mathbf{B} = (\dot{\mathbf{M}}_{\text{rot}} \cdot \mathbf{n}') - (\mathbf{M}_{\text{rot}} \cdot \mathbf{n}' \times \boldsymbol{\omega}) \tag{6.53}$$

Rearranging and using Eq. 6.48 to substitute for $\mathbf{M}$,

$$\begin{aligned} \dot{\mathbf{M}}_{\text{rot}} \cdot \mathbf{n}' &= (\mathbf{M}_{\text{rot}} \cdot \mathbf{n}' \times \gamma\mathbf{B}) + (\mathbf{M}_{\text{rot}} \cdot \mathbf{n}' \times \boldsymbol{\omega}) \\ &= \mathbf{M}_{\text{rot}} \cdot \mathbf{n}' \times (\gamma\mathbf{B} + \boldsymbol{\omega}) \end{aligned} \tag{6.54}$$

To be complete, $\boldsymbol{\omega}$ must also be rewritten in terms with the rotating unit vectors. In general,

$$\boldsymbol{\omega} = \omega_{x'}\,\mathbf{i}' + \omega_{y'}\,\mathbf{j}' + \omega_{z'}\,\mathbf{k}' = \boldsymbol{\omega}_{\text{rot}} \cdot \mathbf{n}' \tag{6.55}$$

Finally, we can write

$$\begin{aligned}\dot{\mathbf{M}}_{\text{rot}} \cdot \mathbf{n}' &= \mathbf{M}_{\text{rot}} \cdot \mathbf{n}' \times (\gamma \mathbf{B}_{\text{rot}} + \boldsymbol{\omega}_{\text{rot}}) \cdot \mathbf{n}' \\ &= [\mathbf{M}_{\text{rot}} \times (\gamma \mathbf{B}_{\text{rot}} + \boldsymbol{\omega}_{\text{rot}})] \cdot \mathbf{n}' \end{aligned} \tag{6.56}$$

Note that this is still an expression based in the lab frame, with each term matched with $\mathbf{n}'$. By extracting the terms matched with each rotating unit vector, we have the equation describing the behavior of the magnetization as viewed in the rotating frame. In this frame, the Bloch equation is

$$\dot{\mathbf{M}}_{\text{rot}} = \mathbf{M}_{\text{rot}} \times \gamma \left(\mathbf{B}_{\text{rot}} + \frac{\boldsymbol{\omega}_{\text{rot}}}{\gamma} \right) \tag{6.57}$$

Defining $\mathbf{B}_{\text{eff}} \triangleq \mathbf{B}_{\text{rot}} + \boldsymbol{\omega}_{\text{rot}}/\gamma$, then

$$\dot{\mathbf{M}}_{\text{rot}} = \mathbf{M}_{\text{rot}} \times \gamma \mathbf{B}_{\text{eff}} \tag{6.58}$$

Interestingly the Bloch equation in the rotating frame takes the same form as that in the lab frame. However in the rotating frame, an effective field $\mathbf{B}_{\text{eff}}$ influences $\mathbf{M}_{\text{rot}}$.

To be more specific, we will choose the frame rotating clockwise about z at frequency ω. Therefore $\boldsymbol{\omega}_{\text{rot}} = -\omega \mathbf{k}$, $\mathbf{k} = \mathbf{k}'$, $M_{z'} = M_z$, and $B_{z'} = B_z$. Also,

$$\mathbf{B}_{\text{rot}} = \begin{pmatrix} B_x \cos \omega t - B_y \sin \omega t \\ B_x \sin \omega t + B_y \cos \omega t \\ B_z \end{pmatrix} \text{ and } \mathbf{B}_{\text{eff}} = \begin{pmatrix} B_{x'} \\ B_{y'} \\ B_z - \dfrac{\omega}{\gamma} \end{pmatrix} \tag{6.59}$$

If in the excitation situation

$$\mathbf{B} = B_1(t)(\cos \omega t\, \mathbf{i} - \sin \omega t\, \mathbf{j}) + B_0 \mathbf{k} \tag{6.60}$$

then

$$\mathbf{B}_{\text{rot}} = \begin{pmatrix} B_1(t) \\ 0 \\ B_0 \end{pmatrix} \text{ and } \mathbf{B}_{\text{eff}} = \begin{pmatrix} B_1(t) \\ 0 \\ B_0 - \dfrac{\omega}{\gamma} \end{pmatrix} \tag{6.61}$$

Appendix II: Small Tip-Angle Selective Excitation

The solution to

$$\frac{dM_r}{dt} = -i\omega(z)M_r + i\omega_1(t)M_\circ \tag{6.62}$$

can be derived using Laplace transforms. Note that $\omega(z) = \gamma G_z z$ and $\omega_1(t) = \gamma B_1(t)$. The Laplace transform of Eq. 6.62 gives

$$s\mathcal{M}_r(s) = -i\omega(z)\mathcal{M}_r(s) + i\Omega_1(s)M_\circ \tag{6.63}$$

where $\mathcal{M}_r(s)$ and $\Omega_1(s)$ denote the Laplace transforms of $M_r(t)$ and $\omega_1(t)$ respectively. Rearranging, we get

$$\mathcal{M}_r(s) = \Omega_1(s)\frac{iM_\circ}{s + i\omega(z)} \tag{6.64}$$

We next take the inverse Laplace transform and invoke the convolution theorem to obtain

$$M_r(t) = \omega_1(t) * iM_\circ e^{-i\omega(z)t} \tag{6.65}$$

where the convolution is of two causal functions. Note that $M_r(t)$ is also a function of z. Finally, we can write out the convolution as (here, s is a dummy variable)

$$\begin{aligned} M_r(t,z) &= iM_\circ \int_0^t e^{-i\omega(z)(t-s)}\omega_1(s)\,ds \\ &= iM_\circ e^{-i\omega(z)t}\int_0^t e^{i\omega(z)s}\omega_1(s)\,ds \end{aligned} \tag{6.66}$$

6.5 Problems

6.1 Let $B_1(t) = A \wedge \left(\frac{t-\tau/2}{\tau/2}\right)$, where the triangle function $\wedge(\cdot)$ is defined as

$$\wedge(t) = \begin{cases} 1-|t| & \text{for } |t|<1 \\ 0 & \text{otherwise.} \end{cases}$$

If B_1 is applied in the presence of G_z, write an expression for the transverse magnetization at time τ, using the small tip-angle solution.

6.2 Consider a nonselective excitation in which a constant pulse of amplitude B_1 and duration τ is applied in the presence of only B_0. If the excitation frequency ω is not exactly tuned to ω_0 (i.e., $\omega \neq \omega_0$), determine the resultant transverse magnetization output at time τ. Use the small tip angle solution based in the frame rotating at the excitation frequency ω.

6.3 Consider the selective excitation pulse $B_1(t)$ plotted below, applied along x' and in the presence of G_z. The components of the distribution $\mathbf{M}_{\text{rot}}(z)$ following this excitation pulse are also plotted.

For the selective excitations shown in (a), (b) and (c), sketch the components $(M_{x'}(z), M_{y'}(z), M_z(z))$ of the resultant distribution $\mathbf{M}_{\text{rot}}(z)$. Although the tip angle is clearly 90°, use the ramifications of the small tip-angle solution to guide your modifications to the slice profile.

For each of the three cases, comment on whether the results would still hold true if the small tip-angle approximation (which allows Fourier analysis of the pulse) was not assumed.

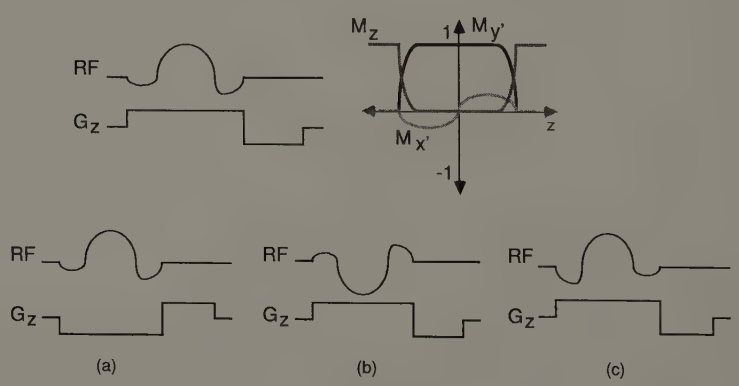

6.4 An RF pulse $B_1(t)$ in the presence of G_z excites a slice in a uniform object (see below). Immediately following the excitation, the slice-select gradient is switched from $+G_z$ to $-G_z$ and a signal is recorded. Sketch the resultant signal that is read out during the $-G_z$ interval. Assume a small tip-angle excitation. Justify your sketch with an explanation or derivation.

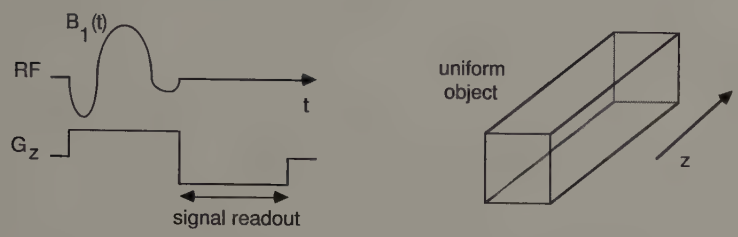

6.5 A nonselective 90° pulse applied along x excites a uniform object. Following this excitation is a z-gradient pulse of amplitude G and duration T. Then, a nonselective $-90°$ pulse along x is applied. Plot the resultant $M_z(z)$ after this sequence. Ignore T_2 effects and assume $\omega = \omega_0$.

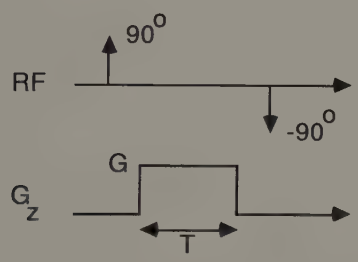

6.6 Consider the selective excitation case in which a constant B_1 pulse is applied for a duration τ in the presence of a z-gradient G_z. The excitation frequency is ω_0, exactly tuned to the center Larmor frequency.

(a) Use the appropriate rotation matrix to determine the *exact* expression for $\mathbf{M}_{\text{rot}}(z)$ (ignore relaxation).

(b) If $B_1\tau$ is set for a 90° excitation at $z = 0$, at what positions z will the transverse profile $M_{xy}(z)$ be zero? How do these z positions compare with those predicted by the small-tip approximation?

(c) If $G_z = 5$ mT/m (0.5 G/cm) and $\tau = 1$ ms, what is the strength of B_1 in Tesla (or Gauss)? How thick is the slice if thickness is defined as the distance between zero crossings of the main lobe?

6.7 Consider the sequence shown below in which a 90°_y pulse, a zero-area gradient waveform, and finally a second 90° pulse is applied. Immediately after the initial 90° excitation, an impulse object (magnetization $M_\circ$), positioned at $(0, y_\circ)$, moves with constant velocity v in the y-direction. Note that in this situation, the relative frequency of the moving impulse object is given by $\gamma G_y(t)(y_\circ + vt)$; i.e., the frequency depends on both the time-varying gradient and the motion. Ignore T_1 and T_2 effects in this problem.

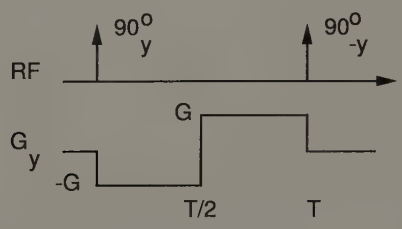

(a) Determine the resultant transverse magnetization (length and direction) of the moving spin just *prior* to the second excitation pulse.

(b) Determine the resultant transverse magnetization (length and direction) of the moving spin after the second excitation pulse.

(c) Determine the smallest velocity $v > 0$ that will result in zero signal.

(d) If $G = 3$ mT/m (0.3 G/cm), $T = 4$ ms, and $v = 200$ mm/s (20 cm/s), along what direction should the second 90° excitation pulse be directed (e.g., x, y, $-x$, $-y$, or some direction in-between) to produce the *maximum* signal? You may sketch it in the rotating frame.

Chapter 7

Imaging Considerations

In Chapter 5, we developed the basic principles of MR imaging under ideal conditions. We now focus on some of the significant nonidealities and constraints—such as off-resonance conditions and T_2 relaxation—that affect the performance and design of MR imaging sequences. This chapter addresses issues such as the limit to the duration of signal readout and how a particular k-space trajectory affects imaging performance. Later in this chapter, we discuss other important imaging sequence considerations such as image contrast and noise.

7.1 Off-Resonance Sources

Thus far we have assumed a perfectly uniform magnetic field B_0 in our analysis of MR imaging. In practice, the resonant frequency will not be uniform across a sample because of three reasons: 1) main field inhomogeneities, 2) susceptibility-induced field variations, and 3) chemical shift. Because we typically reference the frequency with respect to the resonant frequency ω_0, these deviations are often referred to as *off-resonance* conditions.

Main Field Inhomogeneity

Advances in magnet technology have made available high-field magnets with sufficient field uniformity over a volume large enough for whole-body imaging. Auxiliary shim coils are added to produce fields that improve the overall uniformity. By convention, inhomogeneities are expressed in terms of parts per million (ppm) of the main field B_0. For example, if a

main field of 1 T is "shimmed" to a uniformity of 1 ppm over a 480 mm (48 cm) diameter spherical volume, then the maximum field excursion over that volume is 1 μT (0.01 G), corresponding to a maximum frequency offset of 42.6 Hz for protons. Note that specification of inhomogeneity in ppm may be misleading in the sense that the absolute field excursion is often of interest. A 1 ppm inhomogeneity at 1 T may sound better than 10 ppm inhomogeneity at 0.1 T but they are equivalent on an absolute scale.

Susceptibility-Induced Variations

Even with a perfect magnet, resonant frequency differences may exist because of sample-induced B_0 variations due to differences in bulk magnetic susceptibility χ within the sample. Differences in χ among most substances found in the body can be on the order of 10^{-6}–10^{-5}. The amount of field inhomogeneity depends on this susceptibility difference and the geometry, and is usually on the order of a few ppm. The resultant inhomogeneity is most severe near the boundaries between two materials with different susceptibilities such as air and tissue (water is slightly diamagnetic ($\chi < 0$), air is slightly paramagnetic ($\chi > 0$), while only a vacuum is nonmagnetic ($\chi = 0$)). Examples of areas in the body that are subject to these effects include the abdomen (intestinal gases), lungs, and head (sinuses). In certain cases, relatively sharp local gradient inhomogeneities may result.

Chemical Shift

Another source of frequency offset is chemical shift (discussed in Chapter 4). The magnetic field experienced by the nucleus is reduced by a small amount because of electronic shielding. The effective shielded field B_{sh} at the nucleus is written

$$B_{sh} = B_0(1 - \sigma) \tag{7.1}$$

where σ is called a shielding constant representing the small field contributed by the electrons. Therefore a small displacement in the resonant frequency occurs and the resonant frequency is

$$\begin{aligned} \omega &= \gamma B_{sh} = \gamma B_0(1 - \sigma) \\ f &= \frac{\gamma}{2\pi} B_{sh} = \frac{\gamma}{2\pi} B_0(1 - \sigma) \end{aligned} \tag{7.2}$$

This shift in resonant frequency is dependent on the chemical environment of the nuclei and is often specified in terms of parts per million—thus independent of B_0. As a prime example, the hydrogen in fat possess a

chemical shift of about 3.5 ppm with respect to the hydrogen in water. At 1 T, this represents a frequency shift of about 150 Hz. Chemical shift can be therefore regarded as a "discrete" inhomogeneity, although in general, several chemical shift species may reside together.

7.1.1 Off-Resonance Effects on the FID

Because the resonant frequency is directly proportional to the applied field, field inhomogeneities introduce space-dependent resonance offsets that can lead to image distortions and artifacts. We first analyze the effect of inhomogeneities on the signal in the absence of gradient fields, ignoring the more specialized case of chemical shifts. If the z component of the magnetic field is $B_0 + E(\mathbf{r})$, where $E(\mathbf{r})$ represents the field nonuniformity, then the nonuniformity in frequency is $\omega_E(\mathbf{r}) = \gamma E(\mathbf{r})$ and the received baseband signal can be expressed as

$$s(t) = \int_{vol} m(\mathbf{r}) e^{-i\omega_E(\mathbf{r})t} e^{-t/T_2(\mathbf{r})}\, dV \tag{7.3}$$

The phase factor $\exp(-i\omega_E(\mathbf{r})t)$ implies a distribution of frequencies over the object which leads to loss of phase coherence of the spins. When integrated over the volume, this frequency distribution gives rise to destructive phase dispersion that manifests as a more pronounced amplitude decay than that from the intrinsic T_2 processes (Fig. 7.1) and as phase errors in the signal. This destructive dephasing phenomenon is often referred to as $T_2{}^*$ decay, where $T_2{}^*$ is the effective reduced time constant. To be sure, each spin continues to experience a decay dependent on its T_2 value, but it is the collective signal as summed over all spins in the volume (and therefore over a distribution of resonant frequencies) that decays with time constant $T_2{}^*$. Although the tendency is to imagine signal decay as being exponential in nature, this can be a poor approximation as the true decay envelope depends on the distribution of $E(\mathbf{r})$. For example, the decay envelope is a sinc function if a linear field inhomogeneity (i.e., a linear gradient field) exists across a rectangular object. Note that a gradient field used for imaging represents a special and much stronger form of a field inhomogeneity. Thus, the signal envelope will "decay" even more rapidly in its presence (Fig. 7.1).

7.1.2 Off-Resonance Effects on Imaging

Field inhomogeneities give rise to both amplitude and phase aberrations that affect imaging performance in a complex manner dependent on the specific gradient waveforms and k-space trajectory employed. The signal

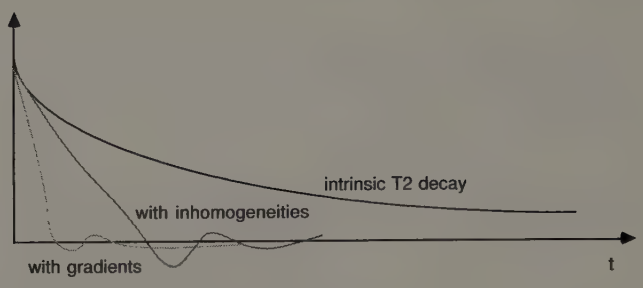

Figure 7.1: Three Types of Signal Decay Envelopes: 1) intrinsic T_2, 2) with inhomogeneities, and 3) with gradient fields.

loss and distortion effects that arise will be space variant, dependent on the spatial distribution of the inhomogeneity.

Amplitude Effects

The implication of the $T_2{}^*$ decay described in the previous section is that appreciable loss in the image signal will occur if the signal readout occurs too long after the excitation. In the context of imaging, the concern is the signal loss in each volume element (voxel); therefore the determining factor is the extent of *intravoxel* inhomogeneity and dephasing. When $E(\mathbf{r})$ is slowly varying over space, signal loss from dephasing will be minimal if the voxel size is small. This raises the possibility that in certain regions, the signal strength may actually *increase* by imaging at finer spatial resolution. In 2D slice imaging, the slice thickness is typically bigger than the in-plane resolution and so inhomogeneity along the slice-select direction is usually the main factor.

To isolate the effects of intravoxel dephasing, we assume that the applied imaging gradients dominate the inhomogeneities and that the traversal through k-space takes place in a time short compared to the rate of phase accrual from off-resonance sources. If TE is the time of signal readout after excitation, then the signal strength in a particular voxel is based on

$$\int_{voxel} m(x,y)e^{-i\omega_E(x,y)TE}e^{-TE/T2}\,dx\,dy \tag{7.4}$$

The amount of signal loss depends not only on intrinsic T_2 decay but on the integration of the phase dispersion over the voxel. Thus the image will depend on the extent of $T_2{}^*$ decay in each voxel.

In this case, the amount of $T_2{}^*$ amplitude decay at the time the k-space origin is sampled provides an accurate measure of the voxel signal strength

across the k-space scan. However, in the case of severe intravoxel inhomogeneity, significant $T_2{}^*$ decay may occur during the signal readout, thereby weighting the k-space trajectory according to its intravoxel-based decay. This weighting creates a blur in the reconstructed image, dependent on the k-space weighting distribution. Severe intravoxel inhomogeneity arises in regions such as the lung where there exists relatively large susceptibility-induced variations over a small spatial range due to the many air/tissue interfaces.

Phase Effects

The previous section dealt with the loss of signal due to intravoxel dephasing and neglected errors that might occur during the finite readout interval. However, even with negligible intravoxel dephasing, off-resonance effects can manifest as image distortion because they create phase errors during the readout interval which are mapped to k-space. Here we focus on the phase term $\exp(-i\omega_E t)$ which competes with the phase modulation associated with the applied gradient fields. To study these effects, we again consider the case of 2D imaging, assuming perfect selective excitation of a slice at $z = z_\circ$. The demodulated signal, ignoring relaxation, is given by

$$s(t) = \int_x \int_y m(x,y) e^{-i2\pi[k_x(t)x + k_y(t)y]} e^{-i\omega_E(x,y)t}\, dx\, dy \tag{7.5}$$

We can analyze the effect of the inhomogeneity factor by examining the impulse response; that is, by letting $m(x,y) = {}^2\delta(x - x_\circ, y - y_\circ)$. The resultant signal is

$$s(t) = e^{-i2\pi[k_x(t)x_\circ + k_y(t)y_\circ]}\, e^{-i\omega_E(x_\circ,y_\circ)t} \tag{7.6}$$

By processing these signals with the conventional reconstruction method, we determine the point spread function (PSF) of the imaging system. Another way of determining the PSF is to find the object function that leads to the same signals without inhomogeneities as that produced by the delta function with inhomogeneities.

For the specific case of 2DFT imaging with G_y the phase-encoding gradient and G_x the readout gradient, we write the signal after the phase-encoding lobe as

$$\begin{aligned} s(t) &= \exp(-i\gamma G_x x_\circ t)\exp(-i\gamma G_y y_\circ t_y)\exp(-i\gamma E(x_\circ,y_\circ)t)\exp(-i\phi_\circ) \\ &= \exp\{-i\gamma[G_x x_\circ + E(x_\circ,y_\circ)]t\}\ \exp(-i\gamma G_y y_\circ t_y)\exp(-i\phi_\circ) \\ &= \exp\left\{-i\gamma G_x\left[x_\circ + \frac{E(x_\circ,y_\circ)}{G_x}\right]t\right\}\ \exp(-i\gamma G_y y_\circ t_y)\exp(-i\phi_\circ) \end{aligned} \tag{7.7}$$

where $\phi_\circ$ accounts for any additional phase accrued during the phase-encoding interval. This signal is equivalent to that produced in a uniform field by the following object:

$$m(x,y) = {}^2\delta\left(x - x'_\circ, y - y_\circ\right) \tag{7.8}$$

where

$$x'_\circ = x_\circ + \frac{E(x_\circ, y_\circ)}{G_x} \tag{7.9}$$

The PSF is therefore a delta function shifted in the readout direction (x-direction) by an amount dependent on the spatially-dependent inhomogeneity and the readout gradient amplitude. This result is readily interpretable by referring to the notion that when a signal is recorded in the presence of a constant x-gradient field, x-position is encoded as temporal frequency. In the presence of inhomogeneity, the resonant frequency shifts and so too will the reconstructed x-position. Equivalently, by invoking the shift theorem of Fourier transforms, one may interpret the geometric shift response as arising from the linear phase error "deposited" in k-space by the inhomogeneity. This geometric distortion can be minimized by *a priori* knowledge of $E(x,y)$ or by increasing the readout gradient amplitude G_x. The distortion becomes negligible if the purposefully applied inhomogeneity, the readout gradient G_x, is increased to an amplitude that dominates the main field inhomogeneity.

Similarly the phase effect of chemical shift is the same as with inhomogeneity because both represent an offset in resonant frequency. However, because of the discrete nature of the offset with chemical shift, the displacement will also be discrete. If (say) water and fat are present at the same object position, then a 2DFT imaging method reconstructs the water component at a slightly different position along the readout direction than the fat component.

If we consider an impulse at position $(x_\circ, y_\circ)$ with a chemical shift of ω_{cs}, then a sequence using a constant readout gradient G_x produces a signal identical to that by an impulse with zero relative chemical shift located at position

$$x'_\circ = x_\circ + \frac{\omega_{cs}}{\gamma G_x} \tag{7.10}$$

Therefore the displacement in position with chemical shift is $\omega_{cs}/\gamma G_x$.

Example: The chemical shift of fat is 3.5 ppm lower relative to water. In a 2DFT sequence, which uses a constant readout gradient (say G_x), the chemical shift artifact is a displacement in the x-direction, proportional to

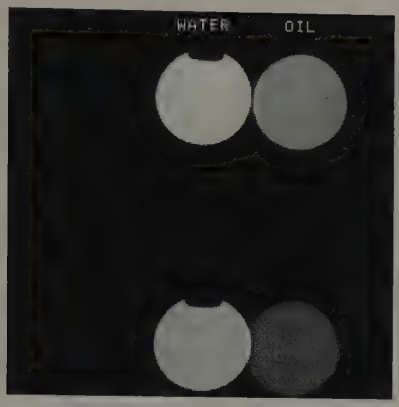

Figure 7.2: Chemical Shift Displacement Artifact—2DFT Imaging: (Top Image) Readout gradient amplitude of 6 mT/m (0.6 G/cm) in horizontal direction. (Bottom Image) Readout amplitude of 1 mT/m (0.1 G/cm). Spatial resolution in both images is 1 mm (0.1 cm). Oil (fat), being lower in frequency than water, displaces to the left in the image. With the lower readout gradient for the bottom image, the displacement of oil is sufficient to cause overlap.

ω_{cs}. Thus fat will be displaced in the x-direction relative to water in the image. At $B_0 = 1.5$ T, the displacement is

$$\Delta x = \frac{\omega_{fat}}{\gamma G_x} = \frac{-2\pi(224)}{\gamma G_x} = \frac{-1407}{\gamma G_x} \tag{7.11}$$

If $G_x = 1$ mT/m (0.1 G/cm), then $\Delta x = -5.3$ mm (-0.53 cm), which can amount to a shift of several pixels.

Figure 7.2 illustrates this chemical shift displacement artifact. Two vials, one containing water and the other cooking oil, were scanned using the 2DFT method, with the readout gradient G_x applied in the horizontal direction. For the top image, $G_x = 6$ mT/m (0.6 G/cm), resulting in a shift of oil with respect to water of about of about 0.8 mm (0.08 cm). The spatial resolution in the image is 1 mm (0.1 cm). For the bottom image, $G_x = 1$ mT/m (0.1 G/cm), leading to a displacement of over five pixels to the left. Because the two vials were positioned next to each other, the oil vial overlaps the water vial in the bottom image.

Another significant effect related to the distinct frequency differences of chemical shift species concerns the relative phases of the spins at the

time the k-space origin is sampled. For example, if the relative phase between water and fat is 180° when the k-space origin is acquired, then the two components add destructively in regions where they co-exist, producing a water minus fat image. Because this "difference" image can be confusing, the sequence timing is often adjusted so that the k-space origin is sampled when water and fat are in-phase.

The effect of inhomogeneity and chemical shift on other imaging methods is more complicated to analyze. For example, in 2DPR imaging where radial spokes are acquired with FID readouts, the PSF is a blur whose extent is frequency dependent. Such a response is usually regarded as more disruptive (qualitatively) than the simple shift experienced by the 2DFT imaging method. The relatively benign response of 2DFT imaging to inhomogeneities is a major reason why 2DFT is the dominant imaging method in MR.

7.1.3 Echoes

In a reference frame rotating at the center frequency ω_0, phase accrues from off-resonance sources and applied gradient fields. The effect on the signal phase from these sources is

$$\begin{aligned} \phi(x,y,z,t) &= \int_0^t \omega(x,y,x,\tau)\, d\tau \\ &= \omega_E(x,y,z)t + \omega_{cs}t + \gamma \int_0^t \mathbf{G}(\tau)\cdot\mathbf{r}\, d\tau \end{aligned} \tag{7.12}$$

The first two terms pertain to the constant phase accrual with time from inhomogeneity and chemical shift respectively while the third term reflects the controllable phase accrual from the gradient fields. As the spatially-dependent phase accumulates, the signal amplitude decays at a faster rate. However an interesting phenomenon in MR is the generation of so-called echoes, where these space-variant phase shifts are removed momentarily, thereby improving the coherence and strength of the signal. Two types of echoes are

1. **gradient echoes:** undoing of phase shifts from gradient fields.

2. **spin echoes:** undoing of phase shifts from field inhomogeneities and chemical shift

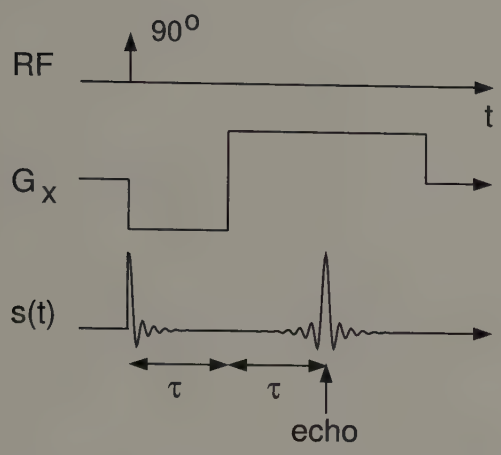

Figure 7.3: Gradient Echo Sequence: The echo peaks at 2τ.

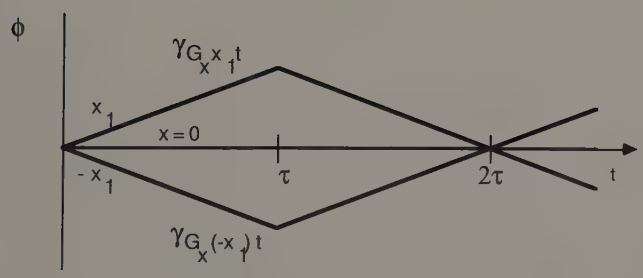

Figure 7.4: Phase Plot: Gradient Echo—Phase progression of spins at x_1, 0, and $-x_1$. Spin at x_1 is at higher frequency from time 0 to τ (gains phase), lower frequency from τ (loses phase). At time 2τ, spins have rephased.

Gradient Echoes

Assuming a perfect main field and no chemical shift ($E(x,y,z) = 0$, $\omega_{cs} = 0$),

$$\phi(x,y,z,t) = \gamma \int_0^t \mathbf{G}(\tau) \cdot \mathbf{r}\, d\tau \tag{7.13}$$

A gradient echo is said to occur when $\phi(x,y,z,t) = 0$. Considering the sequence shown in Fig. 7.3, from $t = 0$ to τ, the gradient field, being a special case of an inhomogeneity field, creates systematic dephasing by warping the spin phases over space. The received signal decays faster than the intrinsic T_2 of the object. At time τ, the gradient field reverses; hence the phase warping accrued from time $t = 0$ to τ begins to unwind because spins that were precessing at a slower frequency are now precessing at a correspondingly higher frequency. An echo begins to form as the spins regain coherence. At $t = 2\tau$ (when the cumulative area of the gradient waveform equals zero), the spin vectors are rephased completely (the warping is unwound) and the gradient echo peaks. For $t > 2\tau$, as the gradient remains on, the phases begin to disperse again. A plot of the phase as a function of time for three different x positions (Fig. 7.4) gives another perspective of the phase progression. Other terms commonly used in place of gradient echo are *gradient-reversed echo*, *gradient-refocused echo*, *gradient-recalled echo* or *field echo*.

Another way of describing a gradient echo is that it corresponds to crossing the origin in k-space. In this sense, the concept of a gradient echo is nothing new; however, the emphasis here is on appreciating the dephasing/rephasing phenomenon that is involved. An extended interpretation of a gradient echo is to consider the point of zero-area under the active time-varying gradient waveform, even though ϕ may not be zero. For example, in a 2DFT sequence, $\phi \neq 0$ when a non-zero phase-encoding lobe is applied, yet it is common to refer to the zero-area occurrence of the readout gradient as a gradient echo.

Spin Echoes

A second type of echo is called a spin echo or inhomogeneity echo, the basic principles of which are illustrated in Fig. 7.5. Beginning at equilibrium (Fig. 7.5a), a 90° excitation along x' tips the magnetization vectors into the transverse plane along the y' axis (Fig. 7.5b). Ignoring gradient fields, the spins then begin to experience phase dispersion from field inhomogeneities. The phase is

$$\phi(x,y,z,t) = \omega_E(x,y,z)t \tag{7.14}$$

(for convenience, we let $\phi = 0$ be along the y'-axis). With inhomogeneities, the rate of phase accrual is constant and beyond our control. At time τ, ϕ will have accumulated to $\omega_E(x,y,z)\tau$ (Fig. 7.5c). To rephase the spins, the key element is to apply a 180° excitation at time τ. If B_1 is along x', the spins are rotated about x' by 180° (Fig. 7.5d). Effectively, this 180° excitation has negated the spin phases. The phase accrual over the next τ occurs as it did before the 180° excitation. At time 2τ, the spins will be exactly rephased (Fig. 7.5e).

We can analyze the phase progression by examining the phase plot of Fig. 7.6. While the phase just prior to the 180° excitation is

$$\phi(\tau^-) = \omega_E(x,y,z)\tau \tag{7.15}$$

the phase just after the 180° excitation is

$$\begin{aligned} \phi(\tau^+) &= \pi - \phi(\tau^-) \\ &= \pi - \omega_E(x,y,z)\tau \end{aligned} \tag{7.16}$$

Following the 180° pulse, the phase continues to accumulate as before; thus at $t = 2\tau$,

$$\begin{aligned} \phi(2\tau) &= \phi(\tau^+) + \int_\tau^{2\tau} \omega_E(x,y,z)\, dt' \\ &= [\pi - \omega_E(x,y,z)\tau] + \omega_E(x,y,z)(2\tau - \tau) \\ &= \pi \end{aligned} \tag{7.17}$$

independent of spatial position. With no spatially-dependent phase, the spins have completely refocused and a spin echo has formed. Although Fig. 7.5 depicts the 180° excitation along the x'-axis, an excitation along any direction in the transverse plane can be used to generate a spin echo.

A popular analogy of a spin echo is a track race, where runners (spins) of different but fixed foot speeds (resonant frequencies) begin the race around a circular track (transverse plane) together at the starting line (in phase). When the race commences, the runners "dephase" as the faster runners move out in front of the slower runners. Then at time τ^-, by some divine intervention (180° excitation), the positions of the runners are reversed. Whatever lead the faster runners were enjoying at time τ^- now becomes their deficit at time τ^+. However, because the runners continue at their fixed speeds, the faster runners will catch the slower runners after another time τ. Hence at time 2τ, they all find themselves at the same position, in phase.

$T_2{}^*$ decay, the dephasing phenomenon caused by field inhomogeneities, masks the intrinsic T_2 decay of the object (for simplicity, we assume a uniform T_2). However with a 90° – 180° sequence, the resultant time signal

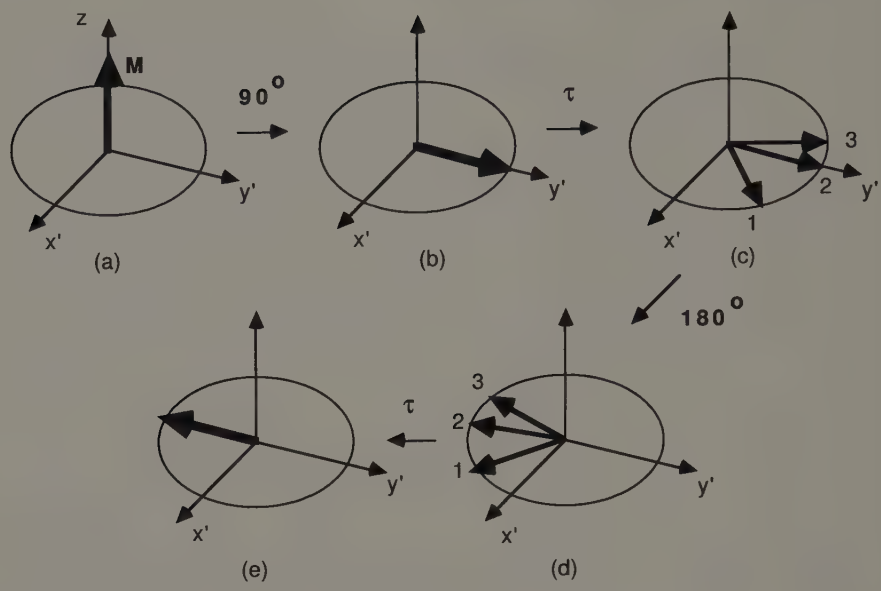

Figure 7.5: Spin Echo Generation: Following a 90° excitation pulse (a–b), the spin vectors begin to fan out and dephase because of precessional frequency differences (c), at time τ, a 180° excitation rotates all the spins about the x'-axis (d). The spin vectors continue to precess at their slightly different frequencies, rephasing at time 2τ (e).

(Fig. 7.7) shows an initial $T_2{}^*$ decay after the 90° pulse, a spin echo following the 180° pulse, and then another $T_2{}^*$ decay. While the 180° pulse serves to reverse the dephasing effects due to inhomogeneity, T_2 decay is irreversible and therefore at time $t = 2\tau$, the spin echo amplitude depends on the intrinsic T_2 of the object.

The 180° pulse plays a central role in the spin-echo formation. Prior to the 180° pulse, the spin vectors, if sufficiently dephased, are fanned out over the entire transverse plane, forming a "pancake" of magnetization vectors. What the 180° pulse does then is flip the pancake over about a particular axis. After the flip, the echoing of the signal due to spin refocusing appears as a time-reversed version of the signal that followed the 90° pulse. Thus the 180° pulse is referred to by several names, including *pancake flipper*, *time-reversal* pulse, *phase-reversal* pulse, and *refocusing* pulse.

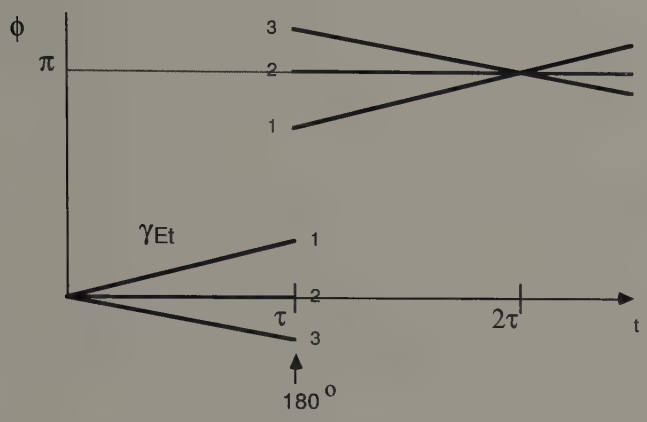

Figure 7.6: Phase Plot: Spin Echo—Spins at different resonant frequencies disperse in phase. At time τ, the 180° pulse reverses the phase about π. The slope of the phase accrual remains the same after the 180° pulse and at time 2τ, the spins rephase.

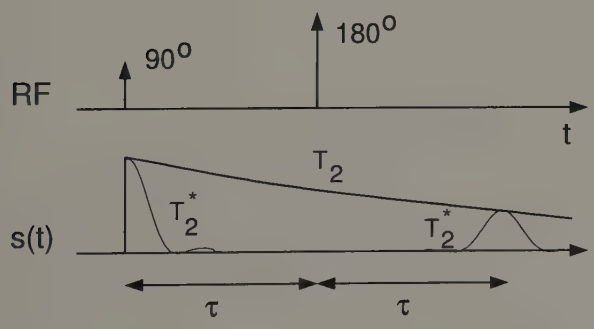

Figure 7.7: Signal envelope after the 90° pulse shows $T_2{}^*$ decay. At time 2τ, a spin echo forms, attaining an amplitude determined by the intrinsic T_2 of the sample. The decay after 2τ also shows the $T_2{}^*$ behavior.

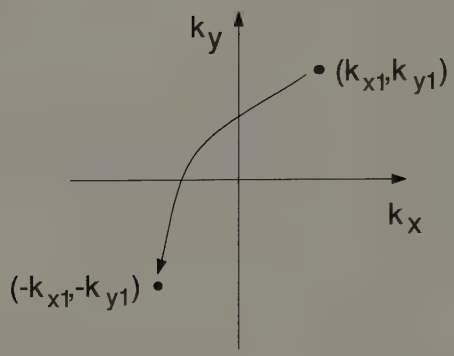

Figure 7.8: Effect of a 180° pulse on the k-space position is to jump to the conjugate position.

7.1.4 Spin Echoes in Imaging

In our discussion on imaging (Chapter 5), we considered the FID or gradient-echo signal that follows a 90° excitation pulse. We have just described however, a $90° - \tau - 180°$ excitation combination that produces a spin echo centered at 2τ. When dealing with spin echoes, the resultant k-space trajectory requires modification because the 180° pulse conjugates the phase terms in the signal equation. If ϕ is the phase of the magnetization vector prior to the 180° pulse, then the phase following the 180° flip (as depicted in Fig. 7.5) is $\pi - \phi$. Hence if the phase at time $t = \tau^-$ is

$$\phi(x, y, \tau^-) = 2\pi[k_x(\tau)x + k_y(\tau)y] + \omega_E(x, y)\tau \tag{7.18}$$

then at time $t = \tau^+$, the phase is

$$\phi(x, y, \tau^+) = \pi - 2\pi[k_x(\tau)x + k_y(\tau)y] - \omega_E(x, y)\tau \tag{7.19}$$

The signal equation therefore becomes

$$s(\tau^+) = \int_x \int_y m(x, y) e^{-i\pi} e^{+i2\pi[k_x(\tau)x + k_y(\tau)y]} e^{+i\omega_E(x,y)\tau}\, dx\, dy \tag{7.20}$$

From the Fourier transform perspective (ignoring the inhomogeneity factor), the position in k-space at time $t = \tau^-$ jumps to its conjugate position at time $t = \tau^+$ (Fig. 7.8).

Imaging methods can be suitably modified to accommodate the inclusion of the 180° pulse. For the 2DFT method, the pulse sequence with spin echoes is displayed in Fig. 7.9 with the corresponding k-space trajectory

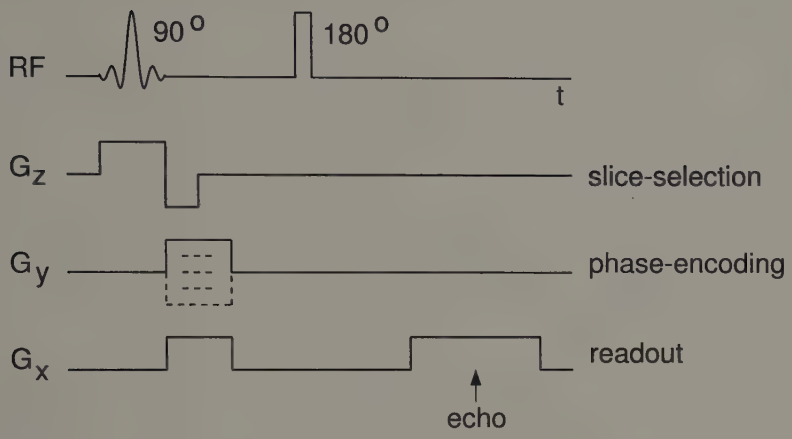

Figure 7.9: 2D Fourier Transform Spin-Echo Sequence.

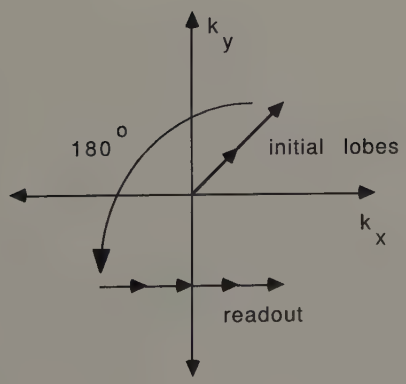

Figure 7.10: k-Space Trajectory of the 2DFT Spin-Echo Sequence.

given in Fig. 7.10. The gradient lobes applied before the 180° excitation move the k-space location out to some spatial frequency. Due to the 180° pulse, the k-space position jumps to the conjugate location. When the readout gradient G_x turns back on, a linear sweep along the k_x-direction occurs. Each recorded signal therefore gives a line in k-space symmetric about the k_y-axis. The timing of the spin echo is typically made coincident with the crossing of the k_y-axis (gradient echo) to ensure that the spins are in-phase at the k-space origin. Noteworthy too is the fact that both lobes of the readout gradient are positive when they are on opposite sides of the 180° pulse. Because of the phase negation by the 180° pulse, two positive gradient lobes with a 180° pulse in-between is effectively a negative lobe and then a positive lobe without the 180° pulse. Of course, if placed entirely on the right side of the 180° pulse, the readout gradient waveform would be the same as in a conventional gradient echo sequence.

Recording of echoes (gradient or spin) for imaging offers some important conveniences and advantages compared to immediate recording of the FID signal. With echoes, the data acquisition interval occurs away from the excitation interval, thereby avoiding the large voltages involved during excitation which far exceed the signals induced by the nuclear magnetization. Better protection circuitry however has minimized this feedthrough problem. More significantly, an echo acquisition avoids problems associated with the finite rise time of gradient switching. Because the gradient can be allowed to switch on and settle before the echo signal is recorded, the accuracy and uniformity of the k-space traversal is improved. Also FID acquisitions imply a k-space trajectory beginning at the origin. Such trajectories tend to suffer greater problems from off resonance effects.

In conventional MR imaging, use of the spin echo predominates. The advantage of recording a spin echo instead of a gradient echo is that a spin echo generates a signal in which all vectors within a volume element (voxel) are in phase with each other. This is not the case with a gradient echo because local B_0 inhomogeneity and chemical shift effects within a voxel are not reversed (only gradient-induced dephasing is reversed) and the resultant dephasing can lead to significant signal loss. Again, it is important to note that this signal decay from dephasing is due to "extrinsic" factors and not the "intrinsic" T_2 decay of the sample. However, a $90° - \tau - 180°$ sequence reverses the dephasing from all off-resonance sources—both B_0 inhomogeneity and chemical shift—and leads to complete refocusing of the spins in each voxel. Another advantage is that the spin echo can be positioned to a specifiable time (perhaps long) after the initial excitation without concern for $T_2{}^*$ effects. Hence valuable T_2 contrast in the image can be obtained with the appropriate echo time.

The principal disadvantage of the spin echo relates to the 180° pulse.

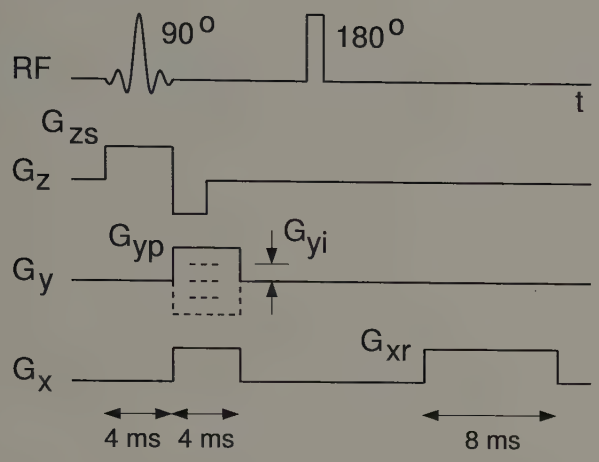

Figure 7.11: Generic 2DFT Pulse Sequence: A selective 90° followed by a nonselective 180° generates a spin echo.

In addition to increasing the RF power deposition into the subject, good selective 180° pulses, needed for multiple slice imaging (see Chapter 8), are difficult to achieve. The time needed for the 180° also constrains the minimum TE of the sequence.

A Generic Spin-Echo 2DFT Sequence

Figure 7.11 shows a simple 2DFT sequence using a spin echo readout, listing some of the pertinent timing values. The specifications are

Δz	$= 10$ mm	(slice thickness)
FOV_x and FOV_y	$= 256$ mm	(field of view)
δ_x and δ_y	$= 1$ mm	(spatial resolution)
$N_{ph} \times N_{read}$	$= 256 \times 256$	(matrix size)

If $B_1(t)$ is the same Hamming-weighted sinc pulse as in Section 6.2, then the amplitude and bandwidth of the selective 90° pulse are as discussed in the example in Section 6.2.

Slice Select:

G_z	$= 4.7$ mT/m (0.47 G/cm)	(slice-select amplitude)
τ_z	$= 4.0$ ms	(slice-select interval)
Δf	$= 2.0$ kHz	(bandwidth of $B_1(t)$)

The refocusing lobe is 2 ms long if the gradient is reversed at the same amplitude. Because only the area under this lobe matters, different amplitudes and durations may be used.

The amplitudes and durations for the phase-encoding and readout gradient are as discussed in Section 5.7.

Phase Encoding:

G_{yp}	= 2.9 mT/m (0.29 G/cm)	(maximum amplitude)
G_{yi}	= 0.023 mT/m (2.3 mG/cm)	(incremental amplitude)
τ_y	= 4.0 ms	(phase encode interval)

Readout:

G_{xr}	= 3 mT/m (0.3 G/cm)	(readout amplitude)
τ_x	= 7.83 ms	(readout interval)
Δt	= 30.58 μs	(sampling period)
f_{samp}	= 32.7 kHz	(sampling frequency)

7.2 T_2 Relaxation

Our imaging equation has thus far ignored the relaxation term. Including T_2, the equation becomes (ignoring inhomogeneities now)

$$s(t) = \int_x \int_y m(x,y) e^{-i2\pi[k_x(t)x + k_y(t)y]} e^{-t/T_2(x,y)}\, dx\, dy \tag{7.21}$$

This signal is the same as in the ideal case except for the $\exp[-t/T_2(x,y)]$ weighting factor.

To gain insight, we simplify matters by assuming $T_2(x,y) = T_2$, a constant over the object. Then

$$s(t) = e^{-t/T_2} \int_x \int_y m(x,y) e^{-i2\pi[k_x(t)x + k_y(t)y]}\, dx\, dy \tag{7.22}$$

or from a k-space perspective,

$$s(t) = \mathcal{M}\left(k_x(t), k_y(t)\right) e^{-t/T_2} \tag{7.23}$$

We note directly from this equation that the values of $s(t)$ equal the values of the 2D Fourier transform of the object but weighted by an exponential factor that decays as the k-space trajectory evolves. The implication is that the transverse decay due to T_2 relaxation limits the duration over which

signal can be recorded and thus limits the extent to which k-space can be scanned for a given gradient strength. In humans (see Chapter 4), the T_2 values range from roughly a few ms to a few hundred ms. If the acquisition time for each measurement, which typically is about 10 ms, is made too long, then severe T_2-dependent weighting can occur over the k-space trajectory.

The specific effect can be analyzed by considering again the impulse response of the system by letting $m(x, y) = {}^2\delta(x - x_\circ, y - y_\circ)$, yielding a signal

$$s(t) = e^{-i2\pi[k_x(t)x_\circ + k_y(t)y_\circ]} e^{-t/T_2(x_\circ, y_\circ)} \tag{7.24}$$

In the case of 2DFT imaging, the MR signal from the delta function object becomes

$$s(t) = e^{-i\gamma G_x x_\circ t} e^{-i\gamma G_y y_\circ t_y} e^{-t/T_2(x_\circ, y_\circ)} \sqcap \left(\frac{t - T/2}{T}\right) \tag{7.25}$$

assuming an acquisition time of T. We continue to fill k-space in a Cartesian grid but now there exists T_2 weighting along the k_x direction. The 2D Fourier transform of the assembled measurements reconstructs a blurred version of the original delta function. "Sinc" blurring occurs owing to the finite duration of the acquisition. More significantly, blurring by a Lorentzian function also occurs in the x-direction because of the exponential T_2 weighting factor along k_x. In a general image, the blurring is space-variant as short T_2 regions experience greater amounts of blurring than longer T_2 regions.

7.3 Other Nonidealities

There are nonidealities associated with the RF and gradient systems that can affect imaging performance and sequence design. For simplicity, we neglect these considerations in our analyses, but they can be important for certain imaging sequences and situations.

7.3.1 Radiofrequency Field Considerations

Inhomogeneities in the RF (B_1) field, both in amplitude and phase, can exist over the volume. Even with good RF coil design, the B_1 field will not be uniform owing to interactions such RF eddy currents and standing waves. These effects become more pronounced at higher frequencies and therefore at higher B_0. Inhomogeneities in the RF amplitude will lead to variations in excitation tip angle over the volume as well as variations in receive

sensitivity–both of which will result in image shading. A simple modification to the signal equation that incorporates the receiver coil's spatial sensitivity is given by

$$s(t) = \int_x \int_y c(x,y)m(x,y)e^{-i2\pi[k_x(t)x+k_y(t)y]}\,dx\,dy \tag{7.26}$$

where $c(x,y)$ represents the complex-valued (magnitude and phase) sensitivity of the coil.

7.3.2 Gradient Field Considerations

There are several imperfections associated with the applied gradient fields. In real MR systems, gradient fields do not vary in a perfectly linear fashion over space. Without calibration and compensation, this nonlinearity will cause spatial warping in the reconstructed image.

Also, the rise times of the gradient waveforms will be of finite duration, given the inherent inductance and resistance of the gradient coil that limit how fast the current in the coil can change. Therefore in practice, gradient waveforms will be trapezoidal in shape instead of rectangular. Gradient systems are typically specified by a maximum amplitude and maximum slew rate.

Gradient waveform distortion due to eddy currents is another important consideration. When the applied gradient magnetic fields are time-varying, eddy currents will be induced in the surrounding conductive structures (e.g., the cryostat of the main magnet). From Lenz's law, these eddy currents produce fields that oppose the change in magnetic field. Hence the effective gradient waveform experienced by the object will be a distorted (filtered) version of the ideal waveform. Shielded gradient coils and waveform pre-emphasis can be used to reduce eddy current effects.

Although we have assumed the applied gradient field to contribute solely to B_z, it turns out that B_x and B_y fields will also be produced by the gradient coil. These other components, derivable from Maxwell's equations, are called concomitant magnetic fields [NH90, BZP+98]. They are often neglected because they are usually small compared to the large B_0 field in the z-direction. However, they can be approximated as adding to the length of the magnetic field by an amount

$$B_c = \frac{1}{2B_0}\left[G_x^2z^2 + G_y^2z^2 + G_z^2\frac{x^2+y^2}{4} - G_xG_zxz - G_yG_zyz\right] \tag{7.27}$$

At lower field strengths, with stronger gradient amplitudes, and for locations far from the center of the magnet, B_c can become appreciable and thus can affect the precessional frequency and phase of the spins.

7.4 Image Contrast

Thus far, our discussion has concentrated on the mechanisms of MR image formation. The flexibility of MR extends also into the area of image contrast since MR offers the ability to produce higher contrast between soft tissue structures than in x-ray CT images. The MR physical parameters that determine signal strength are ρ (spin density), T_1, and T_2, which differ among tissue types (see Chapter 4). In addition, abnormal (e.g., cancerous) tissue typically possess altered T_1 or T_2 values compared to normal tissue. To accentuate differences between these physical parameter values in the image, the focus of attention is on the imaging sequence parameters, principally

- θ—excitation tip angle
- TE—gradient echo time
- TR—sequence repetition time

The resultant MR image will be based on some function of these sequence and physical parameters, from which differences in the physical parameter values can be inferred. The concept of computing quantitative parameter images (e.g., a T_1 image) from a set of MR images with known functional dependencies has been considered; however, the utility of such images remains uncertain because of the impaired accuracy from several systematic error sources and the inherent variability in T_1 and T_2.

Given that the magnetization is constantly changing in length following an excitation, what determines the relative signal intensity in an image? In general, the resulting image $I(x, y)$ represents the magnitude of the transverse magnetization at the time of the gradient echo (TE), when the origin of k-space is sampled. From the zeroth-moment property of Fourier transforms, the value of the k-space origin equals the area (or volume) in the object domain. As discussed in the previous section however, changes in the magnitude of the transverse component during the signal readout (typically less than 10 ms) amount to k-space weighting that manifests as image blurring, depending on the weighting distribution in k-space.

In the following sections, we will examine two standard sequences for establishing image contrast: saturation recovery and inversion recovery. An underlying assumption will be that the repetition time TR $\gg T_2$ (as a rule of thumb, TR $> 3T_2$ suffices). This implies that the transverse magnetization has decayed to zero before the next signal-generating excitation. Sequences where TR $\not\gg T_2$ will be considered later.

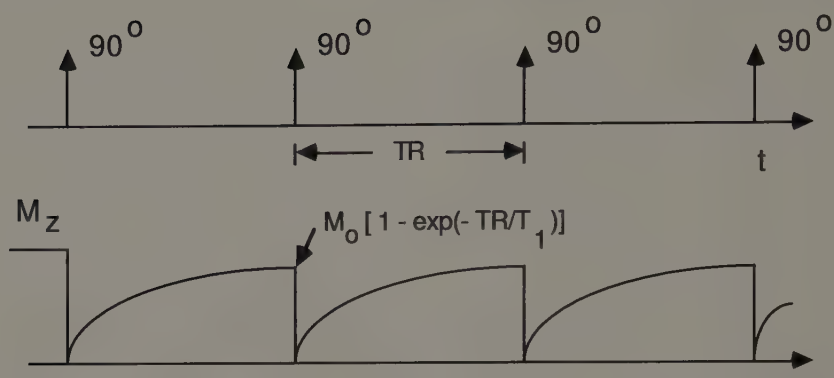

Figure 7.12: (a) Basic Saturation-Recovery Sequence: A string of readout 90° pulses separated by repetition time TR. (b) Time Course of M_z: Value of M_z just prior to the 90° pulse determines the resultant signal generated.

7.4.1 Saturation Recovery

The basic *saturation-recovery* sequence, shown in Fig. 7.12a, consists of a string of 90° pulses, each separated in time by TR. The 90° excitation rotates the M_z component into the transverse plane, producing a signal dependent on the size of M_z just prior to the excitation. M_z is then allowed to recover according to T_1 relaxation during the ensuing TR interval. The 90° excitation is said to *saturate* the magnetization because the resultant M_z component is zero, although this term should not be confused with *demagnetize*, which implies that $|\mathbf{M}|$ becomes zero. With FID readouts, TE = 0 and the image $I(x,y)$ depends on the length of M_z just prior to the excitation. Figure 7.12b shows a plot of the M_z behavior for a particular T_1 species; the behavior reaches a steady state by the time the second 90° pulse is applied. The image $I(x,y)$ is thus

$$\boxed{I(x,y) = K\rho(x,y)\left[1 - e^{-TR/T_1(x,y)}\right]} \tag{7.28}$$

where K is a catch-all gain constant and $M_\circ \propto \rho$. If the readout is delayed by non-zero TE, then

$$I(x,y) = K\rho(x,y)\left[1 - e^{-TR/T_1(x,y)}\right]e^{-TE/T_2{}^*(x,y)} \tag{7.29}$$

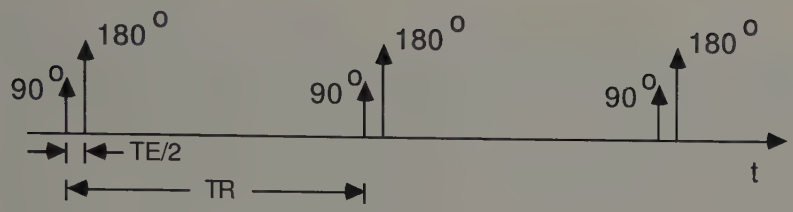

Figure 7.13: Saturation-Recovery Sequence with Spin Echoes.

introducing an additional $T_2{}^*$ dependence. As noted earlier, an exponential function with time constant $T_2{}^*$ approximates the signal decay due to dephasing.

To obtain a longer TE for better T_2 discrimination while avoiding problems with dephasing, a spin-echo sequence can be used (Fig. 7.13). With a spin-echo acquisition, the readout at time TE will depend on the intrinsic T_2, not $T_2{}^*$. Hence, a saturation-recovery sequence with spin echoes leads to

$$\boxed{I(x,y) = K\rho(x,y)\left[1 - e^{-TR/T_1(x,y)}\right]e^{-TE/T_2(x,y)}} \tag{7.30}$$

This equation assumes that TE/2 $\ll T_1$ so that the effect of the 180° on M_z is negligible.

Because of its immunity to dephasing problems and its flexibility in contrast generation, spin-echo saturation recovery with 2DFT imaging is, by far, the most prevalent sequence used in conventional MR imaging. Typically, both T_1-weighted and T_2-weighted scans will be performed. Much work has been done to optimize the selection of TE and TR for the appropriate contrast. As a rough guideline, T_1-weighted scans are obtained with a short TE and TR $\approx T_1$. Then, $\exp(-TE/T_2) \approx 1$ and

$$I(x,y) \approx K\rho(x,y)\left[1 - e^{-TR/T_1(x,y)}\right] \tag{7.31}$$

For example, in brain scans (see Chapter 4 for relaxation values), a typical setting is TE = 20 ms and TR = 600 ms for B_0 = 1.5 T.

For T_2-weighted scans, the timing parameters are set up with a long TR to avoid T_1 contrast, and TE $\approx T_2$ to highlight T_2 differences. With such settings, $\exp(-TR/T_1) \approx 0$ and

$$I(x,y) \approx K\rho(x,y)\, e^{-TE/T_2(x,y)} \tag{7.32}$$

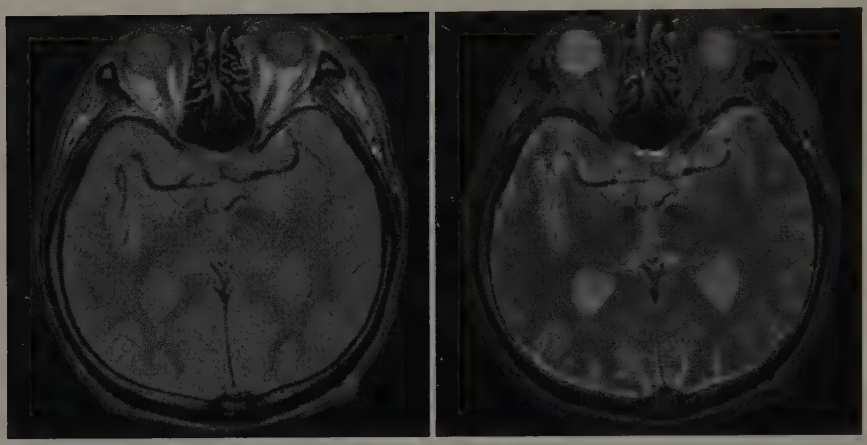

Figure 7.14: Axial T_2-weighted brain images: (a) TE/TR = 40/2500 ms (b) TE/TR = 80/2500 ms.

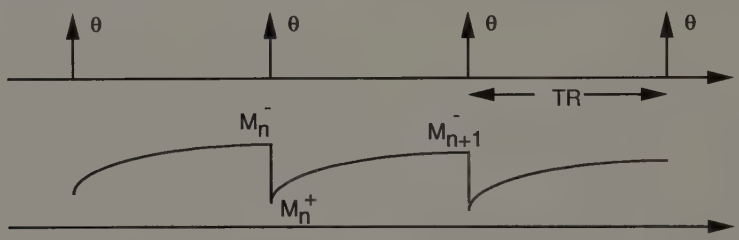

Figure 7.15: Basic excitation-recovery sequence: A string of readout θ pulses separated by repetition time TR. Time course of M_z.

As an example, for T_2-weighted brain scans, TE = 80 ms and TR = 2500 ms. The scan times are significantly longer than T_1-weighted studies because of the long repetition time. An example of such T_2-weighted scan is given in Fig. 7.14.

General Excitation-Recovery

Figure 7.12 may be viewed as a special case of the more general excitation-recovery sequence of Fig. 7.15 in which a θ degree pulse is applied at a repetition time of TR. An important aspect to this sequence is that M_z does not reset to zero after each pulse because the excitation angle is not 90°, and therefore a steady-state condition does not occur immediately. To determine the steady-state signal then, we consider M_n^- and M_n^+, the

M_z component before and after the nth θ pulse. Also we assume that the transverse component of the magnetization decays to zero during TR. These longitudinal components before and after the θ pulse are related by

$$M_n^+ = M_n^- \cos\theta \tag{7.33}$$

During the subsequent interpulse interval, the longitudinal component will relax to

$$M_{n+1}^- = M_n^+ E_1 + M_\circ(1 - E_1) \tag{7.34}$$

where $E_1 \triangleq \exp(-TR/T_1)$. Substituting Eq. 7.33 into Eq. 7.34,

$$M_{n+1}^- = M_n^- E_1 \cos\theta + M_\circ(1 - E_1) \tag{7.35}$$

Steady state is established when $M_{n+1}^- = M_n^- = M^-$; that is, when the longitudinal components prior to the nth and $(n+1)$th pulses are equal. Therefore, in a steady state condition,

$$M^- = M^- E_1 \cos\theta + M_\circ(1 - E_1) \tag{7.36}$$

Solving for M^-,

$$M^- = \frac{M_\circ(1 - E_1)}{1 - E_1 \cos\theta} \tag{7.37}$$

Having determined the steady-state longitudinal component, the steady-state transverse component M_{ss} will be

$$M_{ss} = M^- \sin\theta = \frac{M_\circ(1 - E_1)\sin\theta}{1 - E_1\cos\theta} \tag{7.38}$$

If signal readout occurs immediately after the excitation, the image intensity is

$$I(x,y) = K\rho(x,y)\frac{\left[1 - e^{-TR/T_1(x,y)}\right]\sin\theta}{1 - e^{-TR/T_1(x,y)}\cos\theta} \tag{7.39}$$

If $\theta = 90°$, the above expression simplifies to $K\rho[1 - \exp(-\mathrm{TR}/T_1)]$ as discussed earlier.

To maximize the steady-state signal, a trade-off exists in the choice of θ. Although increasing θ increases $\sin\theta$, this signal gain is offset by the drop in the steady-state longitudinal component M^-. Given a fixed TR and T_1, the tip angle θ that maximizes the steady-state signal can be shown to be

$$\theta_E = \cos^{-1} E_1 = \cos^{-1}\left(e^{-TR/T_1}\right) \tag{7.40}$$

For example, if TR = T_1, then $\theta_E = 68.4°$. This optimum angle θ_E, often called the *Ernst* angle, leads to a maximum steady-state signal given by $M_\circ\sqrt{(1 - E_1)/(1 + E_1)}$.

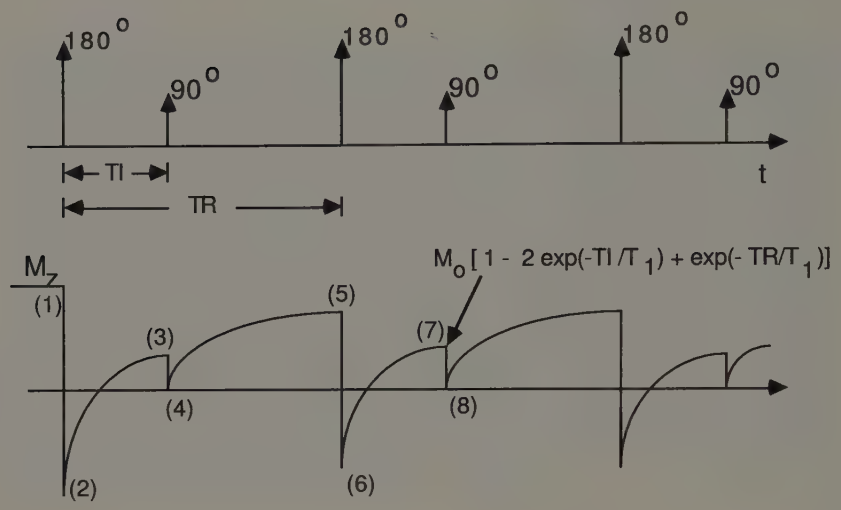

Figure 7.16: (a) Inversion-Recovery Sequence: A 180° pulse inverts the magnetization, a time TI elapses for M_z recovery, and a 90° pulse rotates M_z into the transverse plane for signal. (b) Time course of M_z into steady state.

7.4.2 Inversion Recovery

Another useful sequence, illustrated in Fig. 7.16a, employs a preparatory 180° excitation prior to the 90° readout excitation. This sequence is called *inversion recovery* because the 180° pulse inverts the magnetization, a wait time of TI allows the magnetization to recover along z, and then the 90° pulse rotates the z-magnetization into the transverse plane. To determine the steady-state signal, we can track the time course of M_z, as depicted in Fig. 7.16b. An equation that will be useful for evaluating the recovery of M_z is

$$M_z(t) = M_\circ(1 - e^{-t/T_1}) + M_z(0)e^{-t/T_1} \tag{7.41}$$

Referring now to the number labels in Fig. 7.16b, the sequence of events is as follows:

1. Initial condition is at equilibrium:

$$M_z = M_\circ \tag{7.42}$$

2. The inversion excitation tips the magnetization from $+z$ to $-z$:

$$M_z = -M_\circ \tag{7.43}$$

3. After a T_1 recovery time of TI, the magnetization grows to:

$$M_z = M_\circ \left(1 - 2e^{-TI/T_1}\right) \tag{7.44}$$

4. The 90° excitation rotates the longitudinal magnetization into the transverse plane; hence

$$M_z = 0 \tag{7.45}$$

5. The z-component recovers during the time $(TR - TI)$ to

$$M_z = M_\circ \left[1 - e^{-(TR-TI)/T_1}\right] \tag{7.46}$$

6. The 180° pulse inverts the magnetization, leading to

$$M_z = -M_\circ \left[1 - e^{-(TR-TI)/T_1}\right] \tag{7.47}$$

7. After the ensuing TI, the M_z recovery is

$$\begin{aligned} M_z &= M_\circ \left(1 - e^{-TI/T_1}\right) + \left\{-M_\circ \left[1 - e^{-(TR-TI)/T_1}\right]\right\} e^{-TI/T_1} \\ &= M_\circ \left(1 - 2e^{-TI/T_1} + e^{-TR/T_1}\right) \end{aligned} \tag{7.48}$$

8. The 90° pulse tips the M_z component into the xy plane and we have returned to Stage 4.

If TE = 0, the steady-state output depends on the value of M_z of Stage 7; so

$$I(x,y) = K\rho(x,y)\left[1 - 2e^{-TI/T_1(x,y)} + e^{-TR/T_1(x,y)}\right] \tag{7.49}$$

More generally, with a spin-echo readout at time TE,

$$\boxed{I(x,y) = K\rho(x,y)\left[1 - 2e^{-TI/T_1(x,y)} + e^{-TR/T_1(x,y)}\right] e^{-TE/T_2(x,y)}} \tag{7.50}$$

An inversion-recovery sequence provides images with high T_1 contrast. Another use of inversion recovery is to null a particular T_1 species by timing the 90° readout to occur at the moment M_z crosses the $M_z = 0$ axis. This is done by setting

$$1 - 2e^{-TI/T_1} + e^{-TR/T_1} = 0 \tag{7.51}$$

Solving for TI from Eq. 7.51, we get that

$$TI = -T_1 \ln\left[\frac{1+\exp(-TR/T_1)}{2}\right] \tag{7.52}$$

If TR $\gg T_1$, then

$$TI \approx (\ln 2)\, T_1 = (0.693) T_1 \tag{7.53}$$

Example—Fat Nulling: Inversion-recovery nulling has been used for fat suppression in images as fat is often bright in conventional saturation-recovery images due to its relatively short T_1 at higher field strengths. From Chapter 4, the T_1 of fat at 1.5 T is roughly 260 ms. If TR = 800 ms, then the value of TI that causes the M_z component of fat to be zero at the moment of the 90° pulse is

$$\begin{aligned} TI &= -260 \ln\left[\frac{1+\exp(-800/260)}{2}\right] \\ &= 168 \text{ ms} \end{aligned} \tag{7.54}$$

7.5 Noise Considerations

In this section we will analyze the signal-to-noise ratio (SNR) in MR imaging, one of the fundamental measures of image quality. Analysis of the SNR in absolute terms can be a complicated matter because of the multitude of influential parameters in MR. However, we can divide the SNR considerations into two basic dependencies: 1) physical and instrumental parameters, and 2) imaging sequence parameters. Physical and instrumental parameters include B_0, the receiver coil geometry, conductivity of the coil and sample, and the noise figure of the receiver pre-amplifier. These parameters determine the noise and signal amplitudes intrinsic to the recorded time signals. Imaging sequence parameters include the data acquisition time, total scan time, spatial resolution, sequence timing, excitation tip angles, and k-space coverage. We will consider how the SNR changes as we vary these sequence parameters.

The definition of SNR that we will adopt is

$$\text{SNR} \triangleq \frac{\text{signal amplitude}}{\text{standard deviation of noise}} \tag{7.55}$$

This definition conforms to that commonly used in the MR community, but differs from that used in statistical communication theory, where SNR is based on the ratio of signal to noise *power*. Therefore, given our definition of SNR, the conversion to SNR in decibels (dB) is

$$\mathrm{SNR}_{dB} = 20\log(\mathrm{SNR}) \tag{7.56}$$

Another important measure of image quality is the contrast-to-noise ratio (CNR). In our definition, CNR depends on the difference signal between two structures of interest (e.g., gray and white brain matter). Hence,

$$\mathrm{CNR} \triangleq \frac{\text{signal difference}}{\text{standard deviation of noise}} \tag{7.57}$$

CNR is a measure of how distinguishable two structures are from each other. Note that CNR can be a misleading term because its numerator depends on the signal difference, not the fractional change in signal as contrast is sometimes defined.

7.5.1 Physical and Instrumental Parameters

This section delves into some of the factors determining the strength of the signal $s(t)$, and the strength and statistics of the noise $n(t)$.

Primary Noise Sources

In contrast to x-ray imaging where Poisson-distributed quantum noise dominates and is signal-dependent, the dominant noise source in MR imaging is Gaussian (normal) distributed and additive. Noise in MR is thermal in origin, arising from Brownian motion of electrons and electrolytes which generates random fluctuations. This noise is often termed "resistance noise" or Johnson noise. The primary noise contributors are associated with the resistance R_c of the receiver coil and the resistance R_s of the sample (body) as seen by the receiver coil. In either case, the power spectral density $N(f)$ is given by the classic relation:

$$N(f) = 4kTR \tag{7.58}$$

where k is Boltzmann's constant, T is absolute temperature, and R is the resistance $(R_c + R_s)$. Thus the total noise power within a bandwidth Δf is $4kTR(\Delta f)$ and the resultant standard deviation of the noise is $\sqrt{4kTR(\Delta f)}$. The flat power spectral density implies that the noise is "white."

The inherent resistance of the receiver coil R_c depends on many factors, including the resistivity of the conductor (typically copper), the coil geometry (e.g., the coil radius and number of turns), and the skin depth δ of

the conductor at the particular radio frequency. The resistance is inversely proportional to δ, and δ is proportional to $\omega_0^{-1/2}$. Thus the frequency dependence of the noise power due to coil resistance is $\omega_0^{1/2}$ [HL79].

Because power dissipation is associated with the presence of resistance, the sample resistance R_s can be determined by examining the sources of power loss when an RF coil is coupled to the body. The sample resistance R_s consists of two components: 1) R_d, the resistance associated with dielectric losses arising from electric-field coupling of the coil with the sample, and 2) R_m, the resistance associated with inductive losses arising from magnetic-field coupling. Typically, R_d is made negligible via proper coil design and shielding of the electric fields from the body. However, R_m is unavoidable because the MR received signal depends on inductive coupling. Energy is thus dissipated in the body largely through inductive losses and the pertinent sample resistance is the "magnetic resistance" R_m of the body.

Because magnetic resistance R_m depends on the object, we will consider a simple model–a homogeneous conducting sphere of radius r and electrical conductivity σ [HL79]–to gain an appreciation of the dependencies. The magnetic resistance in this case is

$$R_m = \frac{2\pi\,\omega_0^2\,B_{1xy}^2\,\sigma\,r^5}{15} \tag{7.59}$$

where B_{1xy} is the maximum B_1 amplitude produced in the sample per unit current in the coil. B_{1xy} is indicative of the coupling strength between the coil and sample.

An additional source of noise in MR imaging is from the pre-amplifier through which the signal from the coil is passed. The noise performance of a pre-amplifier is characterized by its noise figure F, defined as

$$F = 10\log_{10}\left(\frac{\text{noise power after pre-amplification}}{\text{noise power before pre-amplification}}\right)\ \text{dB} \tag{7.60}$$

(evaluated at T = 290 K). The ideal amplifier would have a noise figure of 0 dB. A 3 dB noise figure results in a loss in SNR of almost 30%. A typical noise figure for a pre-amplifier used in an MR system is below 2 dB. We will assume that the MR system is designed so that we can ignore this noise source.

To construct an expression for the SNR, a simplified model for the signal amplitude is

$$S = \omega_0\,B_{1xy}\,M_\circ\,(\Delta V) \tag{7.61}$$

The amplitude depends on the resonant frequency ω_0 (owing to the derivative operation in the induction process), the coil sensitivity B_{1xy}, the amount

of nuclear polarization $M_\circ$, and the voxel volume ΔV. Therefore, a general expression for the SNR, ignoring R_d and pre-amplifier noise, is

$$\mathrm{SNR} = \frac{\omega_0 B_{1xy} M_\circ (\Delta V)}{\sqrt{4kT(\Delta f)(R_c + R_m)}} \tag{7.62}$$

SNR Dependence on B_0

Both the signal and noise possess a B_0 dependence. The signal amplitude is proportional to B_0^2 because $\omega_0 = \gamma B_0$ and $M_\circ \propto B_0$. Counteracting the square-law growth in signal with B_0 is the growth in noise with B_0. As noted earlier, the noise power for the receiver coil is proportional to $\omega_0^{1/2}$ while from Eq. 7.59 the noise power from the body is proportional to ω_0^2 (also due to the derivative in the induction process).

Hence,

$$\mathrm{SNR} \propto \frac{B_0^2}{\sqrt{\alpha B_0^{1/2} + \beta B_0^2}} \tag{7.63}$$

where α and β are constants. If the losses from the body dominate the losses from the coil, then the noise power is proportional to B_0^2 and

$$\mathrm{SNR} \propto \frac{B_0^2}{\sqrt{B_0^2}} = B_0 \tag{7.64}$$

Thus SNR varies linearly with B_0 if the body is the primary source of noise. If the opposite is true and coil resistance dominates, then

$$\mathrm{SNR} \propto \frac{B_0^2}{\sqrt{B_0^{1/2}}} = B_0^{7/4} \tag{7.65}$$

In general, SNR and CNR depend on B_0 in a more complex manner because other factors, such as T_1, are also functions of B_0. For example, because T_1 lengthens with increasing B_0, less longitudinal recovery occurs for a given TR, thereby reducing signal and contrast. In addition, RF penetration effects worsen at higher frequencies, leading to greater RF inhomogeneity over the sample.

Body-Noise Dominance

Comparing R_c with R_m, we noted that $R_c \propto \omega_0^{1/2}$ while $R_m \propto \omega_0^2 r^5$ for the simplified sample model. Given its strong dependence on ω_0 and r, R_m can become significant at relatively high field (ω_0) or with relatively large samples (r). If $R_m \gg R_c$, then "body noise" greatly exceeds coil noise

and the scan is said to be body-noise dominant. Body-noise dominance typically exists at the field strengths used and sample sizes scanned by whole-body MR imaging systems. Because coupling of the coil to the sample is fundamental to signal reception, body noise is unavoidable. It is desirable then to make body noise, not coil noise, be the dominant noise source. Note that in special cases, such as in low-field imaging and small-volume imaging (e.g., microscopy), the resistance inherent to the receiver coil may become a significant component of the total noise.

With body-noise dominance,

$$\begin{aligned} \text{SNR} &= \frac{\omega_0 B_{1xy} M_\circ (\Delta V)}{\sqrt{4kT(\Delta f) R_m}} \\ &= \frac{\omega_0 B_{1xy} M_\circ (\Delta V)}{\sqrt{4kT(\Delta f) \dfrac{2\pi \omega_0^2 B_{1xy}^2 \sigma r^5}{15}}} \end{aligned} \tag{7.66}$$

This SNR expression simplifies as both B_{1xy} and ω_0 cancel. Ignoring constants, Eq. 7.66 reduces to

$$\text{SNR} \propto \frac{M_\circ (\Delta V)}{\sqrt{T(\Delta f) \sigma r^5}} \tag{7.67}$$

Several important relationships can be gleaned from this expression: 1) SNR $\propto M_\circ \propto B_\circ$, as shown earlier in Eq. 7.64. SNR increases at higher fields due to greater polarization. 2) SNR $\propto 1/\sqrt{\sigma}$. Higher sample conductivity leads to more fluctuating fields and therefore more noise. 3) SNR is independent of B_{1xy}. If B_{1xy} is boosted by increasing the coupling between the coil and sample, the signal amplitude increases but so does the noise. 4) SNR $\propto 1/\sqrt{r^5}$. A smaller sample produces less noise. Relatedly, SNR improves by designing the coil to be sensitive to just the region of interest, reducing the total "noise volume" seen by the receiver coil. For example, when imaging the eye, a local surface coil sensitive to just the eye would yield a higher SNR than a general volumetric coil that is sensitive to the entire head. While both coils are coupled to receive signal from the eye, the volumetric coil is coupled to a larger noise volume.

Image Noise Statistics

Having discussed the origins of the noise, we will now track the noise statistics from the signal equation to the image (see Fig. 7.17).

Beginning with the signal equation, the physical signal ξ_p is a real-valued function given by

$$\xi_p(t) = s_p(t) + n_p(t) \tag{7.68}$$

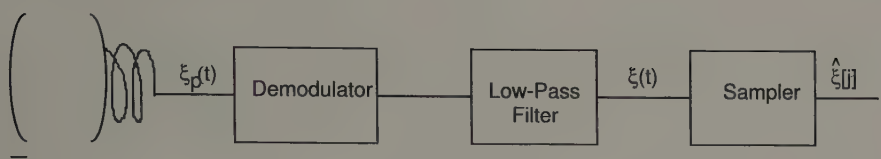

Figure 7.17: Simplified diagram of steps from the signal equation to the image.

where $n_p(t)$ is the additive noise component modeled as a Gaussian random process with zero mean, autocorrelation function $R_n(t) = \sigma^2\delta(t)$, and power spectral density $N(f) = \sigma^2$, where $\sigma^2 \propto 4kRT$.

This signal passes through quadrature detection–demodulator and low-pass filter–(Section 5.2.1), resulting in a frequency shift of the signal by ω_0 down to baseband, and producing

$$\xi(t) = s(t) + n(t) \tag{7.69}$$

If we model $s_p(t)$ as

$$s_p(t) = \alpha(t)\cos[\omega_0 t + \phi(t)] \tag{7.70}$$

then quadrature detection produces

$$s(t) = I(t) + iQ(t) = \alpha(t)e^{-i\phi(t)} \tag{7.71}$$

Thus $I(t)$, the in-phase signal is $\alpha(t)\cos\phi(t)$ while $Q(t)$, the quadrature signal is $\alpha(t)\sin\phi(t)$. Similarly, modeling

$$n_p(t) = a_n(t)\cos[\omega_0 t + \phi_n(t)] \tag{7.72}$$

quadrature detection results in

$$n(t) = n_I(t) + in_Q(t) = a_n(t)e^{-i\phi_n(t)} \tag{7.73}$$

$n_I(t)$ and $n_Q(t)$ are independent Gaussian random processes with power spectral densities

$$N_I(f) = N_Q(f) = \sigma^2|H(f)|^2 \tag{7.74}$$

where $H(f)$ is assumed to be an ideal low-pass filter with a bandwidth matching the bandwidth of the signal $s(t)$. $n(t)$ is therefore a bi-variate Gaussian random process.

Sampling the demodulated signal $\xi(t)$ at the Nyquist frequency yields a discrete-time signal

$$\hat{\xi}(j) = \hat{s}(j) + \hat{n}(j) \tag{7.75}$$

where j is the sample index. Given the bandwidth of the anti-aliasing filter, $\hat{n}$ is characterized as a bi-variate (complex-valued) zero-mean Gaussian random process with the real and imaginary components each possessing variance σ_n^2, autocorrelation function $R_{\hat{n}}(j) = \sigma_n^2\,\delta(j)$ (here, δ is the Kronecker delta function), and power spectral density $S_{\hat{n}}(f) = \sigma_n^2$.

Because $\hat{\xi}(j)$ maps to a position in k-space as determined by the gradient waveforms, the statistics of the noise in k-space are therefore determined by the statistics of $\hat{n}$. In 2DFT imaging, the k-space samples are uniformly spaced on a Cartesian grid and image reconstruction is performed via a 2D DFT. Because the noise statistics for each k-space sample will be the same, and the 2D DFT is a unitary transform, the noise in the image domain will continue to be additive, white, and (bi-variate) Gaussian. Note that such noise characteristics will not hold if the k-space sampling is nonuniformly spaced, as in 2DPR imaging, which leads to colored noise.

Because the reconstructed image $I(a,b)$ is typically not real-valued, the displayed image is based on $|I(a,b)|$. Hence the pertinent noise statistics depend on the effects of the magnitude operation. In background regions where I is zero-mean, the noise of $|I|$ become Rayleigh-distributed (see Chapter 2), which is no longer zero-mean. In signal regions, the noise become Rician-distributed. If the signal mean is substantially greater than the noise variance, then the Rician distribution can be approximated as a Gaussian distribution. However if the signal amplitude is relatively weak, then the magnitude operation causes a noise-thresholding effect in which the resultant SNR is degraded.

7.5.2 Imaging Sequence Parameters

We will consider the effect on SNR of several imaging sequence parameters, including the acquisition time per measurement, the scan time, and the voxel size (spatial resolution). In this section, we will consider the SNR of a particular voxel; hence,

$$\text{SNR} = \frac{\text{voxel signal amplitude}}{\text{noise std. dev. of background}} \tag{7.76}$$

Because there are many parameters to consider, we will divide this section into acquisition time effects and spatial resolution effects.

Effect of Acquisition Time

To understand the effect of acquisition time on SNR, we assume an impulse object that gives rise to a constant signal amplitude in k-space. Also, in comparing situations, we assume that the maximum k-space coverage

remains the same; that is, no change in spatial resolution occurs. If the signal amplitude arising from this impulse object is A, then each of the N time (k-space) samples possesses amplitude A. Also each sample contains independent noise with variance (for the real and imaginary parts)

$$\sigma_n^2 = R_{\hat{n}}(0) = \int_{-1/2}^{1/2} S_{\hat{n}}(f)\, df \tag{7.77}$$

which equals the area under the power spectral density.

For convenience, we will assume that the object is centered at the origin and consider a 1D reconstruction of that element by simply taking the sum of the N samples (that is, taking the inverse DFT evaluated at 0). Thus,

$$\text{SNR} = \frac{\sum_{j=1}^{N} A}{\sqrt{\sum_{j=1}^{N} \sigma_n^2}} = \frac{NA}{\sqrt{N\sigma_n^2}} = \frac{\sqrt{N}A}{\sigma_n} \tag{7.78}$$

The variances add because of independence. This expression represents our reference SNR. Note that we are essentially considering the case where the relevant signal and noise in the 1D image exist in the real part of data; that is, we are neglecting the effect of the magnitude operation.

Signal Averaging

One means to improve SNR is by averaging separate measurements of the same k-space region. By simply adding two measurements together, the signal amplitudes add. However, the noise variances also add, owing to the independence of the noise samples. The resulting SNR is

$$\text{SNR} = \frac{\sum_{j=1}^{N} 2A}{\sqrt{\sum_{j=1}^{N} (2\sigma_n^2)}} = \frac{2NA}{\sqrt{2N\sigma_n^2}} = \frac{\sqrt{2N}A}{\sigma_n} \tag{7.79}$$

The $\sqrt{2}$ increase in SNR occurs because the signal amplitude doubled in the combined measurement while the noise *standard deviation* increased by only $\sqrt{2}$. In general, averaging N_{ave} measurements improves the SNR by $\sqrt{N_{ave}}$.

Readout Time

What happens to the SNR if we double the readout duration T_{read} while continuing to collect N samples? This scenario implies that the sampling interval Δt is also doubled, and, because we are not changing the maximum k-space extent, the readout gradient amplitude G_{read} is halved to maintain

the same $G_{read}T_{read}$ product. Halving of the gradient also halves the pertinent signal bandwidth Δf and the anti-aliasing filter bandwidth. Because the new sampling rate $1/\Delta t$ matches the signal bandwidth Δf (and anti-aliasing filter bandwidth), the noise variance per sample is halved since

$$\sigma_n^2 \propto \Delta f = \frac{1}{\Delta t} \tag{7.80}$$

the area under the power spectral density. Note too that the noise samples remain independent. The signal amplitude A does not change because it is independent of the signal bandwidth (and ignoring T_2 decay). Therefore,

$$\text{SNR} = \frac{NA}{\sqrt{N\sigma_n^2/2}} = \frac{\sqrt{2N}A}{\sigma_n} \tag{7.81}$$

By doubling the readout time, the SNR increases by $\sqrt{2}$. Generally, the SNR varies as $\sqrt{T_{read}}$.

The argument for the SNR improvement with longer readout periods is often cast in terms of bandwidth. While it is true that a reduced signal bandwidth leads to a correspondingly reduced noise bandwidth, this perspective may be misleading in certain cases. For example, consider the case in which the anti-aliasing filter bandwidth is purposefully set to half the value necessary for a given sampling rate. Also, assume that the point object is located at the origin. Because the signal amplitude per sample remains A, it may be tempting to conclude that the SNR will be improved by $\sqrt{2}$ because the noise bandwidth is halved. However it turns out that the SNR of the object will not change. The reason for this discrepancy lies in the nonuniform noise power spectral density created by the lower cut-off frequency of the filter. Although the variance of each noise sample in the signal is half that of the reference case, the resulting correlation of the noise between samples increases the noise variance in the spatial domain upon inverse Fourier transformation of the signal. In the 1D case using a constant readout gradient, half the spatial field of view, as reconstructed by the inverse Fourier transform, is filtered away because of the reduced bandwidth. The signal and noise in the center of the 1D image does not change.

Summary of Acquisition Time Effects

We have shown that

$$\text{SNR} \propto \sqrt{N_{ave}T_{read}} \tag{7.82}$$

The underlying principle is that

$$\text{SNR} \propto \sqrt{\text{measurement time}} \tag{7.83}$$

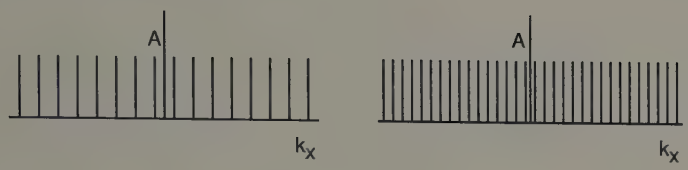

Figure 7.18: Example: 256 readout samples vs 512 readout samples.

It is the *cumulative readout duration* that dictates the SNR.

Using this principle, we can consider multi-dimensional imaging sequences, such as 2DFT, in which N_{pe} phase encodes are acquired. Assuming constant spatial resolution between scenarios,

$$SNR \propto \sqrt{N_{ave} N_{pe} T_{read}} \tag{7.84}$$

Because the total scan time is proportional to N_{ave} and N_{pe}, the SNR is proportional to the square root of the total scan time.

Example: Consider two 2DFT sequences. Sequence 1 acquires 256 readout samples per measurement while sequence 2 acquires 512 readout samples per measurement (i.e., sequence 2 uses twice the sampling rate of Sequence 1) (Fig. 7.18). The gradients are the same for both sequences. What will be their relative SNRs?

The SNRs will be the same. Given the higher sampling rate, the anti-aliasing filter bandwidth for sequence 2 can be doubled. Thus for sequence 2, the noise variance in each sample is double that in sequence 1. However there are more samples collected with sequence 2. Comparing SNR_1 with SNR_2, we find that

$$\mathrm{SNR}_1 = \frac{256A}{\sqrt{256\sigma_n^2}} = \frac{\sqrt{256}A}{\sigma_n} \tag{7.85}$$

and

$$\mathrm{SNR}_2 = \frac{512A}{\sqrt{(512)(2\sigma_n^2)}} = \frac{\sqrt{512}A}{\sqrt{2}\sigma_n} = \frac{\sqrt{256}A}{\sigma_n} = \mathrm{SNR}_1 \tag{7.86}$$

This result should be evident from simply comparing the total readout duration which is the same in both cases.

In terms of k-space coverage, the two sequence cover the same total extent, but sequence 2 has twice the density in the readout direction. In the spatial domain, the resolution in both images is the same, but image 2 has twice the field of view in the readout direction than image 1.

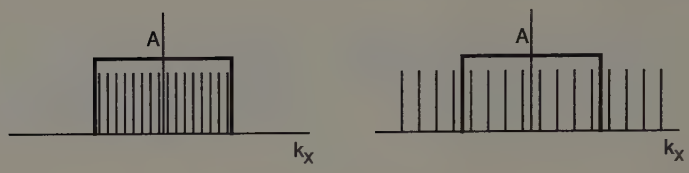

Figure 7.19: Example: If the spatial-frequency content of the object is a square, then halving the voxel size by doubling the readout gradient leads to fewer k-space samples containing signal.

Effect of Spatial Resolution

To consider the effect of spatial resolution on SNR, we will assume a fixed readout time and focus instead on changes in the extent of k-space coverage. We will assume the spatial resolution is specified by the voxel dimensions, δ_x, δ_y, δ_z. In many cases (e.g., a uniform region), the amount of signal in a voxel is proportional to the size of the voxel. If so, then

$$\text{SNR} \propto (\delta_x)(\delta_y)(\delta_z) \tag{7.87}$$

This relation has important consequences with respect to selecting the spatial resolution for a given application. If a high-resolution image is obtained and then the voxels combined to synthesize a low-resolution image, the SNR is not restored to the value attainable by directly acquiring the low-resolution image. For example, if the SNR per voxel in the high-resolution image is 1, then summing two voxels to synthesize the low-resolution image leads to a net SNR of $\sqrt{2}$ due to the averaging operation. In comparison, direct acquisition of a low-resolution image with double the voxel size of the high-resolution image gives an SNR of 2. Therefore one pays a significant SNR penalty by imaging at higher resolution. Hence, in comparing images, it is important to consider the differences in spatial resolution. For example, increasing the SNR of a 5-mm thick slice to that of a 10-mm thick slice requires a scan time that is four times longer.

As a 1D example, we will consider an object whose Fourier transform is a square of amplitude A and of width equal to the highest spatial frequency sampled in readout direction (Fig. 7.19). If N k-space samples are collected, then each of the N samples has a signal amplitude of A. The SNR is

$$\text{SNR} = \frac{NA}{\sqrt{N\sigma_n^2}} = \frac{\sqrt{N}A}{\sigma_n} \tag{7.88}$$

If we compare this situation to one in which the constant readout gradient is doubled, but the readout duration, sampling rate (and N), and anti-

aliasing filter bandwidth are unchanged, then the spatial resolution of the image is improved by a factor of two while the total field-of-view is halved (because N is unchanged). Summing the N samples to reconstruct the center element, the noise remains the same because the readout duration has not changed (equivalently, the filter bandwidth has not changed), but only $N/2$ samples will contain signal. The SNR in this case is

$$\mathrm{SNR} = \frac{(N/2)A}{\sqrt{N\sigma_n^2}} = \frac{\sqrt{N}A}{2\sigma_n} \tag{7.89}$$

half that of the previous case. Thus from an object-domain perspective, the reduction in voxel size by a factor of two leads directly to an SNR reduction by the same factor of two because the object "fills" up the original voxel size. From a frequency-domain perspective, the SNR is halved because only $N/2$ of the k-space samples contain a signal.

The above linear relation with voxel size should be considered a "rule of thumb." The reduction in SNR in the example above will depend on the spatial-frequency content of the object. For example, the relation does not hold when the object is smaller than the voxel size. In those cases, a reduction in voxel size may not create much loss in SNR. Viewed in k-space, the smaller object has a correspondingly wider Fourier transform. Thus, doubling the spatial resolution by doubling the maximum k-space value will not halve the amount of total signal contained by the N samples.

Other Factors

Other factors influencing SNR relate to the signal-strength dependence on the steady-state signal levels as determined by the proton density ρ (because $M_\circ \propto \rho$), the relaxation times T_1 and T_2, and the timing parameters of the sequence employed (e.g., inversion-recovery, saturation recovery). In addition, the uniformity of the k-space sampling will affect the SNR. In general, the most efficient coverage of k-space, from both a time and SNR perspective, is one that is uniform, such as in 2DFT.

Summary

Combining the dependencies of all the imaging sequence parameters discussed above,

$$\boxed{\mathrm{SNR} \propto (\delta_x)(\delta_y)(\delta_z)\sqrt{\text{total readout interval}}\, f(\rho, T_1, T_2)} \tag{7.90}$$

where $f(\rho, T_1, T_2)$ is the pulse-sequence-dependent function that determines the signal amplitudes at readout. This relationship is most applicable when comparing sequences of the same type (e.g., 2DFT) but with different parameter settings.

7.6 Problems

7.1 Modify the single spin-echo 2DFT pulse sequence into a dual spin-echo (i.e., using 90° – 180° – 180°) 2DFT pulse sequence. Design the sequence so that the early-echo image corresponds to $TE_1 = 40$ ms and the late-echo image corresponds to $TE_2 = 100$ ms. Use a constant phase-encoding interval of 4 ms and for each echo acquisition, use a readout gradient interval of 8 ms centered about the echo. Draw a timing diagram and plot the k-space trajectory for this sequence.

7.2 Consider a constant RF excitation pulse of duration τ, tuned to the resonant frequency of water. At $B_0 = 1.5$ T, determine the smallest value of τ such that the fat component is not excited. Assume the small-tip approximation. Using this value of τ, what is the RF strength B_1 that produces a 90° tip angle?

7.3 Maximizing Image Contrast

(a) Given a saturation-recovery spin echo sequence with a specified TE, find an expression for the TR that maximizes the difference signal between tissue A and tissue B. In general, tissue A has $T_1 = T_{1A}$, $T_2 = T_{2A}$; and tissue B has $T_1 = T_{1B}$, $T_2 = T_{2B}$. Assume they both have the same density ρ. Assume TR $\gg$ TE and TR $\gg T_2$.

(b) Using the relaxation times given in Chapter 4 at 1.5 T, compute this TR for maximizing the difference signal between brain white matter and gray matter. Let TE = 20 ms.

(c) Given a saturation-recovery spin echo sequence with a specified TR, now find the expression for the TE that maximizes the difference signal between tissue A and tissue B.

(d) Compute this TE for maximizing the difference signal between brain white matter and gray matter. Let TR = 3000 ms.

7.4 Dr. T. claims that in a 2DFT spin-echo sequence, the baseband signal (the magnitude) peaks at time TE, the center of the spin echo, for each phase-encode level. Dr. C. states that the maximum magnitude of the signal is at the center of the spin echo when the phase encoding lobe is zero but is not necessarily at the center for other phase-encode levels. Discuss the validity of these statements. You may use proofs, physical reasoning, examples, etc... Ignore T_2 decay.

7.5 The object shown below consists of 10 mm by 10 mm (1 cm by 1 cm) square vials of water and lipid (fat). We acquire two images, the first

image with sequence 1 and the second image with sequence 2. The TE for both sequences is the same. Sketch the image that results out of subtracting image 1 from image 2. Assume the frequency of the water component is on-resonance and that the Larmor frequency of lipid is 3.5 ppm lower than that of water. Also assume $B_0 = 1$ T and $G_r = 1$ mT/m (0.1 G/cm). Comment on any SNR differences between the two sequences.

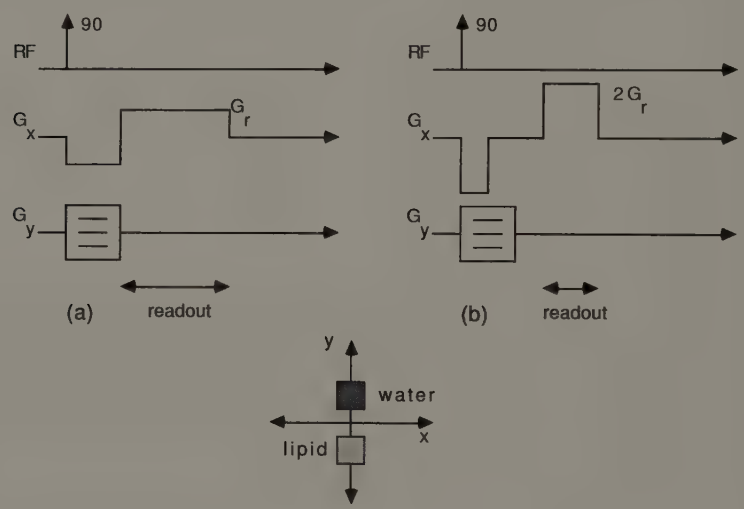

7.6 Compare a conventional 90°_x - τ - 180°_x spin-echo generating sequence with a 90°_x - τ - 90°_x sequence as shown below. Ignore T_1 and T_2 relaxation.

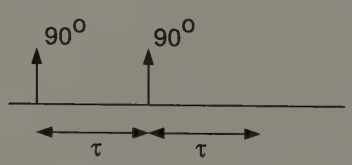

(a) Given an off-resonance spin that precesses (in the rotating frame) by an angle ϕ during the interval τ, what is its resultant magnetization at time 2τ?

(b) If a uniform object contains an ensemble of off-resonance spins such that the precession angle ϕ (after an interval of τ) is uniformly distributed from 0 to 2π radians, determine the relative sizes of the net transverse magnetizations at time 2τ produced by the two sequences. The net transverse magnetization

is based on the integration of the transverse components over the entire ensemble.

(c) Repeat part (b) by comparing the net transverse magnetization at time 2τ of a 90°_x - τ - 180°_x sequence with that of a θ_x - τ - $2\theta_x$ sequence.

7.7 Consider the double-inversion-recovery sequence shown below.

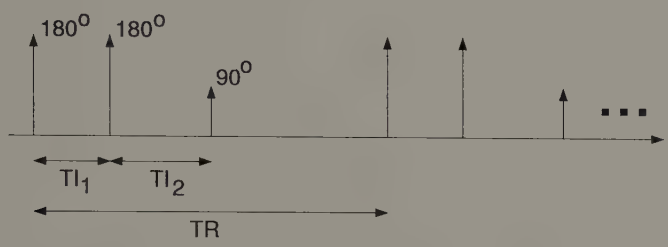

(a) Find an expression for the steady-state signal for a particular T_1 species. (Assume TE = 0.)

(b) If TR = 1000 ms, find the values of the timing parameters TI_1 and TI_2 that will, in the steady state, null muscle and fat simultaneously at the time of readout. (Assume B_0 = 1.5 T.)

7.8 Consider a system that has no y-gradient coil but instead has an *RF* gradient coil that can produce a spatially nonuniform RF field given by $B_{10}(t) + B_{11}(t)y$. This excitation field can be applied only along x in the rotating frame and the excitation frequency is exactly tuned to ω_0.

(a) For any measurement, let $B_{10}(t) = 0$ and $B_{11}(t) = B_{11}$, a constant (over time) applied for time T. As shown below, the amplitude B_{11} is incremented between measurements, each measurement filling in a line in the 2D raw-data array as in a 2DFT sequence. Then a 2D FFT^{-1} of the raw data is used to reconstruct the image.

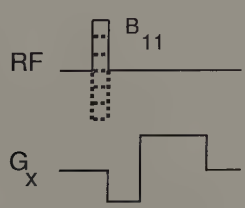

Find an expression for the transverse magnetization after the excitation pulse. Let $m(x, y)$ be the transverse magnetization if a spatially uniform 90°_x pulse had been applied.

Sketch the reconstructed image if the two objects are as shown below.

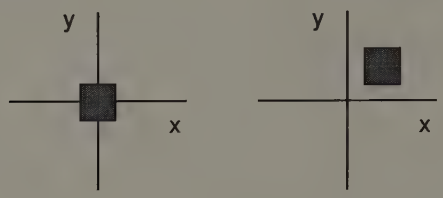

(b) Now let $B_{10}(t)$ and $B_{11}(t)$ be at your total control. ($B_{10}(t)$ and $B_{11}(t)$ are controllable separately).

Design a sequence that will enable imaging in x and y of a real-valued 2D object. Be precise in describing how the excitation (B_{10} and B_{11}) and signal readout are executed from measurement to measurement, and how the data are processed to reconstruct the image. For a given image FOV and spatial resolution, attempt to minimize the number of measurements (excitations) required.

If you feel it is impossible to image the 2D object with such a system, state your reasons.

7.9 Consider the modified 2DFT imaging sequence shown below in which two adjacent lines in k-space are acquired per excitation. On successive excitations, the next two lines are acquired. Assume that the demodulation frequency is tuned to the frequency of water and that the computer is sufficiently "smart" to place the k-space data in the proper positions. As in conventional 2DFT, the image is reconstructed using a standard 2D inverse FFT. Ignore T_2 effects.

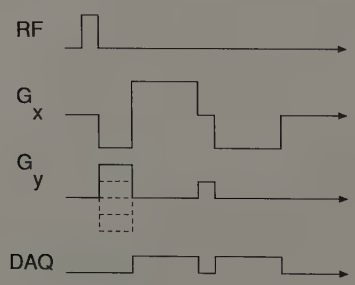

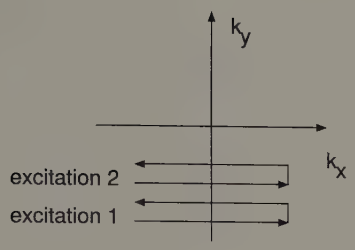

(a) Using this sequence to image the following two impulse objects, sketch the resultant magnitude image for each case. Offer explanations or analyses for your sketches.

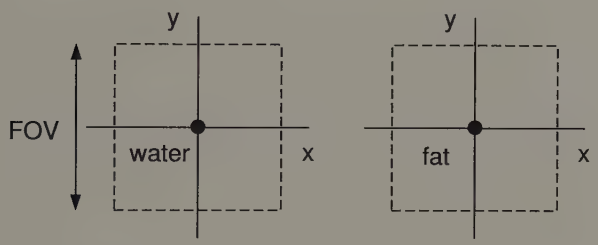

(b) Repeat part (a) for an imaging sequence that acquires 4 phase-encode lines per excitation, as shown below. Under what condition(s) will this sequence produce the same images as in part (a)?

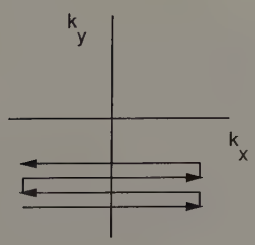

7.10 A reference 2DFT sequence is as follows: 256 phase encodes
10 ms readout duration per measurement, sampled to 256 points.
Field of view: FOV_x, FOV_y.
Spatial resolution: δ_x, and δ_y.
Its k-space coverage is shown below.

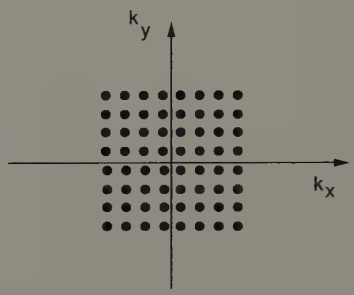

If this sequence produces an SNR normalized to 1, then what are the relative SNR's of the following sequences? Assume that the readout gradient amplitude does not change compared to the reference sequence. Comment on the relative FOV's, spatial resolution, and signal bandwidth.

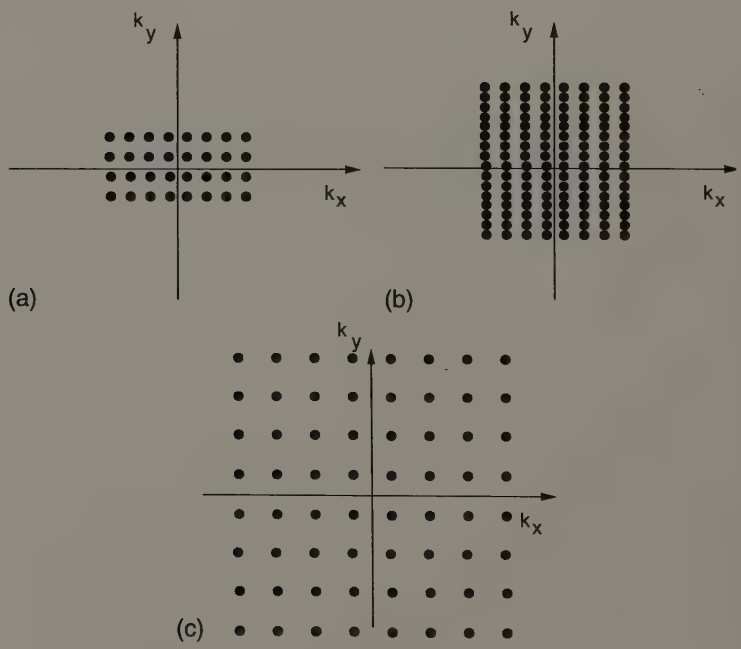

7.11 Consider a 180°–θ inversion-recovery sequence as shown below.

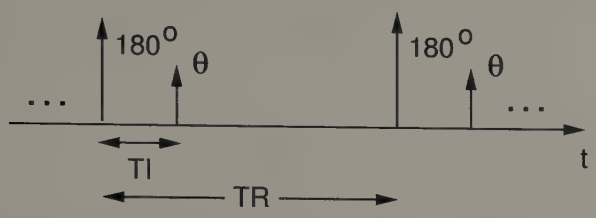

(a) Determine the steady-state signal value M_{ss}. Assume that $M_{xy} = 0$ before the subsequent 180° excitation.

(b) For a fixed TR and TI, find the optimum angle $\theta_\circ$ that maximizes the steady-state signal.

(c) What is $\theta_\circ$ for TR = T_1 and TI = 0.5 TR?

(d) Find an expression for the resulting maximum signal. How does it compare with the signal from a regular inversion-recovery sequence?

7.12 Consider the sequence shown below, in which a small tip-angle excitation pulse $B_1(t)$ is applied on resonance in the presence of a z gradient.

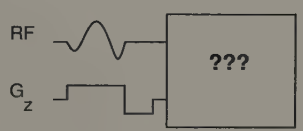

(a) Draw the required addition to the timing diagram that will drive the magnetization vectors in the volume back to the positive z axis (or equilibrium if relaxation effects are ignored). Ignore RF and B_0 inhomogeneities, and also ignore relaxation effects.

(b) Will your sequence still work if we assume that the excitation pulse produces a large tip-angle excitation? Explain why or why not.

(c) Will your sequence work in the presence of B_0 inhomogeneities? Explain why or why not.

(d) Will your sequence work in the presence of RF inhomogeneities? Explain why or why not.

(e) Will your sequence work in the presence of T_1 and T_2 relaxation? Explain why or why not.

(f) Now consider an arbitrary and unknown $\mathbf{M}(x, y, z)$ that may or may not have been set up with an excitation. Is there a (selective) excitation pulse sequence that will drive all of the magnetization back to the positive z-axis? If so, what is this sequence? If not, why not?

7.13 Consider a spherical saline sample with a radius of 0.1 m. If $R_m = 6R_c$ at $B_0 = 1.5$ T, at what field strength will $R_m = R_c$? (Note that this will be an approximation because the conductivity σ also depends on B_0.) What percentage of the noise does the coil resistance contribute at the two field strengths?

Chapter 8

Volumetric Imaging and Fast Imaging

The enormous flexibility of MR imaging stems from the vast number of physical and instrumental parameters at the disposal to the imaging scientist. In this chapter, we examine important variations and extensions to the principles and sequences discussed in the previous chapters. These topics include volumetric imaging and fast imaging.

8.1 Volumetric Imaging

The flexibility of MR is demonstrated by the variety of volumetric imaging methods available. Some methods obtain volumetric data through the acquisition of many 2D slices while other methods image in 3D directly. The general distinction between the two approaches is that multiple-slice acquisition depends on proper selective excitation of these slices while direct volume imaging depends on proper gradient modulation following a volumetric (nonselective) excitation.

8.1.1 3D Imaging by Multiple 2D Slice Acquisition

Multi-Slice Imaging

Perhaps the simplest approach for 3D imaging is to image N_{sl} separate slices sequentially. If a 2DFT sequence with M_{pe} phase encodings is used for imaging each slice, then the scan time for imaging N_{sl} slices sequentially is $N_{sl}M_{pe}TR$, where TR is the repetition time between successive

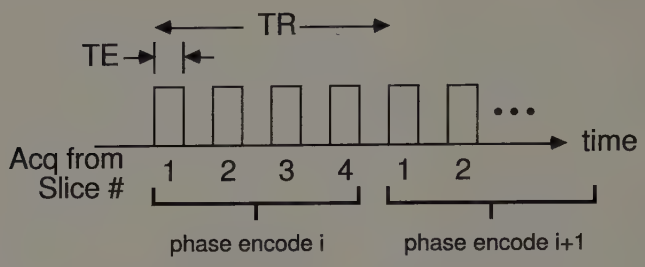

Figure 8.1: Multi-Slice Timing Sequence: Because of the low duty cycle for the acquisition of different measurements from one slice, the quiescent time can be filled with acquisitions from other slices.

phase encodings. However, such a sequence is inefficient as the sequence time for one measurement ($\approx$ TE) is often much shorter than the repetition time TR. For example, in a conventional T_2-weighted scan, TR can be as long as 2 or 3 s with TE being about 100 ms. In such sequences with TR large compared to TE, the long quiescent interval between successive measurements from a slice may be used for acquiring measurements from other slices, thereby increasing the duty cycle of the system. The result is a time-interleaved acquisition of multiple slices, as shown in Fig. 8.1. After a time TR, one phase-encoding is completed for all N_{sl} slices. This form of interleaving is called *multi-slice imaging* and is the most common acquisition mode used in commercial systems. Given a repetition time TR and an echo time TE, the maximum number of slices that can be interrogated is approximately TR/TE. Multi-slice imaging significantly increases the throughput of imaging although for any given slice the scan time is not reduced as its TR remains the same.

Multi-slice imaging is straightforward to implement and does not penalize the scan time. However, its primary disadvantage with respect to volumetric imaging is its demand on high-quality selective excitation for spatial localization along one axis. In practice, thin and well-defined slice excitation is difficult to achieve within system constraints and therefore spatial resolution along the slice-select direction is typically poorer (> 3 mm) than the in-plane resolution (~ 1 mm). To avoid crosstalk between slices, multi-slice imaging with spin-echoes requires slice profiles with minimal out-of-slice ringing for both the 90° and 180° excitations. The slice profile requirements become most stringent in contiguous-slice imaging which is desirable for complete volume coverage without gaps. Hence to obtain contiguous slices while relaxing the slice profile requirements, a common practice is to acquire the odd-indexed slices in one multi-slice scan and

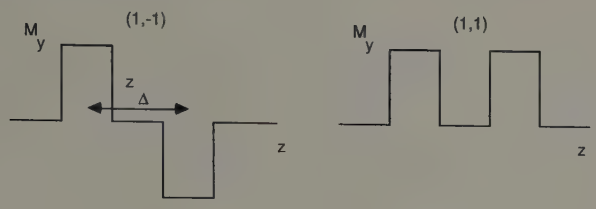

Figure 8.2: Hadamard Encoding: Slice profiles for (1,-1) and (1,1) slice acquisitions. Sum of the two measurements isolates the left slice while the difference gives the right slice.

then repeat the multi-slice scan to acquire the even-indexed slices. In the special case of cardiac imaging, where the heartrate determines TR, multi-slice imaging may still be used but each image in the set corresponds to a different time in the cardiac cycle. Complications may also arise when the movement of the heart in the slice-select direction leads to portions being excited by more than one excitation during one cardiac cycle.

Hadamard Encoding

As mentioned earlier, the third dimension in 3D imaging can be resolved with selective excitation instead of with gradient modulation during the receive portion of the imaging cycle. Whereas gradient-based methods use Fourier encoding to resolve along an axis, selective excitation enables different encoding schemes such as Hadamard encoding to resolve along the excitation axis. Multi-slice imaging is one embodiment of this idea where the basis functions are simply a set of nonoverlapping rectangle functions. However, an alternative is to perform some form of multiple-slice encoding via excitations with the proper excitation profiles. Such profiles are illustrated in Fig. 8.2 for the case of dual-slice encoding. In this example, two excitation profiles, one [1 -1] and the other [1 1], are employed. Using the approximate Fourier transform relationship between the excitation waveform and its excitation profile, and invoking the modulation theorem to produce two slices separated by z_Δ, the applied waveform becomes

$$\mathbf{B}_{rot}(t) = 2B_1(t)\cos(2\pi\Delta f t)\,\mathbf{i} \tag{8.1}$$

for [1 1] and

$$\mathbf{B}_{rot}(t) = 2B_1(t)\sin(2\pi\Delta f t)\,\mathbf{j} \tag{8.2}$$

for [1 -1], where $\Delta f = (\gamma/2\pi)G_z z_\Delta/2$ and $B_1(t)$ is the waveform that would produce a single excited slice on resonance. The decoding of the two slices

simply involves taking the sum and difference of the two measurement sets. This procedure generalizes in a straightforward way to more slices. In MR, because phase is relevant, the Hadamard encoding need not be real-valued. Encoding schemes such as [1 i] and [1 -i] may be employed as well.

Often in multi-slice imaging, averaging of N_{ave} (e.g., two) measurements is required for adequate SNR, resulting in a scan time of $N_{ave}M_{pe}TR$. In such cases, the advantage of Hadamard encoding is that in the same scan time, N_{ave} times more slices can be obtained. The problem with Hadamard encoding concerns the generation of the high-quality excitation slice profiles that (after decoding) avoid crosstalk between the slices. Also, the RF power requirements to play out these pulses is proportional to the number of slices encoded.

8.1.2 3D *k*-Space Acquisition

Volumetric imaging may also be done by direct acquisition of data in 3D *k*-space by appropriate modulation of all three gradients. Compared to multi-slice imaging where imaging times are relatively short but where thin contiguous slices are difficult to obtain, volumetric imaging by 3D *k*-space acquisition typically involves longer acquisition times but easily provides thin contiguous slices.

The extension of the signal equation from 2D imaging to 3D imaging is straightforward. With all three gradients involved, the resultant baseband signal can be expressed as

$$\begin{aligned} s(t) &= \int_x \int_y \int_z m(x,y,z) e^{-i2\pi k_x(t)x} e^{-i2\pi k_y(t)y} e^{-i2\pi k_z(t)z}\, dx\, dy\, dz \\ &= \mathcal{M}\Big(k_x(t), k_y(t), k_z(t)\Big) \end{aligned} \tag{8.3}$$

where as before

$$\begin{aligned} k_x(t) &= \frac{\gamma}{2\pi}\int_0^t G_x(\tau)\, d\tau \\ k_y(t) &= \frac{\gamma}{2\pi}\int_0^t G_y(\tau)\, d\tau \\ k_z(t) &= \frac{\gamma}{2\pi}\int_0^t G_z(\tau)\, d\tau \end{aligned} \tag{8.4}$$

The trajectory through *k*-space is now along all three dimensions, adding even more variety to the possible ways of filling *k*-space. We now consider some specific 3D *k*-space trajectories.

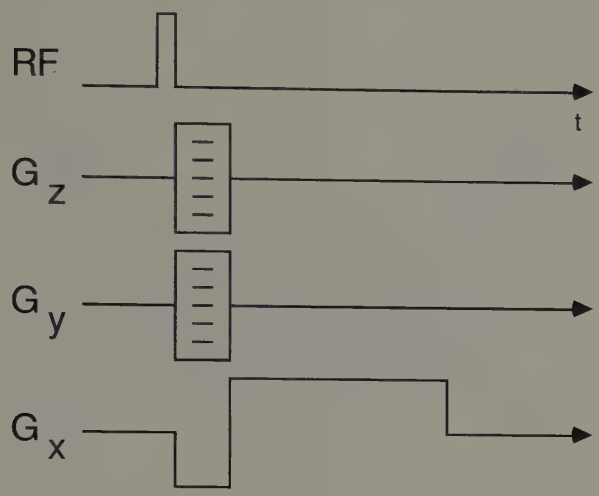

Figure 8.3: 3DFT Timing Diagram: y and z are the phase-encoding axes while x is the readout axis.

3D Fourier Transform

The most popular 3D k-space imaging method is called three-dimensional Fourier transform (3DFT). A straightforward extension of 2DFT, 3DFT employs phase-encoding gradients along *two* axes, and a readout gradient along the third axis. Figure 8.3 shows a representative 3DFT pulse sequence using gradient-recalled echoes. From a k-space perspective, the G_y and G_z phase encoding lobes create movement to some (k_y, k_z) location prior to movement along the k_x axis when the G_x readout gradient and data acquisition turn on. The relative areas under the two phase-encoding lobes are incremented between each excitation to move the trajectory to a different (k_y, k_z) position. The k-space trajectory therefore consists of lines parallel to the k_x axis in a Cartesian orientation (Fig. 8.4), convenient for image reconstruction via a 3D FFT. Typically, to acquire data on both sides of the $k_y k_z$ plane, a dephasing readout lobe on G_x is used. Because phase encoding is along two axes, the scan requires $\mathrm{M}_{pe}\mathrm{N}_{pe}$ excitations, leading to a total scan time of $\mathrm{M}_{pe}\mathrm{N}_{pe}\mathrm{TR}$, where M_{pe} and N_{pe} are the number of phase encodings along each of the two axes. Compared to sequential imaging of N_{pe} slices, 3DFT requires the same scan time but gives $\sqrt{\mathrm{N}_{pe}}$ times better SNR because the entire volume contributes signal from each of the $\mathrm{M}_{pe}\mathrm{N}_{pe}$ excitations whereas in sequential slice imaging, each point contributes signal from only M_{pe} excitations. In 3DFT imaging however,

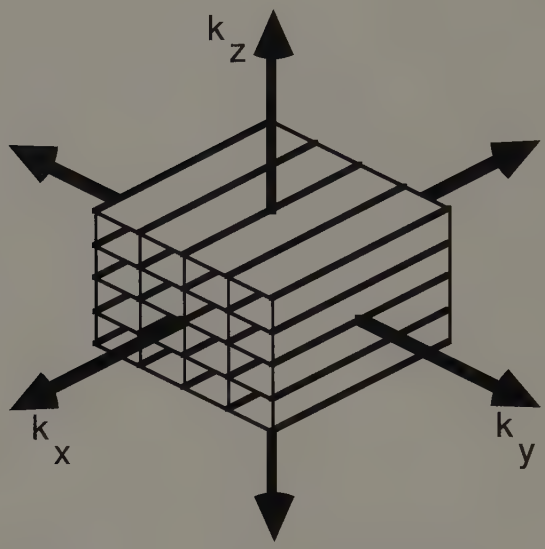

Figure 8.4: 3DFT k-space trajectory consists of lines parallel to the k_x axis.

dynamic range considerations are more important given the greater signal strength being recorded.

The scan time of 3DFT can become prohibitive if M_{pe} or N_{pe} are large, or if TR is long. To ameliorate this scan time problem, one possibility is to apply a mild selective excitation along one of the phase encoding directions to reduce the required number of phase encodes in that direction for a given spatial resolution. Images of the whole volume of interest may then be obtained by a multi-slab imaging sequence, directly analogous to multi-slice imaging, by proceeding to interleave acquisitions of other slabs.

3D Projection Reconstruction

One reason for 3DFT's popularity for volumetric imaging is the convenience of reconstruction with a 3D FFT. Although projection-reconstruction (PR) imaging lacks popularity in MR, the acquisition and reconstruction required in the extension of 2DPR to 3DPR lead to some interesting imaging considerations and insights.

Whereas 3DFT acquires data in a Cartesian coordinate structure, 3DPR acquires data in a 3D spherical coordinate structure (Fig. 8.5). This type of data collection implies that the readout direction is varied through all angles, as shown in the pulse sequence of Fig. 8.6. The readout direc-

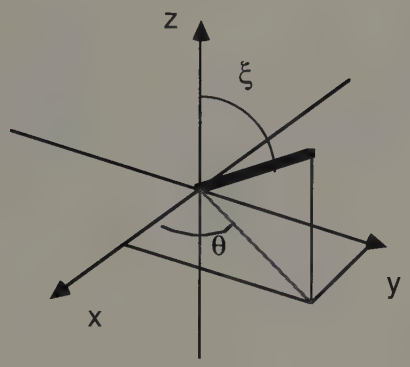

Figure 8.5: Spherical Coordinate System.

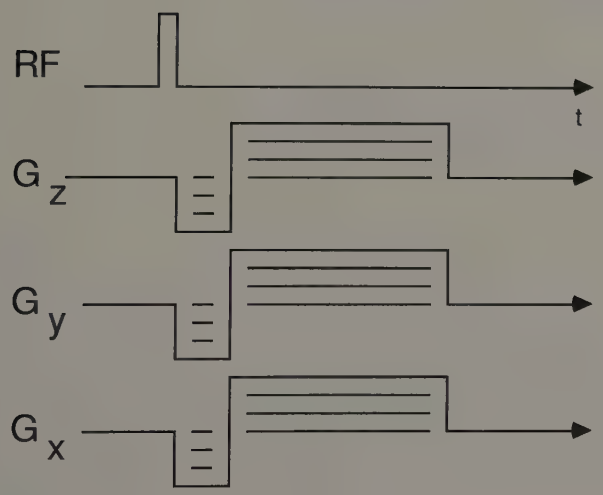

Figure 8.6: 3DPR Timing Diagram: In general all three gradients are on during the readout.

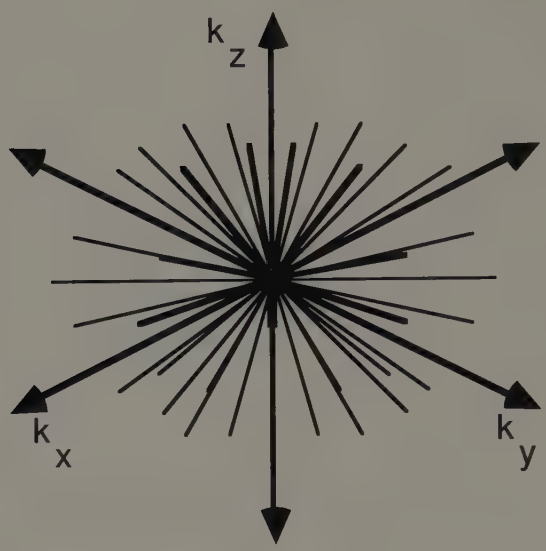

Figure 8.7: 3DPR k-space trajectory for the sequence of Fig. 8.6 consists of radial lines in all directions comprising a sphere, each line passing through the origin (looks like a "koosh®" ball).

tion, parameterized by (θ,ξ), varies in a manner to fill k-space with radial spokes, typically uniformly distributed over a sphere (Fig. 8.7). If the gradient magnitude $G = ({G_x}^2 + {G_y}^2 + {G_z}^2)^{1/2}$, then from Fig. 8.5,

$$\theta = \tan^{-1}\frac{G_y}{G_x} \tag{8.5}$$

$$\xi = \cos^{-1}\frac{G_z}{G} \tag{8.6}$$

Of course, the measurement for a given projection angle is a 1D, not 2D, signal. In 3DPR then, the Fourier transform of $s(t)$ does not correspond to a 2D projection consisting of line integrals; instead, it corresponds to the 1D projection of *planar* integrals of the volume. For example, if G_x is on during the readout, then for a given x-position $x_\circ$, all spins located in the plane at $x = x_\circ$ contribute signal at a particular frequency. From the k-space analysis of $s(t)$, it is obvious that the data collected is along a radial line in 3D Fourier transform space oriented at angles (θ,ξ). It follows then that the 3D extension of the central section theorem is that the Fourier transform of the 1D planar-integral projection $g_{\theta,\xi}(x')$ at an orientation (θ,ξ) is equal to the 3D Fourier transform of the object along

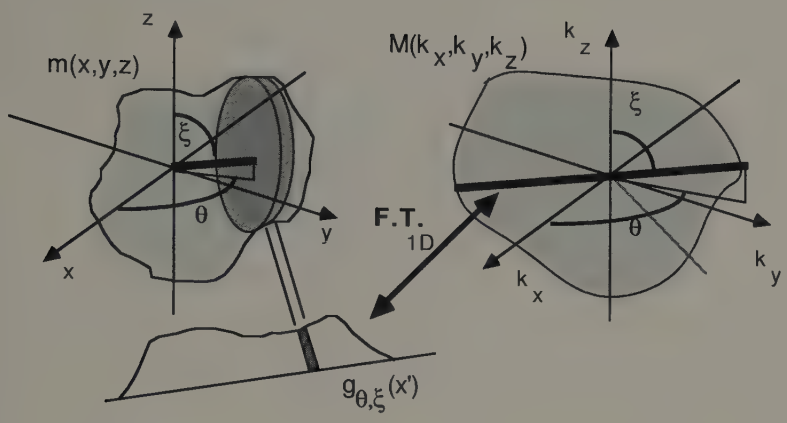

Figure 8.8: 3D Central Section Theorem: Given $g_{\theta,\xi}(x')$, the planar-integral projection of the volume at some orientation (θ, ξ), the 1D Fourier transform of $g_{\theta,\xi}(x')$ gives the radial line through the 3D Fourier transform of $m(x, y, z)$ at that same orientation (θ, ξ).

the radial line at that same orientation (θ, ξ) (Fig. 8.8). For example, when the planar projection angle is $(\theta = 0, \xi = 0)$,

$$\begin{aligned}
\mathcal{F}_{1D}\{g_{\theta=0,\xi=0}(x' = z)\} &= \mathcal{F}_{1D}\left\{\int_x \int_y m(x,y,z)\, dx\, dy\right\} \\
&= \int_z \left[\int_x \int_y m(x,y,z)\, dx\, dy\right] e^{-i2\pi k_z z}\, dz \\
&= \mathcal{M}(0,0,k_z) \qquad (8.7)
\end{aligned}$$

From a Fourier-space perspective, the $|\rho|$ filter that is used in conventional reconstruction algorithms for 2DPR extends to a ρ^2 filter in 3DPR to compensate for the $1/\rho^2$ density of the samples in 3D k-space. It is interesting that the corresponding operation in object space with a ρ^2 filter is a Laplacian, a local operation, not a global operation as it is with a $|\rho|$ filter.

Alternatively, another 3DPR acquisition and reconstruction method, using primarily an object domain perspective, uses a two-step procedure [LL81]. First, for a given angle θ, 1D planar projections at all angles ξ are processed in the same manner as in a 2D projection-reconstruction procedure. The resultant 2D reconstruction corresponds to the 2D projection image of the volume at that angle θ, with each element of this 2D projection image equaling a *line* integral through the volume. Repeating this 2D reconstruction for all θ yields a set of 2D projections at all angles about the z-axis. Second, the lines at the same z-position from each

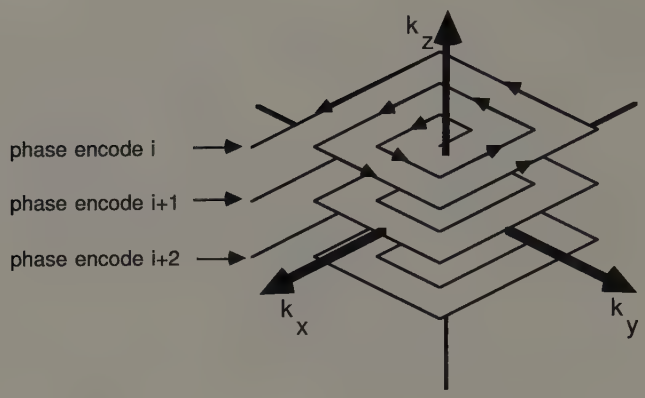

Figure 8.9: k-space trajectory for the hybrid sequence: In this example, a square-spiral 2D k-space scan is combined with phase-encoding for the 3rd dimension.

of these 2D projections are then processed by another conventional 2D projection-reconstruction procedure to reconstruct a slice in the object at that z-position. This 2D projection-reconstruction procedure is repeated at all z-positions to produce a collection of contiguous slices. In effect, the first set of 2D reconstructions converts 1D planar-integral projections into 2D line-integral projections, while the second set of 2D reconstructions converts the 2D line-integral projections into a set of contiguous 2D images spanning the volume.

Hybrid 3D k-Space Trajectories

Given any 2D k-space acquisition for imaging a slice (e.g., echo-planar, spiral scan (see Section 8.2), projection-reconstruction), one effective way to extend the acquisition into 3D k-space is to apply a phase-encoding gradient along the third axis. The 3D k-space filling therefore consists of a planar trajectory that is replicated in the third dimension, one for each phase encoding that is applied. Figure 8.9 shows the 3D k-space trajectory for the example of a hybrid spiral-scan/phase encoding sequence. The 3D reconstruction operation is simply the appropriate 2D reconstruction operation for each of the 2D planes in k-space followed by Fourier transformation along the phase encoding axis with the set of 2D reconstructions.

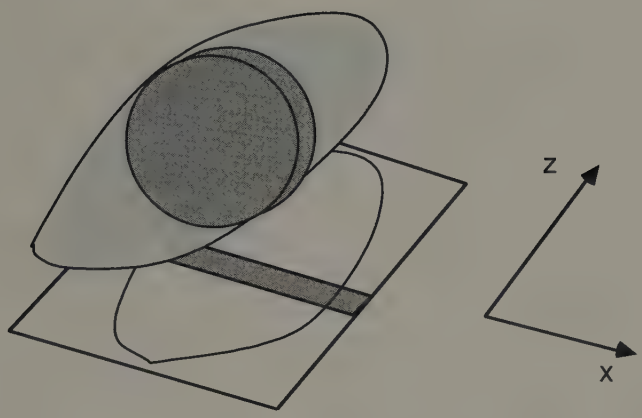

Figure 8.10: Line-Scan Acquisition: In this projective case, excitation of a thin slice in z is followed by a readout in x. Fourier transformation of the signal gives a projection line in the resultant 2D projection image.

8.1.3 Projective Imaging

Another form of volumetric imaging is projective imaging. A 2D "shadow" image of the 3D volume can be obtained in the same scan time as required for a regular 2D image. For example, a 2DFT imaging sequence with the slice-select gradient turned off produces such a projective image. An advantage of projective imaging is its reduced scan time to view the entire volume because only two dimensions of k-space need be acquired. In certain applications such as blood vessel imaging (angiography), where vessels may be tortuous, projective imaging is valuable in enabling visualization of the entire vessel tree without worry of vessels disappearing as they snake in and out of slices. The disadvantage, of course, is the problem of overlying structures (structural noise) which can obfuscate desired structures by limiting the conspicuity and increasing the dynamic range in the image.

As already described, one approach to form such a projection image is to use any 2D k-space imaging sequence with the slice-selective gradient turned off (i.e., the slice thickness is infinite). A second approach however, one that relies on selective excitation and not gradient modulation on readout, is to excite a thin slice and then apply a readout gradient to give the 1D projection of that slice. The 2D projective image is then assembled by sequencing through successive thin slices, each time reading out with the gradient at the same orientation (Fig. 8.10). This second approach is known as a projective line-scan sequence. One advantage is that the scan

time can be short as subsequent slices may be excited immediately after each other. Motion of material during the scan leads to geometric distortion owing to the focal plane shutter effect and not blurring or ghosting as it would in most 2D *k*-space sequences. A disadvantage is that the spatial resolution in the direction of the line scan is limited by the excitation slice profile; therefore higher spatial resolution along that direction is more difficult to achieve versus gradient-based methods. Also the SNR in a line scan sequence is poorer than a 2D *k*-space projective scan because with the 2D *k*-space sequence, every point in the volume is contributing signal for every measurement.

8.2 Fast Imaging

The basic imaging sequence discussed in Chapter 7, saturation-recovery with spin echoes, requires a relatively long scan time because only a single line in *k*-space is acquired per readout and the interval between readouts (TR) is long. However in many situations, fast scanning is desirable to cope with the effects of motion (e.g., respiration) or to capture dynamic events.

From a general perspective, imaging time depends on the total amount of data required for a specified spatial resolution and field-of-view (FOV). Thus changing these image parameters is one approach to shortening the imaging time. For example, a selective excitation restricting the FOV in the phase encoding direction can reduce the required number of phase encoding steps in a 2DFT scan. Alternatively, use of a smaller surface receiver coil (Chapter 11) sensitive to a limited spatial region can effectively reduce the relevant FOV. To build up the FOV, an array of surface coils can be employed.

However for a fixed spatial resolution and FOV, the basic technical goal in fast imaging is to collect more data points per unit time. To achieve this goal, the general strategies are to acquire a greater portion of *k*-space per signal readout and/or to shorten the interval between signal generation. The acquisition of a greater portion of *k*-space per readout involves the appropriate modulation of the gradient waveforms to control the *k*-space trajectory while the means of signal generation depends on the manner in which the RF excitations are played out. Specific approaches within each of the strategies are outlined in the following sections.

8.2.1 k-Space Trajectories

Compared to 2DFT or 2DPR in which a single *k*-space line is acquired per readout, sequences with elaborate time-varying gradient waveforms played

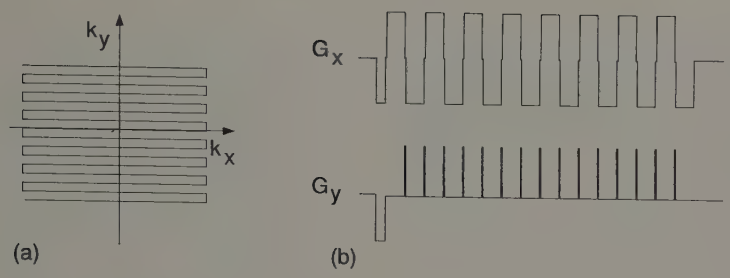

Figure 8.11: Echo-Planar: (a) trajectory; (b) gradient waveforms.

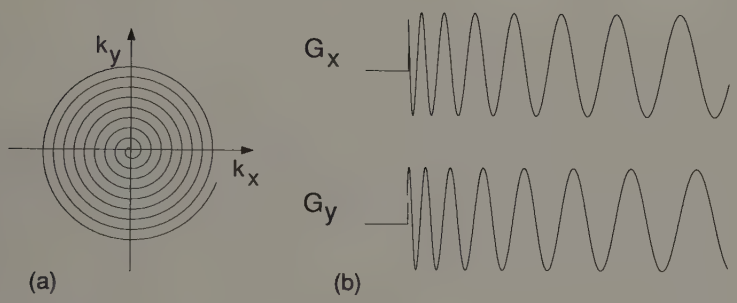

Figure 8.12: Spiral: (a) trajectory; (b) gradient waveforms to produce a constant linear velocity through k-space.

out over usually longer readout intervals enable greater coverage of k-space per measurement. Given the complete control over k-space position, an endless array of trajectories can be devised. However, the more popular trajectories fall into two general families: 1) Cartesian scans, and 2) radial scans. Figures 8.11 and 8.12 show two such trajectories with their gradient waveforms, although numerous variations exist. Figure 8.11 is a Cartesian scan called *echo-planar*, a relative of the standard 2DFT scan. Echo-planar is characterized by the acquisition of multiple raster lines per excitation. After an initial movement to the bottom of k-space, the scan blips upwards in the k_y direction after traversing each line along k_x.

Figure 8.12 is a spiral scan that is related to the radial 2DPR scan. The trajectory starts at the k-space origin and spirals out radially at either a constant angular velocity or constant linear velocity.

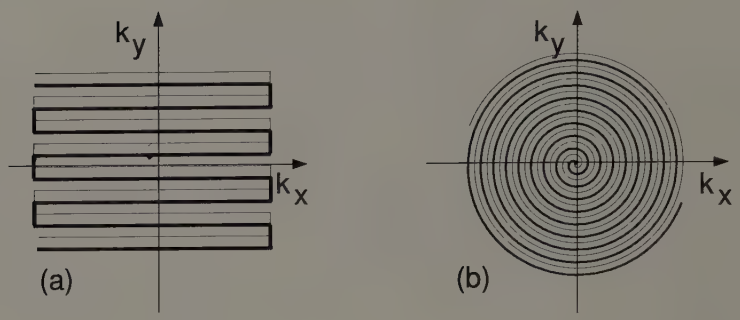

Figure 8.13: Interleaved k-Space Trajectories: (a) echo-planar; (b) spiral.

Considerations

In principle, both the echo-planar and spiral trajectories could complete the scan of k-space in a single readout. Although such "single-shot" sequences represent the fastest possible MR scan, they place significant demands on the hardware, in particular the gradient and receiver subsystems. Enormous gradient power is required to provide the rapid scan through k-space while the receiver bandwidth and data sampling rate must be sufficiently high to accommodate the high signal bandwidth and data throughput. Alternatively, interleaved trajectories, as shown in Figs. 8.13a and 8.13b for echo-planar and spirals, place significantly less demands on the hardware at a slight cost in scan time.

Other considerations of these sequences pertain to off-resonance effects and T2 decay (see Chapter 7). Off-resonance effects are particularly important when relatively long readouts are employed. In echo-planar, the phase error accrued during the signal readout is most significant in the slow (k_y) direction. Figure 8.14a displays this phase error in k-space as a gray level. Along the k_y axis, the phase accrual is linear, leading to a shifted impulse response in the y direction. The amount of shift is proportional to the frequency offset and the readout duration. Because echo-planar readouts can be over 5 times longer than a 2DFT sequence, the off-resonance shift can be over 5 times as much as in a 2DFT image. The simulated image in Fig. 8.14b demonstrates this shift in the image domain in the presence of a linear field variation in the x direction. The center is unshifted while the greatest shifts occur at the edges where the field error is the largest.

The off-resonance behavior of a spiral sequence will be a spatial blur as it is in a 2DPR image. The phase accrual as a function of k-space position is shown in Fig. 8.15a for an interleaved spiral sequence. The radially-varying

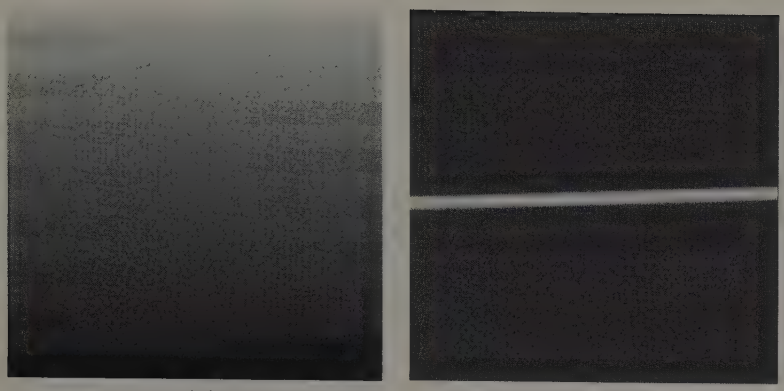

(a) (b)

Figure 8.14: Off-Resonance Response in Echo-Planar: (a) Distribution of phase error in k-space for interleaved echo-planar; (b) Simulated image of tube in the presence of gradient field in the horizontal direction. The off-resonance frequency varies from left to right, leading to a variable vertical shift as a function of horizontal position.

phase error accounts for the blur in the impulse response as opposed to the linear phase error in a Cartesian scan that accounts for the shift in the impulse response.

The corresponding simulated spiral image is Fig. 8.15b for the case where a linear field variation exists in the horizontal direction (and centered about the origin). Thus the extent of blur increases with distance from the origin. To mitigate these off-resonance effects, the field should be made as uniform as possible. To the extent that nonuniformities persists (e.g., due to object-dependent susceptibility differences), deblurring schemes or measurement of the field nonuniformities are desirable.

Another consideration that can be important when relatively long readouts are involved is the T_2 (or $T_2{}^*$) decay that effectively weights the k-space data. This k-space weighting for an interleaved echo-planar scan is presented in Fig. 8.16a. Given the bottom-to-top path of echo-planar, the variation due to T_2 decay is most pronounced in the vertical direction, which leads to a blur mainly in that direction (see Fig. 8.16b).

For an interleaved spiral sequence however, the k-space weighting is radially symmetric (Fig. 8.17a). Therefore, the resultant blur will also be radially symmetric (Fig. 8.17b).

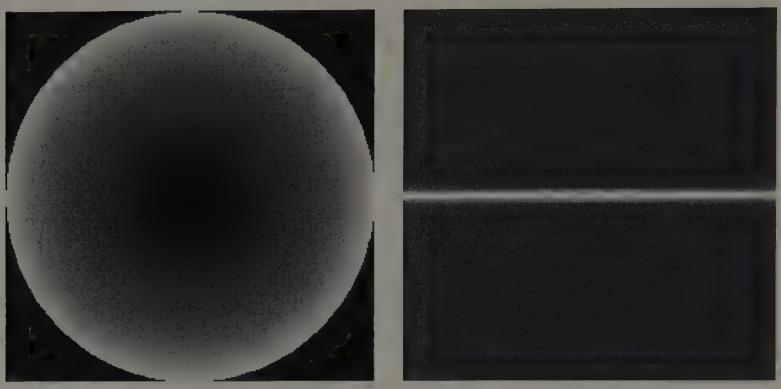

(a) (b)

Figure 8.15: Off-Resonance Response in Spiral Imaging: (a) Distribution of phase error in k-space for interleaved spirals; (b) Simulated image of a tube in the presence of gradient field in the horizontal direction. The off-resonance frequency therefore varies from left to right, leading to a variable blur as a function of horizontal position.

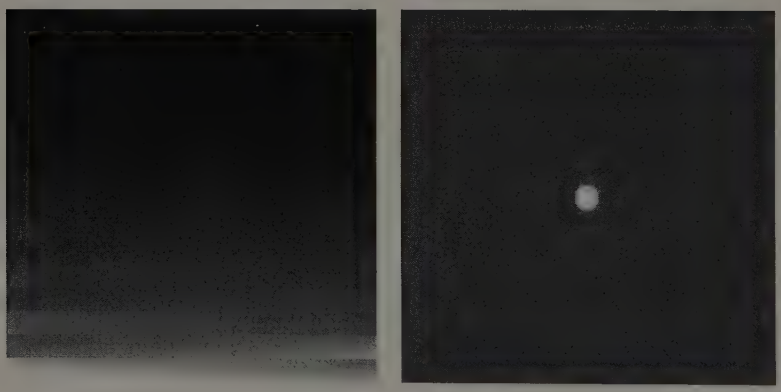

(a) (b)

Figure 8.16: T_2 Weighting in Echo-Planar Imaging: (a) Distribution of weighting in k-space for interleaved echo-planar; (b) Simulated image of circular object demonstrates blurring in y direction.

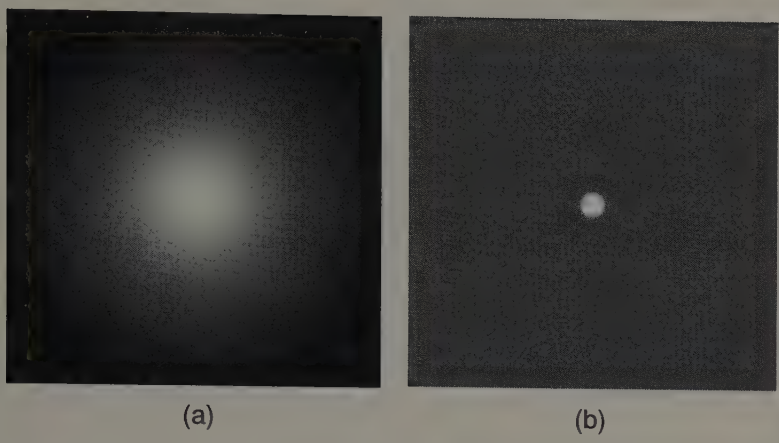

Figure 8.17: T_2 Weighting in Spiral Imaging: (a) Distribution of weighting in k-space for interleaved spirals; (b) Simulated image of circular object demonstrates isotropic blurring.

8.2.2 Signal-Generation Approaches

A wide range of possibilities also exists for signal generation. The parameters involved deal with excitation angles and timing. Some of the more prevalent approaches are plotted in Fig. 8.18.

For reference, Fig. 8.18a is the standard sequence with gradient-echo or spin-echo (180° not shown) generation with a relatively long TR between excitations.

Figure 8.18b is a multiple-spin echo approach in which a train of 180° refocusing pulses are applied after the 90°. Each spin echo provides an opportunity to acquire data from refocused spins. Although standard multi-echo imaging enables images with different T_2 contrast, the scan time for any of those images is not affected. For the purposes of fast imaging however, the multiple echoes can be used to acquire different portions of k-space for a single image. This approach results in a T_2 weighting across k-space depending on the echo times and the trajectory employed.

Figure 8.18c represents a fast-imaging strategy based on increasing the duty cycle by significantly shortening the TR. Because such short TR allows little T_1 recovery before the next excitation, partial tip-angle excitations (α) are commonly used instead of 90° excitations. In addition, this approach is usually applied with a gradient-echo acquisition.

A fourth approach to signal generation is the use of clustered excitations separated by pauses (Fig. 8.18d). This approach is appropriate when

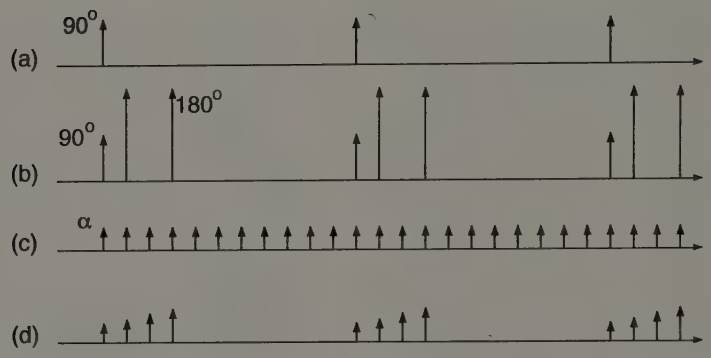

Figure 8.18: Signal-Generation Strategies: (a) conventional; (b) multi-echo; (c) short repetition times with partial tip angle excitations; (d) clustered excitations with partial tip angles.

cardiac synchronization (gating) is involved and constraints exist on the interval allowed each cardiac cycle. During each cardiac cycle, a cluster of excitations allows multiple readouts for greater k-space coverage.

Considerations

In comparing these signal-generation schemes, one of the main considerations deals with the resulting image contrast. In the multi-echo approach, contrast depends on the echo used when the center of k-space is acquired because the low spatial frequencies largely determine the contrast in the image. The T_2 weighting over k-space will degrade the impulse response.

For short-TR sequences, image contrast is complicated because the transverse magnetization has not decayed away before the next excitation pulse is applied. Recall that in conventional scans, the TR is usually long compared to T_2 so that only longitudinal magnetization exists before the next excitation. The presence of transverse magnetization prior to the next excitation must be taken into account.

By combining trajectories with signal-generation methods, one can create a wide variety of fast-scanning methods of varying speeds. For example, an interleaved echo-planar or spiral trajectory can be used in conjunction with a short-TR or clustered excitation method. Similarly, multiple spin-echo acquisitions with interleaved echo-planar or spiral are possible. Because variable signal weighting results with some of these signal-generation methods, more elaborate k-space trajectories (as compared to 2DFT) can lead to more complicated k-space weighting distributions.

Chapter 9

Spectroscopic Imaging

The three NMR parameters that have dominated our discussion are ρ, T_1, and T_2. In this chapter, the focus will be on a fourth NMR parameter, *chemical shift*, a subtle frequency shift in the signal that is dependent on the chemical environment of the particular compound. Chemical shift provides the basis of NMR spectroscopy, which has long been used by chemists to help identify compounds and elucidate molecular structure. Details about chemical shift were provided in Chapter 4. In MR imaging, chemical shift offers the potential for physiological evaluation and material characterization. This chapter delves into the various spectroscopic imaging methods that map the spatial distribution of components with different chemical shifts.

9.1 Effect of Chemical Shift on the Signal Equation

Our original development of the signal equation ignored chemical shift. In the planar imaging case, we desire the image $I(x,y)$ to represent the magnetization distribution $m(x,y)$. To include chemical shift, we add another variable representing the dependence of m on the chemical shift species present. Therefore we let

$$m(x,y) \mapsto m(x,y,f) \tag{9.1}$$

For non-chemical shift imaging, we wish

$$I(x,y) = \int_{\omega} m(x,y,f)\, df \tag{9.2}$$

that is, each image point equals the integrated value of $m(x,y)$ at that point over all chemical shift species. In conventional ^1H imaging of hu-

mans, each element in the image represents a volume consisting largely of water (H_2O) and lipids (CH_2 in fatty acids), whose lines are separated by about 3.5 ppm. The non-chemical shift image should be representative of the combined contributions of both water and fat.

In spectroscopic imaging however, the desired image is $I(x, y, f)$. In other words, the aim is to combine spatial localization with spectroscopy and thereby obtain a spectrum at each (x, y) position. In this way, we gain information of the spatial distribution of water, fat, and any other hydrogenated materials in the region.

Ignoring chemical shift, the signal equation is

$$s(t) = \int_x \int_y m(x, y) e^{-i2\pi k_x(t)x} e^{-i2\pi k_y(t)y} \, dx \, dy \tag{9.3}$$

Including chemical shift, the equation becomes

$$s(t) = \int_x \int_y \int_f m(x, y, f) e^{-i2\pi k_x(t)x} e^{-i2\pi k_y(t)y} e^{-i2\pi f t} \, df \, dx \, dy \tag{9.4}$$

where f equals the chemical shift offset frequency with respect to the demodulation frequency f_0.

9.2 Spectroscopic Imaging Methods

Spectroscopic imaging can be thought of as combined spatial/spectral imaging where the goal is to obtain an NMR spectrum at each spatial position or, equivalently, to display an image of each chemical shift species.

By comparing the signal equation with chemical shift,

$$s(t) = \int_x \int_y \int_f m(x, y) e^{-i2\pi[k_x(t)x + k_y(t)y + ft]} \, dx \, dy \, df \tag{9.5}$$

with the 3D Fourier transform of $m(x, y, f)$,

$$\mathcal{M}(k_x, k_y, k_f) = \int_x \int_y \int_f m(x, y, f) e^{-i2\pi(k_x x + k_y y + k_f f)} \, dx \, dy \, df \tag{9.6}$$

we infer that

$$s(t) = \mathcal{M}\left(k_x(t), k_y(t), k_f(t)\right) \tag{9.7}$$

where

$$\begin{aligned} k_x(t) &= \frac{\gamma}{2\pi} \int_0^t G_x(\tau) \, d\tau \\ k_y(t) &= \frac{\gamma}{2\pi} \int_0^t G_y(\tau) \, d\tau \\ k_f(t) &= t \end{aligned} \tag{9.8}$$

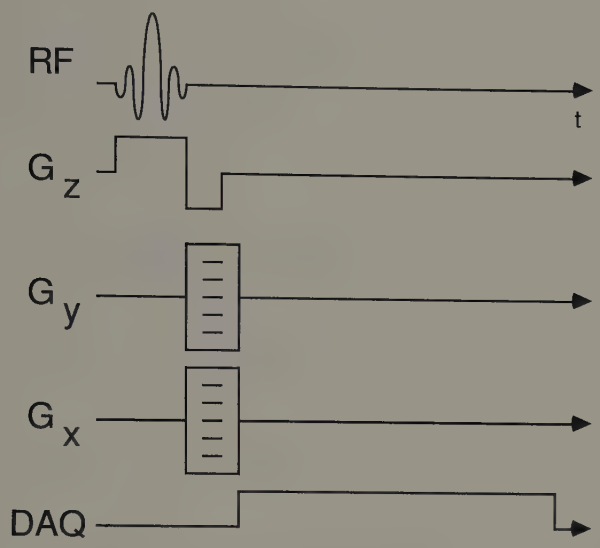

Figure 9.1: 3D Fourier Transform Spectroscopic Imaging Sequence: Phase encoding in x and y is followed by data acquisition (DAQ) with the gradients turned off.

The k-space perspective of the signal equation $s(t)$ now extends to a trajectory through the 3D Fourier transform space of $m(x, y, f)$. We can treat the chemical shift axis f as if it were another "spatial" axis along with x and y. Similarly, although k_f (the reciprocal variable of f) represents time, we can treat k_f in the same way as we do k_x and k_y. The twist in this k-space treatment is that while the position in the k_x and k_y directions is controlled through the time integrals of $G_x(t)$ and $G_y(t)$, the trajectory is constrained to proceed along k_f in a linear fashion without control.

To form a 2D spectroscopic image, we require a filling of $(k_x, k_y, k_f = t)$ space and a subsequent 3D Fourier transform for reconstruction. The result is a 2D image with the third axis corresponding to chemical shift. Note that if we extend 2D spectroscopic imaging to 3D spectroscopic imaging, we would fill in (k_x, k_y, k_z, k_f) space, necessitating a 4D Fourier transform.

9.2.1 3D Fourier Transform Spectroscopic Imaging

3DFT spectroscopic imaging is an extension to 2DFT non-spectroscopic imaging. The timing diagram of the pulse sequence is given in Fig. 9.1. In this sequence, phase encoding is performed in the x and y directions

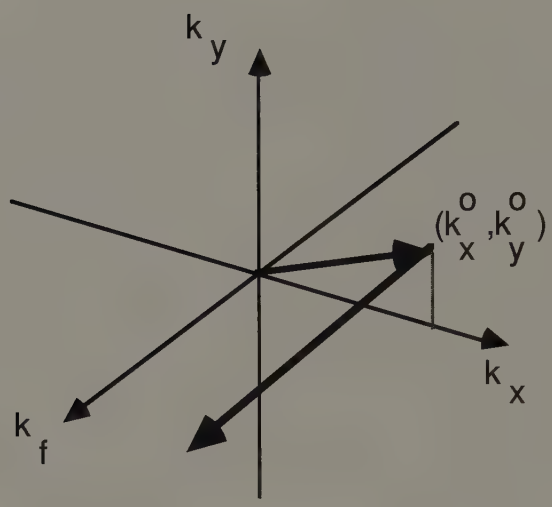

Figure 9.2: k-Space Trajectory of 3DFT Spectroscopic Imaging Sequence: Movement is parallel to k_f axis during readout.

followed by a signal readout with all gradients turned off. The k-space trajectory of this sequence (Fig. 9.2) is in 3D space. Ignoring movement along k_f during the phase-encoding interval, the trajectory initially moves out to a particular (k_x°, k_y°,0) position. Then the signal, recorded without gradients, gives information along a line parallel to the k_f axis, starting from (k_x°, k_y°,0). We therefore fill in 3D k-space with a set of parallel lines, with sufficient sampling in the $k_x k_y$ plane for spatial localization. For an N by N image, we need to sample the $k_x k_y$ plane with N by N points, necessitating a minimum of N^2 separate measurements.

Of course, we cannot ignore the movement along k_f during the phase-encoding interval. This movement implies that the data collection commences at some non-zero k_f position. To collect data that will include (k_x°, k_y°,0), we can use a 180° refocusing pulse that generates a spin echo. Figure 9.3 shows such a sequence. At $t = TE$, the refocusing means that all chemical-shift-dependent phase shifts have been removed, corresponding to being at $k_f = 0$.

The k-space trajectory for the spin-echo sequence is shown in Fig. 9.4. Following the 90° pulse, the trajectory begins at the origin as usual. At time $TE^-/2$ (just prior to the 180°), the phase-encoding lobes have been completed and we have moved out to ($k_x^\circ, k_y^\circ, k_f = TE/2$). At time $TE^+/2$ (just after the 180°), the k-space position has jumped to ($-k_x^\circ, -k_y^\circ, k_f =$

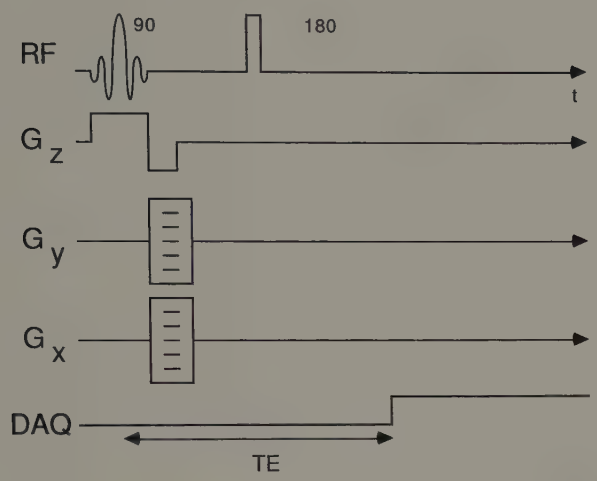

Figure 9.3: 3DFT Spin Echo Spectroscopic Imaging Sequence: Readout begins at the echo time TE.

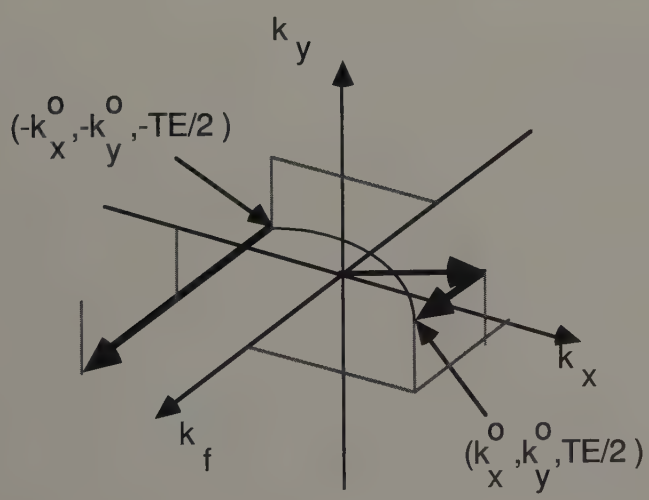

Figure 9.4: k-Space Trajectory of 3DFT Spin Echo Spectroscopic Imaging Sequence: The k-space position jumps from $(k_x^\circ, k_y^\circ, \mathrm{TE}/2)$ to $(-k_x^\circ, -k_y^\circ, -\mathrm{TE}/2)$ due to the 180° pulse. At t = TE, the trajectory crosses the $k_f = 0$ plane.

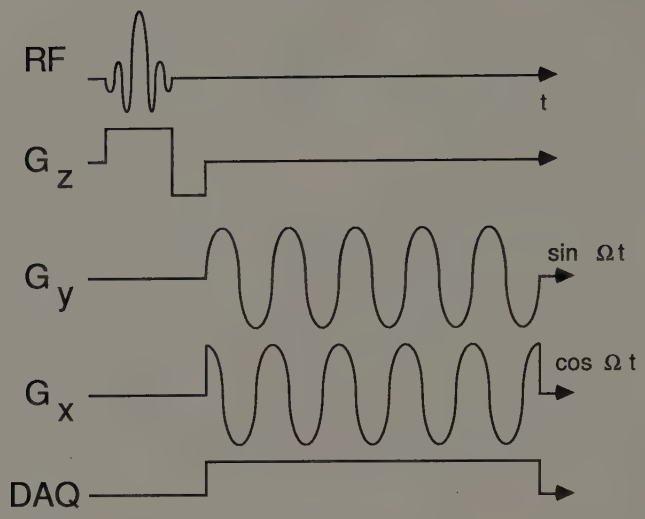

Figure 9.5: Spectroscopic Imaging Sequence with Rotating Gradients: Angular frequency of rotation is Ω.

$-TE/2$) owing to the conjugation of the phase from the 180° rotation. As time elapses after the 180°, we continue to traverse along the k_f axis (in the same direction as before the 180°, so that at T = TE (the echo time), we are at position $(-k_x^\circ, -k_y^\circ, 0)$; that is, crossing the plane at $k_f = 0$.

In 3DFT spectroscopic imaging, the k-space sampling in a Cartesian format lends itself to convenient image reconstruction with a 3D FFT. The main problem with 3DFT spectroscopic imaging is that the scan time can be long (with N^2 excitations, the scan time is N^2TR). Hence reasonable scan times force poorer spatial resolution (N must be of moderate size—e.g., 32).

9.2.2 Spectroscopic Imaging with Time-Varying Gradients

An example of another possible pulse sequence for spectroscopic imaging is shown in Fig. 9.5. In this case, the signal is read out in the presence of a gradient which is rotating at angular frequency Ω. Figure 9.6 depicts the k-space trajectory. Ignoring chemical shift, the trajectory is simply a circle tangent to the origin that is retraced with each gradient cycle. With the more complete description that includes chemical shift, the trajectory is a helix that extends along the k_f axis.

By using a rotating gradient, we actively acquire data over a range of

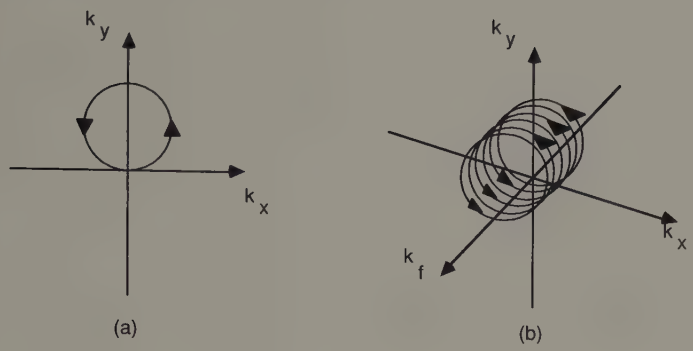

Figure 9.6: k-Space Trajectory of Rotating Gradient Sequence: (a) Ignoring chemical shift, the trajectory in the $k_x k_y$ plane is a circle. (b) Including chemical shift, the trajectory in $k_x k_y k_f$ space is a helix moving outwards along k_f.

spatial frequencies (a circle in this case), but for a particular (k_x, k_y), we have now reduced the number of k_f samples. Knowing the range of chemical shifts however, we can specify the required sampling rate along k_f to avoid aliasing. Thus this sampling constraint dictates the minimum rotation frequency Ω. The allure of using periodic gradient waveforms is that more territory in k_x and k_y can be covered while preserving the chemical shift spectrum. In comparison, the 3DFT spectroscopic imaging method involves reception without gradients, leading to fine sampling along k_f but coarse sampling along both k_x and k_y.

9.2.3 N-Component Chemical Shift Imaging

If given *a priori* knowledge about the number of chemical shift components (N) and their relative frequencies, then it is possible to form images of each component in substantially less scan time than a full-scale spectroscopic imaging sequence. A common example is the case of water/fat imaging in which N = 2 and the relative chemical shift is 3.5 ppm. In this case, we require only two images to isolate these spectral components [Dix84]. The first image is based on Fig. 9.7a, a conventional spin-echo sequence in which the gradient echo and the spin-echo coincide at t = TE. Ignoring main-field inhomogeneities, the two sources of dephasing are the gradient fields and the frequency differences between water and fat. The $90° - 180°$ spin-echo combination refocuses the phase dispersion caused by the chemical shift while proper gradient-area calibration undoes the dispersion created

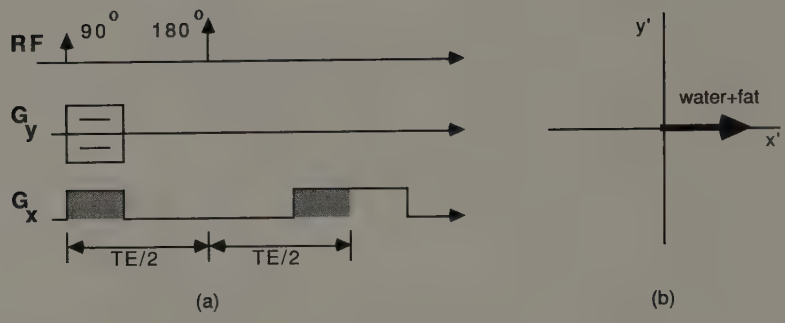

Figure 9.7: Two-Component Imaging—Sequence 1 : (a) Timing Diagram: Gradient echo and spin echo coincide at time TE. (b) At gradient echo (t = TE), water and fat are in-phase.

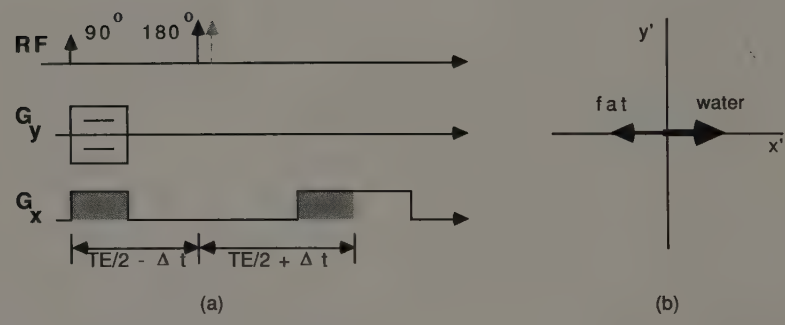

Figure 9.8: Two-Component Imaging—Sequence 2 : (a) Timing Diagram: The 180° excitation pulse is offset in time by Δt, leading to a spin echo at time TE - 2 Δt. The gradient echo remains at time TE. (b) By knowing the difference frequency Δf, Δt can be selected to create 180° of relative phase shift between water and fat at the gradient echo.

by the gradient fields. When the gradient and spin-echo coincide at time TE, water and fat are in-phase (Fig. 9.7b) when the origin of k-space is sampled, and the image represents the sum of the two components. Of course, using 2DFT imaging, fat will continue to reconstruct at a shifted position with respect to water because of its frequency shift. Figure 9.8a shows the sequence for the second image. The only difference between Fig. 9.7a, and Fig. 9.8a is the timing of the 180° excitation. For the second image, the 180° is offset by an amount Δt; the gradient echo continues to occur at time TE, but now the spin echo occurs at time (TE - $2\Delta t$). At time TE, when sampling of the k-space origin takes place, the water component will no longer be in phase with the fat component because the spin-echo refocusing of the two chemical-shift species happened a time $2\Delta t$ earlier. By knowing the difference frequency Δf between water and fat, we can select Δt such that

$$2\pi(\Delta f)(2\Delta t) = \pi \tag{9.9}$$

rendering water and fat 180° out of phase at the gradient echo (Fig. 9.8b). This second image therefore represents a difference image between water and fat.

Given these two images—(water + fat) and (water - fat)—it remains to take the sum and differences of them to isolate each component. Note that the scan time is only twice the conventional scan time and these chemical shift images have the same spatial resolution as a conventional image.

Example: At $B_0 = 1.5$ T, the difference frequency between water and fat is $\Delta f = (\gamma/2\pi)(1.5)(3.5 \times 10^{-6}) = 224$ Hz, where $\gamma/2\pi = 42.577$ MHz/T. Therefore, for the out-of-phase image,

$$\Delta t = \frac{\pi}{(2\pi)(224)2} = 1.12 \text{ ms} \tag{9.10}$$

More generally, this chemical shift imaging situation can be formulated as a linear algebra problem in which the number of images equals the number of components present. The timing of the 180° excitation pulse must be altered for each image to create different phase shifts between the components. The phase shifts need not be based on π radians, although for the two-component case, such an in-phase/out-of-phase pair is convenient for post-processing.

Chapter 10

Flow Imaging

The MR signal is very sensitive to flowing material. Because of this sensitivity, image artifacts can arise from flow during conventional imaging. However, it is also possible to take advantage of this sensitivity to measure or highlight flowing material. This chapter provides an introduction into both flow effects and flow-measurement methods.

10.1 Flow Effects

There are two types of flow effects: 1) time-of-flight (TOF) effects and 2) phase effects. Whereas TOF effects depend on flow with respect to the RF excitation sequence (tip angle θ, timing, spatial selectivity), phase effects depend on flow in the presence of the applied gradient waveforms. TOF effects often manifest as a change in magnitude of the magnetization while phase effects manifest as a change in phase of the transverse component.

10.1.1 TOF Effects

Consider a 2DFT spin-echo sequence with both the 90° and 180° pulses spatially selective. As blood flows through the slices excited by these pulses, TOF effects will occur in the form of distorted signal in position and amplitude.

Signal Washout

A diminished signal can result as only those spins experiencing both the 90° and 180° pulses produce a spin echo (Fig. 10.1). Only a fraction of

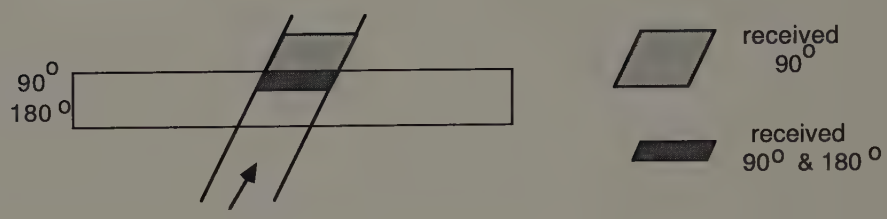

Figure 10.1: Washout in a spin echo sequence. Only blood experiencing both the 90° and 180° excitations will produce a spin echo signal. Complete signal loss may occur given sufficiently fast flow. As blood continues to flow, its reconstructed position may be displaced as well.

the flowing blood will have remained in the slice to be excited by both pulses. In addition, if the vessel is oriented obliquely to the excited slice, the location of the bolus of blood may appear displaced in the image. If flow is sufficiently fast, blood could completely miss the 180° excitation and produce no spin-echo signal.

Inflow (Wash-in) Enhancement

If blood displacement is sufficiently small over TE/2 to avoid significant washout effects, but sufficiently large over TR, then an in-flow enhancement effect will occur. Because blood in the imaged slice becomes replenished between successive 90° excitations, an increased signal will result as this fresh fully magnetized blood will produces a relatively large signal as compared to previously excited blood that undergoes longitudinal recovery (note: blood's T_1 is relatively long (~1 s at 1.5 T)).

The amount of washout and wash-in depends on vessel orientation and flow velocity. Positional displacement occurs when the vessel is oblique to the imaged slice. A distribution of velocities across the vessel lumen (e.g., laminar flow) leads to a distribution of TOF effects.

In gradient-echo imaging, there is no refocusing 180° pulse and therefore no washout effect as described above. Instead, inflow enhancement effects can be significant. The level of inflow enhancement depends on the excitation tip angle and TR of the gradient-echo sequence.

Compensation

Compensation for these TOF effects is difficult. Making the 180° pulse nonselective to avoid (say) washout effects precludes multi-slice imaging

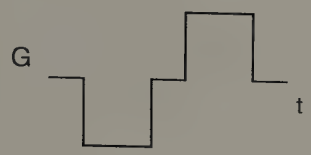

Figure 10.2: Bipolar gradient waveform. Two lobes of opposite polarity with a net area of zero can give rise to significant flow-dependent phase shifts.

because other slices in volume experience the 180° pulse. In multi-slice imaging, these TOF effects are further complicated and become dependent on the order of slice acquisition and flow direction in the blood vessels.

10.1.2 Phase Effects

Flow in the presence of the applied gradient fields creates additional, often undesired, phase shifts. In general, the phase expression for a flowing spin is

$$\phi = \gamma \int_0^t \mathbf{G}(\tau) \cdot \mathbf{r}(\tau) d\tau \tag{10.1}$$

As an example, consider just the x-gradient and a Taylor series expansion of motion in the x-direction. Then the resultant phase of the flowing spin will be

$$\begin{aligned} \phi &= \gamma \int_0^t G_x(\tau) \left(x_o + v_x \tau + \frac{1}{2} a_x \tau^2 + \ldots \right) d\tau \\ &= \gamma x_o \int_0^t G_x(\tau) d\tau + \gamma v_x \int_0^t G_x(\tau) \tau d\tau \\ &\qquad + \gamma \frac{a_x}{2} \int_0^t G_x(\tau) \tau^2 d\tau + \ldots \\ &= \gamma \left(x_o M_0 + v_x M_1 + \frac{a_x}{2} M_2 + \ldots \right) \end{aligned} \tag{10.2}$$

where M_n are the nth moments of the gradient waveform. Hence, flow-dependent phase shifts depend on velocity and acceleration via the gradient's first and second moments respectively.

An important case is that of a bipolar gradient waveform (Fig. 10.2) with a constant-velocity spin (note: "bipolar gradient waveform" is often referred to as simply "bipolar gradient"). The waveform's area is zero but its first moment is M_1. Hence,

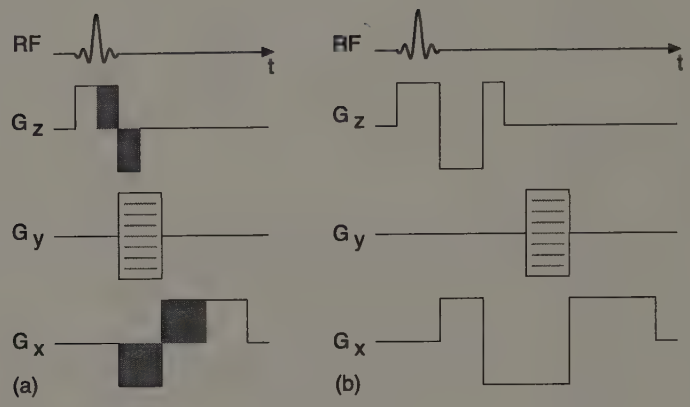

Figure 10.3: (a) Bipolar gradients naturally arise in a 2DFT sequence in the slice-select and readout directions. (b) Modified 2DFT sequence with velocity-compensated waveforms in the slice-select and readout directions.

$$\phi = 0 + \gamma v_x M_1 \tag{10.3}$$

Thus, phase is proportional to velocity and not on the starting position of the spin. Bipolar gradient waveforms are important because they naturally arise in MR imaging. For example, the readout gradient is a bipolar waveform at the center of the readout interval (center of k-space) in a conventional 2DFT gradient-echo sequence (Fig. 10.3a). Likewise, the slice-select gradient is effectively a zero-area bipolar waveform after refocusing. Therefore the signal phases of this sequence will be dependent on flow. Among the problems created by flow-dependent phase shifts are signal loss from dephasing, degraded impulse response (blur and "splatter"), and displacement.

Signal Dephasing

Signal loss can occur if a voxel is comprised of spins moving at different velocities. Ideally, spins will be all in phase to produce a coherent signal when the center of k-space is collected. However, if a bipolar gradient exists to create a velocity-dependent phase shift at that point in time, then a range of phases will exist within the voxel, leading to phase dispersion and resultant signal loss. In a conventional 2DFT sequence, such flow dephasing often occurs in the presence of relatively fast flow with a component of velocity in the slice-select or readout directions. Higher-order motion can

also create significant phase shifts that could ultimately lead to signal loss. Note that in the phase-encoding direction, the center of k-space is acquired with G_y turned off; hence, flow-dependent phase shifts due to flow along y are not significant.

Distorted Impulse Response

A degraded impulse response can also arise from flow-dependent phase shifts. Whereas the signal-dephasing effect can be analyzed based on the amount of flow-dependent phase shifts at the center of k-space, the effect on the impulse response depends on the distribution of flow-dependent phase shifts over k-space. If flow is in the readout direction, then the velocity-dependent phase will evolve quadratically over the readout interval. This quadratically varying phase in the k_x direction leads to an impulse response that is a complex blur function in x. However, given the streaming nature of flow in a vessel, such blurring is often not apparent.

In the k_y (phase-encoding) direction, the consideration is different because k_y is the "slow" direction. What matters in that direction is how the phase progresses from excitation to excitation. Any inconsistency in velocity from one phase encode to the next will create inconsistency in the phase in the k_y direction. The source of this phase can be from flow in any direction, not just in y. In fact, the most significant source is usually from flow in either x or z because of the bipolar waveforms in those directions. The effect of this inconsistency on the impulse response will often be a "splatter" of energy in the y-direction. The impulse response will no longer be a spike because of the inconsistent phase. "Ghosting" (replication) of signal in the phase-encode direction will occur to the extent that the velocity inconsistency (and hence phase inconsistency) is periodic.

Oblique-Flow Displacement

Another flow effect, germane to 2DFT imaging, is an oblique-flow displacement artifact. In the presence of oblique flow, the phase-encoded position is based at a different time than the readout position, as the phase-encoding lobe is played out prior to the readout interval. Therefore, the y component of the reconstructed position will be based on an earlier time than the x component of the reconstructed position. The net effect will be that obliquely flowing blood will reconstruct at a displaced position.

Compensation

Compensation for flow-dependent phase shifts is possible by modifying the gradient waveforms. A standard method is called gradient-moment nulling. The idea is simply to null the first moment to compensate for velocity effects. For (say) the readout gradient, such compensation involves adding another preparatory lobe. For example, if a conventional readout gradient is bipolar (up to the gradient echo), of form $[-1\ 1]$, then a first-moment compensated waveform is of form $[1\ \ -2\ 1]$. A 2DFT pulse sequence with compensated waveforms in the slice-select and readout directions is shown in Fig. 10.3b.

Other strategies to reduce the flow sensitivity include offset gradient-echo acquisitions (acquiring a fraction of the k_x line) and shorter readouts. These methods shorten the gradient intervals and therefore reduce the gradient moments, particularly the higher-order moments which depend on increasing powers of time. Trade-offs, however, include a lower SNR (with shorter readout intervals) and potential blurring of the impulse response (with an offset-echo acquisition). To minimize signal splatter in the phase-encoding direction, gradient-moment nulling can be very effective.

The acquisition can also be synchronized to the cardiac cycle (gating) to stabilize the flow velocity for each measurement. In addition, the sequence can be timed to occur during a quiescent interval (e.g., diastole). However, cardiac synchronization constrains TR. As well, TR becomes variable with heart rate. To minimize the oblique-flow displacement artifact in 2DFT imaging, the phase-encoding lobe is often placed as close as possible to the readout interval.

10.2 Flow Imaging Methods

A wide variety of methods have been developed to exploit these flow effects to highlight flow, measure flow, and discriminate flow from stationary material. Examples of flow imaging methods include those for anatomic blood vessel imaging (angiography), flow quantitation and characterization, and characterization of cardiac motion. These flow-imaging methods can be categorized into those reliant principally on TOF effects and those on phase effects.

10.2.1 TOF-Based Methods

Several methods have been devised to measure or highlight flow based on TOF effects. These methods include bolus tracking, inflow enhancement, and tagging.

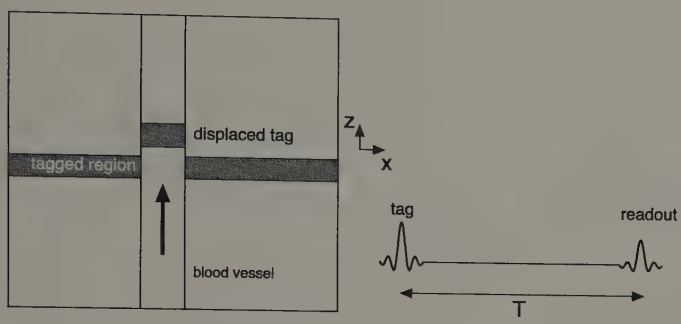

Figure 10.4: Tagging for Flow Assessment. A selective tag darkens a thin strip. Following a displacement time of T, a readout excitation is applied and an xz image is formed. The bolus of darkened blood will be displaced by an amount vT.

Bolus Tracking

One general method is called bolus tracking. For example, in the context of spin-echo signal generation, one can apply a selective 180° excitation that is displaced spatially downstream from the selective 90° pulse. Only moving material experiencing both pulses will produce a spin echo. Stationary material yields no signal if the selective 90° and 180° pulses do not overlap spatially.

Inflow Enhancement

Another general method takes advantage of the inflow enhancement effect. By repeatedly exciting a thin slice with large tip-angle excitations and with relatively short TRs, the steady-state signal from relatively saturated stationary material will be low while the signal from fresh blood flowing into the region will be high. This approach is easy to implement and has been widely adopted for 3D blood vessel imaging by acquiring a set of contiguous slices in this fashion. 3DFT imaging of a slab can also be performed. In this case, because blood will experience more excitations after it enters the thicker imaging volume, the tip angle needs to be scaled back to reduce the rate of blood saturation.

Tagging

A third general method is based on tagging and observing the subsequent displacement. Tagging is performed with a spatially selective excitation.

Many approaches in this category are possible. One example, illustrated in Fig. 10.4, is to excite (tag) a thin cross section through a vessel with a 90° pulse and then image in an x and z spatial format after waiting a time T. Assuming little T_1 recovery between the tag and readout, the tag effectively darkens the thin strip in the xz image because it saturates the magnetization (reduces M_z to zero). The bolus of blood, darkened by the tagging pulse and allowed to move by waiting a time T, will appear displaced relative to the rest of the darkened strip. Measuring the amount of displacement and knowing the displacement time T enables assessment of the blood velocity. Excitations that apply an array of tags are also possible to monitor displacements over multiple positions in the region of interest.

10.2.2 Phase-Based Methods

Two general methods have been developed for measuring flow that exploit the flow-dependent phase shift effect. One method is called phase contrast and the other is Fourier velocity imaging.

Phase Contrast

In phase contrast, two images are acquired, each using a different gradient first moment to sensitize to flow in a particular direction (often the first moment is negated with respect to the other measurement). A difference image can then be formed that shows only signal from moving material that has a component of velocity in the flow-sensitive direction. Under ideal conditions, the phase would be strictly proportional to velocity and subtraction with a second image would be unnecessary. In practice however, spurious phase shifts across the image necessitate an additional image to obtain a phase reference. To sensitize to all possible flow directions, the acquisition is usually repeated with flow sensitization applied in each of the two other orthogonal directions. It is not possible to generate flow sensitivity in all possible directions with a single acquisition.

Two types of subtraction can be performed in phase-contrast imaging. Consider the case in which v_x is encoded with gradient first moments of M_1 and $-M_1$ for the two images respectively. Then the two signals, s_1 and s_2, for a particular voxel in the component images can be expressed as

$$\begin{aligned} s_1 &= \rho e^{-i\gamma v_x M_1} \\ s_2 &= \rho e^{+i\gamma v_x M_1} \end{aligned} \tag{10.4}$$

where ρ is the signal amplitude of that voxel. One form of subtraction is to take the difference in phase; that is,

$$\Delta\phi = \angle s_2 - \angle s_1 = \gamma v_x (2M_1) \tag{10.5}$$

The velocity can then be derived from

$$v_x = \frac{\Delta\phi}{\gamma(2M_1)} \tag{10.6}$$

Because the phase difference is limited to $-\pi$ to π, there is a maximum velocity V_{enc} that can be unambiguously encoded for a given change in first moment ΔM_1 (= $2M_1$ in our example), where

$$V_{enc} = \frac{\pi}{\gamma(\Delta M_1)} = \frac{\pi}{\gamma(2M_1)} \tag{10.7}$$

If the actual velocity is higher than V_{enc}, then that velocity component will alias as a lower velocity.

Phase-difference processing is susceptible to noise problems in regions where the signal magnitude is low. This problem stems from the fact that for a complex-valued signal s, the standard deviation of its phase, σ_ϕ, is given by [CS90]

$$\sigma_\phi = \frac{\sigma_{|s|}}{|s|} = \frac{1}{SNR_{|s|}} \tag{10.8}$$

The phase noise is high for regions where the SNR of the magnitude of s is low. Therefore, another way to process the data is to take the complex signal difference; that is,

$$\Delta s = s_2 - s_1 = \rho\, 2\sin(\gamma v_x M_1) \tag{10.9}$$

Complex signal subtraction avoids the phase-noise problem but quantitative velocity information is confounded by the presence of the magnitude ρ in the difference signal Δs.

Fourier Velocity Imaging

The second method for flow measurement based on flow-dependent phase shifts is Fourier velocity imaging. This method is more general than the two-measurement phase-contrast method mentioned above. With a conventional unipolar gradient, phase is linearly related to spatial position. Similarly, with a bipolar gradient, phase is linearly related to velocity. This relationship lends itself to a powerful Fourier interpretation: a k_v space that is analogous to k_x and k_y space. By sequencing through a set of bipolar gradients of increasing first moments, one can perform velocity phase encoding, analogous to spatial phase encoding. (One can also do velocity "readout" but this requires more elaborate time-varying gradients.) Thus k-space can be expanded to include k_{v_x}, k_{v_y}, and k_{v_z} axes, with analogous concerns for FOV_v (velocity range) and δ_v (velocity resolution). The resultant reconstruction provides information about the velocity distribution

(spectrum) in the imaged region. In comparison, phase-contrast imaging, which acquires only two k_v encodes, does not attempt to resolve the velocity distribution. Instead, it attempts to produce an image representing the average velocity at each location.

Chapter 11

Instrumentation

A block diagram of the basic components of an MR imaging system is shown in Fig. 11.1. An MR imaging system requires hardware for producing the magnetic fields and for sequence control, data acquisition, processing, and image display. In this chapter, we summarize the basic considerations involved for the three types of magnetic fields produced by the system.

11.1 Main Field

MR imaging systems are often identified by the strength of the main field B_0. For whole-body imagers, typical field strengths range from 0.02 T to 3 T. These numbers are a moving target as more recently, scanners at 7 T and above have become available. Low-field scanners have been of interest because they are typically less expensive and easier to site. In terms of imaging performance, a primary drawback of low-field scanners is the lower SNR due to the reduced polarization. Some SNR is regained from the shorter T_1s at lower B_0 which lead to faster longitudinal recovery. Also, off-resonance and RF power deposition are less of a concern at lower fields. High-field systems are attractive because of the higher intrinsic SNR which affords shorter scan times and better spatial resolution. High-field systems are also attractive for spectroscopic imaging because of the greater spectral separation. On the other hand, B_0 inhomogeneities, RF inhomogeneities and RF power deposition are worse at higher fields.

Main-field magnets come in three types: permanent, resistive, and superconducting. Permanent magnets offer lower fringe fields and lower operating costs (e.g., no cryogens). However, they are typically heavy (several tons), lower in field strength (< 0.4 T) and poorer in terms of homogene-

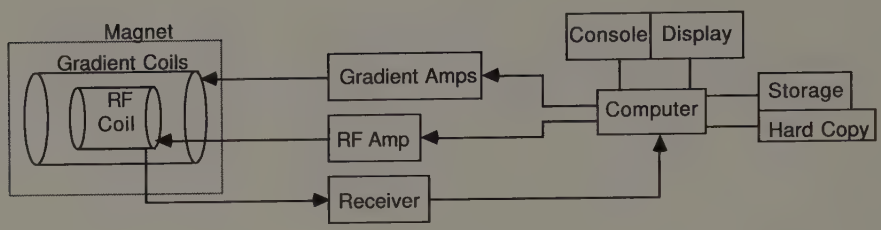

Figure 11.1: Block Diagram of an MR Imaging System

ity and temporal stability. Resistive magnets (air-core or iron-core), which reach strengths of about 0.6 T, also offer lower fringe fields and they can be turned off easily. However, they require external power, water (for cooling), and, like permanent magnets, suffer from relatively poor homogeneity and temporal stability. Scanners based on superconductive magnets are most common because these magnets offer higher field strengths, good homogeneity, and good temporal stability. However, they are usually more expensive and often require cryogens (liquid He) which must be periodically replenished. Although occurrences are rare, superconducting magnets can quench (lose their superconductivity) which leads to a loss of field and rapid boil-off of the liquid He as the superconducting wires become resistive. In such cases, the restoration of the field can be time consuming and costly due to liquid He replenishment.

11.2 Radiofrequency Field

The main sources of noise in MR imaging are from 1) the RF coil (RF coil is a lossy inductor) and pre-amplifier, and 2) the subject (the body is a conducting medium that can be modeled as a resistor, dissipating energy). In designing an RF coil (inductance L_{coil}), we desire low intrinsic coil losses (which implies a high unloaded quality factor ($Q = \frac{\omega L_{coil}}{R_{coil}} >> 1$)). This ensures that the dominant source of noise will be from the subject (Brownian motion of the body electrolytes), in which case the loaded Q of the coil (with the subject inside the coil) is significantly lower than the unloaded Q. In general, there may be both electric and magnetic coupling of an RF coil to the body. Good MR coil design strives to minimize the amount of electric coupling to avoid dielectric losses because electric fields play no role in NMR detection. Thus losses due to inductive coupling should play the dominant role. These losses are unavoidable as inductive coupling is a fundamental aspect of MR signal reception. Ideally, the receiver coil should be

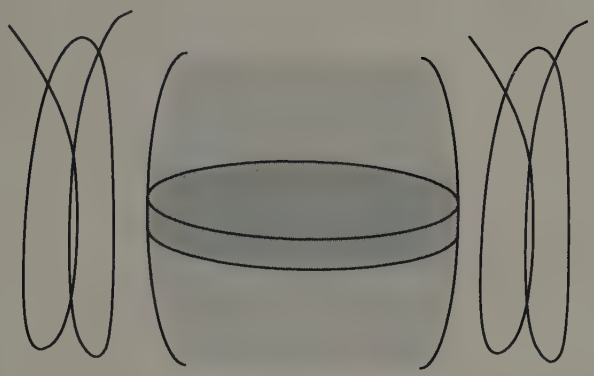

Figure 11.2: The body coil is designed to be uniformly sensitive to entire volume encompassed by coil. Such a design lends flexibility in imaging a large region (for example, with multi-slice imaging) but, for any given slice, will produce a lower SNR image because of the large noise volume seen by the coil.

sensitive to only the imaged region (e.g., a slice) because while signal is received from that imaged region, noise is picked up from the entire volume of sensitivity. Thus it is desirable from an SNR perspective to maximize the ratio of imaged volume to "noise volume" seen by receiver coil. However, in the case of an all-purpose body coil (Fig. 11.2), the noise volume can be significantly greater than the particular slice that is being imaged. The SNR is therefore poorer than it need be, but the body coil is often used because it offers flexibility and convenience of use in imaging a large region.

Coil Geometry There are several common RF coil geometries that produce relatively uniform fields. They include solenoidal coils, which are applicable when the B_0 field is perpendicular to the body axis. When B_0 is parallel to the body axis, the most common B_0 orientation, "birdcage" coils [HES+85] have proven popular.

Polarization Linear drive coils produce a linearly polarized field that is decomposable into two counter-rotating circularly polarized fields. Quadrature drive coils (basically 2 linear coils in space quadrature (90° apart)) produce a circularly polarized RF field. Compared to linear drive coils, quadrature drive coils reduce transmit power (hence less RF heating of subject), produce more uniform excitation, and give an SNR improvement of $\sqrt{2}$ (averaging the signal from two coils) [GHP+85].

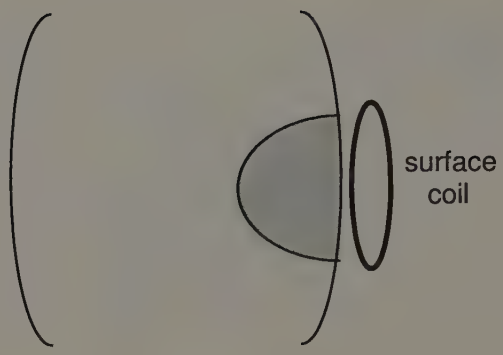

Figure 11.3: Surface coil sensitive to superficial region of body. Better SNR is achieved in the proximal regions because of the smaller noise volume seen by the coil.

Transmit/Receive Set-Up Conventionally, a single coil is used for both transmit and receive. Protective circuitry is required because the received signals are in microvolt range. However, separate coils may be used for the transmit and receive portions. The transmit coil must be isolated from the receiver coil during signal reception. It is often desirable to achieve uniform excitation with a head or body coil (for uniform image contrast generation), but to receive signal from a localized region using a *surface coil* for better SNR, as described below.

Surface Coils and Coil Arrays Surface coils are localized coils that are coupled to a limited region of the body (Fig. 11.3). Although they may operate as transmit/receive coils, they are often used in receive mode only owing to their highly nonuniform B_1 distribution. Surface coils are appropriate for imaging superficial structures (e.g., eyes, spine, extremities). Compared to using a head coil or body coil as the receiver coil, surface coils achieve a better SNR in superficial regions because of a higher imaged-volume to noise-volume ratio. However, surface coils are less suitable for imaging deep-lying structures because of the falloff of sensitivity with depth. For a circular surface coil of radius a situated at $x = 0$, the B_1 sensitivity of the RF field a distance x along the main axis away from the coil is [HA85]

$$B_1(x,a) \propto \frac{a^2}{(a^2+x^2)^{3/2}} \tag{11.1}$$

For $x = a$, the B_1 sensitivity falls off by a factor of 0.35 relative to its sensitivity at $x = 0$.

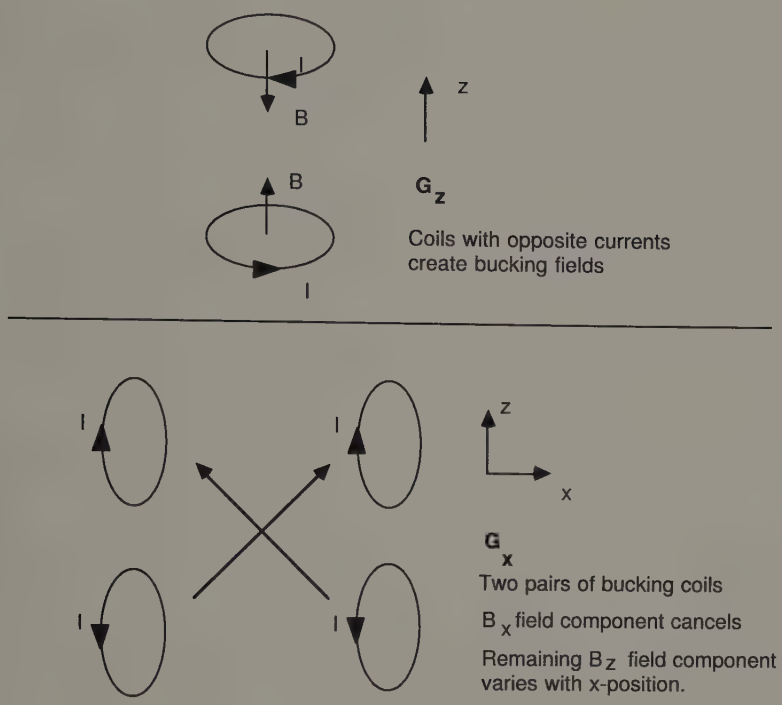

Figure 11.4: (Top) Basic configuration for z-gradient. (Bottom) Basic configuration for x-gradient (similar configuration for y-gradient).

While a single surface coil provides higher SNR in a localized region, surface coil arrays are commonly used because they extend the available FOV while retaining the high SNR advantages [REH+90]. Coil arrays are also useful for scan acceleration. Simplistically, imaging with each coil in the array requires fewer phase encodes because of the smaller FOV seen by the coil. The full-FOV image can be pieced together through appropriate processing of the outputs from the individual coils in the array. To the extent that the spatial sensitivities of the coils overlap, the reconstruction of the full-FOV image may involve intricate unraveling of this overlap.

11.3 Gradient Fields

Separate coils are needed to produce the three orthogonal linear gradient fields: $G_x = dB_z/dx$, $G_y = dB_z/dy$, and $G_z = dB_z/dz$. Figure 11.4 illus-

trates the basic configuration for these gradient coils. Conceptually, a pair of coils passing current in opposite directions produces bucking magnetic fields that result in a spatially varying field with the desired null in the middle [Tur93]. On whole-body systems, these coils are driven by powerful amplifiers to achieve gradient field amplitudes that are typically < 50 mT/m (< 5 G/cm). The maximum slew rate of these fields is roughly < 200 mT/m/ms (< 20 G/cm/ms). At these amplitudes and switching rates, coil heating can be a consideration as well as peripheral nerve stimulation. In addition, as current is pulsed through these coils in the presence of B_0, Lorentz forces are generated on the coil assembly that can lead to significant acoustic noise.

Appendix A

Useful Constants and Conversions

1 T	magnetic flux density	10^4 G
10 mT m^{-1}	magnetic gradient field	1 G cm^{-1}
γ	gyromagnetic ratio (^{1}H)	267.52×10^6 rad s^{-1} T^{-1} 267.52×10^3 rad s^{-1} mT^{-1} $26,752$ rad s^{-1} G^{-1}
$\gamma/2\pi$	gyromagnetic ratio (^{1}H)	42.577 MHz T^{-1} 42.577 kHz mT^{-1} 4.2577 kHz G^{-1}
10 mT m^{-1}	gradient field to frequency	425.77 kHz m^{-1}
1 G cm^{-1}	gradient field to frequency	4.2577 kHz cm^{-1}
k	Boltzmann's constant	1.381×10^{-23} J K^{-1}
h	Planck's constant	6.626×10^{-34} J s
μ_0	permeability of vacuum	400π nH m^{-1}

Bibliography

[Abr61] A. Abragam. *The Principles of Nuclear Magnetism.* Oxford University Press, London, England, 1961.

[BHAAM87] P. A. Bottomley, C. J. Hardy, R. E. Argersinger, and G. Allen-Moore. A review of ^{1}H nuclear magnetic resonance relaxation in pathology: Are T_1 and T_2 diagnostic? *Med. Phys.*, 14:1–37, 1987.

[Blo46] F. Bloch. Nuclear induction. *Phys. Rev.*, 70:460–473, 1946.

[Bra56] R. N. Bracewell. Strip integration in radio astronomy. *Aust. J. Phys.*, 9:198–217, 1956.

[Bra00] R. N. Bracewell. *The Fourier Transform and its Applications.* McGraw-Hill, San Francisco, third edition, 2000.

[BZP+98] M.A. Bernstein, X.J. Zhou, J.A. Polzin, K.F. King, A. Ganin, N.J. Pelc, and G.H. Glover. Concomitant gradient terms in phase contrast MR: Analysis and correction. *Magn. Reson. Med.*, 39(2):300–308, 1998.

[CS90] T.E. Conturo and G.D. Smith. Signal-to-noise in phase angle reconstruction: Dynamic range extension using phase reference offsets. *Magn. Reson. Med.*, 15:420–437, 1990.

[Dix84] W.T. Dixon. Simple proton spectroscopic imaging. *Radiology*, 153:189–194, 1984.

[EKH+85] R.L. Ehman, B.O. Kjos, H. Hricak, R.C. Brasch, and C.B. Higgins. Relative intensity of abdominal organs in mr images. *J. Comput. Assist. Tomogr.*, 9(2):315–319, 1985.

[EMB94] F.H. Epstein, J.P. Mugler, and J.R. Brookeman. Optimization of parameter values for complex pulse sequences by simulated

annealing: Application to 3D MP-RAGE imaging. *Magn. Reson. Med.*, 31(2):164–177, 1994.

[FB71] T.C. Farrar and E.D. Becker. *Pulse and Fourier Transform NMR: Introduction to Theory and Methods.* Academic Press, Inc., New York, NY, 1971.

[Gad82] D.G. Gadian. *Nuclear Magnetic Resonance and Its Applications to Living Systems.* Oxford University Press, New York N.Y., 1982.

[GGM74] A. N. Garroway, P. K. Grannell, and P. Mansfield. Image formation in NMR by a selective irradiative. *J. Phys. C: Solid State Phys.*, 7:L457–L462, 1974.

[GHP+85] G.H. Glover, C.E. Hayes, N.J. Pelc, W.A. Edelstein, O.M. Mueller, H.R. Hart, C.J. Hardy, M. O'Donnell, and W.D. Barber. Comparison of linear and circular polarization for magnetic resonance imaging. *J. Magn. Reson.*, 64:255–270, 1985.

[Gol88] M. Goldman. *Quantum Description of High-Resolution NMR in Liquids.* Oxford University Press, New York, NY, 1988.

[HA85] C.E Hayes and L. Axel. Noise performance of surce coils for magnetic resonance imaigng at 1.5 t. *Medical Physics*, 12(5):604–607, 1985.

[HES+85] C.E. Hayes, W.A. Edelstein, J.F. Schenck, O.M. Mueller, and M. Eash. An efficient highly homogeneous radiofrequency coil for whole-body NMR imaging at 1.5 t. *J. Magn. Reson.*, 63:622–628, 1985.

[HL79] D. I. Hoult and Paul C. Lauterbur. The sensitivity of the zeugmatographic experiment involving human samples. *Journal of Magnetic Resonance*, 34:425–433, 1979.

[Lau73] P.C. Lauterbur. Image formation by induced local interactions: Examples employing nuclear magnetic resonance. *Nature*, 242:190–191, 1973.

[Lju83] S. Ljunggren. A simple graphical representation of fourier-based imaging methods. *J. Magn. Reson.*, 54:338–343, 1983.

[LL81] C.-M. Lai and P. C. Lauterbur. True three-dimensional image reconstruction by nuclear magnetic resonance. *Phys. Med. Biol.*, 26(5):851–856, 1981.

[MM82] P. Mansfield and P.G. Morris. *NMR Imaging in Biomedicine.* Academic Press, Inc., Orlando, Florida, 1982.

[NH90] D.G. Norris and J.M. Hutchison. Concomitant magnetic field gradients and their effects on imaging at low magnetic field strengths. *Magn. Reson. Imag.*, 8(1):33–37, 1990.

[Pap62] A. Papoulis. *The Fourier Integral and its Applications.* McGraw-Hill, New York, 1962.

[PNM89] J. Pauly, D. Nishimura, and A. Macovski. A k-space analysis of small-tip-angle excitation. *Journal of Magnetic Resonance*, 81:43–56, 1989.

[PTP46] E.M. Purcell, H.C. Torrey, and R.V. Pound. Resonance absorption by nuclear magnetic moments in a solid. *Physics Review*, 69:37–38, 1946.

[REH+90] P.B. Roemer, W.A. Edelstein, C.E. Hayes, S.P. Souza, and O.M. Mueller. The NMR phased array. *Magn. Reson. Med.*, 16(2):192–225, Nov. 1990.

[Sli80] C. P. Slichter. *Principles of Magnetic Resonance.* Springer-Verlag, Berlin, 1980.

[Tur93] R. Turner. Gradient coil design: A review of methods. *Magn. Reson. Imag.*, 11:903–920, 1993.

[Twi83] D. B. Twieg. The k-trajectory formulation of the NMR imaging process with applications in analysis and synthesis of imaging methods. *Medical Physics*, 10:610–621, 1983.

Index

T_1 relaxation, 50
T_2 relaxation, 50–51
    effect on imaging, 144–145, 189
T_2*, 129, 130, 137

acquisition time
    effect on SNR, 160–163
aliasing, 13, 87–89
    avoidance, 89
anti-aliasing filter, 89, 162

Bloch equation, 27, **51**, 57
Bloch, Felix, 2

central section theorem, 11–12, 34, 77, 182
chemical shift, **53–55**, 128–129, 193
CNR, *see* contrast-to-noise ratio
complex numbers, 5
concomitant gradients, 146
contrast-to-noise ratio
    definition, 155

demodulation, 64, 67–68, 159
dephasing, 129, 130, 137

echo-planar imaging, 187
echoes, 134–144
eddy currents, 146
Ernst angle, 151
excitation, 24, 49, 99–123
    180°, 138, 152
    analytical solution, 104–107
    graphical solution, 104–107
    nonselective, 99–107
    selective, 29–30, 107–120
        practical considerations, 117
        pulse design, 120
        refocusing, 112–115
        slice profile example, 114–117
        slice profiles, 107, 114
        small tip-angle, 111–114, 118, 123
excitation angle, *see* tip angle

Faraday's law, 26, 49, 66–67
fast imaging, 186–192
FID, *see* free induction decay
field of view, 84
flip angle, *see* tip angle
flow, 203–212
    flow effects, 203–208
    flow imaging methods, 208–212
        Fourier velocity imaging, 211–212
        phase contrast, 210–211
        time-of-flight, 208–210
Fourier transform, 6–9
    one-dimensional, 6
    spatial frequency, 7
    table of, 8
    two dimensional, 7–9
free induction decay, 26, 49

Gaussian density, 18
Gibb's artifact, *see* truncation artifact
Gibb's ringing, 92
gradient echo, 134, 136
gradient field, 26–27, 61, 217–218
gyromagnetic ratio, 24, 45
  table of, 48

Hadamard imaging, 177–178

image contrast, 41, 147–154
image reconstruction, 93
imaging methods, 29–40, 74–83
  three-dimensional, 175–186
inhomogeneities, *see* magnetic fields, inhomogeneities
instrumentation, 41–42
inversion recovery, 152–154
  signal nulling, 154

Johnson noise, 155

k-space, 70–74
  effect of 180° excitation, 140
  excitation, 118–119
  illustration of, 72–74
  readout, 70–74
  sampling, 84–89
  three-dimensional, 178
  with chemical shift, 195

Larmor frequency, 24, 48

magnetic fields
  gradient G, 26–27, 217–218
  gradient field G, 61
  inhomogeneities, 41, 127–128
  radiofrequency B_1, 24–26, 29–30, 48–49, 100, 214–217
    circularly polarized, 102
    linearly polarized, 100
  static B_0, 24, 46–48, 213–214
magnetic resonance
  imaging, 29–40
    contrast, 41, 147–154
    other approaches, 40
    projection reconstruction, 32–34, 74–78
    spectroscopic, 193–201
    three-dimensional, 175–186
    three-dimensional hybrid, 184
    two-dimensional Fourier transform, 35–40, 78–83
  physics, 23–26, 45–55
magnetization, 46
magnitude image display, 83
multi-slice imaging, 175–177

noise, 41, 154–160
  phase noise, 211
  sources, 155
  statistics, 158–160
nonselective excitation, 99–107

off resonance
  during excitation, 109
  effects on fast sequences, 188–189
  effects on imaging, 129–134
  effects on signal, 129
  sources, 127–129

phase, 5
phase encoding, 37, 38, 80
phase sensitive detection, *see* demodulation
physics, 23–26, 45–55
projection, 32, 35
projection reconstruction, 32–34, 74–78
  three-dimensional, 180–184
  timing diagram, 75
  trajectory, 75
projection slice theorem, *see* central section theorem

projections, 10
projective imaging, 185–186
Purcell, Edward, 2

radiofrequency fields, 24–26, 214–217
  surface coils, 216
random processes, 19
random variables, 17
Rayleigh density, 18, 160
readout gradient, 80
relaxation, 26, 50–51, 59
  spin-lattice T_1, 50
  spin-spin T_2, 50–51
    effect on imaging, 144–145
  values of, 52
resonant frequency, *see* Larmor frequency
RF inhomogeneities, 145
Rician density, 19, 160
rotating frame transformation, 102–104, 121–122
rotation matrices, 15

sampling, 12
  in k-space, 84–89
saturation recovery, 148–150
selective excitation, 29–30, 107–120
shimming, 127
signal equation, 63–70
  baseband, 64
  for three-dimensional imaging, 178
  simple derivation of, 69
  with chemical shift, 194
signal-to-noise ratio, 41, 154
  B_0 field dependence, 157
  body-noise dominance, 157–158
  definition, 154
  effect of acquisition time, 160–163
  effect of spatial resolution, 164–165
  sequence parameter dependence, 160–163
  summary, 165
slice-select gradient, 80
small tip-angle approximation, 111–114, 123
SNR, *see* signal-to-noise ratio
spatial frequency, 7
spatial resolution, 89–92
  effect on SNR, 164–165
spectroscopic imaging, 193–201
  3DFT, 195–198
  N-component imaging, 199–201
  with time-varying gradients, 198–199
spin angular momentum, 23, 45
spin density, 51
spin echo, 134, 136–144
  multiple echoes, 191
spins, *see* spin angular momentum
spiral imaging, 187
susceptibility, 128

TE, 147
three-dimensional Fourier transform, 179–180
tip angle, 106
TR, 147
truncation artifact, 92
  reduction of, 92
two-dimensional Fourier transform, 35–40, 78–83
  field of view, 86
  off resonance effects, 131
  spatial resolution, 89–92
  spin echo pulse sequence, 140
  timing diagram, 78, 79
  trajectory, 78, 79

Nor
800118 106336